

Electronic phase behaviors in spin-orbit coupled magnets at the localized and itinerant limits

Author: Xiang Chen

Persistent link: <http://hdl.handle.net/2345/bc-ir:108183>

This work is posted on [eScholarship@BC](#),
Boston College University Libraries.

Boston College Electronic Thesis or Dissertation, 2018

Copyright is held by the author. This work is licensed under a Creative Commons Attribution 4.0 International License (<http://creativecommons.org/licenses/by/4.0>).

Electronic phase behaviors in spin-orbit coupled magnets at the localized and itinerant limits

Xiang Chen

A dissertation submitted to
the Faculty of the Department of Physics
in partial fulfillment of the requirements for the degree of
Doctor of Philosophy

Boston College
Morrissey College of Arts and Sciences
Graduate School

May 5, 2018

© 2018 by
XIANG CHEN
All rights reserved

Abstract

Electronic phase behaviors in spin-orbit coupled magnets at the localized and itinerant limits

Xiang Chen

Advisor: Prof. Stephen D. Wilson

The magnetic interaction in materials generally can be categorized into two extremes: localized and itinerant. This work will focus on the electronic and magnetic properties of two prototypical magnetic compounds, which fall into the opposite extremes, *i.e.*, the spin-orbit coupled Mott insulator Sr_2IrO_4 (Sr214) described by the localized Heisenberg model and the itinerant helical (nearly-ferromagnetic) metal MnSi pictured with band or Stoner magnetism.

The single layered cuprate analogue Sr_2IrO_4 has attracted considerable attentions in recent years, due to its unusual electronic and magnetic properties and the potential to access superconducting states. The exotic $j_{\text{eff}} = 1/2$ ground state for the Ir^{4+} ($5d^5$) ions results from the delicate balance of competing/cooperating energy scales, such as the stronger spin-orbit coupling (SOC) in $5d$ materials as compared to $3d$ transition metal oxides (TMOs), crystal electric field (CEF) splitting and electron-electron correlations. Superconducting states are theoretically predicted to be achievable if sufficient carriers are introduced into this spin-orbit assisted compound, which later triggers tremendous experimental works toward the realization of superconductivity. Here in this work a combined study of various probes, such as transport, magnetization, X-ray and neutron scattering measurements, focusing on the electronic and magnetic properties, is presented in the perturbed spin-orbit cou-

pled Mott (SOM) state. Specifically in electron doped $(\text{Sr}_{1-x}\text{La}_x)_2\text{IrO}_4$, a detailed mapping of magnetism with respect to electron doping is presented, demonstrating the gradual transition from long range magnetic order in parent state, to intermediate short range order, and eventually into the incommensurate (IC) spin density wave (SDW) state with increasing electron doping. Our picture supports the conjecture that the quenched Mott phases in electron-doped Sr_2IrO_4 and hole-doped La_2CuO_4 share common competing electronic phases.

On the other hand, the prototypical itinerant metal MnSi is examined by inelastic neutron scattering (INS). Our experimental data directly demonstrate the collapse of linear spin wave theory for localized Heisenberg magnets in the large energy limit, although the low energy dispersion is still described by the ferromagnetic spin wave theory. Most importantly, our observations display the chimney-like dispersion spectrum up to the energy scale of at least 240 meV, which is more than one order of magnitude larger than the Heisenberg interaction energy scale. For the first time, solid characterizations of Stoner excitations in itinerant helimagnet (nearly ferromagnetic) have been demonstrated up to an exceedingly large energy scale. Our intriguing results will greatly promote further understanding and exploration of Stoner excitations in itinerant magnets.

Acknowledgements

I'd like to begin by expressing my sincere gratitude to my advisor Prof. Stephen Wilson. I am very fortunate to have the great opportunity to join his group and work with him for the past several years. He is a real model of a good scientist and group leader that I should follow. First of all, his expertise and knowledge in condensed matter experiments are truly amazing, which clarify my now and then confusions in research. His broad connection to collaborators from all of the world and strong motivations to innovate in new directions and experience new experimental techniques are so incredible and beneficial to all of us in his group. I am also very lucky to have the opportunity to closely observing his great communicating and presenting skills in demonstrating good science. Another aspect I want to emphasize is his group management. The Wilson group is like a second family to me. Thanks to Stephen's great management, I had the great freedom to endeavour in my own pace. I also had great experience with all of the group members which makes my research and life much more fun and easier. Last but not least, I am thankful in following him to relocate to a new place Santa Barbara, which is not only cozy and beautiful, but also great for research in material science and condensed matter physics.

I also want to thank the other members of my committee: Prof. Kevin S. Bedell, Prof. Kenneth Burch and Prof. Ilija Zeljkovic. Kevin is like a second advisor to me. I am really grateful to him for guiding me a whole summer, before I joined Wilson group. He is also one of the initiators of my project in investigating the itinerant magnetic excitations. His great insights greatly relieve our puzzling interpretation of the intriguing experimental data. Here I want to thank the whole committee again for their valuable suggestions and insightful criticisms during my

research proposal and defense, and the time and efforts in careful reading of my thesis.

On the professional level, I am fortunate to have great collaborators from various universities and national labs, which makes the experimental data collection and theoretical interpretation much simpler. Those great scientists include: Zac Ward, Alexander Kolesnikov, Matthew Stone, Wei Tian and Athena Sefat from Oak Ridge National Lab; D Parshall, Yang Zhao, Leland Harriger and Jeffrey Lynn from NIST Center for Research; Jacob Ruff and Kenneth D.Finkelstein from CHESS at Cornell; Zahirul Islam from Argonne National Lab; R. J. Birgeneau from Berkeley; Dmitry Reznik from CU Boulder; Zahra Yamani from CNBC. There are also lots of unnamed scientists and staff, who provided the great supports and made the experiments and research possible.

Back to campus, I am really grateful to all of the professors in the department who spent time teaching me all of the physics. To name a few: Vidya Madhavan, Ziqiang Wang, Ying Ran, Baldassare Di Bartolo and Pradip Bakshi. I'd like to emphasize the close collaborations and great supports from professors in the department, such as Vidya Madhavan, Cyril Opeil, Michael Graf and Ruihua He. Other than research, I would like to thank lots of great companions and assistances back then from my seniors, classmates, friends, etc. It would be a long list if the complete list is presented, therefore I would only mention a few: Yuan-Ming Lu, Yi Zhang, Yun Peng, Tianyi Sun, Hua Li, Fan Ye, Kevin Lucas, Steven Disseler, D Walkup, Wenwen Zhou, Mani Pokharel, Xinyu Liu, Claire Watts, Bing Ye, Mengliang Yao, Kun Jiang, Bolun Chen, Shenghan Jiang, etc. Last but not least, I would like to thank all of the staff members such as Jane, Sile, Nancy, etc and the other unnamed friends and scientists who made my graduate student life unforgettable and meaningful.

I would also like to say thanks to the assistances and valuable suggestions I got from professors, colleagues and friends at Santa Barbara, where I spent the last three years. Those names include Michael Chabiny, Ram Seshadri, Susanne Stemmer, James Allen and all of their group members. A few more names that I would like to

add to my thank-you-list are those helpful staff like Amanda Strom, Gang Wu, Bob Hanson, Mark Cornish. Last but not least, I would like to express my special thanks to my officemates Jamie and Katie at Elings, who are very friendly, humorous and made my life much more fun and memorable.

Certainly the dissertation won't be possible without the general supports and helpful discussions from the whole Wilson group members, including Chetan Dhital, Tom Hogan, Zhensong Ren, Rebecca Dally, Ryan Need, Julian Schmehr and so on. Specifically, I want to mention my senior colleague Chetan Dhital, and also Tom Hogan, who is just so friendly, patient and offered me tremendous help.

Before I end, here I want to say thank you to my family. Although you are not directly involved, but thank you so much for the supports in all of these years. Last but not least, I'd like to thank my girlfriend Yi for her patience and great supports all of the time.

I was really fortunate that I spent years at two totally different places and met so many nice people around. To those friends, staff, scientists, professors and my family, unnamed and named, here I want to express my sincere gratitude again. This is not possible without you!

Xiang Chen

03/2018

Santa Barbara

Contents

1	Introductory Material	1
2	Basic magnetic properties: from localized magnets to band magnetism	5
2.1	Magnetic moment of free ions	6
2.2	Spin orbit coupling (SOC)	8
2.3	Magnetic properties of localized magnets	9
2.3.1	Non-interacting system	9
2.3.2	Interacting system	10
2.3.3	Spin Hamiltonian of localized magnets	11
2.3.4	Low energy magnetic excitations in localized magnets	14
2.3.5	Spin orbit coupling in localized systems	15
2.4	Magnetic properties of itinerant metals	16
2.4.1	Brief history	16
2.4.2	Non-interacting electron gas: Pauli paramagnetism	17
2.4.3	Spontaneous magnetization: Stoner criterion	18
2.4.4	Random phase approximation (RPA) theory of spin fluctuations	21
2.4.5	Self-consistent renormalization (SCR) theory	23
2.5	General remarks: Localized vs. Itinerant systems	26
2.5.1	Curie-Weiss behavior	26
2.5.2	Magnetic excitations in the long wavelength limit ($q \rightarrow 0$)	27

2.5.3	General comparison of characteristic magnetic properties between localized and itinerant ferromagnets: degree of itineracy	28
3	Experimental techniques	31
3.1	Sample growth	32
3.1.1	Solid state synthesis	32
3.1.2	Flux based single crystal growth	32
3.2	Sample characterizations	35
3.2.1	X-ray diffraction	35
3.2.2	Energy-dispersive X-ray spectroscopy	37
3.2.3	Transport measurement	39
3.2.4	Magnetization measurement	40
3.3	Neutron scattering	42
3.3.1	The basics of neutrons	42
3.3.2	The principle of neutron scattering	44
3.3.3	Coherent elastic nuclear scattering	46
3.3.4	Coherent inelastic nuclear scattering	46
3.3.5	Coherent magnetic scattering	47
3.3.6	Neutron scattering instruments	49
3.4	X-ray scattering	52
3.4.1	The principle of X-ray scattering	52
3.4.2	REXS cross section	54
3.4.3	REXS instrument	56
3.5	Comparison between X-ray and neutron	58
4	Collapse of spin orbit assisted Mott insulating state in electron doped Sr_2IrO_4	61
4.1	Introduction	62
4.2	Background information	63
4.3	Influence of electron doping on the ground state of $(\text{Sr}_{1-x}\text{La}_x)_2\text{IrO}_4$	66

4.3.1	Sample synthesis	66
4.3.2	Structure information	66
4.3.3	Charge transport measurements	68
4.3.4	Magnetization measurements	70
4.3.5	Neutron scattering measurements	74
4.3.6	Scanning tunneling microscopy measurements	77
4.3.7	Discussion	79
4.3.8	Section summary	82
4.4	Unidirectional spin density wave state in metallic $(\text{Sr}_{1-x}\text{La}_x)_2\text{IrO}_4$	83
4.4.1	Introduction	83
4.4.2	Synchrotron X-ray scattering experiments	84
4.4.3	Scattering geometry	84
4.4.4	Remnant long-range and short-range order ($x < 0.04$)	85
4.4.5	Observation of spin density wave phase ($x = 0.04$)	87
4.4.6	Unidirectionality of spin density wave phase ($x = 0.04$)	90
4.4.7	Further evolution of spin density wave phase ($x = 0.041$)	92
4.4.8	Comparison of spin-spin correlation lengths	93
4.4.9	Phase diagram: Magnetic order in $(\text{Sr}_{1-x}\text{La}_x)_2\text{IrO}_4$	96
4.4.10	Discussion	97
4.4.11	Conclusions	100
5	Isovalent destabilization of spin-orbit Mott state in Ca doped Sr_2IrO_4	101
5.1	Introduction	102
5.2	Experimental details	103
5.3	Experimental results	104
5.3.1	$0 \leq x \leq 0.11$, $y = 0$, $z = 0$, $(\text{Sr}_{1-x}\text{Ca}_x)_2\text{IrO}_4$ Ruddlesden-Popper phase	104
5.3.2	$x = 1/4$, $y = 0$, $z = 1/2$, $\text{Sr}_3\text{CaIr}_2\text{O}_9$ honeycomb lattice phase	112
5.3.3	$x \geq 0.75$, $y = 1/3$, $z = 0$, $(\text{Sr}_{1-x}\text{Ca}_x)_5\text{Ir}_3\text{O}_{12}$ edge-sharing IrO_6 chain phase	116
5.4	Discussion	120

5.5	Conclusions	123
6	Itinerant excitations in prototypical helimagnet MnSi	125
6.1	Introduction	126
6.2	Bulk properties of MnSi	127
6.2.1	Basic properties	127
6.2.2	Energy scales and Hamiltonian	129
6.2.3	Early neutron scattering experiments	130
6.3	Experimental details	133
6.4	Experimental results	134
6.4.1	Separation of phonon contributions	134
6.4.2	High energy magnetic excitations in MnSi	136
6.4.3	Local dynamic susceptibility	138
6.5	Discussion	139
6.6	Conclusions	141
7	Conclusions and perspective	142
	Bibliography	144

List of Figures

1.1	Schematic phase diagram as a function of electronic correlation U/t and SOC λ/t in the unit of t , where t is the hopping amplitude. In the limit of $\lambda/t \rightarrow 0$, the SOC is minimized, and the Hubbard model is recovered as described above, where conventional metallic band picture and Mott insulating phases are expected. The inclusion of comparable SOC energy scale induces the novel ground states, including the spin-orbit assisted Mott insulating state, Weyl semimetal and topological insulating states in iridates. Adopted from Ref [1]	2
2.1	Hydrogen like atom with only one electron.	6
2.2	Total magnetic moment $\boldsymbol{\mu}_J = \boldsymbol{\mu}_L + \boldsymbol{\mu}_S$ with $\mathbf{J} = \mathbf{L} + \mathbf{S}$	7
2.3	Illustration of DM vector	12
2.4	Pauli paramagnetism results from field induced band splitting	18
2.5	(a) Spontaneous band splitting with spin up majority band and spin down minority band. Single spin up electron can hop to the empty state in the minority band, leaving an effective hole in the majority band, and forms the Stoner electron-hole pair. (b) Stoner continuum (grey region) results from the single spin flip excitation. The blue line shows the low energy spin wave excitations predicted from random phase approximation (RPA) theory.	21
2.6	Dynamical susceptibility in a ferromagnetic electron gas: (a) RPA approximation (b) Stoner's excitations. Adopted from [2].	22

2.7	$\chi_0/\chi(T)$ vs. T simulated with SCR theory (solid lines) and Stoner's theory (dash line). An electron-gas like band was used. Adopted from [2].	24
2.8	Temperature dependence of mean-square local amplitude of spin fluctuations S_L^2 in weak FM metals and local moment systems. Adopted from [2].	25
2.9	Temperature dependence of itinerant and localized moment systems. Adopted from [3].	27
2.10	Rhodes-Wohlfarth plot: p_c/p_s vs. T_c . Adopted from [4].	30
3.1	Cartoon showing flux growth of single crystals inside a box furnace	33
3.2	A typical heating sequence profile for the flux growth of Sr_2IrO_4 single crystals	33
3.3	Sr_2IrO_4 single crystals from one typical batch of SrCl_2 flux growth.	34
3.4	Typical power X-ray diffraction patterns during polycrystal Sr_2IrO_4 solid state synthesis	36
3.5	SEM image of cleaved surface of one La doped Sr_2IrO_4 single crystal	37
3.6	Histogram of repeated EDS measurements on a 5%La doped Sr_2IrO_4 single crystal.	38
3.7	Typical EDS spectrum from one La doped Sr_2IrO_4 single crystal . .	39
3.8	Typical four-probe measurement of resistivity in a sample. The inner two probes 2 and 3 measure the voltage, while the outer probes are for the current.	40
3.9	Schematics of the MPMS system. Adopted from [5].	41
3.10	Variation of coherent scattering length b with atomic number (empty symbols). Some isotopes are shown in solid symbols. Adopted from [6].	43
3.11	Various applications of inelastic neutron scattering in terms of energy and momentum transfer. Adopted from [6].	44
3.12	(a) Schematic of a triple-axis spectrometer at HB1A of Oak Ridge National Lab (ORNL); (b) Real image of HB1A. Adopted from [7].	50

3.13	Schematic view of the time of flight spectrometer SEQUOIA at SNS of ORNL, indicating all of the major instrument components. Adopted from [8].	51
3.14	Interaction of a photon with an atomic electron. (a) Photoelectric absorption, (b) Thomson scattering, (c) Resonant elastic scattering. Adopted from [9].	53
3.15	Resonant elastic X-ray scattering (REXS) geometry. A vertical scattering plane was employed. The incoming beam was horizontally polarized perpendicular to the scattering plane.	57
3.16	REXS instrument at 6-ID-B at advanced photon source.	57
3.17	(left) Average and peak brilliance for synchrotron facilities. (Right) Thermal neutron flux at neutron facilities. Adopted from [10].	58
4.1	Crystal and magnetic structure of Sr_2IrO_4 , for simplicity tetragonal space group $I4_1/acd$ is adopted.	64
4.2	Bulk properties of Sr_2IrO_4 . (a) Magnetization, (b) isothermal magnetization, (c) In-plane resistivity, (d) $J_{\text{eff}} = \frac{1}{2}$ ground state, (e) Formation of $J_{\text{eff}} = \frac{1}{2}$ ground state, considering energy scales CEF, SOC and U.	65
4.3	Synchrotron powder X-ray diffraction data of $(\text{Sr}_{1-x}\text{La}_x)_2\text{IrO}_4$ at 300 K, collected at 11-BM line at Advanced Photon Source at Argonne National Laboratory. (a) parent $x = 0$, (b) $x = 0.04$, (c) $x = 0.05$	67
4.4	Refined structural parameters in $(\text{Sr}_{1-x}\text{La}_x)_2\text{IrO}_4$ at 300 K: lattice a , lattice c , unit cell volume V , in-plane Ir-O-Ir bond angle α and octahedral canting angles θ	68
4.5	Temperature dependent in-plane resistivity on select $(\text{Sr}_{1-x}\text{La}_x)_2\text{IrO}_4$ single crystals.	69
4.6	Efros-Shklovskii form of variable range hopping fit to the resistivity data of $x = 2\%$	70

- 4.7 Temperature dependent in-plane magnetization data from $(\text{Sr}_{1-x}\text{La}_x)_2\text{IrO}_4$ single crystals. The high temperature onset of static canted AF correlations are present on both zero field cooled (ZFC, empty symbols) and field cooled (FC, solid symbols) data. The low temperature cusps are due to the formation of spin glass phase. 71
- 4.8 Subtraction between FC and ZFC magnetization data in 4.7. Inset shows enlarged window, tracking the canted AF onset temperatures with black arrows. 72
- 4.9 AC susceptibility data showing frequency dependent T_F in $x = 0.01$ La doped Sr214 sample. The DC data on the same sample is also shown (empty olive circles) for comparison. 73
- 4.10 Isothermal magnetization data from $(\text{Sr}_{1-x}\text{La}_x)_2\text{IrO}_4$ single crystals, collected at 5 K with in-plane magnetic field. 74
- 4.11 Temperature dependence of the inverse of the spin susceptibility χ , with the constant Pauli term χ_0 subtracted, for the $x = 0$ and $x = 0.06$ samples. Solid lines are Curie-Weiss fits to the high-temperature data. 75
- 4.12 Neutron scattering data showing momentum scans through the magnetic Bragg position $Q = (1,0,2)$. (a) Radial Q scans through the AF Bragg peak $(1, 0, 2)$ collected at 4 K for both $x = 0.01$ and $x = 0.02$. The background is subtracted and then the intensity is normalized to the intensity from the $(0, 0, 4)$ nuclear Bragg peak. (b) Radial Q scans through the AF Bragg peak $(1, 0, 2)$ for $x = 0.02$ sample at both 4 and 250 K. 76
- 4.13 Evolution of the low-temperature ordered AF moments in La-doped Sr214. Solid symbols: ordered AF moment measured through neutron scattering; open symbols: estimated AF moment assuming the AF canted spin structure of Sr214 together with refined octahedral canting angles for each doping concentration. Shaded region represents the long range order region. 77

- 4.14 (a) A representative, $12 \times 12 \text{ nm}^2$ STM topography of a sample with $x \approx 0.05$ nominal La doping, taken at $V_b = +300 \text{ mV}$ at $I_{\text{set}} = 80 \text{ pA}$. (b) Gap map extracted from a $\frac{\delta I}{\delta V}$ map, $15 \times 15 \text{ nm}^2$, taken on the same sample as in (a) but over a different area. (c) Dopant density map taken in the same area as (b); dopants were counted visually. (d) Line cut showing the evolution of the $\frac{\delta I}{\delta V}$ spectra from fully gapped (purple) to no gap (red). The position and orientation of the line cut is indicated by the black arrows in (b) and (c). 78
- 4.15 Evolution of magnetic order in La-doped Sr214. Blue circles denote the AF ordering transition measured directly with neutron scattering data, and pink triangles denote the onset of irreversibility in magnetization data. Dashed lines mark the suggested boundaries between short- and long-range AF order. The proposed low-temperature spin glass phase boundary is denoted by cyan pentagons. 81
- 4.16 REXS data in the polarization flipped $\sigma - \pi$ channel of sample $x = 0.02$ (purple) and $x = 0.028$ (blue). **a** and **b** show K and L scans through the $(0, 1, 14)$ position at $T = 10 \text{ K}$ respectively. **c** Energy dependence of the $(0, 1, 14)$ peak at 10 K and its comparison to the Ir L_3 fluorescence line. **d** Temperature dependence of the $(0, 1, 14)$ peaks for both samples. Data have been normalized to appear on the same scale. The solid lines in (**a**, **b**, **d**) are the fits to the data. Data are collected at the energies of 11.217 and 11.215 keV for the $x = 0.02$ and $x = 0.028$ sample, respectively. All vertical error bars in the figure represent 1 standard deviation (s.d.) statistical errors. 86
- 4.17 REXS data from sample $x = 0.04$ collected at 6-ID-B. **a**, **b** H, K maps at the $(0, 0, 16)$ and $(0, 1, 14)$ zones at $T = 10 \text{ K}$ 87

- 4.18 Additional REXS data from sample $x = 0.04$ collected at 6-ID-B. **a**, H scans at select $(0, 1, 4N + 2)$ ($N = 2, 3, 4$) magnetic zone centers at 10 K collected both in the $\sigma - \pi$ channel and the $\sigma - \sigma$ channel. Solid lines are fits to the data with three Lorentzian peaks, which are individually represented by blue tan and cyan shaded areas. Data collected at different zones and in different channels are offset for comparison. **b**, L scans at the commensurate $(0, 1, 14)$ and incommensurate $(-0.0035, 1, 14)$ positions at 10 K (solid symbols) and at 200 K (empty symbols). The solid lines are fits to the data with a single Lorentzian peak and the dashed line denotes the instrumental resolution. **c**, Energy scans at the commensurate and incommensurate peak positions. Data are offset for clarity. **d**, Temperature dependence of the three peaks resolved in the H scan of $(0, 1, 14)$ from **a**. Other than **(c)**, all data are collected at the energy of 11.214 keV. All vertical error bars in the figure represent 1 *s.d.* statistical errors 88
- 4.19 REXS data from sample $x = 0.04$ collected at 6-ID-B after the sample was rotated counterclockwise by 90° . **(a)**, K scan at $(1, 0, 10)$ at $T = 10$ K. The inset shows the H, K map about the $(1, 0, 10)$ position and the magenta line denotes the scan direction in the main panel. **(b)**, the detailed H, K map around the resulting $(1, 0, 10)$ reflection. Data from K scans through this map (cuts #1 and #2) are shown in panels **(c)** and **(d)**. No splitting along K is observed, and additional analysis suggests a splitting still occurs along the H direction. 90
- 4.20 Additional REXS data from sample $x = 0.04$ collected at 6-ID-B after the sample was rotated counterclockwise by 90° . **(a)** Energy dependence of H scans about the $(1, 0, 14)$. Select H scans around $(1, 0, 14)$ at energies $E = 11.209$ keV (dark cyan) and $E = 11.217$ keV (red) are illustrated as lines with the corresponding data plotted in **(b)**. 91

- 4.21 REXS data from sample $x = 0.041$ taken at CHESS, A2. **a** and **b** show H, K maps $T = 10$ K around the nuclear $(0, 0, 16)$ and magnetic $(0, 1, 14)$ zones respectively. **c**, H scan at $(0, 1, 14)$ at 10 K exhibiting two IC peaks at $(-0.003, 1, 14)$ and $(0.006, 1, 14)$. **d**, H scan at $(-1, 0, 20)$ showing the two IC peaks split along the H direction 10 K and their absence at 190 K. IC peaks in **c** and **d** are both separated by 0.009 *r.l.u.* **e**, The temperature dependence of the two IC peaks. Both IC peaks disappear at the same temperature $T_{\text{SDW}} = 182 \pm 8$ K. **f**, Energy dependence of the IC peak at $(0.006, 1, 14)$ and its comparison to the $(0, 0, 16)$ charge peak. The solid lines in **c–e** are the fits to the data. Other than **f**, all data are collected at the energy of 11.217 keV. All vertical error bars in the figure represent 1 *s.d.* statistical errors. 93
- 4.22 Resolution deconvolved c -axis correlation lengths for the saturated antiferromagnetic states ($T = 10$ K) are plotted as a function of doping x in $(\text{Sr}_{1-x}\text{La}_x)_2\text{IrO}_4$. Below $x \approx 0.02$, the magnetic peaks are resolution limited, indicating the true long range nature. With increasing doping, the correlation length decreases drastically before the emergence of the incommensurate order above the critical doping $x = 0.04$. Vertical error bars originate from the uncertainties in deconvolving the magnetic peak full width at half maximum (FWHM) Γ_{Mag} from the experimental resolution peak FWHM Γ_{Res} and are obtained through the error propagation from $\xi_c = \frac{0.44c}{2\pi(\Gamma_{\text{Mag}} - \Gamma_{\text{Res}})}$, where c is the lattice parameter along L 94
- 4.23 Comparison of magnetic and charge peak widths for the $x = 0.04$ (**a**) and $x = 0.041$ (**b**) samples. Upper right insets in (**a–b**) show the charge peak widths and these widths are over-plotted as dashed lines inside of the magnetic peaks for reference. The magnetic peaks around $(0, 1, 14)$ are reproduced from Fig. 4.18a and Fig. 4.21c. Vertical error bars represent 1 *s.d.* statistical errors. 95

- 4.24 Phase diagram of $(\text{Sr}_{1-x}\text{La}_x)_2\text{IrO}_4$, as determined from a combination of magnetization and neutron scattering [11], RIXS [12], and REXS (this work) measurements. The long-range to short-range canted antiferromagnetic (CAF) transition occurs near $x = 0.02$. At the critical doping $x = 0.04$, part of the material transitions into an incommensurate spin density wave (SDW) state. Dash lines are guides to eyes. The insets with red dots schematically represent commensurate and incommensurate (IC) peak positions investigated in this experiment. Horizontal error bars originate from repeated energy dispersive spectroscopy (EDS) measurements. Vertical error bars are estimated from the disappearance of magnetic peak intensity in Fig. 4.16d and Fig. 4.18d and Fig. 4.21e. 96
- 4.25 Illustration of how domain structure can alter apparent incommensurate positions. (a) Tetragonal and orthorhombic axes for the IrO_2 planes. Tetragonal here denotes the smaller unit cell where H and K point along the Ir-Ir bond direction while orthorhombic denotes the larger unit cell with H and K parallel to the bond diagonals. Two potential domains A and B are marked if the lattice were to be subtly orthorhombic. (b) H and K axes again in the larger cell are depicted with circles denoting the aligned (1,0) and (0,1) positions assuming $a_{\text{orth}} = b_{\text{orth}}$ and the relative orientations of the A and B domains are also illustrated under this assumption. Stars denote the unidirectional splitting from each domain with modulation along its local H_{orth} -axis. 99
- 5.1 Synchrotron powder x-ray diffraction collected at 300 K on select Ca concentrations of $(\text{Sr}_{1-x}\text{Ca}_x)_2\text{IrO}_4$ with (a) $x = 0.02$, (b) $x = 0.05$, (c) $x = 0.07$ (d) $x = 0.11$. Inset shows expanded portion of the data and corresponding fit. 105

- 5.2 Lattice parameters and in-plane IrO_6 canting angles θ determined at 300 K from synchrotron PXRD refinement. (a) a -axis lattice parameters, (b) c -axis lattice parameters, and (c) in-plane IrO_6 octahedral canting angles θ are plotted as a function of Ca-substitution x . For comparison, data resulting from La^{3+} substitution reported previously [11] are overplotted with effect of Ca^{2+} substitution. Pink symbols represent Ca substitution, while dark cyan symbols represent La doping. 106
- 5.3 The temperature dependence of the ab -plane resistivity of $(\text{Sr}_{1-x}\text{Ca}_x)_2\text{IrO}_4$ plotted for Ca concentrations of $x = 0.02$ (grey symbols), $x = 0.05$ (dark red symbols), $x = 0.07$ (dark green symbols), and $x = 0.11$ (blue symbols). 108
- 5.4 Magnetization data collected on $(\text{Sr}_{1-x}\text{Ca}_x)_2\text{IrO}_4$ samples. (a) Temperature dependent magnetization data collected under ZFC and FC with the magnetic field applied in the ab -plane and $\mu_0 H = 0.03$ T. (b) Irreversibility of the magnetization data plotted in panel (a) determined by subtracting FC and ZFC data. 109
- 5.5 (a) ab -plane isothermal magnetization of $(\text{Sr}_{1-x}\text{Ca}_x)_2\text{IrO}_4$ collected at $T = 5$ K. Inset shows an expanded subset of the data with the field swept between -0.6 T to 0.6 T. (b) Saturated magnetization plotted as a function of Ca concentration x and collected with $\mu_0 H = 5$ T applied parallel to the ab -plane. Overplotted are the canted projections of the net magnetization using an assumed ordered moment $m_{AF} = 0.455 \mu_B/\text{Ir}$ and the measured IrO_6 octahedral canting angles θ 111
- 5.6 Synchrotron PXRD of crushed $\text{Sr}_3\text{CaIr}_2\text{O}_9$ single crystals collected at (a) 100 K, (b) 295 K, and (c) 473 K. The data are indexed fit within space group $P2_1/c$. Inset in panel (c) shows the magnified view of the data and fit. 112

- 5.7 (a) Crystal structure of $\text{Sr}_3\text{CaIr}_2\text{O}_9$. For oxygen at the vertices of Ca and Ir centered octahedra are omitted. Sr atoms are represented by green balls. Ca-centered octahedra are plotted in blue and Ir-centered octahedra are plotted in green. (b) Projected bc -plane view of the lowest three layers of $\text{Sr}_3\text{CaIr}_2\text{O}_9$ from panel (a) showing the formation of buckled honeycomb lattice of Ir-octahedra. Distinct Ir-octahedra positions are labeled as Ir1 and Ir2. VESTA software was used for crystal structure visualization [13]. 113
- 5.8 Resistivity plotted as a function of temperature measured on a $\text{Sr}_3\text{CaIr}_2\text{O}_9$ single crystal. Inset shows the same data plotted as $\ln\rho$ versus $T^{-\frac{1}{3}}$ where the orange line shows a fit to VRH behavior with $D = 2$ and $T_0 = 5800\text{K}$ 115
- 5.9 (a) Temperature dependent susceptibility of $\text{Sr}_3\text{CaIr}_2\text{O}_9$ under an applied magnetic field of 0.03T. Cyan line is the Curie-Weiss fit across the whole temperature range, which lead to a small Curie temperature $\Theta_{CW} = -1.7 \pm 0.1\text{K}$ and a small effective moment $\mu_{\text{eff}} = 0.18 \pm 0.01\mu_B$. (b) Isothermal magnetization measured at $T = 5\text{K}$. Green line is the Brillouin function fit multiplied by an additional scaling constant 0.015, assuming $g = 2$ and $J = 1/2$. The necessity of applying the scaling constant is because not all Ir contribute to the magnetism, whereas the magnetization is normalized to the total number of Ir sites. 117
- 5.10 Temperature dependence of resistivity measured along the a and c -axes of $(\text{Ca}_{0.89}\text{Sr}_{0.11})_5\text{Ir}_3\text{O}_{12}$. The main panel shows ρ_a along the a -axis and the lower left inset plots ρ_c along the c -axis. Upper inset shows plot of $\ln\rho_a$ versus $T^{-\frac{1}{2}}$ and the corresponding VRH fit of resistivity with $D = 1$ and $T_0 = 23800\text{K}$ 118

- 5.11 Temperature dependence of the magnetization of $(\text{Ca}_{0.89}\text{Sr}_{0.11})_5\text{Ir}_3\text{O}_{12}$ collected under FC (closed symbols) and ZFC (open symbols) with $\mu_0 H = 0.03$ T applied within the ab -plane and along the c -axis. Inset shows the corresponding inverse susceptibilities with temperature independent background and Van Vleck terms removed, $1/(\chi - \chi_0)$. CW fits to the data are plotted as solid lines. 120
- 5.12 Phase diagram generated based on the growth sequence and procedures detailed in Section 5.2. Predominant structure types of $(\text{Sr}_{1-x}\text{Ca}_x)_{2-y}\text{IrO}_{4+z}$ that crystallize in each region of the phase diagram are shaded as light green (Sr_2IrO_4), light cyan ($\text{Sr}_3\text{CaIr}_2\text{O}_9$), and light purple ($\text{Ca}_5\text{Ir}_3\text{O}_{12}$). Regions of overlap denote concentrations where mixed phase crystals were obtained with the relative phase fractions denoted on the phase percentage axis. We note here that the bottom axis denotes the nominal, starting concentration (x_{nominal}) of Ca in the synthesis run. 122
- 6.1 Crystal structure of MnSi. Mn (cyan spheres) and Si (dark yellow spheres) 128
- 6.2 Magnetic phase diagram of MnSi at ambient pressure. At $B = 0$, MnSi develops the helical order below $T_c = 29.5$ K. The helical order can be polarized by external field with the transition from helical to conical to field-polarized state with increasing fields. Near the board between paramagnetic state and ordered state, an anomalous phase can be stabilized by a small external field. This phase is later identified as the topological skyrmions. Adopted from [14]. . . 128

- 6.3 Inelastic neutron scattering data on MnSi observed at 5 K in a field of 10 kOe along [100] direction around (011) zone with different energies. (a) Spin wave excitations with constant \mathbf{Q} scans using $E_f = 14.8$ meV. M is monitor counts. Arrows indicate the FWHM. (b) Contour maps of magnetic scattering with $E_f = 24$ meV. Spin wave dispersion determined from (a) is also included as circles. Phonon contribution was subtracted. Quadratic dispersion is shown by broken lines. (c) Intrinsic linewidth (upper panel) as well as integrated intensity (b) of spin waves with three different conditions $14.8 E_i$, $14.8 E_f$ and $24 E_f$ plotted against q . Adopted from [15]. 130
- 6.4 Magnetic excitation in a ferromagnetic electron gas calculated from RPA theory. (a) Schematical plot. (b) Magnetic excitation at 0 K. Excitation in the Stoner continuum is displayed as contour lines. Adopted from [15]. 131
- 6.5 Measured (symbols with colors correspond to different symmetries of the phonon modes) and calculated (solid lines) phonon frequencies in MnSi at $T = 15$ K. Curves obtained from spin polarized GGA calculations using the experimental value of the lattice constant while optimizing the positions of the Mn and Si atoms in the unit cell. Adopted from [16]. 133
- 6.6 Raw inelastic neutron scattering (INS) data of MnSi, scanned along [0,0,1] direction around the (1,1,0) zone with the incident energy $E_i = 18$ meV. Data was collected at 5 K without external field. Phonon dispersions are marked by black symbols, obtained by performing the detailed constant E scans. The magenta symbols represent the spin wave dispersions obtained by constant E scans of the map. . . . 134

- 6.7 INS data of MnSi, collected with the incident energy $E_i = 150$ meV at 5 K. (a) Momentum-energy map along the $[1,0,0]$ direction around the $(0, 1 -2)$ zone, highlighting the "pillar" like magnetic signals. (b) Constant E slices with H fixed to -2 . Since there is little dispersion along momentum direction, the energy is integrated from 66 to 116 meV, highlighting the broad ring like features in the KL plane. 135
- 6.8 Anisotropic spin wave dispersions in MnSi at 5 K, with a combination of data from various incident energies. The "chimney" or "pillar" effect is apparent. 136
- 6.9 Energy dependent damping coefficients at 5 K. Damped simple harmonic oscillators are adopted to fit the constant Q scans. 137
- 6.10 Local dynamic susceptibility of MnSi at 5K. 138
- 6.11 Magnetic dispersion relation along $\langle 1, 1, 0 \rangle$ direction in MnSi, collected at 5 K (orange symbols). The generalized ferromagnetic Fermi liquid theory (FFLT) for itinerant ferromagnets are applied to fit the data with two branches of collective modes, *i.e.* gapless Goldstone mode (dark green line) and gapped Higgs amplitude mode (dark cyan line). Spin wave stiffness constant D is obtained from fit to the low-lying Goldstone mode in the small q limit. The fit parameters $\Delta_{\text{Higgs}} = 48$ meV, and $D = 46$ meV \AA^2 139

List of Tables

2.1	Comparison of different energy scales in $3d$ and $5d$ compounds. Ref. [17, 18, 19, 20]	9
2.2	Characteristic magnetic properties in comparison between localized and weak itinerant ferromagnets. M , magnetization; χ , susceptibility; C_m , magnetic contribution to specific heat; p_{eff} , effective moment from Curie-Weiss law above critical temperature; p_s , low temperature saturation moment from isothermal magnetization. Ref. [2, 4]	29
4.1	Summary of samples measured, their crystal mosaic, and corresponding beam lines. The relative shifts in energy calibration for each beam line are also tabulated by denoting the observed Ir L_3 absorption edge energies.	84
5.1	Structural and refinement parameters for $(\text{Sr}_{1-x}\text{Ca}_x)_2\text{IrO}_4$ phase ($0 \leq x \leq 0.11$) at $T=295\text{K}$ with space group $I4_1/acd$. The atomic positions of (Sr/Ca), Ir, O1 and O2 are $(0, 0.25, z)$, $(0, 0.25, 0.375)$, $(x, x+0.25, 0.125)$, $(0, 0.25, z)$ respectively. The isotropic thermal parameters U of O1 and O2 at $x = 0.11$ are constrained to be the same.	107
5.2	Structural and refinement parameters for $\text{Sr}_3\text{CaIr}_2\text{O}_9$ phase at select temperatures. The space group $P2_1/c$, initial atom positions and fixed thermal parameters are adopted from D.C. Wallace <i>et al.</i> [21].	114

List of Symbols and Abbreviations

AF	Anti-ferromagnetic / Anti-ferromagnetism
BM	Band Magnetism
CEF	Crystal Electric Field
CW	Curie-Weiss
DFT	Density Functional Theory
DMFT	Dynamical Mean Field Theory
DM	Dzyaloshinskii-Moriya
DMI	Dzyaloshinskii-Moriya Interaction
DSDW	Diagonal Spin Density Wave
EDX/EDS	Energy-Dispersive X-ray Spectroscopy
FM	Ferromagnetic / Ferromagnetism
FWHM	Full Width at Half Maximum
IC	Incommensurate
INS	Inelastic Neutron Scattering
LSW	Linear Spin Wave
LD	Landau Damping
MIT	Metal Insulator Transition
NN	Nearest Neighbor

PPM	Pauli Paramagnetism
PXRD	Powder X-ray Diffraction
REXS	Resonant Elastic X-ray Scattering
RIXS	Resonant Inelastic X-ray Scattering
RP	Ruddlesden-Popper
RPA	Random Phase Approximation
SCR	Self-Consistent Renormalization
SDW	Spin Density Wave
SEM	Scanning Electron Microscope/Microscopy
SOC	Spin-Orbit Coupling/Coupled
SOM	Spin-Orbit Mott state
SQUID	Superconducting Quantum Interference Device
SW	Stoner-Wohlfarth
STM/STS	Scanning Tunneling Microscopy/Spectroscopy
TEM	Transmission Electron Microscopy
TMO	Transition Metal Oxides
TOF	Time Of Flight
XRD	X-ray Diffraction
Z	Atomic number

Chapter 1

Introductory Material

Emergent quantum phenomena from the interplay of spin, orbit, charge and lattice degrees of freedom can be very intriguing and never cease to bring surprises [22, 1, 17]. Prominent examples include unconventional high T_c superconductivity [23, 24, 25, 26], colossal magnetoresistance [27], quantum spin liquids [28, 29], *etc.* The effective $j_{\text{eff}} = 1/2$ state resulting from the interplay of competing/cooperating energy scales such as the celebrated strong spin orbit coupling (SOC), crystal electric field (CEF) and Coulomb repulsion in $5d$ materials, also attracted considerable attentions recently [30, 31, 1, 17]. A very simple model to understand the electronic behaviors consist of electron Coulomb repulsion U and the hopping amplitude t , which is summarized in the famous mean field single band Hubbard Hamiltonian [32, 22]:

$$\mathcal{H} = - \sum_{\langle i,j \rangle, \sigma} t_{ij} c_{i\sigma}^\dagger c_{j\sigma} + U \sum_i n_{i\uparrow} n_{i\downarrow} \quad (1.1)$$

where $c_{i\sigma}^\dagger$ ($c_{j\sigma}$) represent operators that create (annihilate) an electron with spin $\sigma = \uparrow$ or \downarrow at site i or j , $\langle i, j \rangle$ represents summation over nearest-neighbor (NN) sites, t_{ij} is the hopping amplitude between NN sites and $n_{i\sigma} = c_{i\sigma}^\dagger c_{i\sigma}$ is the spin-density operator.

In the limit of $U/t \rightarrow 0$, electrons will hop between sites with hardly any energy cost as U is much smaller than t . In this scenario, electrons are delocalized, behaving like free electrons described by band theory in metallic systems. In the

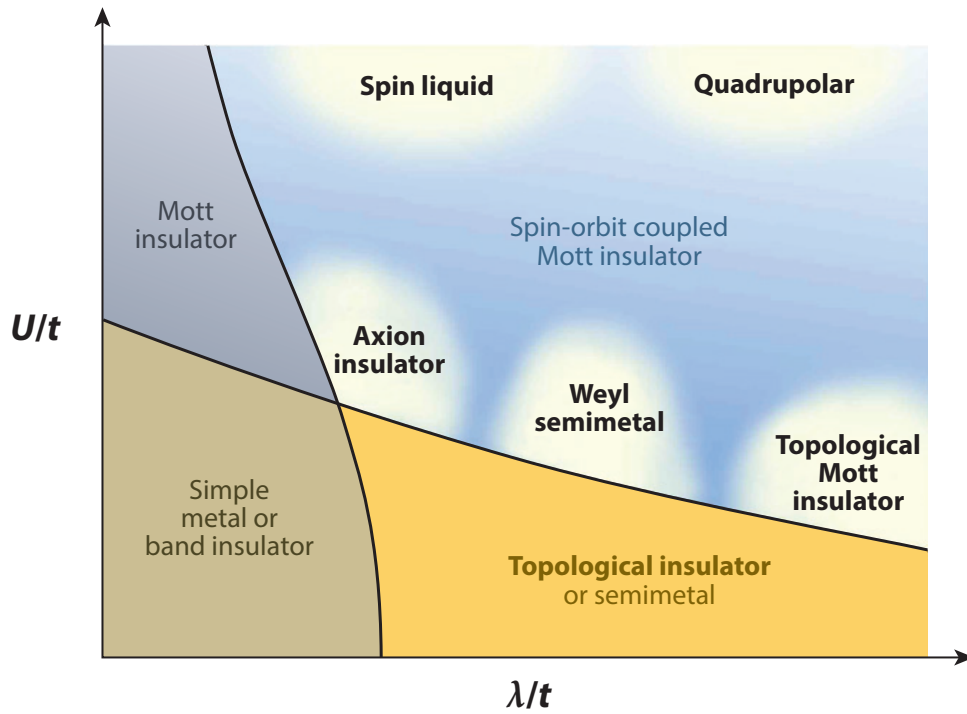


Figure 1.1: Schematic phase diagram as a function of electronic correlation U/t and SOC λ/t in the unit of t , where t is the hopping amplitude. In the limit of $\lambda/t \rightarrow 0$, the SOC is minimized, and the Hubbard model is recovered as described above, where conventional metallic band picture and Mott insulating phases are expected. The inclusion of comparable SOC energy scale induces the novel ground states, including the spin-orbit assisted Mott insulating state, Weyl semimetal and topological insulating states in iridates. Adopted from Ref [1]

opposite limit with $t/U \rightarrow 0$, however, the energy cost for electrons to hop between NN sites is so large, such that electron-electron correlation will localize electrons within sites and therefore drive the system into an insulating ground state. Naturally, a metal insulator transition (MIT) is expected if the U/t ratio in the system can be tuned systematically from 0 ($U \ll t$) to ∞ ($U \gg t$). This simple model describes a broad variety of MIT behaviors encountered in $3d$ transition metal oxides (TMO).

The inclusion of additional spin-orbit coupling energy scale further enriches the phase diagram, as compared to $3d$ TMOs. A schematic phase diagram is proposed, as a function of the electronic correlation U/t , and the SOC λ/t , in the unit of the hopping amplitude t (see Fig. 1.1). The novel ground states include spin-orbit assisted Mott insulating state, Weyl semimetal and topological insulating states, as expected in $5d$ materials where Iridium (Ir) based compounds stood out

and received considerable attentions in recent years. As an example, the novel $j_{\text{eff}} = 1/2$ state is realized in the prototypical spin-orbit coupled Mott insulator Sr_2IrO_4 ($\text{Sr}214$) and well elucidated the puzzling insulating behavior before taking the SOC effects into account [30, 31, 1, 17]. This novel $j_{\text{eff}} = 1/2$ ground state is expected in varieties of $5d$ TMOs, especially iridates. Therefore the persuasion of novel ground states in systems with intertwined degrees of freedom, which have tremendous future applications, are still the center topics.

On the other hand, in describing the magnetic excitations, the celebrated Heisenberg model turns out to be quite powerful and successful. It can not only be applied to localized magnets including the unconventional superconducting parent compounds like cuprates and iron pnictides [33, 34, 35, 36], whether in $3d$ TMOs [37] or $5d$ iridates [38, 39], but also to the low energy excitation of itinerant magnetic metals [2, 40, 41, 42]. Although there are some theoretical developments on the magnetic excitation of itinerant magnetic metals in the large q or energy limit [2], not much experimental work had been shown due to the intrinsic experimental difficulties because of the weak and broad distribution of spectrum weight. However, the advancement of new generations of large facilities like synchrotron light sources and neutron scattering facilities in national labs make it possible to escape the dilemma.

In this work, I will focus on the electronic and magnetic properties of two prototypical material, *i.e.*, the localized spin orbit coupled Mott insulator $\text{Sr}214$ and the itinerant helical (nearly-ferromagnetic) metal MnSi . The former is perturbed by electron and isovalent carrier doping, aiming for realizing novel ground states such as the proposed superconducting state as an analogue to the hole doped cuprate. The latter is studied by inelastic neutron scattering (INS) technique, focusing on the magnetic excitation in itinerant magnets, which is not well understood in the large q or energy limit.

In Chapter 2, I will begin with the introduction of the basics of magnetism, covering from localized magnets to itinerant magnetic metals. The picture about the magnetic moment will be introduced first, then the magnetic properties of local-

ized moment systems will be discussed in general. Then, as a comparison, magnetic properties from materials in the opposite extreme, *i.e.* itinerant magnetism, will be discussed as well. Finally, the general comparison between the two will be summarized.

In Chapter 3, the preliminary knowledge on the experimental techniques will be briefly discussed, from sample growth, to characterizations. Then the main techniques such as neutron scattering and X-ray scattering for probing magnetic properties will be introduced separately. Lastly, a general comparison between the two different techniques will be presented.

In Chapter 4, this chapter focuses on the electronic and magnetic properties in electron doped Sr_2IrO_4 . A combination of experimental techniques, such as transport, magnetization, scanning tunneling microscopy (STM), neutron scattering and resonant X-ray scattering, will be utilized to explore the perturbed spin-orbit assisted Mott state in Sr_2IrO_4 . A phase diagram will be presented in the end.

In Chapter 5, the electronic and magnetic properties of isovalent Ca doping on Sr_2IrO_4 will be examined in details, from a combined transport and magnetization measurements. This isoelectronic substitution and steric effects presents an alternative approach to destabilizing the spin-orbit coupled Mott state in Sr_2IrO_4 . Our results demonstrate lattice geometry freedoms in iridates could provide a variety of platforms for hosting exotic quantum phases.

In Chapter 6, the magnetic excitation on the prototypical itinerant helical metal MnSi will be studied in details. The anisotropic spin wave dispersions are mapped to high energies (~ 240 meV), establishing the existence of a transition to another regime where spin wave excitation spectrum are "chimney"-like. The experimental observations are compared to the ferromagnetic Fermi liquid theory (FFLT), which exhibit good agreement between our experimental data and theory. Thus our high energy INS study on MnSi provides a complete picture of magnetic excitation in itinerant compounds.

In Chapter 7, the final chapter, a brief summary of the present work and outlooks will be presented.

Chapter 2

Basic magnetic properties: from localized magnets to band magnetism

Magnetism is a very old subject yet a surprisingly rich variety of magnetic properties in real systems can be found [40, 41]. The fundamental entity in magnetism is the magnetic moment. In the classical picture described by electromagnetism it is treated as a current loop. In quantum mechanical view, the electrons (so as neutrons and protons, but usually with negligible contributions) carry the spin and orbit magnetic moment. An ensemble of electrons interact with each other, obeying the fundamental interaction rules like Coulomb repulsion, Pauli exclusion principle, spin orbit coupling, *etc.*, eventually spawn the diversified complexity of magnetism in real systems. In general, magnetic interaction in materials can be categorized into two opposite regimes, *i.e.*, localized and itinerant magnetism. In the following, the brief introduction of the two categories of magnetism are presented ¹.

¹A lot of the details can be referred from these good references: [2, 40, 41, 42]

2.1 Magnetic moment of free ions

Magnetism are the intrinsic properties of the "elementary" particles such as electrons, protons and neutrons. Since the nuclear magnetic moments are typically 10^{-3} times smaller than that of an electron, the magnetic properties are mainly determined by the electrons in the system. Therefore, electrons are the corner stones in determining the magnetic properties in real materials.

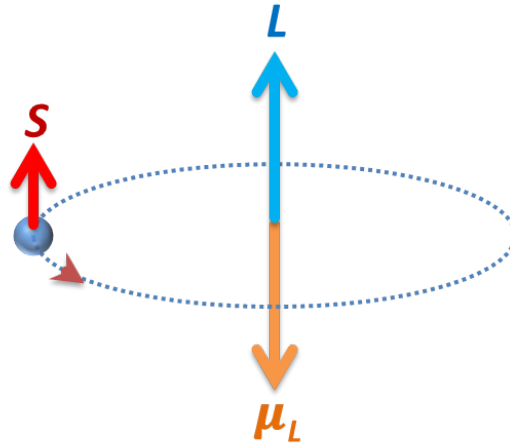


Figure 2.1: Hydrogen like atom with only one electron.

Consider one electron first (Fig. 2.1), as in the case of an Hydrogen atom, moving in the orbital around the nuclei in the quantum mechanical picture. The intrinsic spin magnetic moment is

$$\boldsymbol{\mu}_S = -g_S \mu_B \frac{\mathbf{S}}{\hbar} \quad (2.1)$$

Here g_S is the spin g factor and is approximately 2 for free electrons, μ_B the Bohr magneton, \hbar the reduced Planck constant, \mathbf{S} the electron spin angular momentum, and the '-' sign indicates that spin magnetic moment $\boldsymbol{\mu}_S$ is antiparallel to the spin angular momentum \mathbf{S} .

Similarly, the orbital contribution to magnetic moment resulting from the revolution of an electron can be expressed as

$$\boldsymbol{\mu}_L = -g_L \mu_B \frac{\mathbf{L}}{\hbar} \quad (2.2)$$

Here g_L is the electron orbital g factor and is exactly equal to one, by a quantum-mechanical argument.

The total magnetic moment consists of both the spin and orbital angular momenta of an electron and can be expressed as total angular momentum \mathbf{J} by a similar equation, as shown in Fig. 2.2.

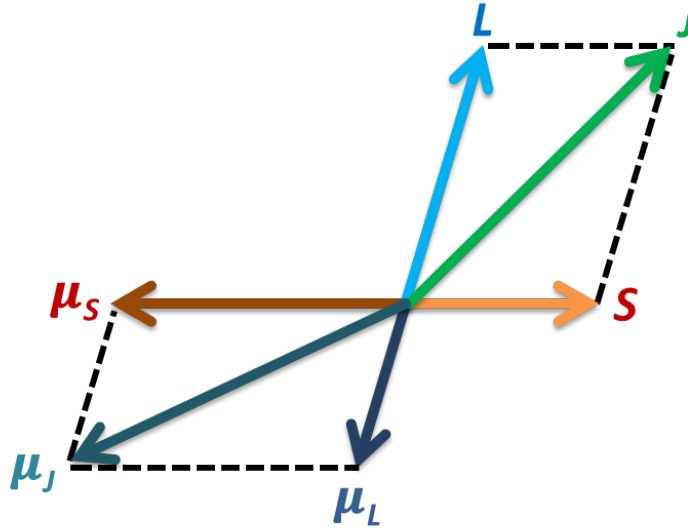


Figure 2.2: Total magnetic moment $\mu_J = \mu_L + \mu_S$ with $\mathbf{J} = \mathbf{L} + \mathbf{S}$

$$\mu_J = -g_J \mu_B \frac{\mathbf{J}}{\hbar} \quad (2.3)$$

with

$$g_J = \frac{3}{2} + \frac{1}{2} \frac{S(S+1) - L(L+1)}{J(J+1)} \quad (2.4)$$

When considering more electrons occupying the orbitals around an ion, Hund's rules are usually good references to begin with. In real materials, however, there are various types of interactions that could complexify the picture, such as crystal electric field splitting, spin orbit interaction, Coulomb repulsion, Pauli exclusion, *etc.* For example, the successful applications of Hund's rules are shown in numerous $4f$ -element based compounds, while in a variety of $3d$ TMOs the angular momentum \mathbf{L} is quenched [40, 41]. Therefore, the determination of magnetic moment for different systems should rely on both theoretical calculations and experimental

observations.

2.2 Spin orbit coupling (SOC)

Since at least one half of my research had been focused on the $5d$ materials, with considerable SOC energy scale, it is necessary to introduce this type of interaction along. Here the spin-orbit interaction is presented in a semi-classical picture.

Consider an Hydrogen-like atom again with atomic number Z . In the non-inertial frame of the electron, the positive nuclei charges orbit around the electron, producing a magnetic field \mathbf{B} , which follows

$$\mathbf{B} = -\frac{\mathbf{v} \times \mathbf{E}}{c^2} = \frac{\hbar}{m_e c^2} \frac{\mathbf{L}}{r} \frac{dV(r)}{dr} \quad (2.5)$$

where $V(r) = \frac{Ze}{4\pi\epsilon_0 r}$ is the electrostatic potential from the nuclei and \mathbf{v} is the velocity of the electron (nucleus). Thus the spin magnetic moment $\boldsymbol{\mu}_S$ will experience and respond to the generated magnetic field with the interaction Hamiltonian given by

$$\mathcal{H}_{SOC} = -\boldsymbol{\mu}_S \cdot \mathbf{B} = \frac{Ze^2 \hbar^2}{4\pi\epsilon_0 m_e^2 c^2} \frac{\mathbf{L} \cdot \mathbf{S}}{r^3} \quad (2.6)$$

Consider the realistic effect by adding the $\frac{1}{2}$ factor and evaluate the Hamiltonian in the $|n, l\rangle$ electronic state, then spin-orbit interaction Hamiltonian reaches

$$\mathcal{H}_{SOC} = \frac{e^2 \hbar^2 Z^4}{4\pi\epsilon_0 m_e^2 c^2 a_0^3 n^3 l(l+1)(2l+1)} \mathbf{L} \cdot \mathbf{S} = \lambda \mathbf{L} \cdot \mathbf{S} \quad (2.7)$$

Thus the SOC strength λ scales with Z^4 in isolated Hydrogen like atoms. However, in real materials with more than 1 electron filling the orbitals, effective atomic number Z_{eff} should be adopted and $\lambda \sim Z_{\text{eff}}^2$ applies instead of the former relation, because of the Coulomb screening effects from other electrons [41]. Nevertheless, λ in $5d$ materials are typically much larger ($\lambda_{5d} \approx 200 - 600$ meV) compared to the $3d$ analogues ($\lambda_{3d} \approx 10 - 40$ meV) and can no longer be treated as an perturbation

	3d	5d
Electron correlation U	5 ~ 7 eV	~ 2 eV
Hund's coupling J_H	0.6 ~ 1.1 eV	~ 0.2 eV
Crystal field splitting Δ (Exp.)	0.5 ~ 3 eV	~3 eV
Spin orbit coupling λ	10 ~ 40 meV	200 ~ 600 meV
Band width W	2 ~ 4 eV	4 ~ 10 eV

Table 2.1: Comparison of different energy scales in 3d and 5d compounds. Ref. [17, 18, 19, 20]

(Table 2.1). As an matter of fact, such non-negligible energy scale directly competes/cooperates with other energy scales, which eventually stabilizes the so-called spin-orbit coupled Mott state in the prototypical 5d Sr₂IrO₄ (Sr214) compound, which I will elaborate later in the following chapters.

2.3 Magnetic properties of localized magnets

2.3.1 Non-interacting system

Consider the localized magnets with total angular momentum quantum number J under applied magnetic fields \mathbf{H} , if the interactions between magnetic moments are negligible, then the Hamiltonian follows

$$\mathcal{H}_{\text{Non-Interacting}} = -\boldsymbol{\mu}_J \cdot \mathbf{H} \quad (2.8)$$

Then the magnetization can be determined

$$M = g_J \mu_B J \cdot \left[\frac{2J+1}{2J} \coth\left(\frac{2J+1}{2J}x\right) - \frac{1}{2J} \coth\left(\frac{1}{2J}x\right) \right] \quad (2.9)$$

where M is the magnetization per unit magnetic ion and $x = \frac{g_J \mu_B J B}{k_B T}$. In the low field or high temperature limit, M is linearly proportional to external field H , therefore the unit magnetic susceptibility χ

$$\chi = \frac{C}{T} = \frac{\mu_B^2}{3k_B T} g_J^2 J(J+1) = \frac{\mu_{\text{eff}}^2}{3k_B T} \quad (2.10)$$

with $\mu_{\text{eff}} = g_J \sqrt{J(J+1)} \mu_B$ the effective magnetic moment, and $C = \frac{\mu_{\text{eff}}^2}{3k_B}$ the Curie constant. Therefore, if there is no interaction between the magnetic moments, the system will remain paramagnetic at high temperatures, following Curie's law.

2.3.2 Interacting system

Based on the empirical observations that a ferromagnet behaves like a paramagnet above the critical temperature Θ_{CW} , except that the magnetic susceptibility follows $\chi = \frac{C}{T - \Theta_{\text{CW}}}$, Weiss introduced the additional molecular field term that the average ionic magnetic moment will experience other than the external magnetic field, although he had no idea what's the origin for this term at that time. In fact, the microscopic nature of the effective molecular field is understood only after Heisenberg formulated the famous law of interaction between two magnetic atoms with spins, *i.e.*, the Heisenberg exchange interaction.

The Heisenberg exchange interaction is quantum mechanical effect resulting from the overlap of neighboring orbitals. It describes the spin-spin interaction and has a simple form:

$$\mathcal{H}_{\text{EX}} = - \sum_{\langle i,j \rangle} J_{ij} \mathbf{S}_i \cdot \mathbf{S}_j \quad (2.11)$$

Here J_{ij} is the exchange constant between spins \mathbf{S}_i and \mathbf{S}_j and can be positive or negative. The magnetic moments experience the interactions from neighboring moments, giving rise to the Weiss molecular field term and the system will tend to order, with the exact nature of order depending on the type of interaction and lattice geometry. Therefore, the new Hamiltonian which includes the spin-spin interaction term is

$$\mathcal{H}_{\text{Interacting}} = \mathcal{H}_{\text{Non-Interacting}} + \mathcal{H}_{\text{EX}} = -\boldsymbol{\mu}_S \cdot \mathbf{H} - \sum_{\langle i,j \rangle} J_{ij} \mathbf{S}_i \cdot \mathbf{S}_j \quad (2.12)$$

Here for simplicity, assuming \mathbf{L} is quenched, so that $\mathbf{J} = \mathbf{S}$, which is valid

for most $3d$ ions. By repeating the similar procedures the Curie Weiss behavior is recovered finally

$$\chi = \frac{C}{T - \Theta_{\text{CW}}} \quad (2.13)$$

with critical temperature

$$\Theta_{\text{CW}} = \frac{2zJ_{ij}}{3k_{\text{B}}}S(S+1) \quad (2.14)$$

Here z is the number of nearest neighbors for each spin. Thus with the inclusion of interactions between moments, the system remains paramagnetic at high temperatures, but stabilizes long range magnetic order below the critical temperature Θ_{CW} . On the other hand, once knowing the experimental ordering temperature and the magnetic structure, the exchange coupling strength can be estimated at a mean field level, which is usually the dominating energy scale and determines the low energy magnetic excitations.

2.3.3 Spin Hamiltonian of localized magnets

In a very general case the Hamiltonian of a spin system includes all possible interactions. Though the Heisenberg exchange interactions are most common and often the dominating ones, there are other types of interactions that could also contribute under certain circumstances. A general Hamiltonian should be aware of, in order to understand the magnetic properties in real materials.

$$\mathcal{H} = \mathcal{H}_{\text{EX}} + \mathcal{H}_{\text{B}} + \mathcal{H}_{\text{DM}} + \mathcal{H}_{\text{Ani}} + \mathcal{H}_{\text{Dipolar}} \quad (2.15)$$

- Heisenberg exchange & Zeeman term: The first and second terms correspond to the aforementioned Heisenberg exchange and magnetic coupling to external fields, respectively.
- Dzyaloshinskii-Moriya (DM) interaction [43, 44]: The third term is the antisymmetric exchange interaction, known as Dzyaloshinskii-Moriya interaction.

tion, which originates from the spin orbit coupling and absence of the inversion symmetry in the crystal. The symmetric Heisenberg exchange interaction prefers a collinear alignment of spins (parallel or anti-parallel) while DM interaction favors a non-collinear ground state. Although the absolute energy scale of DM interaction is not significant, it is responsible for the canted anti-ferromagnetic (AF) magnetic ground state in Sr214 [31, 45, 46] and helical structure in MnSi [47, 48] which I will elaborate in the following chapters. The DM interaction is given by

$$\mathcal{H}_{\text{DM}} = - \sum_{i,j} \mathbf{D}_{ij} \cdot \mathbf{S}_i \times \mathbf{S}_j \quad (2.16)$$

where \mathbf{D}_{ij} is the DM vector. Consider the superexchange between two spins mediated by a third ion. The orientation of \mathbf{D}_{ij} follows (Fig. 2.3)

$$\mathbf{D}_{ij} \propto \mathbf{r}_i \times \mathbf{r}_j \quad (2.17)$$

Apparently if the third ion (smaller orange sphere) is in line with the two magnetic ions (light blue sphere), which restores the inversion symmetry, then the DM vector will disappear. The direction of the DM vector is perpendicular to the plane extended by the three ions.

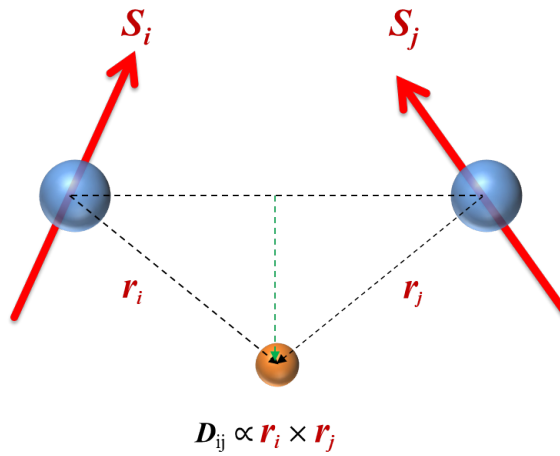


Figure 2.3: Illustration of DM vector

- Magnetic anisotropy: The fourth term is the magnetic anisotropy term. The microscopic origins for the anisotropy can be multiple folds, such as strain, magnetostrictions, dipolar interactions, spin orbit coupling, *etc.*. To simplify, assuming the magnetic anisotropy is of uniaxial character, the Hamiltonian of the anisotropy term can be written as:

$$\mathcal{H}_{\text{Ani}} = -K(\mathbf{S} \cdot \mathbf{e}_i)^2 \quad (2.18)$$

Here K is the magnetic anisotropy constant and \mathbf{e}_i denotes the spin easy axis. Literally, this term is responsible for the directionality and magnetic anisotropy of the magnetic ground state. For instance, there is no directional preference of the ferromagnetic (FM) ground state in a 1-D Ising model. If the magnetic anisotropy term is added to the Hamiltonian, then the moments will tend to align along the magnetic easy axis to minimize the ground state energy.

- Long-range dipolar interaction: As an analogue to the electric dipole-dipole interaction, the spin will also experience the magnetic fields induced by other spins. This type of interaction is of long range nature and falls off rapidly as a function of spin-spin distance. It has the form:

$$\mathcal{H}_{\text{Dipolar}} = - \sum_{i,j} \frac{(g\mu_B)^2}{r_{ij}^3} \left[(\mathbf{S}_i \cdot \mathbf{S}_j) - 3 \frac{(\mathbf{r}_{ij} \cdot \mathbf{S}_i)(\mathbf{r}_{ij} \cdot \mathbf{S}_j)}{r_{ij}^2} \right] \quad (2.19)$$

where \mathbf{r}_{ij} represents the displacement vector between spins $\mathbf{S}_{i,j}$. As a rough estimate, two $\frac{1}{2}$ spins at a distance of 1 \AA has a dipolar interaction energy scale of only $\sim 1K$ (or $\sim 0.08 \text{ meV}$). Although usually this dipolar term is ignored because of its small energy scale, but it turns out this long range interaction term is the dominating term and plays the crucial role in stabilizing the spin ice states in frustrated magnetic pyrochlores such as $\text{Ho}_2\text{Ti}_2\text{O}_7$ [49].

- Other types of interactions: Some common and important types of interactions are included in Eq. 2.15, but evidently there are other types of couplings

that are not necessarily negligible in certain materials, such as the bond directional Kitaev interactions in $(\text{Na, Li})_2\text{IrO}_3$ [50] and $\alpha\text{-RuCl}_3$ [51]. Only dominating energy scales are decisive in determining the static and dynamic magnetic properties. In order to understand the underlying physics, cooperations between theory and experiment are necessary.

2.3.4 Low energy magnetic excitations in localized magnets

Dynamic magnetic excitations are of fundamental interests because of the crucial importance towards the understanding of a plethora of physical phenomena, such as the proposed assisting roles of AF fluctuations in facilitating the formation of Cooper pairs in unconventional high T_c superconductors [52]. In the following, low-energy excitations from an ordered ground state will be considered.

As an simple example, consider the low temperature spontaneous FM order in a cubic lattice (lattice constant a). The low temperature order breaks the continuous rotational symmetry and therefore the excitations are gapless Goldstone modes, termed as spin wave or magnons as an analogue to lattice vibrations. Assuming the nearest neighbor (NN) Heisenberg interaction only, the Hamiltonian can be written as

$$\mathcal{H} = \mathcal{H}_{\text{EX}} = - \sum_{\langle i,j \rangle} J_{ij} \mathbf{S}_i \cdot \mathbf{S}_j \quad (2.20)$$

To better describing the magnon interactions, Holstein-Primakoff bosonization scheme is adopted. The exchange Hamiltonian is transformed into the Fourier components

$$\mathcal{H}_{\text{EX}} = -N_z J S^2 + 2zJS \sum_{\mathbf{q}} (1 - \gamma_{\mathbf{q}}) a_{\mathbf{q}}^\dagger a_{\mathbf{q}} \quad (2.21)$$

where $J_{ij} = J$, spin moment $S_i = S_j = S$, $\gamma_{\mathbf{q}} = \frac{1}{3}[\cos(q_x a) + \cos(q_y a) + \cos(q_z a)]$, and $a_{\mathbf{q}}^\dagger$ ($a_{\mathbf{q}}$) is the magnon creation (annihilation) operators. Therefore, the spin system behaves like a Boson. In the small q limit, the spin wave mode takes the following form

$$\hbar\omega_q = Dq^2 \quad (2.22)$$

where $D = 2JSa^2$ is the spin wave stiffness constant.

Other low temperature properties can also be obtained. For example, the finite temperature magnetization follows the famous Bloch's $T^{\frac{3}{2}}$ law, which is verified by experiments.

$$M(T) = M(0) \left[1 - \left(\frac{T}{T_c} \right)^{\frac{3}{2}} \right] \quad (2.23)$$

with the critical temperature

$$T_c = \left(\frac{M(0)}{0.117g\mu_B} \right)^{\frac{2}{3}} \frac{D}{k_B} \quad (2.24)$$

Another thermal dynamic quantity, *i.e.*, the magnetic specific heat C_m , follows the similar $T^{\frac{3}{2}}$ dependence, in addition to the well-known T^3 contribution from phonons in insulators.

$$C_m(T) = 0.113k_B \left(\frac{k_B T}{D} \right)^{\frac{3}{2}} \quad (2.25)$$

Thus spin wave excitations play important roles in renormalizing the finite temperature properties of the system. The examples above present only the simplest case, the exact details in materials belonging to different categories vary dramatically and should be treated separately.

2.3.5 Spin orbit coupling in localized systems

In $5d$ iridates, the spin orbit coupling term is no longer negligible. The simple Hubbard Hamiltonian introduced before will be modified by including the spin-orbit coupling term [53, 1, 17]:

$$\mathcal{H} = - \sum_{\langle i,j \rangle, \sigma} t_{ij} c_{i\sigma}^\dagger c_{j\sigma} + U \sum_i n_{i\uparrow} n_{i\downarrow} + \lambda \sum_i L_i \cdot S_i \quad (2.26)$$

Exotic quantum phases emerge in heavy transition metal compounds when considering both the electron correlation and spin orbit coupling. The inclusion of spin orbit coupling energy scale pushes the ground states from the left to the right side of the phase diagram, as shown in Fig 1.1, where exotic new ground states are expected, such as Kitaev spin liquids, Weyl semimetals, and spin-orbit Mott insulators. For instance, simple metallic phases are naively expected comparing to the $3d$ counter-parts, turns out to be the opposite in the prototypical Mott insulator Sr_2IrO_4 , which results from the multiple competing energy scales [30]. As an another example, the honeycomb lattice iridates such as Na_2IrO_3 and Li_2IrO_3 are proposed to host the Kitaev physics [17]. Indeed, dominant bond-directional interactions have been reported in Na_2IrO_3 [50]. Those comparable energy scales in $5d$ materials, including the important SOC energy scale, together with varieties of lattice geometry freedoms provide fertile playgrounds for hosting distinct quantum states.

2.4 Magnetic properties of itinerant metals

2.4.1 Brief history

The quantum mechanical description of localized magnetic moments on the atomic level (ions) provides fruitful insights into magnetic phenomena on the microscopic scale in a great variety of materials, such as the f electrons of the rare earth compounds. However, this description turns out to be inadequate in explaining magnetism in itinerant magnets, even for the common $3d$ transition metals. For instance, from the atomic picture we would expect the magnetic moment be integer values in the unit of Bohr magneton. However, magnetic moments of $3d$ transition metals are experimentally determined to be non-integers. To account for such discrepancy, Stoner along with work followed by Wohlfarth and co-workers proposed the now-days so-called the Stoner-Wohlfarth (SW) theory to explain the $T = 0 \text{ K}$ ground state, with the core idea of spontaneous band splitting of the conduction electron

states. While it is quite successful in its description of itinerant electrons at $T = 0$ K , the prediction of finite temperature properties failed dramatically.

Later, the development of dynamical mean field theory (DMFT) or random phase approximation (RPA) theory successfully predicted the existence of the new collective mode in addition to Stoner's spin flip excitations. Although the spin fluctuations have been incorporated in this theory, the renormalized equilibrium state is not taken in consideration, therefore the interpretation of high temperature magnetic properties such as the experimentally observed Curie-Weiss behavior of static susceptibility is still unsatisfying.

In contrast to the SW theory, roles of thermal magnetic fluctuations are particularly emphasized in the well known self-consistent renormalization (SCR) spin fluctuation theory pioneered by Moriya and Kawabata in 1973. The renormalized thermal equilibrium state and the spin fluctuations are now treated at the same time in a self-consistent way. In this way, SCR theory provides a quantitative description of itinerant magnetism consistent with the experimental observations.

2.4.2 Non-interacting electron gas: Pauli paramagnetism

Electrons in metals are delocalized, the simplest approximation to begin with is to treat them as free electron gas. With external magnetic fields polarizing the electronic bands, leaving unbalanced up and down spin states, Pauli paramagnetism (PPM) emerges from those itinerant electrons in opposite spin states, with net magnetization directly proportional to imbalanced number of electrons in up and down spin states (Fig 2.4):

$$M = -(n_{\uparrow} - n_{\downarrow})\mu_S = -(n_{\uparrow} - n_{\downarrow})\mu_B \quad (2.27)$$

In the low field and low temperature approximation, the exchange splitting is small and only electrons close to the Fermi surface play an important role, so the magnetization can be approximated as

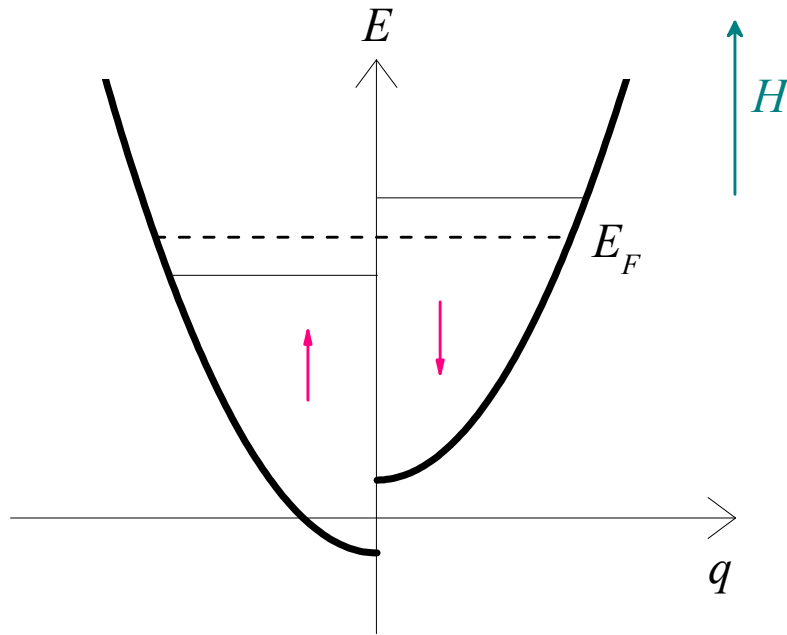


Figure 2.4: Pauli paramagnetism results from field induced band splitting

$$M = \mu_B^2 \rho(E_F) H \quad (2.28)$$

where $\rho(E_F)$ is the density of states (DOS) at the Fermi level E_F . Therefore, the Pauli susceptibility is

$$\chi_{\text{Pauli}} = \rho(E_F) \mu_B^2 \quad (2.29)$$

From this equation, the magnitude of PPM simply depends on $\rho(E_F)$ only, implying that system with larger DOS at E_F will have a larger temperature independent term of PPM contribution. Nevertheless, PPM in real metals is usually very small, because only a small portion of imbalanced states near E_F contributes to the net magnetization.

2.4.3 Spontaneous magnetization: Stoner criterion

Similarly to localized magnets, where the moment-moment interaction stabilizes the long range magnetic order ground state, the inclusion of interatomic coupling I

in itinerant electron systems could also induces a spontaneous band splitting state following the criterion proposed by Stoner.

Take the itinerant ferromagnetic system as an example², the total energy gain ΔE resulting from the potential energy gain and kinetic energy loss should be positive, in order to realize spontaneous band splitting without applying external field.

$$\Delta E = \frac{1}{2}\rho(E_F)(\delta E)^2[1 - I\rho(E_F)] \leq 0 \quad (2.30)$$

Therefore, the Stoner criterion is obtained:

$$I\rho(E_F) \geq 1 \quad (2.31)$$

Correspondingly, the susceptibility in systems when the Stoner criterion is met

$$\chi_{\text{Stoner}} = \frac{\mu_B^2 \rho(E_F)}{1 - I\rho(E_F)} = \frac{\chi_0}{1 - I\rho(E_F)} = S\chi_0 \quad (2.32)$$

where $S = \frac{1}{1 - I\rho(E_F)}$ is the Stoner enhancement factor, which measures the material's proximity to a magnetic instability. χ_0 is the susceptibility without turning on interatomic coupling I , which is essentially χ_{Pauli} .

More thermal dynamic properties can be obtained following Stoner's original concept of spontaneous band splitting (Ref [4]). Here are some of the key features

- Non-integer spin moment

Magnitude of atomic magnetic moment in principle can take any value in itinerant systems within Stoner's model, because it is determined by the spin splitting of conduction electron bands, not from the individually quantized spin or orbital moments.

- Non-saturated isothermal magnetization

Since the net magnetization is proportional to the unbalanced number of electrons in opposite spin polarized states, its magnitude will not reach the maximum unless the system being in fully polarized state, which usually requires

²For simplicity, only ferromagnetic systems are considered here and in the remaining chapter.

an exceptional large field. Therefore, for most itinerant systems, the low temperature isothermal magnetization is non-saturated in small fields.

- Smaller contribution to thermal dynamic properties

The underlying reason is the same as above, which concerns with the less availability of itinerant electrons contributing to thermal dynamic properties.

- Sensitive to DOS at Fermi level E_F

Since only a small portion of conduction electrons close to Fermi level contributes to the thermal dynamic properties, the overall contribution is less significant compared to localized systems. The larger DOS at Fermi level means more itinerant electrons participating in the thermal dynamics.

- Spontaneous magnetization

$$M(T) = M(0) \left[1 - \frac{T^2}{T_c^2} \right]^{\frac{1}{2}} \quad (2.33)$$

- Weakness of Stoner's theory

Stoner's model is quite successful in explaining the ground state magnetic properties, but difficulties are encountered in describing the finite temperature properties, especially when the temperature is close to or above the critical temperature. For instance, the predicted critical temperature T_c is much larger than experimentally established values; nor the theory can explain the observed Curie-Weiss like behavior of susceptibility at high temperatures. The main shortcoming of Stoner's theory is that no spin fluctuations are incorporated in this model, which are necessary to account for high temperature thermal dynamic properties in the system.

2.4.4 Random phase approximation (RPA) theory of spin fluctuations

To remedy the serious drawbacks in Stoner's mean-field theory, spin fluctuations must be incorporated in the new theory. The random phase approximation (RPA) theory for the dynamical susceptibility is therefore developed to describe spin waves and other magnetic excitations in the ferromagnetic ground state.

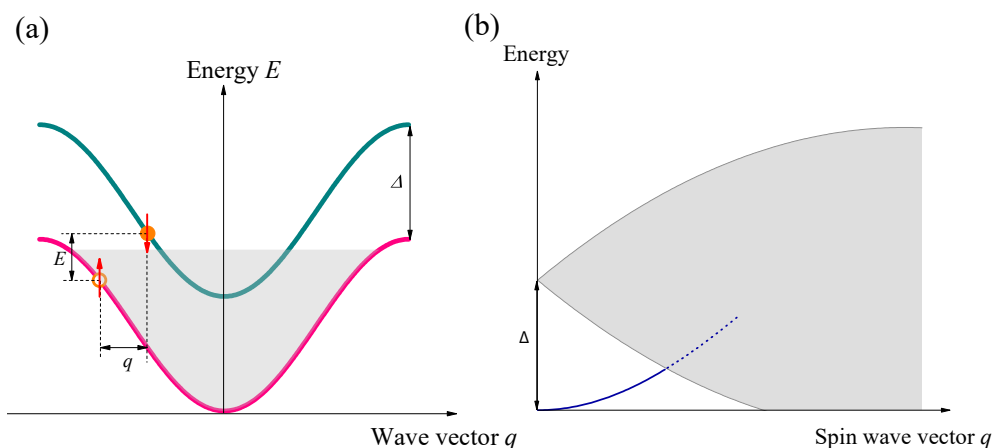


Figure 2.5: (a) Spontaneous band splitting with spin up majority band and spin down minority band. Single spin up electron can hop to the empty state in the minority band, leaving an effective hole in the majority band, and forms the Stoner electron-hole pair. (b) Stoner continuum (grey region) results from the single spin flip excitation. The blue line shows the low energy spin wave excitations predicted from random phase approximation (RPA) theory.

Following Stoner's phenomenology in itinerant ferromagnetic metals, spontaneously band splitting occurs, resulting with spin up majority band and spin down minority band, as shown in Fig. 2.5. Single spin up electron can hop to the empty state in the minority band, leaving an effective hole in the majority band, and forms the Stoner electron-hole pair. In the mean field level, the spin flip excitation has the energy:

$$E_{Stoner}(k, q) = \Delta + E_{k,\uparrow} - E_{k+q,\downarrow} \quad (2.34)$$

where Δ is the energy of uniform band splitting.

The dynamical susceptibility of Stoner excitations is given by

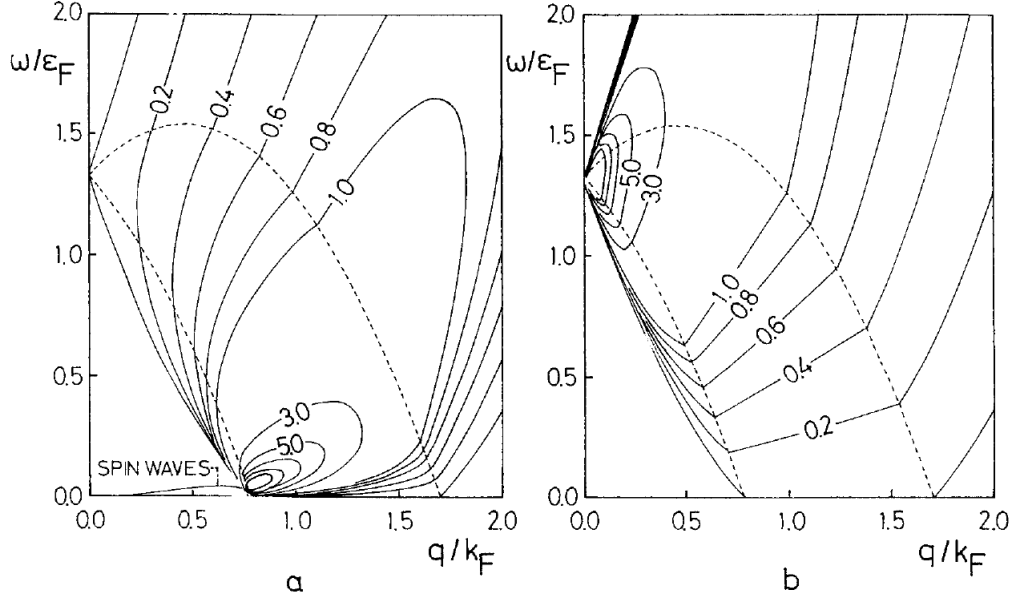


Figure 2.6: Dynamical susceptibility in a ferromagnetic electron gas: (a) RPA approximation (b) Stoner's excitations. Adopted from [2].

$$\chi_{\Delta 0}^{+-}(E, q) = \sum_k \frac{\langle n_{k+q} \rangle - \langle n_k \rangle}{E_{k,\uparrow} - E_{k+q,\downarrow} + \Delta - E} \quad (2.35)$$

Neglecting the mode-mode interactions, the random phase approximation (RPA) dynamical susceptibility follows

$$\chi_{RPA}^{+-}(E, q) = \frac{\chi_{\Delta 0}^{+-}(E, q)}{1 - I\chi_{\Delta 0}^{+-}(E, q)} \quad (2.36)$$

This expression has important consequences, *i.e.*, the pole in the denominator suggests new collective excitations outside of the Stoner continuum. The numerical simulations are shown in Fig 2.6, the excitation spectra are dramatically different between the RPA susceptibility and its mean field analogue. The electron-hole pair bound states give rise to additional spin wave excitations in the RPA approximation, which are analogous to the localized magnon excitations and share similar q^2 dependence comparing to localized FM systems in the long wavelength limit. In general, the low energy excitations are strongly enhanced in the RPA approximation, especially when the spin wave modes directly interact with Stoner excitations. The comparison between the two, *i.e.* RPA approximation and Stoner's model, explains

the unreasonable prediction of anomalously large critical temperatures in Stoner's mean field theory comparing to much smaller experimental numbers.

2.4.5 Self-consistent renormalization (SCR) theory

Although the RPA theory is quite successful in predicting the new collective excitations other than Stoner's spin flip excitations, the fundamental drawbacks in Stoner's mean field theory remain, such as the unaccounted Curie-Weiss like behavior of static susceptibilities in weak itinerant ferromagnets ZrZn_2 and Sc_3In [2, 4]. To overcome such difficulties, the effect of nonlinear mode-mode coupling among thermal magnetic fluctuations are particularly emphasized in the nowadays call Self-consistent renormalization (SCR) theory [2, 4]. In this theory, the renormalized thermal equilibrium state and the spin fluctuations are considered at the same time in a self-consistent way, so that the static and dynamic susceptibilities in long wavelength limit agree with the values calculated from the renormalized free energy. With the further consideration of renormalized equilibrium state, the SCR theory now provides a quantitative description of itinerant magnetism consistent with the experimental observations.

For a weak ferromagnetic metal above the critical temperature T_c , the magnetic susceptibility in SCR theory can be expressed as:

$$\chi_0/\chi(T) = 1 - I' + \lambda(T) \quad (2.37)$$

where χ_0 is the static susceptibility in Stoner's theory with coupling strength $I = 0$, I' is related to I and close to 1. The last term $\lambda(T)$ is the correction term to RPA theory and linearly depends on T , which is responsible for the high temperature Curie-Weiss behavior in itinerant systems. The numerical simulations of $\chi_0/\chi(T)$ vs. T have been performed and compared to Stoner's theory (Fig. 2.7), where the linear behavior of $1/\chi(T)$ clearly demonstrates the Curie-Weiss behavior in itinerant metals.

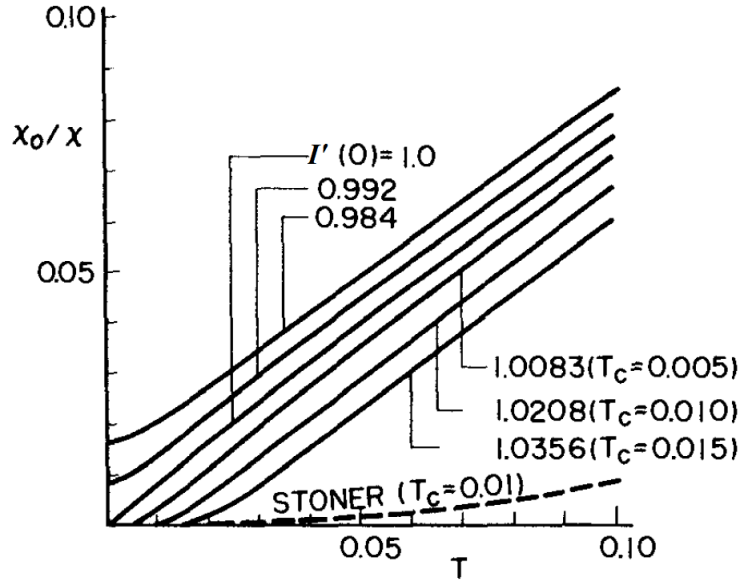


Figure 2.7: $\chi_0/\chi(T)$ vs. T simulated with SCR theory (solid lines) and Stoner's theory (dash line). An electron-gas like band was used. Adopted from [2].

This linear T depended term $\lambda(T)$ is directly proportional to the mean-square local amplitude of spin fluctuations S_L^2 , which plays important roles in determining the thermal magnetic properties, including the mentioned Curie-Weiss behavior of susceptibility above the critical temperature. Fig 2.8 shows the temperature dependence of S_L^2 in weak FM metals and in a localized system. While S_L^2 is independent of temperature in the localized moment systems, its linear- T behavior is directly responsible for the Curie-Weiss behavior observed in itinerant metals, which is in contrast to the moment-moment exchange interaction induced Curie-Weiss behavior of susceptibility above the critical temperature in localized systems.

The inclusion of spin fluctuations in SCR theory enables the satisfying quantitative descriptions of thermal dynamic properties in itinerant metals. For instance, in weak FM metals, the dynamical susceptibility can be obtained similarly to the form expressed in RPA theory. Below the critical temperature, the transverse dynamical susceptibility under a small applied field h :

$$\chi_{MI}^{-+}(q, E) = \frac{\chi_{M0}^{-+}(q, E)}{(h/2M)\chi_{M0}^{-+}(0, 0) + I[\chi_{M0}^{-+}(0, 0) - \chi_{M0}^{-+}(q, E)]} \quad (2.38)$$

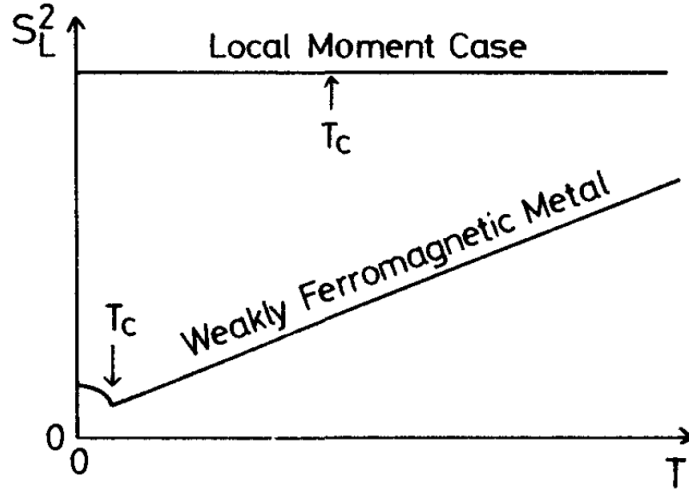


Figure 2.8: Temperature dependence of mean-square local amplitude of spin fluctuations S_L^2 in weak FM metals and local moment systems. Adopted from [2].

where $\chi_{M0}^{-+}(q, E)$ is the transverse dynamical susceptibility in a non-interacting electron system.

Similarly, above the critical temperature, the imaginary part of dynamical susceptibility $Im\chi(q, E)$ is written by the double Lorentzian:

$$Im\chi(q, E) = \frac{\chi(0, 0)}{1 + q^2/\kappa^2(T)} \frac{E\Gamma(q)}{E^2 + \Gamma^2(q)} \quad (2.39)$$

where $\kappa(T)$ and $\Gamma(q)$ represent the momentum and energy widths of the spin fluctuation spectrum. These expressions obtained from SCR theory are in line with the polarized neutron scattering experiments on MnSi above T_c [54].

Although the SCR theory is quite successful in describing important thermal physical properties in itinerant metals, there are difficulties in this theory as well. Such as the temperature dependence of spontaneous magnetization always discontinuously drops to zero at the critical temperature T_c and the specific heat shows a spurious negative peak just above the critical temperature. Later works of spin fluctuation theory based on the total spin amplitude conservation and global consistency in the effect of magnetic field solve those difficulties and offer beautiful revisions on the Rhodes-Wohlfarth plot and critical magnetic isotherm, which are verified by later experiments [4].

Still there are some features that the SCR theory and its variants are not able to comprehend. Such as the dynamical excitations in the large q limit in weak itinerant metals and the dynamical properties of spin fluctuations in the intermediate regime where both localized and itinerant electrons contribute. Density functional theory (DFT) which takes the electron-electron correlations into account shows the potential to deal with systems with both the local and itinerant characters. For more details, the readers can refer to [19, 55].

2.5 General remarks: Localized vs. Itinerant systems

The Hubbard model in Eq. 1.1 is the simple yet useful model to understand phenomena in two opposite extremes. In the localized moment picture, each atom or ion carries the magnetic moment, localized in real space in the large U/t limit; On the other hand, in the large t/U approximation, the electrons can hop from site to site, bearing itinerant nature in real lattice, or in other words, localized in reciprocal space. As shown in Fig. 2.9, the moment pictures under the two opposite extremes are represented. Although, the exact natures of the two are dramatically different, similar behaviors are still observed experimentally, such as the Curie-Weiss susceptibility at high temperatures and magnetic excitations follows the same q^2 dependence in the long wavelength limit, which will be briefly elucidated below.

2.5.1 Curie-Weiss behavior

In the local moment picture, the moment-moment exchange interactions stabilize the low temperature long range magnetic order, breaking the continuous rotation symmetry, and resulting in gapless spin wave excitations, which are termed as magnons as a close analogue to quantized lattice vibrations, *i.e.*, phonons. Thermal excitations induce random rotations of spin moments, gradually restore the broken symmetry and suppress the magnetic order with increasing temperatures. Above the

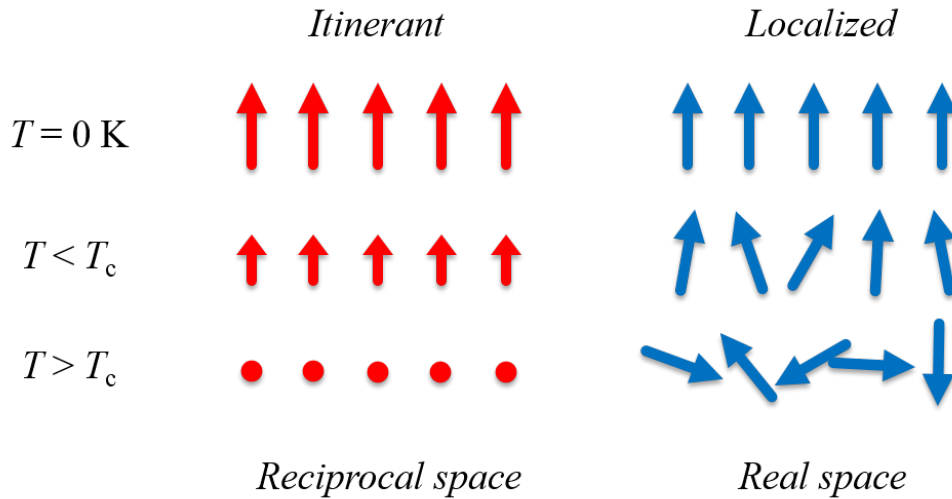


Figure 2.9: Temperature dependence of itinerant and localized moment systems. Adapted from [3].

critical temperature T_c , the random flips of local moments completely destroy the long range magnetic order. However, short range correlations persist between local moments and are responsible for the Curie-Weiss behavior of static susceptibility.

In the itinerant systems, the Curie-Weiss behavior of static susceptibility is also observed experimentally, such as in weak itinerant ferromagnetic metals. However, the underlying mechanism for the observed similar behaviors is utterly different comparing to localized moment scenario. The Stoner's model successfully explains the origin of magnetic moment (or magnetization) at $T = 0$ K, which results from the spontaneous band splitting, but fails to predict the correct finite temperature dependence of static susceptibility. As pointed out later by SCR spin fluctuation theory, the linear- T dependence of mean-square local amplitude of spin fluctuations S_L^2 is the ultimate driving force of Curie-Weiss like susceptibility above the critical temperature.

2.5.2 Magnetic excitations in the long wavelength limit ($q \rightarrow 0$)

Take the ferromagnetic system as an example. The Goldstone theorem in localized FM system guarantees the gapless magnetic excitations since the magnetic order continuously breaks the spatial invariance symmetry. These excitations are

quantized magnons and obey the $E = Dq^2$ dispersion in the long wavelength limit ($q \rightarrow 0$). In weak itinerant FM metals, collective excitations are also predicted with the same dispersion relation in both RPA and SCR spin fluctuation theories and are confirmed experimentally such as on the prototypical itinerant compound MnSi by inelastic neutron scattering experiments [15]. Although no localized moments exist in the completely itinerant limit, the coherent superposition of Stoner electron-hole pairs which carry $1\hbar$ total spin angular momentum will support spin wave excitations in itinerant systems. The couplings between spin wave excitations and single particle Stoner excitations cause the rapid reduction of "magnon" lifetime, resulting in broader spin wave excitations in itinerant systems. This broadening is even more pronounced in the large q limit when the spin wave modes enter the Stoner continuum, rendering the experimental characterizations extremely difficult.

2.5.3 General comparison of characteristic magnetic properties between localized and itinerant ferromagnets: degree of itineracy

Although some magnetic properties are shared in both localized and itinerant ferromagnets, there are more contrasting magnetic properties when comparing the two opposite systems, where some of characteristic features are shown in Table 2.2. The defining property in itinerant systems is that only a portion of electrons close to Fermi level prone to spontaneous splitting will contribute to magnetism. Therefore, the degree of itineracy can be characterized by the number of contributing electrons, comparing to the same number in otherwise localized system.

Consider localized ferromagnets first. Recall Curie-Weiss law, the spin only magnetic moment $\mu_{\text{eff}} = g_s \sqrt{S(S+1)} \mu_B$, thus the effective number of electrons contributing to Curie-Weiss behavior can be defined as

$$\begin{aligned} \mu_{\text{eff}} &= p_{\text{eff}} \mu_B \\ p_{\text{eff}}^2 &= g_s^2 S(S+1) = g_s S(g_s S + 2) \end{aligned} \tag{2.40}$$

Table 2.2: Characteristic magnetic properties in comparison between localized and weak itinerant ferromagnets. M , magnetization; χ , susceptibility; C_m , magnetic contribution to specific heat; p_{eff} , effective moment from Curie-Weiss law above critical temperature; p_s , low temperature saturation moment from isothermal magnetization. Ref. [2, 4]

Magnetic properties	Localized moment systems	Weak itinerant ferromagnets
$M/(N\mu_B)$	Integer	$\ll 1$
$M/H (T \rightarrow 0)$	Saturated	Non-saturated
$M(T)$ (below T_c)	$M(0)[1 - (T/T_c)^{3/2}]$	$M(0)(1 - T/T_c)^{1/2}$
$\chi(T)$ (above T_c)	Curie-Weiss law	Curie-Weiss law
C_m	$\sim T^{3/2}$	See Ref. [2, 4]
p_{eff}/p_s	~ 1	$\gg 1$
Spin wave dispersion ($q \rightarrow 0$)	Dq^2	Dq^2

where spin g -factor $g_s = 2$ is assumed.

At low temperatures, the isothermal saturation magnetization reveals the effective saturation moment

$$p_s = \left(\frac{M_{\text{iso}}}{N} \right) / \mu_B = g_s S \quad (2.41)$$

where $\frac{M_{\text{iso}}}{N}$ is the isothermal magnetization M_{iso} normalized by the total number of magnetic atoms (ions) N .

If we further defines p_c as

$$p_{\text{eff}}^2 = p_c(p_c + 2) \quad (2.42)$$

then p_c/p_s is exactly 1 in localized ferromagnets.

For itinerant systems, we can define the same effective numbers, but p_c/p_s will be much larger than 1 in this scenario. The reason is that the exact number of itinerant electrons N_{iti} contributing to effective isothermal magnetization is not known, but with the relation $N_{\text{iti}} \ll N$. If we re-define $p_{s, \text{iti}} = \left(\frac{M_{\text{iso}}}{N_{\text{iti}}} \right) / \mu_B$, then the ratio $p_c/p_{s, \text{iti}}$ shall recover to 1. In other words, in itinerant systems, a much larger number N is adopted instead of the smaller unknown effective one, which results in the significant reduction of p_s . Hence, the ratio of p_c/p_s is much larger than 1 in itinerant systems, compared to the exact ratio of 1 in localized systems. Therefore,

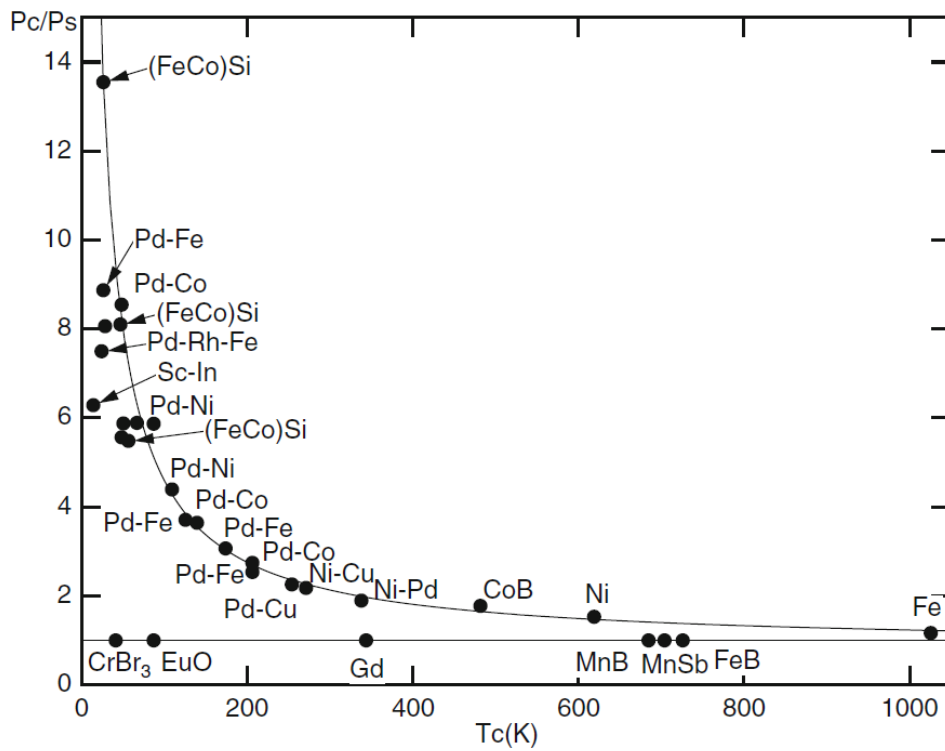


Figure 2.10: Rhodes-Wohlfarth plot: p_c/p_s vs. T_c . Adopted from [4].

this ratio can be exploited as an indication of itinerancy, since in real systems most materials lie in between the two opposite extremes. Plotting the ratio against the Curie temperature is the Rhodes-Wohlfarth plot, as shown in Fig 2.10, which is an intuitive way to show the degree of itinerancy comparing various systems of magnetic materials.

Chapter 3

Experimental techniques

Having introduced the background and preliminary knowledge of magnetism in both localized and itinerant magnets, here experimental tools for characterizing the physical properties will be introduced. First, the sample preparations and characterizations will be discussed, since this is the first step toward interpretation of physical phenomena behind the two contrasting systems. Then experimental techniques including neutron and X-ray scattering for exploring the electronic and magnetic properties will be presented.

3.1 Sample growth

There are a vast variety of methods for crystal growth [56], serving for different purposes, such as the conventional solid state reactions for powder synthesis and the floating zone mirror furnace growth for larger single crystals. In the following, I will only mention the methods that will be directly applied to my studies, including solid state synthesis and flux based single crystal growth.

3.1.1 Solid state synthesis

The basic idea behind solid state synthesis is actually quite simple. Weigh the right amount of precursor compounds, fully grind and mix the powers and then press into a pellet, which is then placed into the furnace and subject to a controlled reaction sequence. For instance, the Sr_2IrO_4 polycrystal can be made by mixing the stoichiometric amount of SrCO_3 and IrO_2 power (2 : 1 ratio), then the power is pressed into a pellet. Afterwards, the pellet can be placed into a crucible inside the high temperature furnace, which is programmed to ramp up to 1400C for one day, before it is cooled down to room temperature. After this short sequence, the pellet will be fully ground and can be tested by XRD. If the obtained phase is not pure, repeat the above sequence for another couple of times. Usually, three times should be good enough to obtain phase pure power Sr_2IrO_4 .

3.1.2 Flux based single crystal growth

The flux growth method is adopted to grow the single crystals as it is relatively straightforward and inexpensive. Sometimes it is the only possible way to grow the crystals as the flux reduces the activation energy for nucleation and doesn't necessarily require an excessively high temperature to melt the precursor materials.

Desired stoichiometric amounts of starting materials are weighed and mixed in power and placed into a Pt crucible and covered by a certain amount of flux (e.g. SrCl_2). Usually, the whole crucible with starting powders is inserted into a larger

alumina crucible for protection, before placing into the high temperature furnace. Next, the furnace follows the heating sequence set up by the operator. When the sequence is completed after cooling to room temperature, the crucible is taken out. Fresh crystals can be pulled out inside the crucible once the flux is dissolved.

Fig 3.1 is the cartoon showing the main components of the flux growth inside a box furnace with a typical heating sequence shown in Fig 3.2. One typical batch

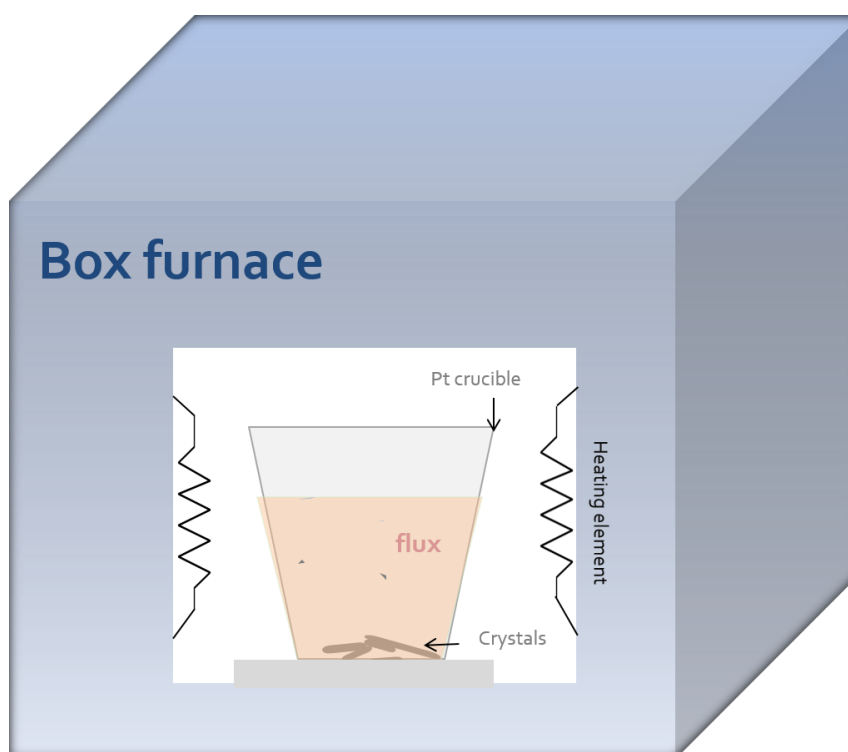


Figure 3.1: Cartoon showing flux growth of single crystals inside a box furnace

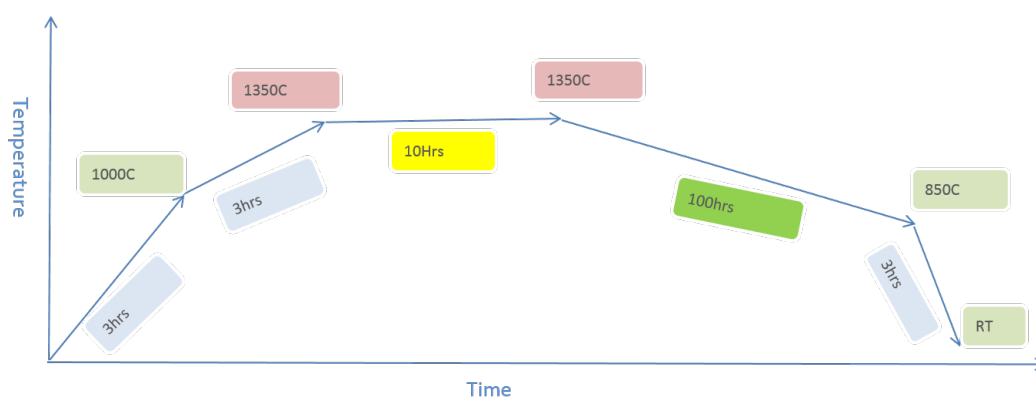


Figure 3.2: A typical heating sequence profile for the flux growth of Sr_2IrO_4 single crystals

of flux based growth of Sr_2IrO_4 single crystals using SrCl_2 as flux is shown in Fig 3.3, where the nice plate-like single crystals are standing vertically on the bottom of the Pt crucible.

Although the flux growth is very straightforward for obtaining single crystals with reasonable sizes, there are some shortcomings along this method:

- **A lot of trial and error before success.** (Ratio of starting materials, sequence, etc.)

Finding the right type and amount of flux and how to control the heating sequence is not obvious. Therefore, for this type of growth, it will take a while of trial and error before success.

- **The single crystals obtained are usually very small.**

This method is very straightforward, but usually produce small single crystals, compared to other growth method such as the crystal growth from floating zone mirror furnace.

- **Possible inclusions of flux.**

Depending the desired materials and the type of flux, the final product may be contaminated by the flux during the growth.

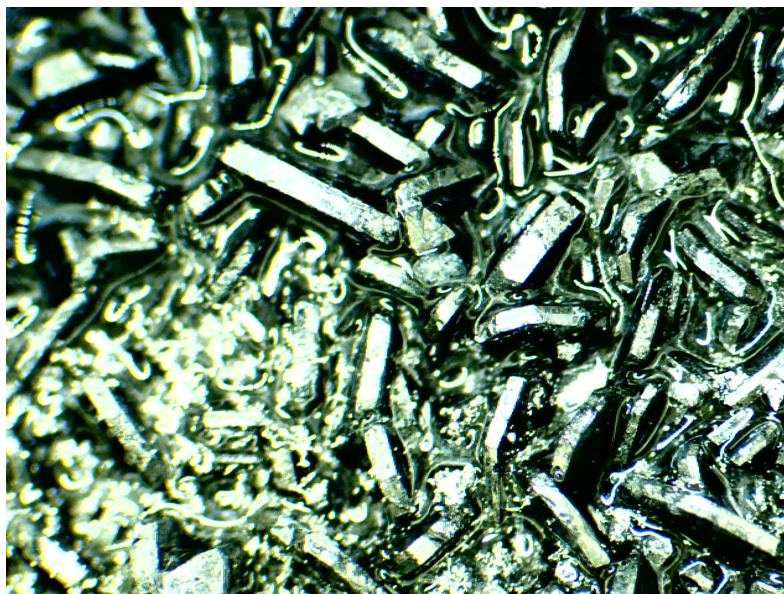


Figure 3.3: Sr_2IrO_4 single crystals from one typical batch of SrCl_2 flux growth.

3.2 Sample characterizations

Sample characterizations are crucial, since the methods utilized for crystal growth do not guarantee that the obtained crystals are of high quality or right in the desired phase. For instance, in the flux growth of Sr_2IrO_4 single crystals, tuning the amount of flux alone can result in the final products either in the desired Sr_2IrO_4 phase or in the unwanted $\text{Sr}_3\text{Ir}_2\text{O}_7$ phase, or most commonly in the mixture of the two phases. Therefore to ensure the obtained crystals are qualified for future studies, the sample characterizations are absolutely necessary. Some common procedures to characterize samples include powder or single crystal X-ray diffraction (XRD), Energy-dispersive X-ray spectroscopy (EDS/EDX), etc.

3.2.1 X-ray diffraction

X-ray diffraction technique is extensively applied and can generally be divided into two categories, *i.e.*, single crystal X-ray diffraction or power X-ray diffraction (PXRD). The underlying principle is the same famous Bragg's law (Eq. 3.1). For simplicity, in the following only PXRD technique will be covered.

$$n\lambda = 2d\sin\theta \quad (3.1)$$

where n is positive integer, d is the interplanar distance between crystallographic planes, λ is the wavelength of X-ray, and θ is the incident angle.

The Bragg's law (Eq. 3.1) states the conditions for constructive interference of X-rays (or neutrons) from a crystal lattice. When the X-rays are incident on the sample, electromagnetic interactions between X-rays and electron clouds inside the crystal lattice take place, before the re-emission of X-rays with the same frequency. With incident X-rays of fixed wavelength, the interplanar distances between crystallographic planes inside the crystal lattice determine the right angles for constructive/destructive interference. Therefore, the resulting allowed angles together with the relative intensity distribution associated at each angle will act like the fingerprint

for this unique phase, which can be used to differentiate the unwanted phases from different crystal lattices.

Fig 3.4 shows the typical PXRD patterns during power Sr_2IrO_4 synthesis. The final PXRD pattern (dark brown symbols, labelled as 1400C-3) was obtained after repeating the short 2-day solid state reaction of precursor powers for three times. The peak positions and intensities are consistent with the published data, indicating the success of power Sr_2IrO_4 synthesis. Apparently, after the first and second short sequences (dark and red symbols, labelled as 1400C-1 and 1400C-2 respectively), there are some tiny impurity peaks locating at $2\Theta \sim 17^\circ$, which indicates the incomplete reaction of precursor powders. By repeating the same process for three times, eventually the obtained power is phase pure and qualified, as monitored from the PXRD patterns collected after each short sequence. This is a good example emphasizing the necessity of applying PXRD to characterize the samples. If the wrong

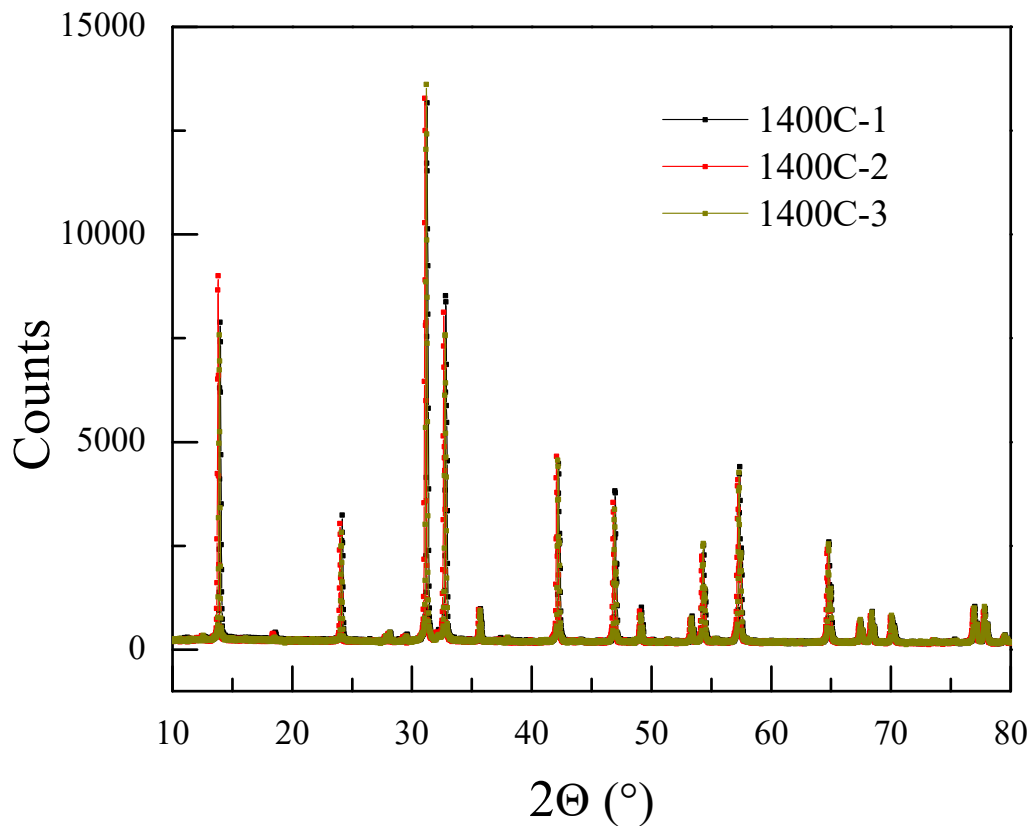


Figure 3.4: Typical power X-ray diffraction patterns during polycrystal Sr_2IrO_4 solid state synthesis

heating sequence is applied or something else goes wrong, the obtained PXRD may be way different compared to the desired pattern, signaling that attentions should be paid to alter the sequence or scrutinizing the experimental details to improve the sample growth for next round.

3.2.2 Energy-dispersive X-ray spectroscopy

X-ray diffraction technique is sensitive to the atomic arrangement, however, to know the exact elements inside the sample, especially when a small amount of certain elements are introduced, it is necessary to apply other techniques such as Energy-dispersive X-ray spectroscopy (EDS/EDX) to characterize the concentrations of each element.

The EDS is an analytical technique for elemental characterizations. The basic principle is that each chemical element has its unique atomic structure with unique electromagnetic emission spectrum. Thus the experimentally collected emission spectrum from an unknown sample can be compared to the characteristic emission spectrums, which renders the determination of chemical elements inside the sample. The quantitative analysis of the emission spectrum further enables the possibility

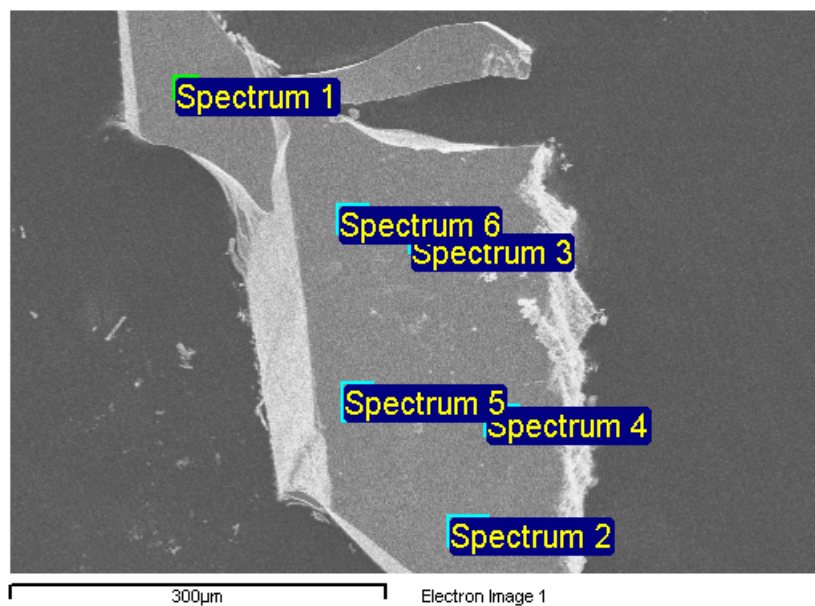


Figure 3.5: SEM image of cleaved surface of one La doped Sr_2IrO_4 single crystal

of quantitative characterizations of atomic ratios between each element inside the sample.

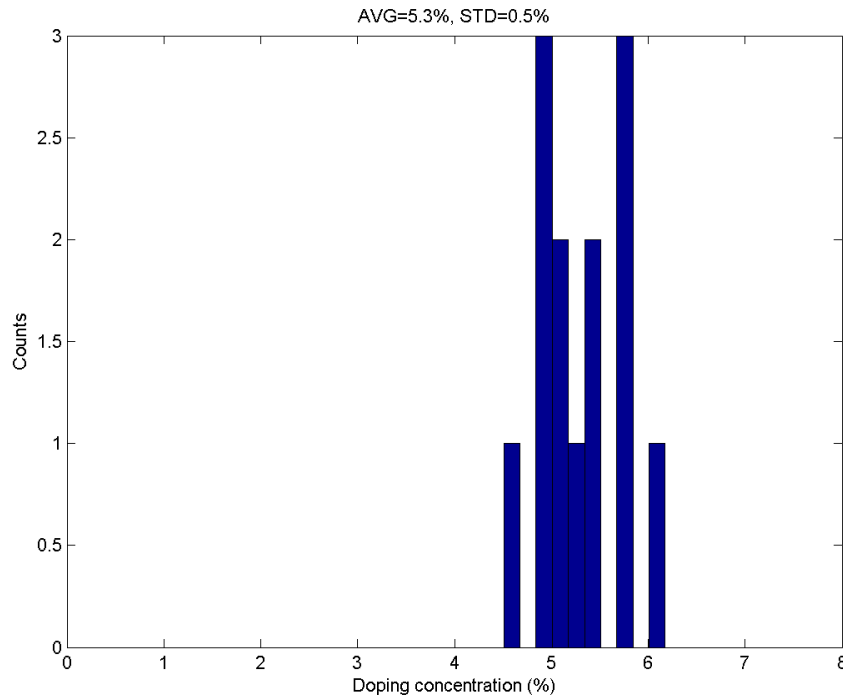


Figure 3.6: Histogram of repeated EDS measurements on a 5%La doped Sr_2IrO_4 single crystal.

High energy electrons are generated to bombard the sample surface, which can kick the core electrons inside the atoms out to the empty states, leaving empty holes in the deep core and forming the unstable intermediate state. In a short moment, the electrons occupying the high energy states will fill the empty hole states, emitting characteristic X-ray radiations, which characterize the chemical element. The energy and intensity of the emitted X-rays can be measured by an energy dispersive spectrometer. By referring to the unique characteristic X-ray radiations for each chemical elements, the elemental compositions of the specimen can be quantified.

Fig 3.5 shows the SEM image of one La doped Sr_2IrO_4 single crystal during the EDS measurement. The nice surface of the crystal is revealed by cleaving the sample. Then EDS measurements are performed at random spots on the sample surface using slightly different spot sizes. By repeating the same process several times, the average doped La concentration can be obtained. Fig 3.6 shows the his-

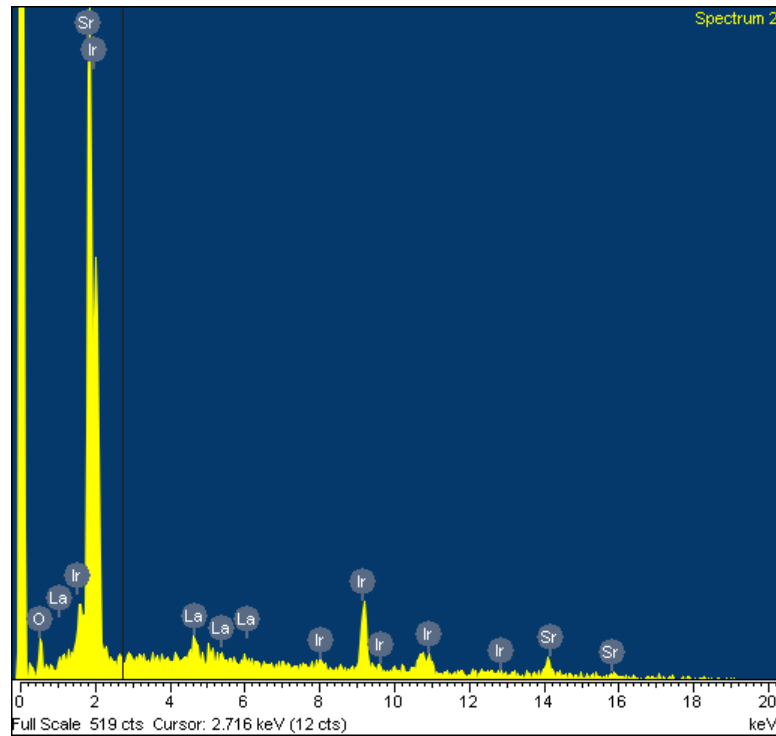


Figure 3.7: Typical EDS spectrum from one La doped Sr_2IrO_4 single crystal

togram of repeated EDS measurements on a 5% La doped Sr_2IrO_4 single crystal. The obtained average La concentration is $x = 5.3\% \pm 0.5\%$, which is very close to the nominal 5% La doping concentration. One typical EDS spectrum is shown in Fig 3.7, with the three peaks at the energy of 4.5 – 6 keV, indicating the presence of La in this doped sample. A quantitative fit to the spectrum is necessary in order to quantify the exact doping concentrations.

3.2.3 Transport measurement

There are other experimental probes that can also help characterize the samples, such as measurements from transport, magnetization, *etc.*... Samples with different levels of disorder, off-stoichiometry, oxygen vacancies and defects are characterized with different electronic and magnetic properties. Sometimes the differences between these samples can be dramatic. Therefore the electronic and magnetic measurements will provide crucial information about the sample quality.

The transport measurement is the simple and direct way to characterize the

electronic behavior. The underlying principle for transport is simply the Ohm's law. The most direct way to obtain the resistivity from a sample is the so-called two-probe method, which simply measures the voltage and current across the sample using the same probe. To reduce the contact resistance and obtain a better and accurate measurement of resistivity from the sample, the four-probe method is usually adopted as illustrated in Fig 3.8, where two inner probes are for the voltage and the other two for the current flow. The four-probe method significantly improves the accuracy and quality of the measured resistivity data. This method is especially important for measurements on samples with very small resistivity such as metals and superconductors.

$$V = IR = I\rho \frac{L}{wt} \quad (3.2)$$

3.2.4 Magnetization measurement

Bulk measurements of magnetization provide important insights on the magnetic properties of measured samples, which can also offer meaningful information about the sample quality. Just like the electronic properties can be affected by disorders, defects, impurities, *etc.*, the magnetic responses could also be influenced by those factors. For instance, the presence of magnetic $J_{\text{eff}} = \frac{1}{2} \text{Sr}_3\text{CaIr}_2\text{O}_8$ impurities could totally cover the nonmagnetic $J_{\text{eff}} = 0$ signal in $\text{Sr}_3\text{CaIr}_2\text{O}_9$, where these two

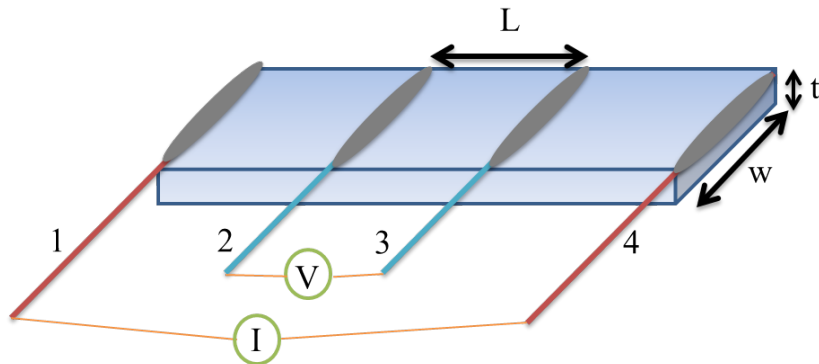


Figure 3.8: Typical four-probe measurement of resistivity in a sample. The inner two probes 2 and 3 measure the voltage, while the outer probes are for the current.

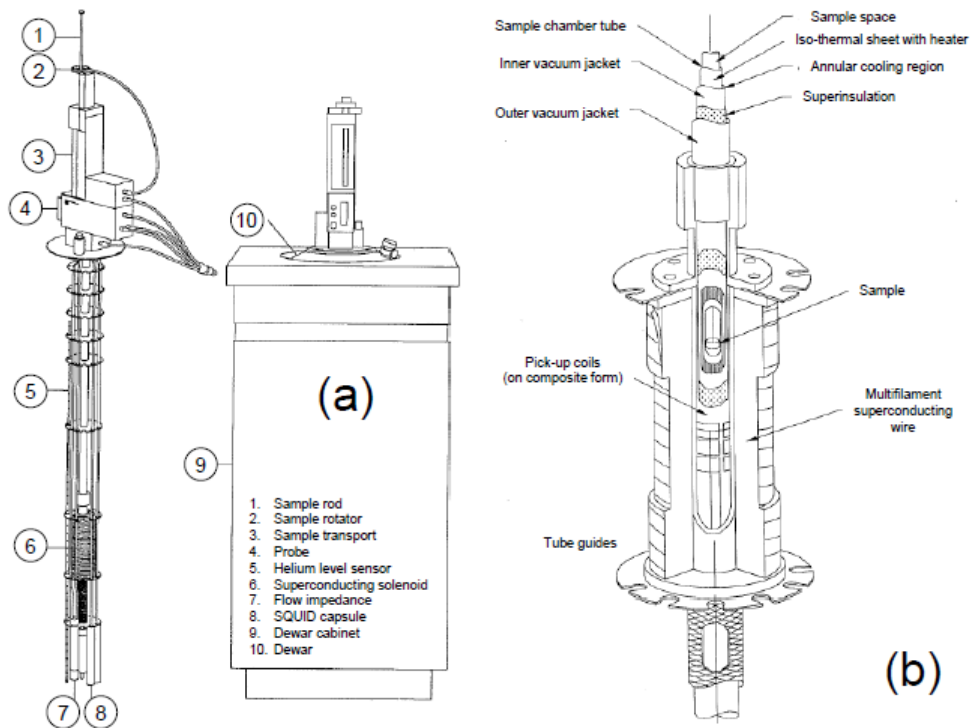


Figure 3.9: Schematics of the MPMS system. Adopted from [5].

compounds can hardly be discriminated by both XRD and EDS measurements if the portion of $\text{Sr}_3\text{CaIr}_2\text{O}_8$ impurity phase is very small compared to the majority $\text{Sr}_3\text{CaIr}_2\text{O}_9$ phase [57]. By performing the magnetization measurement, this puzzle will be alleviated to a minimum degree, thanks to the exceptional sensitive magnetization measurement. Furthermore, bulk DC or AC susceptibility measurement is usually the first step towards the microscopic understanding of detailed magnetic properties, probed by other techniques such as neutron and X-ray scattering.

The magnetization from a sample can be measured in several ways, including the force method, the torque method and the induction method, where the last one is the most widely adopted method. An example would be the SQUID (Superconducting Quantum Interference Device), which is the core component of the commercial Quantum Design (QD) Magnetic Property Measurement System (MPMS), shown in Fig 3.9.

The underlying working principle is induction. The moving sample under an applied DC field induces the current in the coils, which are coupled to the SQUID

sensor. By measuring the induced voltage and fitting the response curve, the net magnetization can be obtained. The SQUID measurement is sensitive to the bulk net magnetic response from sample, with the detection limit as high as 10^{-8} emu. Although this tool is super sensitive to magnetic moment, but not much microscopic details such as the magnetic structure can be obtained from this type of measurement. Therefore, it is necessary to apply other techniques such as μ SR, neutron and X-ray scattering to unveil the other aspects of magnetic properties.

3.3 Neutron scattering

The neutron scattering techniques are indispensable tools for investigating a broad array of electronic and magnetic properties in condensed matter and material science, for example, the static structural and magnetic properties, collective excitations like spin waves, critical phenomena and quantum phase transition. Such broad applicability is associated with the nature of neutron particles. Here in the following section, the basics of neutron and principles of the scattering techniques will be introduced. Note: excellent textbooks on this subject are referred in the following [58, 6, 59].

3.3.1 The basics of neutrons

The neutron is a massive and charge-neutral particle. The collective neutrons generated from nuclear fission or spallation source will interact with atomic nuclei via the strong short range nuclear force. Because neutron has no electric charge, it can penetrate deeply into a sample, without experiencing Coulomb repulsions between charged particles, probing the true bulk nature of the sample. Neutron also has a magnetic moment $\mu_n = 1.913\mu_N$, which is responsible for the weak interactions between neutrons and the unpaired electrons in magnetic atoms. The cross-sections for both nuclear and magnetic scattering of neutrons are of the same order of magnitude and are characterized by the scattering length b , which is element and isotope specific (Fig 3.10). Unlike X-ray, the scattering length is not directly related to

the atomic number Z . For instance, neutrons are sensitive to light elements such as Hydrogen (H) and Oxygen (O) in samples, which can be extremely useful for investigating the static and dynamic properties of O atoms in oxides. This unique feature along with other characteristics establish the important role of neutron scattering techniques, which are complementary to X-ray scattering techniques.

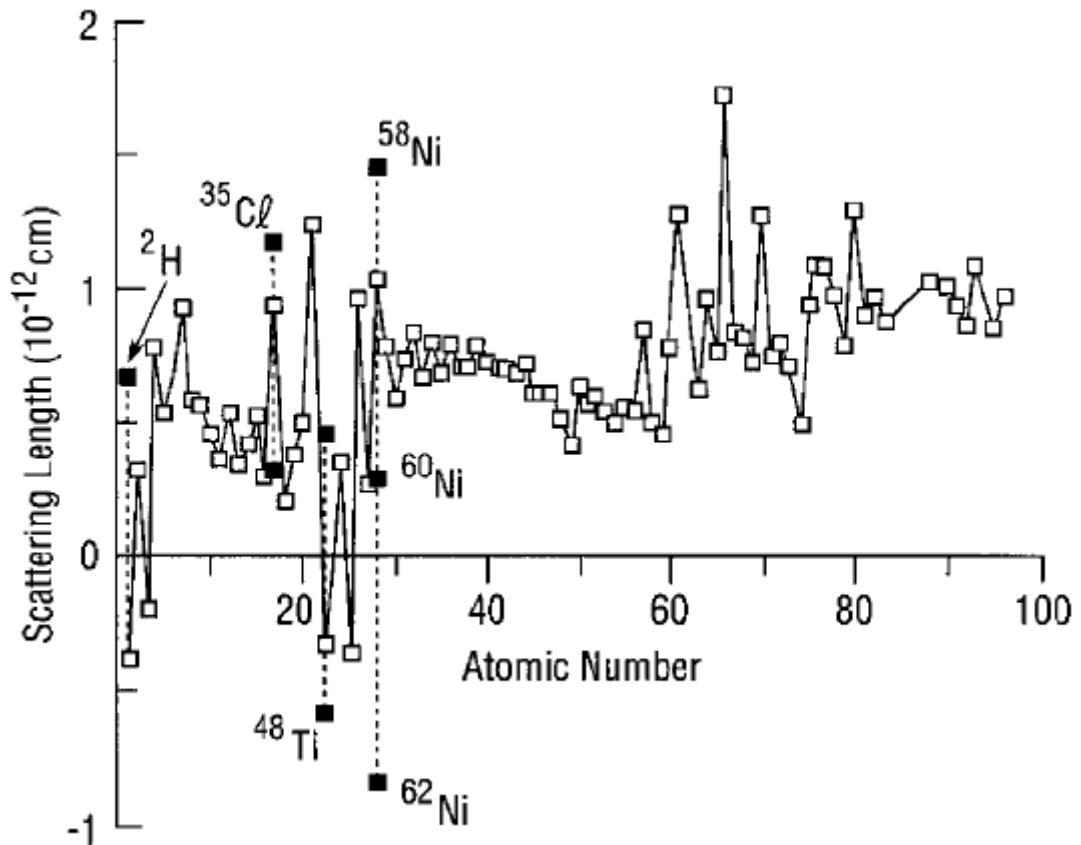


Figure 3.10: Variation of coherent scattering length b with atomic number (empty symbols). Some isotopes are shown in solid symbols. Adopted from [6].

Another important aspect that makes neutron scattering technique essential for studying emergent phenomena in condensed matter is the energy scales of neutrons, which are close to energies of various types of excitations such as phonons and spin waves. The applications of inelastic neutron scattering in terms of energy and momentum transfer are shown in Fig 3.11. Accordingly, the neutron scattering techniques are quite powerful in exploring a large variety of quantum phenomena in condensed matter.

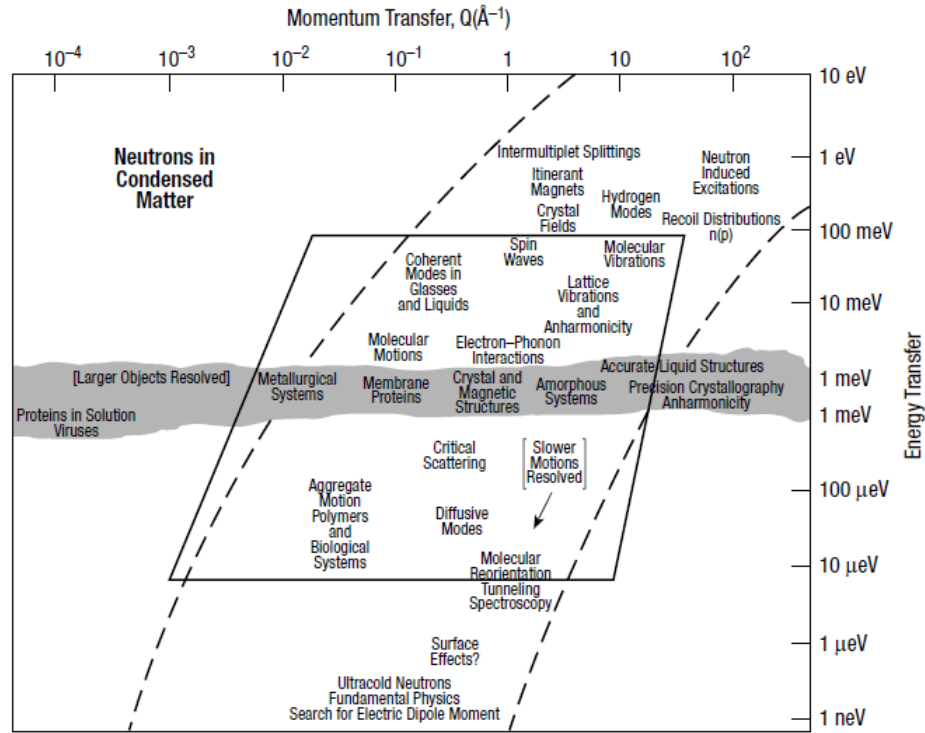


Figure 3.11: Various applications of inelastic neutron scattering in terms of energy and momentum transfer. Adopted from [6].

3.3.2 The principle of neutron scattering

The principle behind a neutron scattering experiment is to measure the initial and final states of each neutron before and after the interactions with the sample. Before the scattering events, the monoenergetic beam of neutrons is characterized by wave vector k_i and flux ϕ_{k_i} . The scattering rate is given by $\phi_{k_i} \sigma$, where σ is the scattering cross section. After the scattering events, the rate at which the neutrons are scattered into a given solid angle $d\Omega_f$, in the direction of the wave vector k_f , with the final energy between E_f and $E_f + dE_f$, is given by the product of ϕ_{k_i} and the double-differential cross section $d^2\sigma/d\Omega_f dE_f$. This double-differential cross section term can be expressed into a sum of two terms, *i.e.*, the coherent and incoherent parts:

$$\frac{d^2\sigma}{d\Omega_f dE_f} = \left(\frac{d^2\sigma}{d\Omega_f dE_f} \right)_{coh} + \left(\frac{d^2\sigma}{d\Omega_f dE_f} \right)_{inc} \quad (3.3)$$

In general, the coherent part contains important information about correlations between atoms, such as elastic Bragg scattering and/or inelastic scattering

by phonons or magnons. The incoherent part is related to the time correlations of an atom with itself and often is a source of isotropic background in inelastic neutron scattering experiments. Therefore, this incoherent part will not be discussed in details in this section.

The weak interacting nature of neutrons with atoms enables the treatment of small perturbation theory to neutron scattering plausible, *i.e.*, the scattering events cause the transitions from initial quantum states to the final states without altering the nature of the quantum states. Therefore, time dependent perturbation theory using Fermi's Golden rule can be applied to neutron scattering, which essentially probes the intrinsic properties of materials.

Assume the interaction operator for the neutron with the sample is V and label the initial (final) states of the samples by λ_i (λ_f), then the double-differential cross section for non-polarized neutron scattering process is given by

$$\left. \frac{d^2\sigma}{d\Omega_f dE_f} \right|_{\lambda_i \rightarrow \lambda_f} = \frac{k_i}{k_f} \left(\frac{m_n}{2\pi\hbar^2} \right)^2 \sum_{k_i, k_f} | \langle k_f \lambda_f | V | k_i \lambda_i \rangle |^2 \delta(\hbar\omega + E_i - E_f) \quad (3.4)$$

This cross section term is shown to be proportional to the scattering dynamic structure $S(\mathbf{Q}, \omega)$

$$\left. \frac{d^2\sigma}{d\Omega_f dE_f} \right|_{\lambda_i \rightarrow \lambda_f} = N \frac{k_i}{k_f} b^2 S(\mathbf{Q}, \omega) \quad (3.5)$$

where

$$S(\mathbf{Q}, \omega) = \frac{1}{2\pi\hbar N} \sum_{l, l'} \int_{-\infty}^{\infty} dt \langle e^{-i\mathbf{Q}\cdot\mathbf{r}_{l'}(0)} e^{i\mathbf{Q}\cdot\mathbf{r}_l(t)} \rangle e^{-i\omega t} \quad (3.6)$$

N is the number of nuclei. The goal of neutron scattering experiments is to measure $S(\mathbf{Q}, \omega)$ and hence determines the microscopic properties of the system. Of course, the conservation laws shall be respected during the scattering process:

$$E = \hbar\omega = \frac{\hbar^2}{2m_n} (k_i^2 - k_f^2) \quad (3.7)$$

$$\mathbf{Q} = \mathbf{k}_f - \mathbf{k}_i = \mathbf{G} + \mathbf{q}$$

here the momentum transfer \mathbf{Q} is referred to the nearest reciprocal lattice vector \mathbf{G} and reduced momentum transfer vector \mathbf{q} .

3.3.3 Coherent elastic nuclear scattering

Considering the coherent part of neutron scattering, the double differential cross section for crystalline sample consisting of a single element is

$$\left. \frac{d^2\sigma}{d\Omega_f dE_f} \right|_{coh} = N \frac{k_i}{k_f} \frac{\sigma_{coh}}{4\pi} S(\mathbf{Q}, \omega) \quad (3.8)$$

If the j th atom within the unit cell occupies the site with position vector \mathbf{r}_j , then the coherent elastic differential cross section generalizes to

$$\left. \frac{d\sigma}{d\Omega} \right|_{coh,el} = N \frac{(2\pi)^3}{v_0} \sum_{\mathbf{G}} \delta(\mathbf{Q} - \mathbf{G}) |F_N(\mathbf{G})|^2 \quad (3.9)$$

$$F_N(\mathbf{G}) = \sum_j \bar{b}_j e^{i\mathbf{G} \cdot \mathbf{r}_j} e^{-W_j}$$

where v_0 is the unit cell volume, $F_N(\mathbf{G})$ is static nuclear structure factor and e^{-W_j} is related to the Debye-Waller factor, which reflects the atomic displacements relative to the equilibrium state. Thus elastic nuclear Bragg scattering reveals valuable information about the structural properties of the sample under investigation.

3.3.4 Coherent inelastic nuclear scattering

The coherent elastic nuclear scattering contains information on the static structural information; while the inelastic counterpart reflects the dynamic structural fluctuations, *i.e.*, phonons. An celebrated property of the scattering function is the principle of detailed balance:

$$S(-\mathbf{Q}, -\omega) = e^{-\hbar\omega/k_B T} S(\mathbf{Q}, \omega) \quad (3.10)$$

This relation indicates that the probability of a transition in a sample depends on the statistical weight factor for the initial states.

The scattering factor is related to the imaginary part of the dynamical susceptibility $\chi''(\mathbf{Q}, \omega)$ via the fluctuation-dissipation theorem:

$$S(\mathbf{Q}, \omega) = \frac{\chi''(\mathbf{Q}, \omega)}{1 - e^{-\hbar\omega/k_B T}} \quad (3.11)$$

Consider a lattice with n atoms per unit cell, for the case when a neutron scattered from the lattice creates or destroys a single phonon, the dynamical susceptibility is given by

$$\chi''(\mathbf{Q}, \omega) = \frac{1}{2} \frac{(2\pi)^3}{v_0} \sum_{\mathbf{G}, \mathbf{q}} \delta(\mathbf{Q} - \mathbf{q} - \mathbf{G}) \sum_s \frac{1}{\omega_{\mathbf{q}s}} |\mathcal{F}(\mathbf{Q})|^2 \times [\delta(\omega - \omega_{\mathbf{q}s}) - \delta(\omega + \omega_{\mathbf{q}s})]$$

$$\mathcal{F}(\mathbf{Q}) = \sum_j \frac{\bar{b}_j}{\sqrt{m_j}} (\mathbf{Q} \cdot \boldsymbol{\xi}_{j_s}) e^{i\mathbf{Q} \cdot \mathbf{r}_j} e^{-W_j} \quad (3.12)$$

Here $\omega_{\mathbf{q}s}$ indicates the phonon frequency with s labelling different phonon modes, $\boldsymbol{\xi}_{j_s}$ is the polarization vector for the j th atom inside the unit cell. The $\mathcal{F}(\mathbf{Q})$ term is the dynamic structure factor, which is analogous to the static structure factor in Eq. 3.9 and contains significant knowledge on the dynamic properties of the system. For instance, this dynamic structure factor is proportional to $\mathbf{Q} \cdot \boldsymbol{\xi}_{j_s}$ so that the intensity of phonon scattering increases with larger Q , which is in contrast to the Q -dependence of magnetic scattering cross-sections.

3.3.5 Coherent magnetic scattering

The neutron has a magnetic dipole moment $\boldsymbol{\mu}_n = -\gamma\mu_N\boldsymbol{\sigma}$, where γ is the gyromagnetic ratio, μ_N is the nuclear magneton and $\boldsymbol{\sigma}$ is the spin operator. Therefore, neutrons can be scattered by magnetic moment of an atom via the dipole-dipole

interaction. Consider unpolarized neutrons and localized moments only, the total coherent differential cross section for magnetic scattering is given by

$$\begin{aligned} \frac{d^2\sigma}{d\Omega_f dE_f} \Big|_{coh,mag} &= \frac{N k_i}{\hbar k_f} \left(\frac{\gamma r_0}{2} \right)^2 g^2 f^2(\mathbf{Q}) e^{-2W} \sum_{\alpha\beta} \left(\delta_{\alpha\beta} - \frac{Q_\alpha Q_\beta}{Q^2} \right) S^{\alpha\beta}(\mathbf{Q}, \omega) \\ S^{\alpha\beta}(\mathbf{Q}, \omega) &= \int dt \frac{1}{2\pi\hbar N} \sum_{j,j'} \left\langle e^{-i\mathbf{Q}\cdot(\mathbf{R}_j - \mathbf{R}_{j'})} S_j^\alpha S_{j'}^\beta \right\rangle e^{-i\omega t} \end{aligned} \quad (3.13)$$

where $\frac{\gamma r_0}{2} = 0.27 \times 10^{-12}$ cm, $f(\mathbf{Q})$ is the magnetic form factor and $S^{\alpha\beta}(\mathbf{Q}, \omega)$ is the dynamical structure factor given by the Fourier transform of the time dependent spin-spin correlation function. This expression describes both coherent elastic magnetic scattering and coherent inelastic magnetic scattering, which contains meaningful information of the static and dynamic magnetic excitations. The geometric factor $\left(\delta_{\alpha\beta} - \frac{Q_\alpha Q_\beta}{Q^2} \right)$ results from magnetic dipole-dipole interaction, which demonstrates that magnetic neutron scattering is only sensitive to magnetic components that are perpendicular to the momentum transfer \mathbf{Q} .

The magnetic form factor $f(\mathbf{Q})$ is the Fourier transform of the normalized unpaired magnetization density on single atom, which is an analogue to the structure form factor. It contains both spin and orbital components.

$$f(\mathbf{Q}) = \frac{g_S}{g} f_S(\mathbf{Q}) + \left(1 - \frac{g_S}{g} \right) f_L(\mathbf{Q}) \quad (3.14)$$

To the leading order, magnetic form factor can be evaluated using the dipole approximation in terms of spherical harmonics.

$$\begin{aligned} f_S(\mathbf{Q}) &= \langle j_0(\mathbf{Q}) \rangle \\ f_L(\mathbf{Q}) &= \frac{1}{2} [\langle j_0(\mathbf{Q}) \rangle + \langle j_2(\mathbf{Q}) \rangle] \end{aligned} \quad (3.15)$$

The rapid suppression of $\langle j_{2k}(\mathbf{Q}) \rangle$ respect to $|\mathbf{Q}|$ indicates that the intensity of magnetic neutron scattering is usually the strongest at small $|\mathbf{Q}|$, which is in contradictory to the behavior of structure form factor in Eq. 3.12. Therefore, the contrasting Q dependent properties can be employed to distinguish structural and

magnetic excitations.

Another important aspect of coherent magnetic scattering is the existence of a sum rule, which governs the distribution of spectral weight between elastic and inelastic processes. By integrating the dynamic structure factor over the whole first Brillouin zone and over the entire energy transfer, a simple sum rule is obtained:

$$\int_{-\infty}^{\infty} d\omega \int_{BZ} d\mathbf{Q} S^{\alpha\beta}(\mathbf{Q}, \omega) = S(S+1) \delta_{\alpha\beta} \quad (3.16)$$

In the large spin S limit and at low temperatures compared to the ordering temperature of a magnetically ordered system, the elastic magnetic scattering is proportional to S^2 , then the spectral weight for spin wave excitations is proportional to S , which is only $1/S$ of the elastic contribution.

3.3.6 Neutron scattering instruments

In this section, the neutron scattering spectrometers will be briefly introduced: triple-axis spectrometer and time-of-flight spectrometer. While the former can be utilized to explore both the elastic and inelastic neutron scattering contributions with high resolutions, the limited accessible range in four dimension (\mathbf{Q}, ω) phase space calls for the need of time-of-flight spectrometer, which can essentially map the whole (\mathbf{Q}, ω) phase space, although with poorer resolutions compared to the former.

• Triple-Axis Spectrometer

The three-axis instrument is the versatile and useful instrument for investigating both elastic and inelastic neutron scattering in a precisely controlled manner. Here Fig 3.12 shows the typical schematic of a triple axis spectrometer (TAS) at HB1A of Oak Ridge National Lab (ORNL). Another TAS instrument used for experiment is at BT7 of NIST Center for Neutron Research, which essentially shares the same core designs. As shown in the schematic of HB1A in Fig 3.12(a), the three



Figure 3.12: (a) Schematic of a triple-axis spectrometer at HB1A of Oak Ridge National Lab (ORNL); (b) Real image of HB1A. Adopted from [7].

axes correspond to the axis of rotation of the monochromator, the sample, and the analyzer, respectively. The monochromator (analyzer) controls the direction and momentum of the incident beam (final beam after scattering); while the axis for sample restrains the scattering at desired momentum transfer \mathbf{Q} .

• Time-of-Flight Spectrometer

Neutron time-of-flight (TOF) spectrometer exploits the particle nature of neutrons to measure and explore the momentum and energy transfer during scattering events. Fig 3.13 shows the typical schematic view of a time of flight spectrometer SEQUOIA at Spallation Neutron Source (SNS) of ORNL, which adopts the direct geometry with fixed incident neutron wavevector \mathbf{k}_i and varying final wavevector \mathbf{k}_f based on the neutrons' time of flight between the sample and the detector banks. The working principle is to count the time for neutron to travel, which is equivalent to the neutron travelling velocity or its energy and the position sensitive detector banks record the information of the neutron momentum after the scattering event. Knowing the energy and momentum of a neutron before and after the scattering event authorizes the determination of inelastic scattering process.

A broad spectrum of polychromatic neutrons are generated, before the modulation through a series of choppers such as the T_0 chopper, which removes the

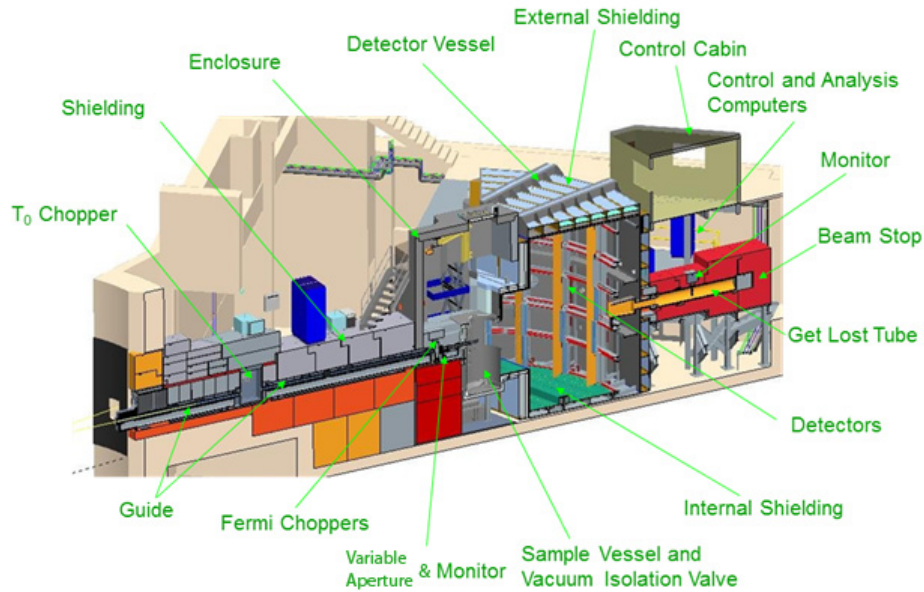


Figure 3.13: Schematic view of the time of flight spectrometer SEQUOIA at SNS of ORNL, indicating all of the major instrument components. Adopted from [8].

undesired high energy neutrons. Then the Fermi chopper monochromates the neutrons, before being scattered by the sample. Then the position sensitive banks record the arrival position of scattered neutrons in three-dimensional coordinate space. The arrival time and the positions determine the neutron final state with (E_f, \mathbf{k}_f) . With the knowledge of the initial and final states of neutrons and from the conservation laws of energy and momentum during the scattering process, the information of the dynamic excitations can be extracted.

Compared to TAS which only probes one point in the enormous (\mathbf{Q}, ω) phase space at one time, the TOF measurement scans a much larger portion of the phase space at the same time. The time resolved nature of TOF technique enables the feasible exploration of energy up to the incident energy of neutrons. Further more, in the direct geometry TOF spectrometer like SEQUOIA, the sample can be rotated to broaden the coverage of phase space. This rotating crystal method was initially pioneered by Toby Perring at the ISIS spallation source, and is now routinely employed for TOF measurements.

3.4 X-ray scattering

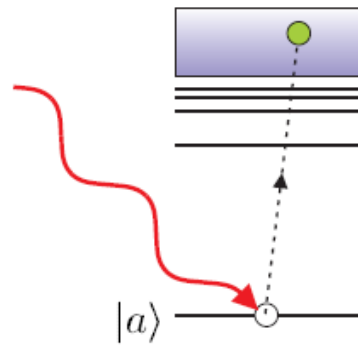
The neutron scattering techniques introduced above are powerful tools to investigate nuclear and magnetic properties. However, there are intrinsic difficulties that can hamper the explorations on certain systems, such as iridates which are the focus of the current study. The two main weaknesses for studying iridates by neutron scattering techniques are the strong absorption of neutrons by iridium (Ir) and the small sample size (or mass), respectively. Because neutron scattering is a weak perturbation to the system and neutron source produces relative low flux, strong absorption of neutrons by Ir together with the small sample sizes significantly constrained the applications of neutron scattering to iridates. These problems are greatly mitigated by employing X-ray scattering techniques, because of the available high flux of synchrotron X-ray sources and large atomic number Z of Ir, along with some other benefits. In this section, I will briefly introduce the resonant elastic X-ray scattering (REXS) technique, which demonstrates impressive capabilities in investigating the magnetic properties in iridates. Please note: there are a lot of good references that I referred to in this section [9, 60, 61, 62, 63].

3.4.1 The principle of X-ray scattering

The scattering of X-ray from matter is different from the scattering mechanism in neutron scattering. Nevertheless, it turns out X-ray scattering techniques can be advantageous as well to survey nuclear and magnetic properties, especially in iridates which will be focus of the current study.

The X-ray interacts with matter through electromagnetic fields with electric fields of static charges and the magnetic moment of electrons in solid. The former is the well-known charge scattering or Thomson scattering; while the latter is due to small relativistic effects and was first examined by de Bergevin and Brunel [64]. These effects are typically very small. It is only possible to study the magnetic properties as a competing/complementary tool to neutron scattering, until the advent of high-brilliance synchrotron X-ray sources and the discovery of strong en-

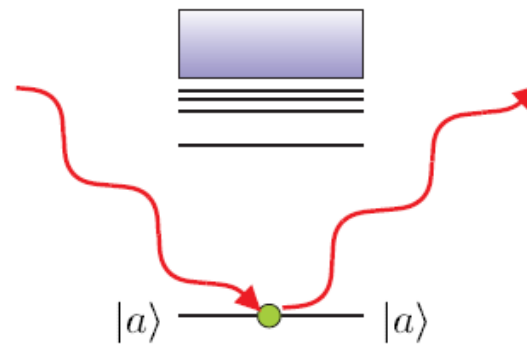
(a) Photoelectric absorption



1st order:

$$\frac{e\mathbf{A}\cdot\mathbf{p}}{m}$$

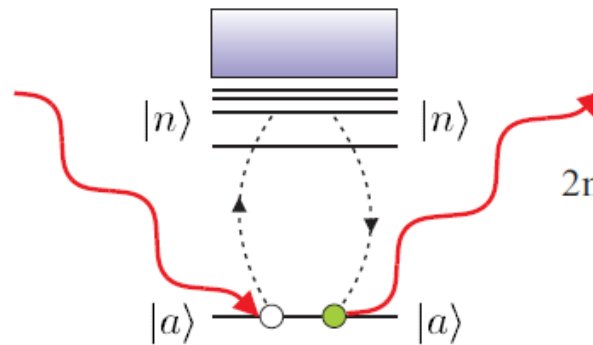
(b) Thomson scattering



1st order:

$$\frac{e^2\mathbf{A}^2}{2m}$$

(c) Resonant scattering



2nd order:

$$\frac{e\mathbf{A}\cdot\mathbf{p}}{m}$$

Figure 3.14: Interaction of a photon with an atomic electron. (a) Photoelectric absorption, (b) Thomson scattering, (c) Resonant elastic scattering. Adopted from [9].

hancement of magnetic scattering intensity when the energy of photons is tuned to an absorption edge of the material [60].

Let's consider one photon interacts with an isolated atom first. The resonant X-ray scattering is a second order process, which can be viewed as a two-step mechanism, as shown in Fig 3.14(c). In the first step, the incident photon with energy

$\hbar\omega_{\mathbf{k}}$ strikes the atom, promoting one electron from the core level to the valence band, leaving one hole in the core; such unstable intermediate state will quickly decay, with one electron filling the hole and emitting a photon with energy $\hbar\omega_{\mathbf{k}'}$ (Note: In the following, all final states are characterized by $'$, as in the final wavevector \mathbf{k}'). The energy and momentum conservations impose the constraints:

$$\begin{aligned} E = \hbar\omega &= \hbar\omega_{\mathbf{k}} - \hbar\omega_{\mathbf{k}'} \\ \mathbf{Q} &= \mathbf{k} - \mathbf{k}' \end{aligned} \quad (3.17)$$

In the elastic scattering process, $\hbar\omega_{\mathbf{k}} = \hbar\omega_{\mathbf{k}'}$, only momentum is transferred to the system.

3.4.2 REXS cross section

For resonant energies smaller than 100 keV, the X-rays weakly interact with samples, which suggests the validity of weak perturbation theory such as Born-Oppenheimer approximation [65, 63]. Consider the differential cross section for REXS on single crystals with lattice site j :

$$\frac{d\sigma}{d\Omega} = r_0^2 \left| \sum_j e^{i\mathbf{Q}\cdot\mathbf{R}_j} f_j(\mathbf{Q}, \mathbf{k}, \mathbf{k}', \boldsymbol{\varepsilon}, \boldsymbol{\varepsilon}', \omega_k) \right|^2 \quad (3.18)$$

where $r_0 = e^2/mc^2$ is the classical electron radius, \mathbf{R}_j is the site position vector, $\boldsymbol{\varepsilon}$ ($\boldsymbol{\varepsilon}'$) is the in-going (out-going) polarization vector and $f_j(\mathbf{Q}, \mathbf{k}, \mathbf{k}', \boldsymbol{\varepsilon}, \boldsymbol{\varepsilon}', \omega_k)$ is the scattering amplitude at site j .

Dropping the site index j , the scattering amplitude f can be decomposed into several terms:

$$f(\mathbf{Q}, \mathbf{k}, \mathbf{k}', \boldsymbol{\varepsilon}, \boldsymbol{\varepsilon}', \omega_k) = f^{Charge}(\mathbf{Q}, \boldsymbol{\varepsilon}, \boldsymbol{\varepsilon}') + f^{NRMXS}(\mathbf{Q}, \mathbf{k}, \mathbf{k}', \boldsymbol{\varepsilon}, \boldsymbol{\varepsilon}', \omega_k) + f^{RMXS}(\mathbf{k}, \mathbf{k}', \boldsymbol{\varepsilon}, \boldsymbol{\varepsilon}', \omega_k) \quad (3.19)$$

The first term f^{Charge} is the leading first order Thompson charge scattering term. The second term f^{NRMXS} is the non-resonant magnetic X-ray scattering term,

due to the scattering from spins of unpaired electrons. This term is typically 5-6 orders of magnitude smaller compared to the first charge scattering term, because of the weaker scattering amplitude and the smaller numbers of available spins for scattering. The last term f^{RMXS} is the focus of the current study, *i.e.*, the energy dependent resonant magnetic X-ray scattering amplitude. Although the nature of last term is also magnetic, it has a different origin compared to the second term.

• Non-resonant cross section

In the non-resonant regime, where the energy is far from the absorption edge, the contribution of the last term in 3.19 is negligible. Therefore, the scattering amplitude can be written as

$$f = f^{Charge} + f^{NRMXS} = \rho(\mathbf{Q}) \boldsymbol{\epsilon}'^* \cdot \boldsymbol{\epsilon} + ir_0 \left(\frac{\hbar\omega}{m_e c^2} \right) [\mathbf{L}(\mathbf{Q}) \cdot \mathbf{A} + \mathbf{S}(\mathbf{Q}) \cdot \mathbf{B}] \quad (3.20)$$

Here $\rho(\mathbf{Q})$, $\mathbf{L}(\mathbf{Q})$ and $\mathbf{S}(\mathbf{Q})$ are the Fourier transforms of the electron charge, the orbital and spin magnetization density, respectively. The matrices \mathbf{A} and \mathbf{B} are polarization and wavevector dependent. In principle by taking advantage of the polarizations, it is possible to separate the spin \mathbf{S} and orbital \mathbf{L} moment contributions to the total magnetic moment in the system under investigation.

• Resonant cross section

When the energy of the incident photons is tuned to the absorption edge, additional resonant scattering term contribute to the magnetic scattering, which has a different nature compared to the non-resonant magnetic scattering contribution. This resonant component arises mainly because of two important ingredients: the Pauli principle and the SOC. Since the resonant term belongs to a second order process, it will increase significantly when the energy difference denominator is minimized, *i.e.*, near the absorption edge. In an alternative way, the enhancement of resonant magnetic X-ray scattering results from the virtual transitions to the intermediate excited states near the Fermi level. Pauli principle and SOC polarize the valence states and ensure the availability of intermediate state. The resonant scat-

tering amplitude can be expressed within the dipole approximation by ignoring the multipole order [65, 60, 61, 63]:

$$f^{RMXS} = F^0(\boldsymbol{\epsilon}'^* \cdot \boldsymbol{\epsilon}) - iF^1(\boldsymbol{\epsilon}'^* \times \boldsymbol{\epsilon}) \cdot \mathbf{e}_m + F^2(\boldsymbol{\epsilon}' \cdot \mathbf{e}_m)(\boldsymbol{\epsilon} \cdot \mathbf{e}_m) \quad (3.21)$$

Here F^n are factors determining the strength of resonant scattering and \mathbf{e}_m is the unit vector along the magnetic moment direction. The last term is quadratic in magnetic scattering and can often be ignored. If the incident and final polarizations are flipped ($\boldsymbol{\epsilon}'^* \cdot \boldsymbol{\epsilon} = 0$), then only the second term contributes to the magnetic signal. Thus the scattering amplitude can be approximated in a simple form:

$$f^{RMXS} \approx -iF^1(\boldsymbol{\epsilon}'^* \times \boldsymbol{\epsilon}) \cdot \mathbf{e}_m \quad (3.22)$$

Correspondingly, magnetic scattering intensity can be cast as

$$I(\boldsymbol{\omega}, \mathbf{k}) \propto \left| \sum_j -iF^1(\boldsymbol{\epsilon}'^* \times \boldsymbol{\epsilon}) \cdot \mathbf{e}_{m,j} e^{i\mathbf{Q} \cdot \mathbf{R}_j} \right|^2 \quad (3.23)$$

Employing this simplified form, simulations of the scattering intensity can be performed with different magnetic models, which can essentially determine the magnetic structure with the best fit to the experimental observations. Therefore, REXS can be utilized to explore the magnetic properties serving as a strong complementary tool to neutron scattering technique.

3.4.3 REXS instrument

The REXS instrument share similar design principles with TAS for neutron diffraction, as both are scattering techniques which essentially utilize the same Bragg's law. For X-ray scattering experiments, reflection geometry is often adopted because of the less penetrative nature compared to neutrons. Fig 3.15 shows the typical vertical scattering geometry of REXS. The incident X-rays are horizontally polarized

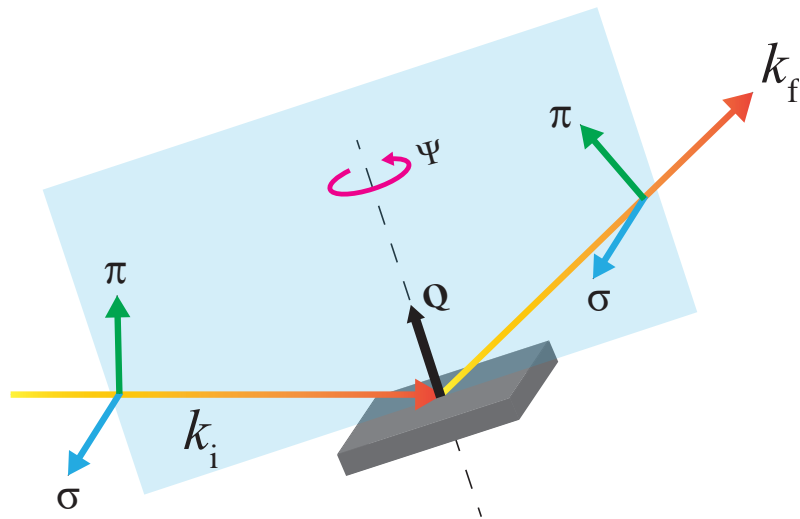


Figure 3.15: Resonant elastic X-ray scattering (REXS) geometry. A vertical scattering plane was employed. The incoming beam was horizontally polarized perpendicular to the scattering plane.

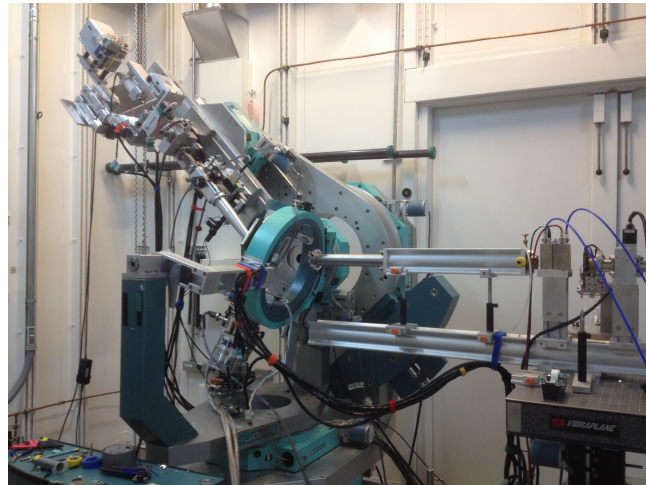


Figure 3.16: REXS instrument at 6-ID-B at advanced photon source.

before impinging on samples, where the azimuthal diffractometer allows the ψ rotation of the sample around the scattering vector \mathbf{Q} . This type of rotation can be performed to discriminate the multiple scattering signals. After the scattering with samples, the final signals can be examined in different polarizing states, which is essential for discriminating charge or magnetic signals.

Fig 3.16 shows the instrument at 6-ID-B at advanced photon source. For a complete overview of the experimental setup of REXS, refer to [66] for example.

3.5 Comparison between X-ray and neutron

Both X-ray and neutron scattering techniques have their own strengths and weaknesses, thus often a combination of the two techniques are necessary in order to understand the electronic and magnetic properties. Here only the comparison between resonant elastic X-ray scattering and neutron diffraction will be discussed. A detailed comparison in every aspect is beyond the scope of the current focus.

★ Flux

Higher flux means larger scattering intensity and better chances for examining weak features. The flux for both synchrotron and neutron sources are shown in Fig 3.17. The 3rd generation synchrotron sources typically have an average spectral brightness larger than 10^{18} photons/s/mm²/mrad²/0.1%BW, where 0.1%BW denotes a bandwidth $10^{-3}\omega$ centered around the frequency ω [10]. Future facilities are expected to have even higher flux with three more orders of magnitude than current ones. The typical spallation sources generate greater than 10^{17} neutrons/s/cm², while the reactor based sources now produce 10^{15} neutrons/s/cm² [10]. Therefore, in terms of flux, X-ray sources are more promising.

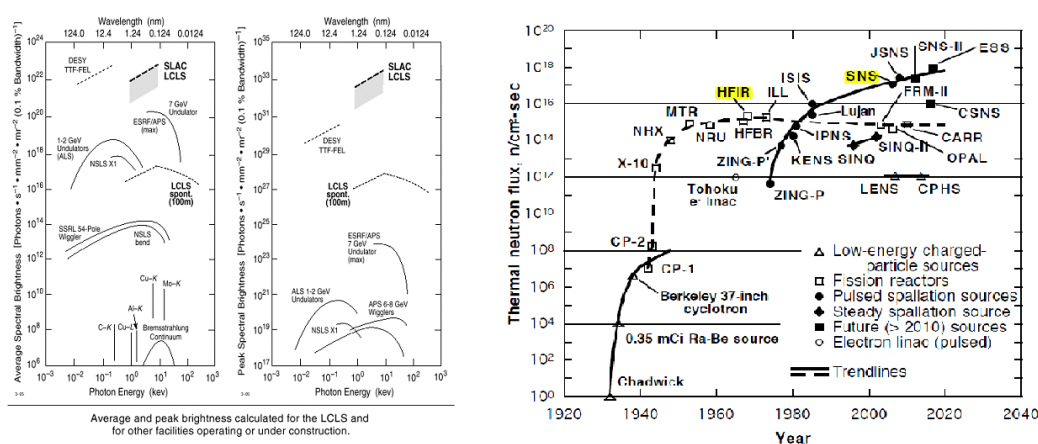


Figure 3.17: (left) Average and peak brilliance for synchrotron facilities. (Right) Thermal neutron flux at neutron facilities. Adopted from [10].

★ Bulk sensitivity

Both X-ray and neutron diffraction can be considered as bulk sensitive, although

the former is less penetrative even in the typical hard X-ray regime. For instance in iridates, the resonant energy on Ir L_3 edge is 11.215 keV, which means within the hard X-ray regime with a penetration depth reaching the order of several microns. For neutron diffraction, the typical penetration depth is much larger, approaching the order of centimeters.

★ **Element specificity**

Both techniques can be considered as element specific, although with different characteristics. X-ray scattering favors elements with large atomic number Z . Naturally, it is rather inefficient for light elements such as H or O. Another weakness is the poor contrast between elements with close atomic numbers. For neutrons, those difficulties mentioned are greatly mitigated and neutrons can even differentiate isotopes. However, there are some elements which are strong neutron absorbers, such that the experimental intensity is significantly reduced for studying those strong absorbers, limiting the functionality of neutron scattering in examining those compounds.

★ **Oxidation state**

For RXS, it is possible to tune the energy to the absorption edge, which is sensitive to the local environment, such as the oxidation state. This type of sensitivity is absent in neutron scattering because of the charge neutral property of neutron particles.

★ **Orbital sensitivity**

Since the microscopic mechanism of X-ray scattering involves specific orbitals, the orbital contribution can be separated from the total magnetization; while for neutrons, it is not straightforward to disentangle the orbital component from the total magnetic moment.

★ **Polarization analysis**

Although polarization analysis can be done on both techniques, X-rays gain another advantage over neutrons, since synchrotron radiation generated by planar undulator is almost completely linearly polarized, with the polarization rate as high as

99.99%. Naturally produced neutrons are unpolarized. In order to perform neutron polarization analysis, polarizing filters (for instance) can be applied to polarize the neutrons, which will reduce the neutron flux. Therefore, the polarization analysis is limited in neutron scattering experiments.

★ **Momentum and energy resolution**

For highly collimated X-ray beam, a high momentum resolution can be achieved, which is significantly better than the neutron counter-part; while in terms of energy resolution, neutrons are much better. The thermal energy of neutrons can be as small as the order of meV, not to mention the resolution in energy. For X-ray diffraction, the typical energy resolution is on the order of eV, with the incident energy on the order of keV in the hard X-ray regime.

★ **Sample size and quality requirements**

This is the crucial difference between X-ray and neutron scattering techniques. Since X-ray beams can be highly collimated and have high brilliance, small samples on the orders of μm can still be studied, while on the other hand for neutrons, usually samples with the minimum size of mm is required.

On the other hand, because of high spatial resolution in X-ray diffraction, samples with a better mosaic are required in order to obtain meaningful data. For neutrons, this requirement is less tightened.

Brief summary:

In summary, both X-ray and neutron scattering techniques have their pros and cons. It is necessary to utilize both techniques in order to explore the electronic and magnetic properties in different systems.

Chapter 4

Collapse of spin orbit assisted Mott insulating state in electron doped Sr_2IrO_4

As mentioned in the first chapter, the inclusion of strong spin orbit coupling together with other competing energy scales provide fertile playground for realizing exotic phases in iridates. Here in this chapter, the influence of electron doping on the prototypical spin orbit assisted Mott insulator Sr_2IrO_4 (Sr214) will be explored. Our results evidence the collapse of Mott insulating gap and emergence of spin density wave state with increasing La doing, indicating that quenched Mott phases in electron-doped Sr_2IrO_4 and hole-doped La_2CuO_4 support common competing electronic states.

4.1 Introduction

Iridium oxides have captured substantial attention in recent years, due to the possibility of realizing a variety of exotic ground states, such as Kitaev quantum spin liquids, Weyl semimetals, and spin orbit coupled Mott insulators [1, 17, 28, 50, 67, 68, 30, 31, 69]. The essential element is strong spin-orbit coupling's interplay with other comparable energy scales, such as the on-site Coulomb repulsion U and crystal electric field splitting Δ (See Table 2.1). One direct consequence is the formation of a spin and orbital angular momenta entangled $J_{\text{eff}} = \frac{1}{2}$ wave function for Ir^{4+} valence electrons in a cubic crystal field. Further richness is ensured through the existence of diverse stable lattice geometries embracing this entangled wave function, which in turn supply a variety of platforms for hosting diverse quantum states [70]. Celebrated examples include the honeycomb lattice $(\text{Na,Li})_2\text{IrO}_3$ [71, 72, 50, 73, 74, 75], hyper-Kagome lattice $\text{Na}_4\text{Ir}_3\text{O}_8$ [76, 77, 78], pyrochlore geometries $\text{A}_2\text{Ir}_2\text{O}_7$ ($\text{A} = \text{Y, Yb, Pr, Nd, Sm, Eu, Tb} \dots$) [79, 80, 81, 82] and the layered square lattice Ruddlesden-Popper (R.P.) $\text{A}_{n+1}\text{Ir}_n\text{O}_{3n+1}$ ($\text{A} = \text{Sr, Ca, Ba}$) iridates [30, 31, 69, 83, 84, 85, 38, 86, 87, 88, 89], which will be the focus of this study.

Within the $n = 1$ R.P. lattice, the spin orbit-coupled $J_{\text{eff}} = \frac{1}{2}$ state was proposed to account for the insulating ground state [30, 31, 69], which is also expected in other commonly encountered $5d$ TMOs. Although this system has long been of interest due to structural similarities comparing to its $3d$ -electron high T_c analogue La_2CuO_4 [83, 84, 90], more recent electronic analogies have been mapped through the single-band Hubbard model of hole doped cuprates to electron doped $\text{Sr}214$ and proposed that unconventional superconductivity may emerge from carrier doped SOM state [91, 92, 93, 94]. Signatures of d -wave gap symmetry are indeed reported from angle-resolved photoemission (ARPES) and scanning tunneling microscopy (STM) measurements of surface-electron-doped Sr_2IrO_4 [95, 96], which supports the theoretical mapping between hole doped cuprates to electron doped iritates.

Tremendous experimental efforts have since focused on perturbing the spin orbit Mott ground state via a variety of methods such as carrier substitution and

through applying external pressure [97, 98, 99, 11, 100, 101, 102, 103, 104, 105, 106], yet detection of bulk superconductivity remains elusive. This is potentially due to limits imposed by chemical solubility [11] and extrinsic disorder [11] such as oxygen vacancies [97, 107] and other potential defects; however regardless of these hindrances, diverse unique phenomena have been reported in carrier substituted R.P. iridates. Some examples include the emergence of nearby competing magnetic states in hole-doped Sr214 [108, 109], electronic phase separation in hole-doped Sr₃Ir₂O₇ [110] and negative electronic compressibility in La-doped Sr₃Ir₂O₇ [111]. This growing list is a demonstration of the fragility of delicate balance between competing energy scales inherent to the spin orbit coupled state, and it further points toward the potential of realizing novel electronic and magnetic phases within these compounds stemming from quenched underlying Mott state.

4.2 Background information

Before presenting the details of experimental results, it is necessary to introduce the key background information related to the system under investigation.

Sr₂IrO₄ was first synthesized more than 50 years ago by Randall *et al.*, who originally suggested the structure symmetry as K₂NiF₄ type (space group *I4/mmm*) [112]. Later neutron diffraction work on this compound established a reduced tetragonal space group *I4₁/acd*, resulting from staggered rotations of IrO₆ octahedra respect to the crystallographic *c* axis by roughly 12° (Fig 4.1) [83, 84]. A subtle structural symmetry lowering was further reported, resulting from two unique Ir sites per plane within the space group of *I4₁/a* [45, 46, 113, 114].

As shown in Fig 4.2, charge transport reveals an insulating ground state, explained by the novel $J_{\text{eff}} = \frac{1}{2}$ ground state [30, 31, 69], consistent with a charge gap of about 600 meV observed in STM [115, 116]. A canted antiferromagnetic (CAF) state is stabilized in the parent state of Sr214 below $T_{\text{AF}} \approx 230$ [31], with the order moment of $\mu_{\text{AF}} \approx 0.35\mu_B$ per Ir site remaining locked to the in-plane octahedral tilts [45, 46, 117]. Metamagnetic transition beyond a critical $\mu_0 H_C \approx 0.2$ T exists with

an applied in-plane field [31], which complicates detailed analysis of static spin susceptibility. Therefore, scattering techniques such as X-ray and neutron provide the clearest picture of the continuous evolution of AF magnetic structure.

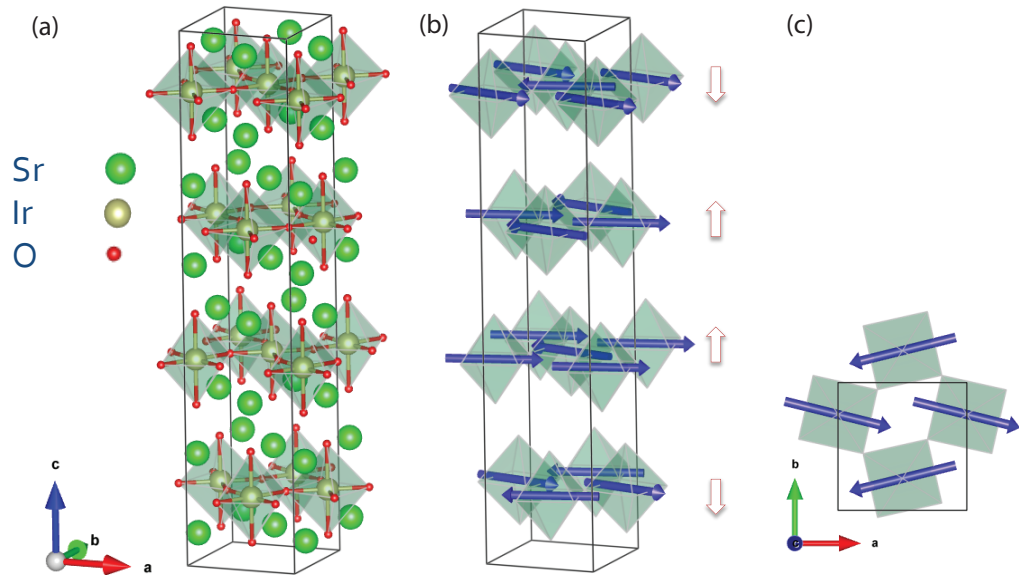


Figure 4.1: Crystal and magnetic structure of Sr_2IrO_4 , for simplicity tetragonal space group $I4_1/acd$ is adopted.

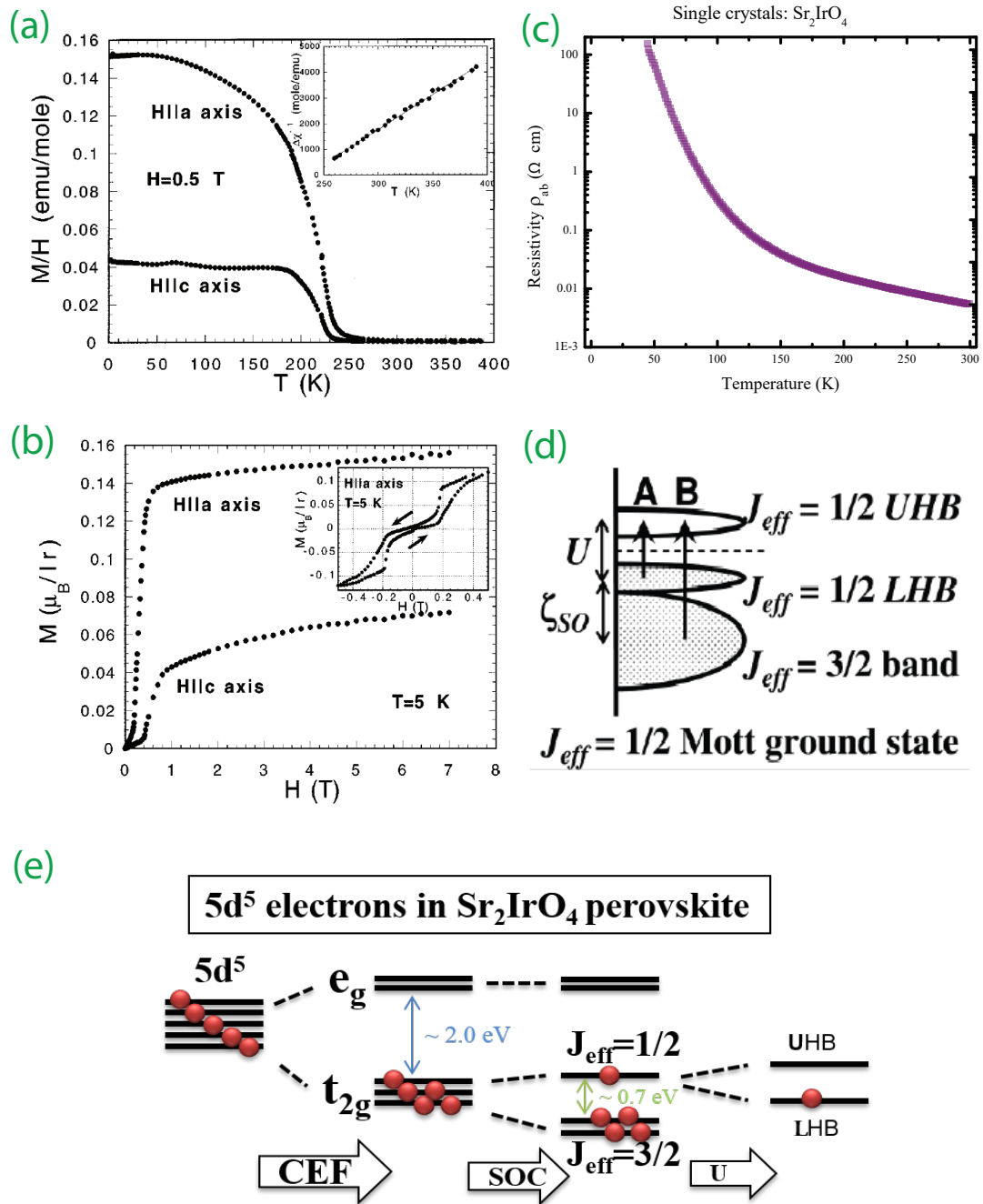


Figure 4.2: Bulk properties of Sr_2IrO_4 . (a) Magnetization, (b) isothermal magnetization, (c) In-plane resistivity, (d) $J_{\text{eff}} = \frac{1}{2}$ ground state, (e) Formation of $J_{\text{eff}} = \frac{1}{2}$ ground state, considering energy scales CEF, SOC and U .

4.3 Influence of electron doping on the ground state of $(\text{Sr}_{1-x}\text{La}_x)_2\text{IrO}_4$

The work presented here has been published as "Influence of electron doping on the ground state of $(\text{Sr}_{1-x}\text{La}_x)_2\text{IrO}_4$ " by Xiang Chen, Tom Hogan, D. Walkup, Wenwen Zhou, M. Pokharel, Mengliang Yao, Wei Tian, Thomas Z. Ward, Y. Zhao, D. Parshall, C. Opeil, J. W. Lynn, Vidya Madhavan, and Stephen D. Wilson, Phys. Rev. B 92, 075125 (Ref [11]).

4.3.1 Sample synthesis

Single crystals of $(\text{Sr}_{1-x}\text{La}_x)_2\text{IrO}_4$ were grown through flux growth method in the Pt crucible (Ref [31, 11]). Stoichiometric amounts of precursor powders of SrCO_3 (99.99%, Alfa Aesar), LaCO_3 (99.99%, Alfa Aesar), IrO_2 (99.99%, Alfa Aesar), and anhydrous SrCl_2 (99.5%, Alfa Aesar) were weighted in the $2(1-x) : 2x : 1 : 6$ molar ratio, where x is the nominal La concentration. The precursor materials were fully ground, mixed and sealed inside a Pt crucible, covered by a Pt lid, and inserted into an outer alumina crucible, before placing into a high temperature furnace subject to a controlled heating sequence. The mixed powders were heated slowly to 1350°C , soaked for 10 hours, slowly cooled to 850°C over 100 hours and then naturally cooled to room temperature. Black plate-like single crystals were then pulled out after removing the excess SrCl_2 flux using deionized water. The obtained single crystals are then subject to characterizations by XRD and EDS measurements.

4.3.2 Structure information

Select $(\text{Sr}_{1-x}\text{La}_x)_2\text{IrO}_4$ crystals were crushed into powder in order to survey any possible symmetry lowering resulting from La doping. Synchrotron powder X-ray diffraction data of $(\text{Sr}_{1-x}\text{La}_x)_2\text{IrO}_4$ at 300 K, were collected at 11-BM line at Advanced Photon Source at Argonne National Laboratory, as shown in Fig 4.3.

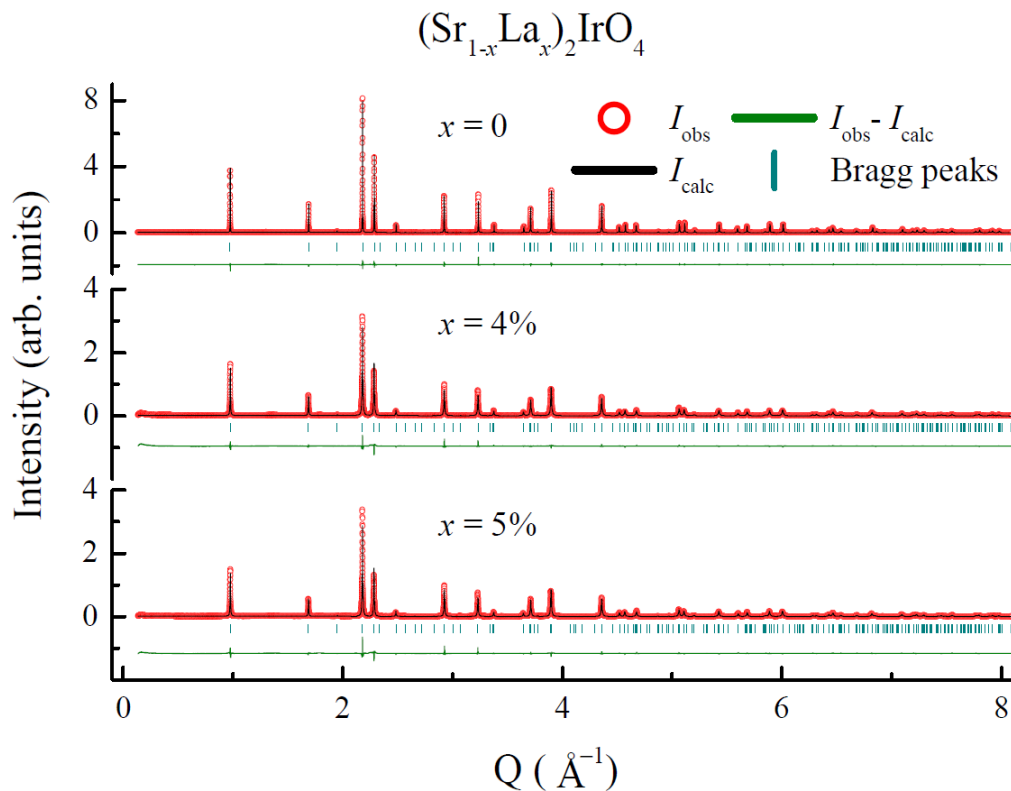


Figure 4.3: Synchrotron powder X-ray diffraction data of $(\text{Sr}_{1-x}\text{La}_x)_2\text{IrO}_4$ at 300 K, collected at 11-BM line at Advanced Photon Source at Argonne National Laboratory. (a) parent $x = 0$, (b) $x = 0.04$, (c) $x = 0.05$.

Although symmetry lowering than space group $I4_1/acd$ has been reported before [45, 46, 113, 114], originating from oxygen distortion induced two distinct Ir sites at each plane, which is not sensitive to X-rays. Therefore, our data are still refined with the $I4_1/acd$ space group. Up to the La doping solubility, no structural phase transition resulting from La substitution is observed at room temperature. Our powder XRD also preclude the possible inclusion of $\text{Sr}_3\text{Ir}_2\text{O}_7$ phase after La substitution during the growths.

Structural parameters in $(\text{Sr}_{1-x}\text{La}_x)_2\text{IrO}_4$ at 300 K from refinements of the synchrotron PXRD data are shown in Fig 4.4. The reduction of Ir octahedra angle with respect to La doping is consistent with early study in the same system [98]. With La substitutions, the lattice a and c are behaving in the opposite trend, resulting with the expansion of unit cell with increasing electron doping. This electronically driven lattice behavior is similar to that reported in $(\text{Sr}_{1-x}\text{La}_x)_3\text{Ir}_2\text{O}_7$ [118] where

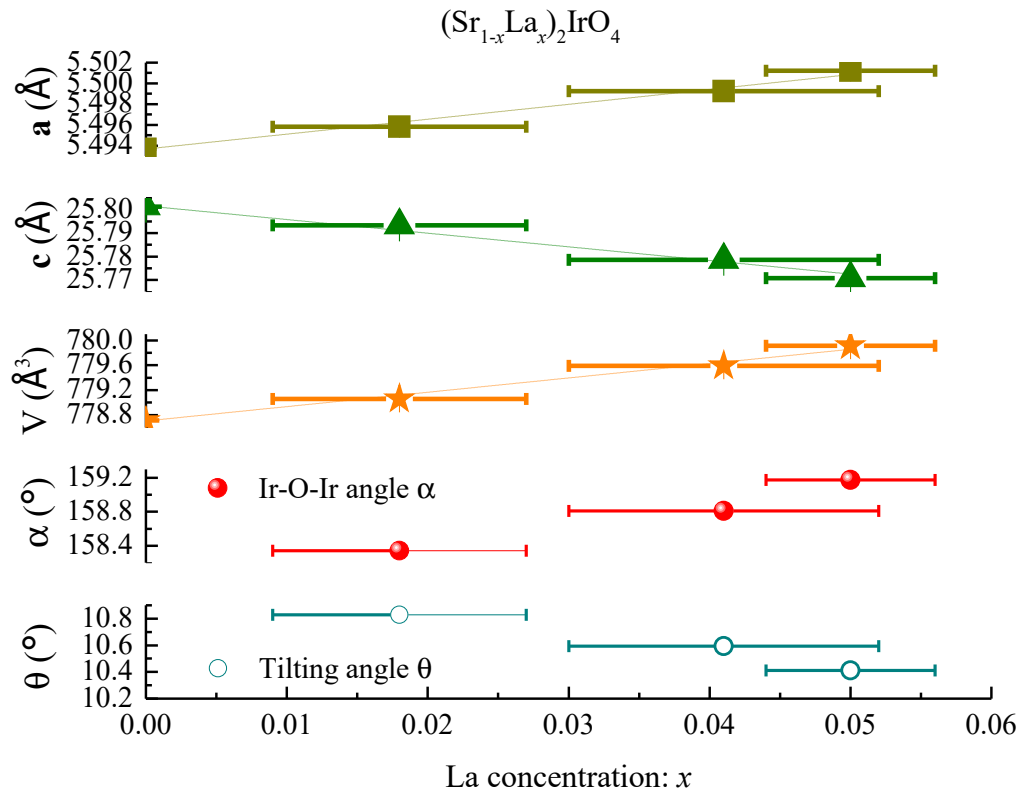


Figure 4.4: Refined structural parameters in $(\text{Sr}_{1-x}\text{La}_x)_2\text{IrO}_4$ at 300 K: lattice a , lattice c , unit cell volume V , in-plane Ir-O-Ir bond angle α and octahedral canting angles θ .

an interplay between correlation effects and modified lattice deformation potentials dominate simple steric effects [119].

4.3.3 Charge transport measurements

Charge transport measurements are performed on select $(\text{Sr}_{1-x}\text{La}_x)_2\text{IrO}_4$ single crystals, as shown in Fig 4.5. Upon slight La substitution, the resistivity data show a dramatic decrease in magnitude, with the reduction of nearly two orders of magnitude even at room temperature. Upon further electron doping, metal insulator transition is observed with $x \geq 0.04$ with induced metallic responses persisting at high temperatures (Fig 4.5 inset). Interestingly, upon cooling, insulating behavior persists in all samples up to the chemical solubility of La doping, with the magnitudes of low temperature resistivity approaching those of disordered metals.

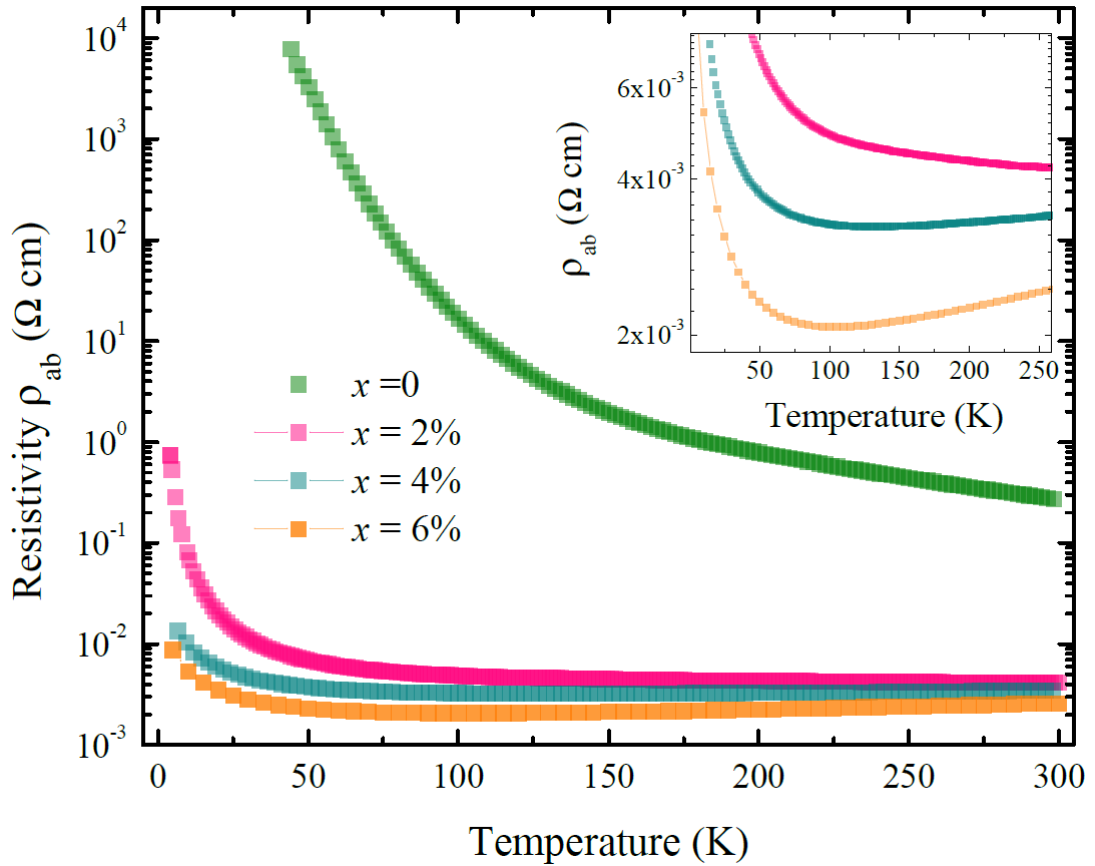


Figure 4.5: Temperature dependent in-plane resistivity on select $(\text{Sr}_{1-x}\text{La}_x)_2\text{IrO}_4$ single crystals.

To gain insights into the low temperature insulation ground state, data from $x = 2\%$ sample is analyzed with a best fit to an Efros-Shklovskii form of variable range hopping (VRH) [120] with a characteristic temperature $T_0 = 112$ K (Fig 4.6), which indicates the departure from three dimensional Mott VRH behavior reported in the parent system [121, 90]. This deviated form of transport suggests intergranular hopping in an electronically phase separated metal with La substitutions, which is similar to the case of doped cobaltites [122, 123]. Upon further electron doping, this functional form fails as MIT is approached. The persistent low temperature insulation ground state may imply weak localization effects or alternatively, thermally induced shifts in percolation pathways within an inhomogeneous electronic ground state.

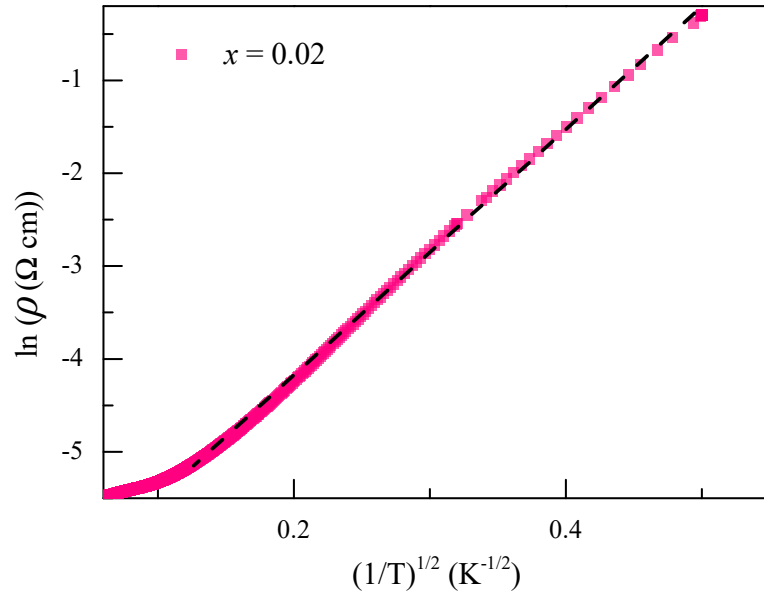


Figure 4.6: Efros-Shklovskii form of variable range hopping fit to the resistivity data of $x = 2\%$.

4.3.4 Magnetization measurements

The evolution of magnetic order in $(\text{Sr}_{1-x}\text{La}_x)_2\text{IrO}_4$ is explored through bulk magnetization measurements, shown in Fig 4.7 and Fig 4.8. As La is introduced into the system, the AF onset temperature is quickly suppressed, as clearly indicated by the black arrows in Fig 4.8 inset. The low temperature moment magnetite is also reduced as more electrons are introduced. Data collected from the sample at the limit of La doping ($x = 0.06$) show a persistent weak ferromagnetic upturn and accompanying irreversibility, signaling the survival of static magnetic correlations up to this limit.

Another persistent feature is the low temperature cusp in ZFC data and the inflection in irreversibility, denoted as T_F , in all of the doped samples and shifts downward in temperature with increasing electron doping. As a further probe of the freezing transition at T_F , low temperature AC susceptibility measurements were performed on an $x = 0.01$ sample, where DC measurement on the same sample indicates an $T_F = 13$ K. The cusp in the ZFC data shifts towards higher temperatures with increasing applied AC frequency, confirming the low temperature spin glass state below T_F (Fig 4.9).

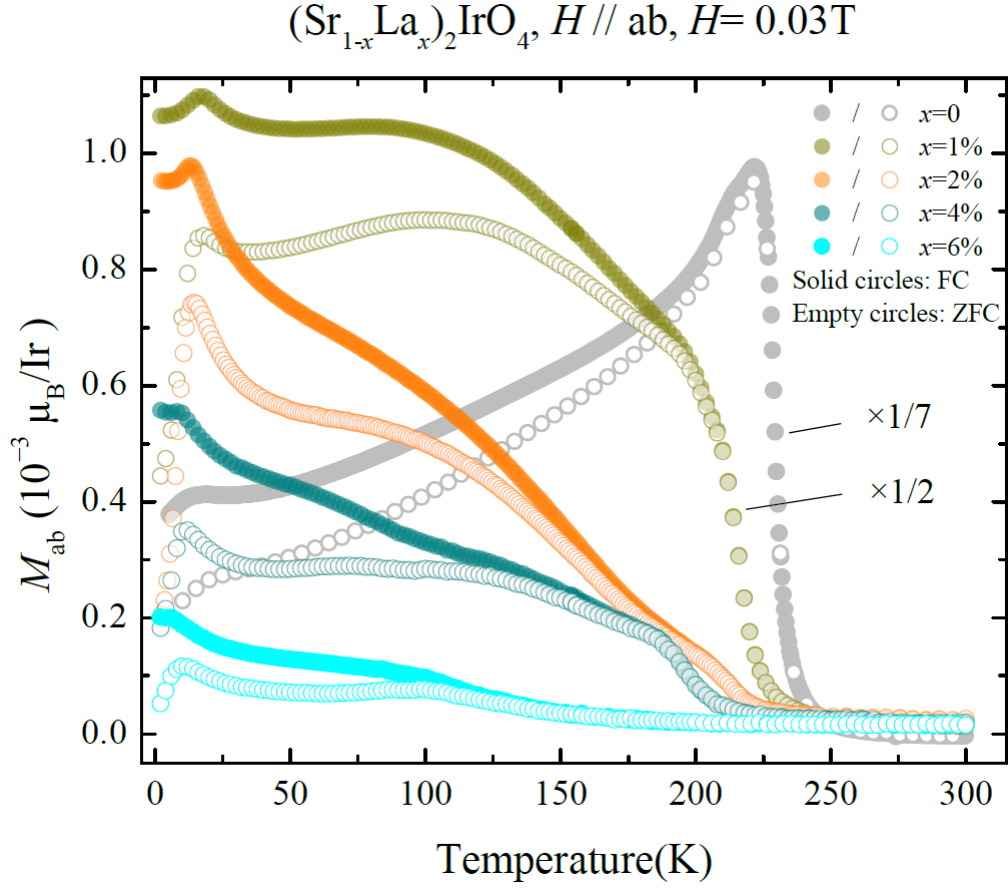


Figure 4.7: Temperature dependent in-plane magnetization data from $(\text{Sr}_{1-x}\text{La}_x)_2\text{IrO}_4$ single crystals. The high temperature onset of static canted AF correlations are present on both zero field cooled (ZFC, empty symbols) and field cooled (FC, solid symbols) data. The low temperature cusps are due to the formation of spin glass phase.

The low temperature spin glass phase likely arises from the partial fragmentation of the parent state's long range AF order into small glassy puddles that survive up to the chemical solubility $x = 0.06$. The magnitude of the frequency shift is represented by the value

$$K = \frac{\delta T_F}{\delta \ln(f)} \frac{1}{T_F} \quad (4.1)$$

which is estimated to be 0.07. This K value is much larger compared to one obtained from canonical spin glasses [124], suggesting the glassy dynamic nature is driven by interacting CAF clusters segregated from the parent SOC Mott state.

To gain further insights into the low temperature magnetic phase, low tem-

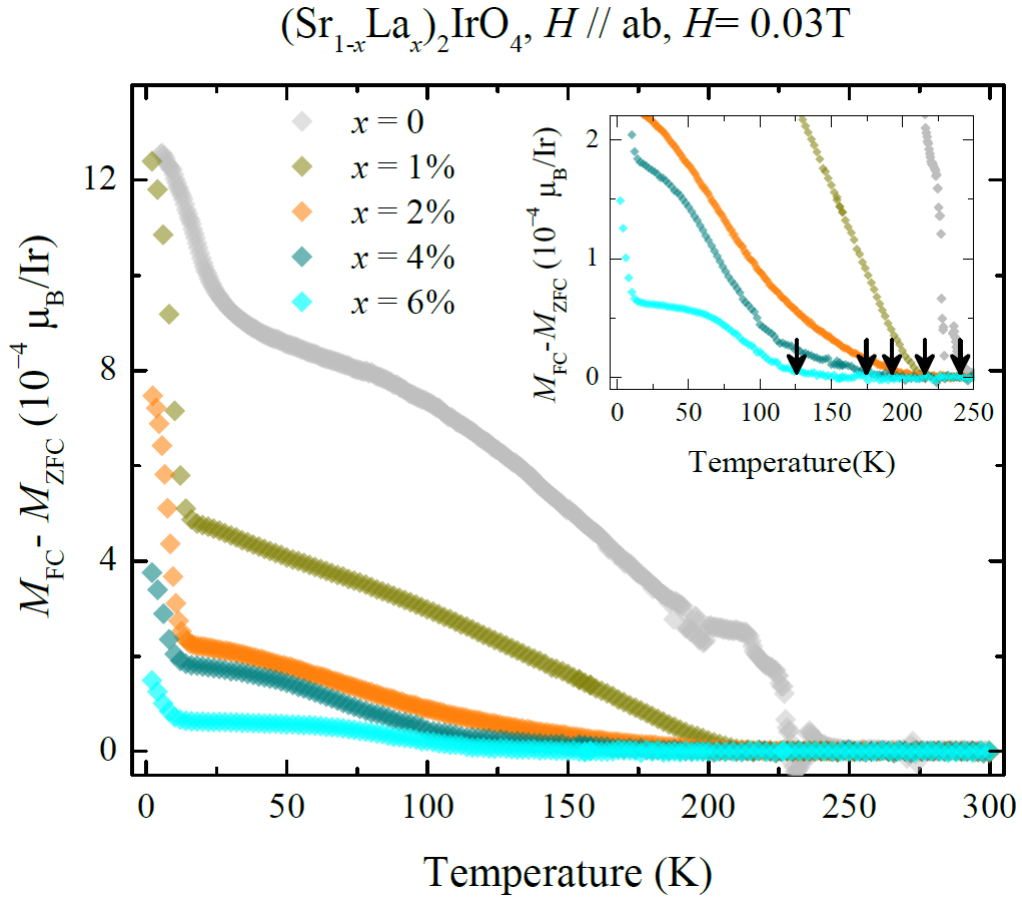


Figure 4.8: Subtraction between FC and ZFC magnetization data in 4.7. Inset shows enlarged window, tracking the canted AF onset temperatures with black arrows.

perature isothermal magnetization are performed, as shown in 4.10. With increasing doping level, the metamagnetic transition at H_c inherent to the polarization of canted AF state is broadened and the saturation moment per Ir rapidly diminishes. The enhanced hysteresis indicates the interplay between weak ferromagnetic order with spin glass phase, where similar isothermal responses have been reported before [125]. On the other hand, the rapid suppression of magnetic moment respect to the number of Ir suggests either the rapid suppression of CAF state with increasing electron doping or a reduced volume of magnetic ordered state within the phase separated regime.

Curie-Weiss fits to the static spin susceptibility data, shown in Fig 4.11, reveals the decrease of CW temperature, supporting the notion that magnetic order is suppressed when electrons are introduced. Yet effective local moment from the CW

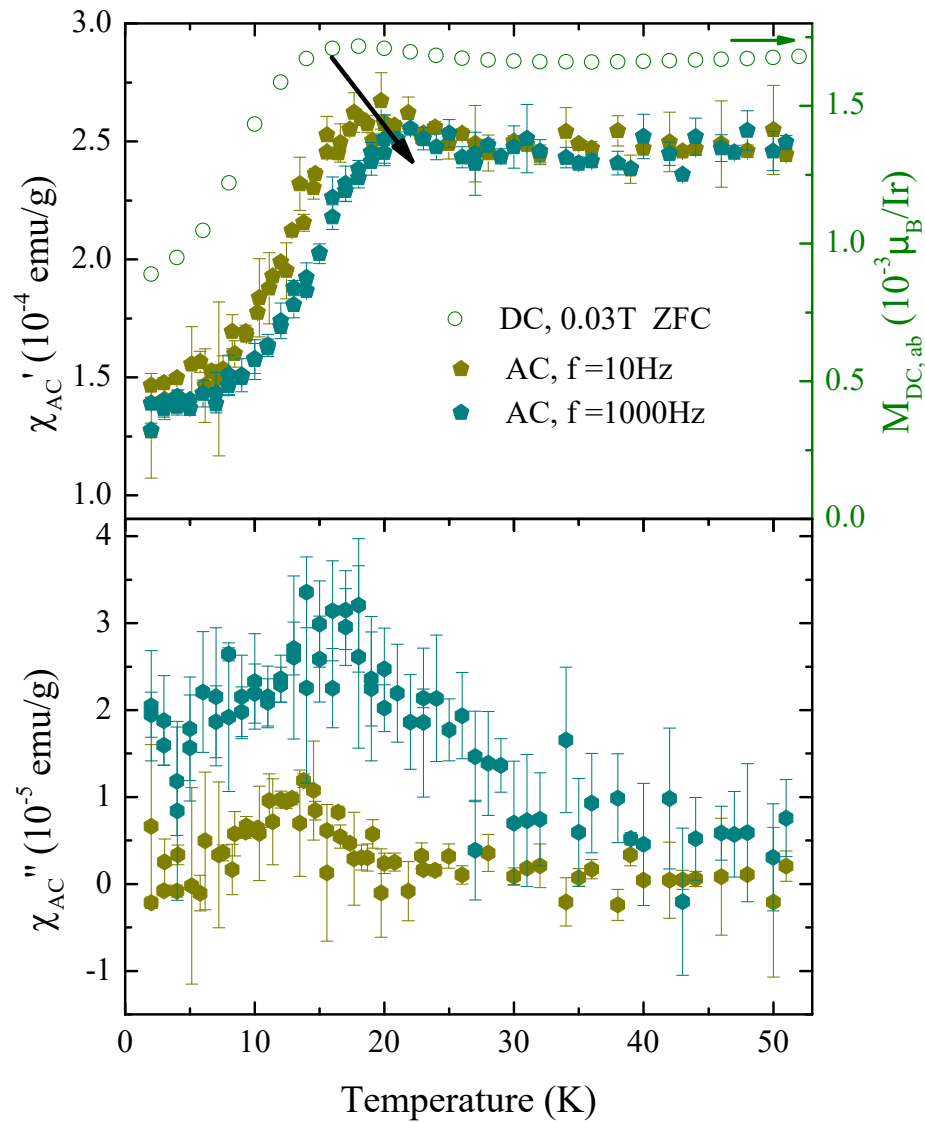


Figure 4.9: AC susceptibility data showing frequency dependent T_F in $x = 0.01$ La doped Sr214 sample. The DC data on the same sample is also shown (empty olive circles) for comparison.

fit renders $\mu_{\text{eff}} = 0.57 \pm 0.03 \mu_B$, which is close to value obtained from the parent compound and therefore suggests that local moment survives at the highest doping concentrations where metal insulating transition arises. Although CW law provide invaluable insights into the magnetic responses upon electron doping, the microscopic details remain elusive, thus it is necessary to adopt other tools to examine the microscopic details.

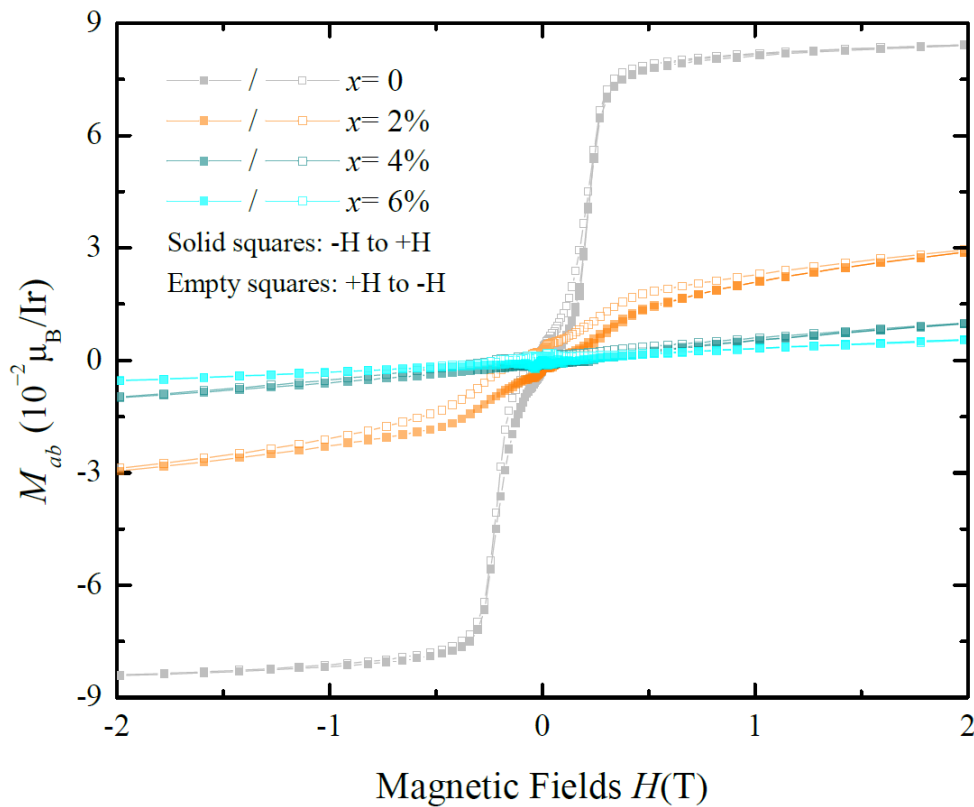


Figure 4.10: Isothermal magnetization data from $(\text{Sr}_{1-x}\text{La}_x)_2\text{IrO}_4$ single crystals, collected at 5 K with in-plane magnetic field.

4.3.5 Neutron scattering measurements

Neutron diffraction experiments were performed in order to explore the microscopic details of the evolution of the long range AF order upon electron doping in Sr214. The data is summarized in Fig 4.12. Momentum scans through the AF Bragg peak $(1, 0, 2)$ show the rapid suppression of the strongest peak intensity as electrons are introduced. Notice that the intensity for $x = 0.02$ sample is multiplied by 5 as the intensity is significantly reduced compared to $x = 0.01$ sample. The nature of the weak peak is confirmed from the temperature dependence as shown in Fig 4.12(b). A sample with larger La doping $x = 0.04$ was also explored; however, no magnetic Bragg peak could be resolved at the $\mathbf{Q} = (1,0,2)$ or equivalent positions. This indicates the complete suppression of long range AF order within the detection limit of measurement ($\approx 0.06 \mu_B$).

The suppression of long range order with increasing electron doping from neu-

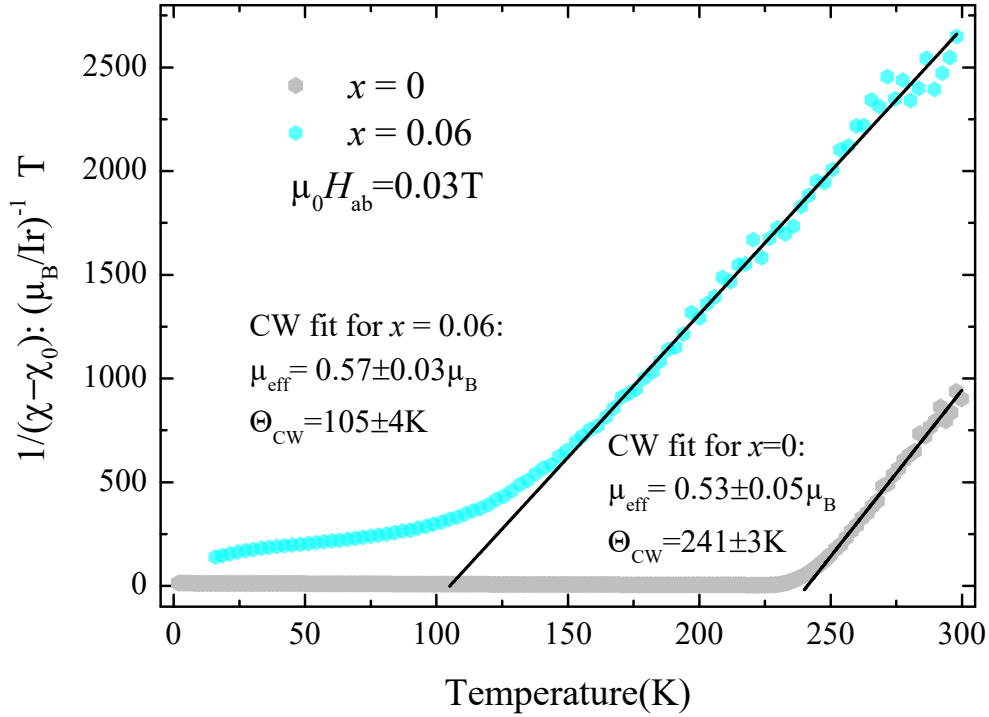


Figure 4.11: Temperature dependence of the inverse of the spin susceptibility χ , with the constant Pauli term χ_0 subtracted, for the $x = 0$ and $x = 0.06$ samples. Solid lines are Curie-Weiss fits to the high-temperature data.

tron scattering experiment, together with the irreversibility observed in magnetization data of all samples suggest a transition from long range ordered state to short range above doping level $x > 0.03$. Diffuse scattering from such a short range ordered state would be below the detection limit from neutron experiments, considering the small sample size and strong absorption of neutrons by Iridium. As an estimation, assuming the similar canted spin structure in doped sample where the spin canting angles locked to in-plane octahedral rotation angles, which are refined through synchrotron PXRD data, the order moment can be obtained from the isothermal magnetization data at high fields (6 T). The data are over-plot with those directly measured from neutron scattering measurements, as shown in Fig 4.13, whereas the shaded region denotes long range magnetic order.

For samples where long range order is still resolvable, the moments obtained from both methods agree reasonably well. For doping concentration $x > 0.03$, however, weak ferromagnetism remains in magnetization data while this state is beyond

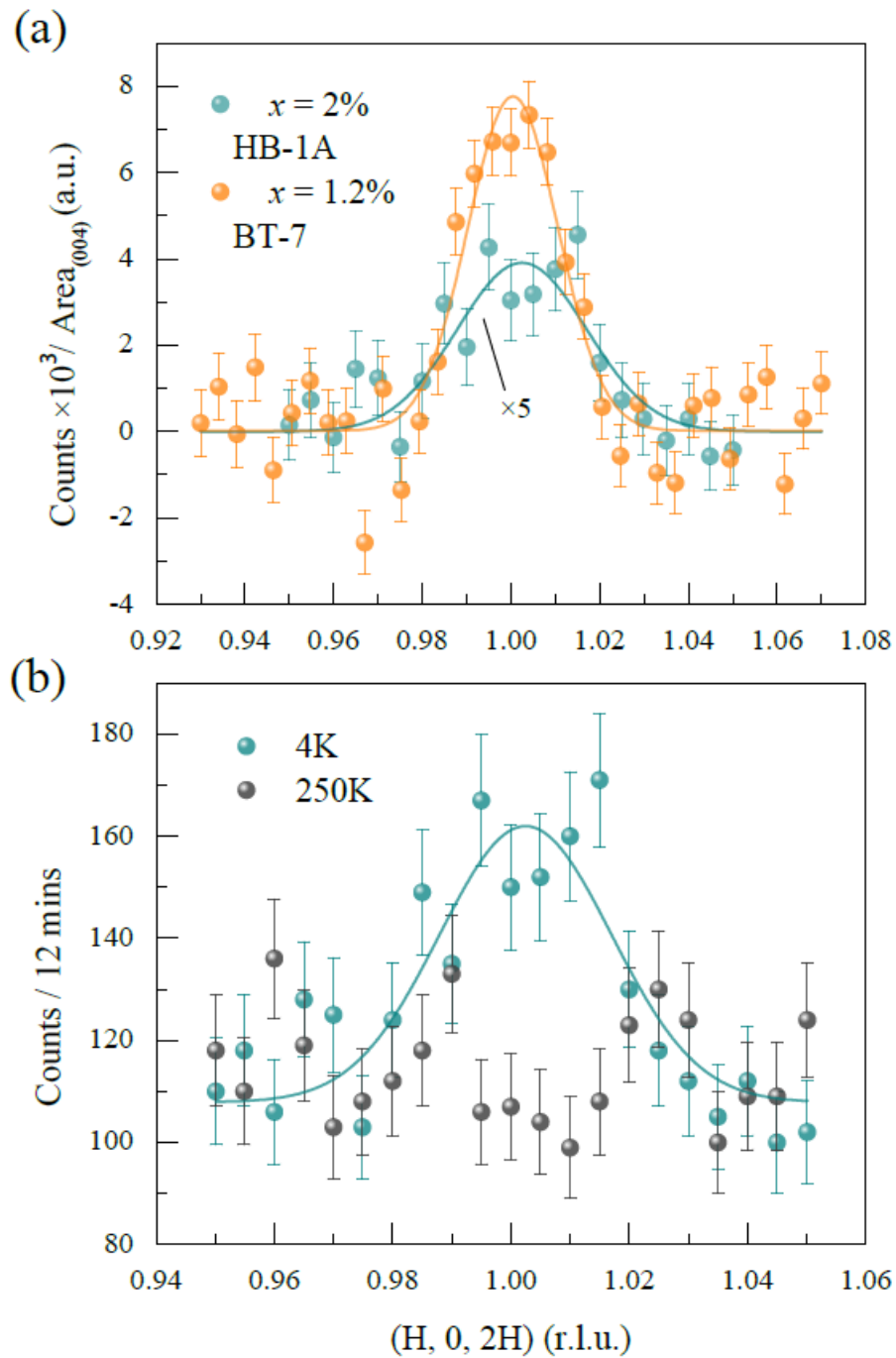


Figure 4.12: Neutron scattering data showing momentum scans through the magnetic Bragg position $Q = (1,0,2)$. (a) Radial Q scans through the AF Bragg peak $(1, 0, 2)$ collected at 4 K for both $x = 0.01$ and $x = 0.02$. The background is subtracted and then the intensity is normalized to the intensity from the $(0, 0, 4)$ nuclear Bragg peak. (b) Radial Q scans through the AF Bragg peak $(1, 0, 2)$ for $x = 0.02$ sample at both 4 and 250 K.

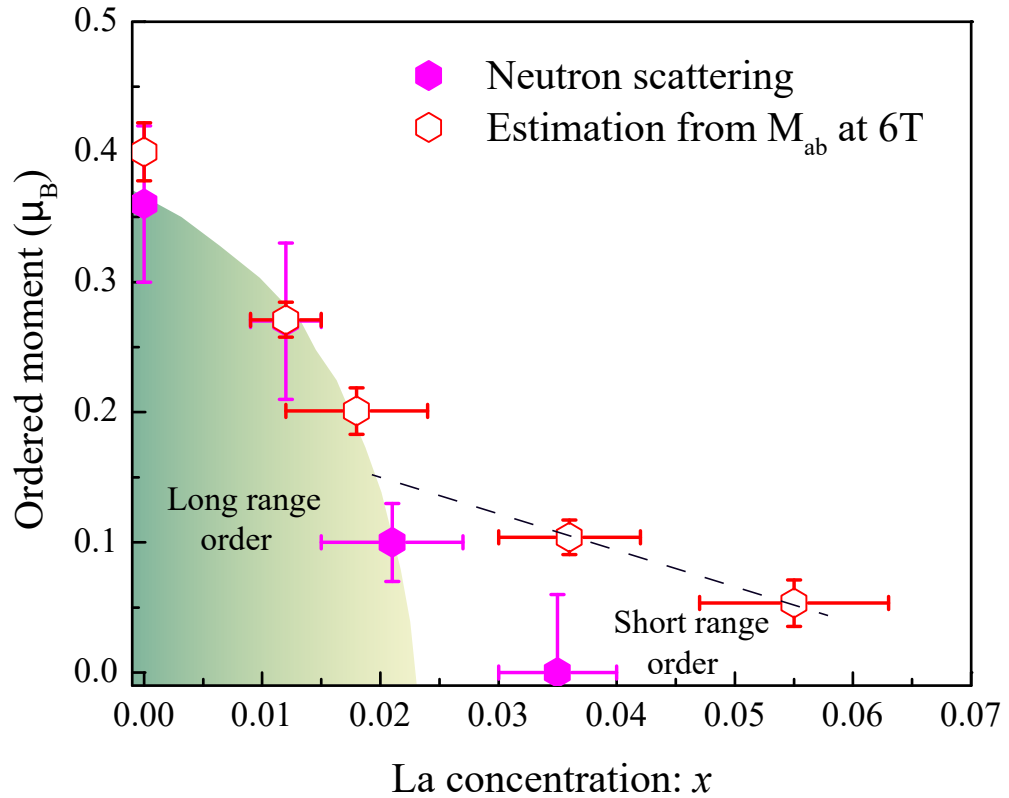


Figure 4.13: Evolution of the low-temperature ordered AF moments in La-doped Sr214. Solid symbols: ordered AF moment measured through neutron scattering; open symbols: estimated AF moment assuming the AF canted spin structure of Sr214 together with refined octahedral canting angles for each doping concentration. Shaded region represents the long range order region.

the detection limit by neutron scattering experiments, signaling remnant short-range order not apparent. Extending the analysis to higher La doping concentrations, the survival of weak AF magnetization suggests the persistence of short range order beyond the doping level $x > 0.03$, where survived AF order exists in local pockets within an electronically phase separated ground state.

4.3.6 Scanning tunneling microscopy measurements

Low-temperature scanning tunneling microscopy and spectroscopy (STM/STS) measurements were performed to explore whether electronic phase separation occurs in La-doped Sr214. A typical STM topography for an $x = 0.05$ sample is shown

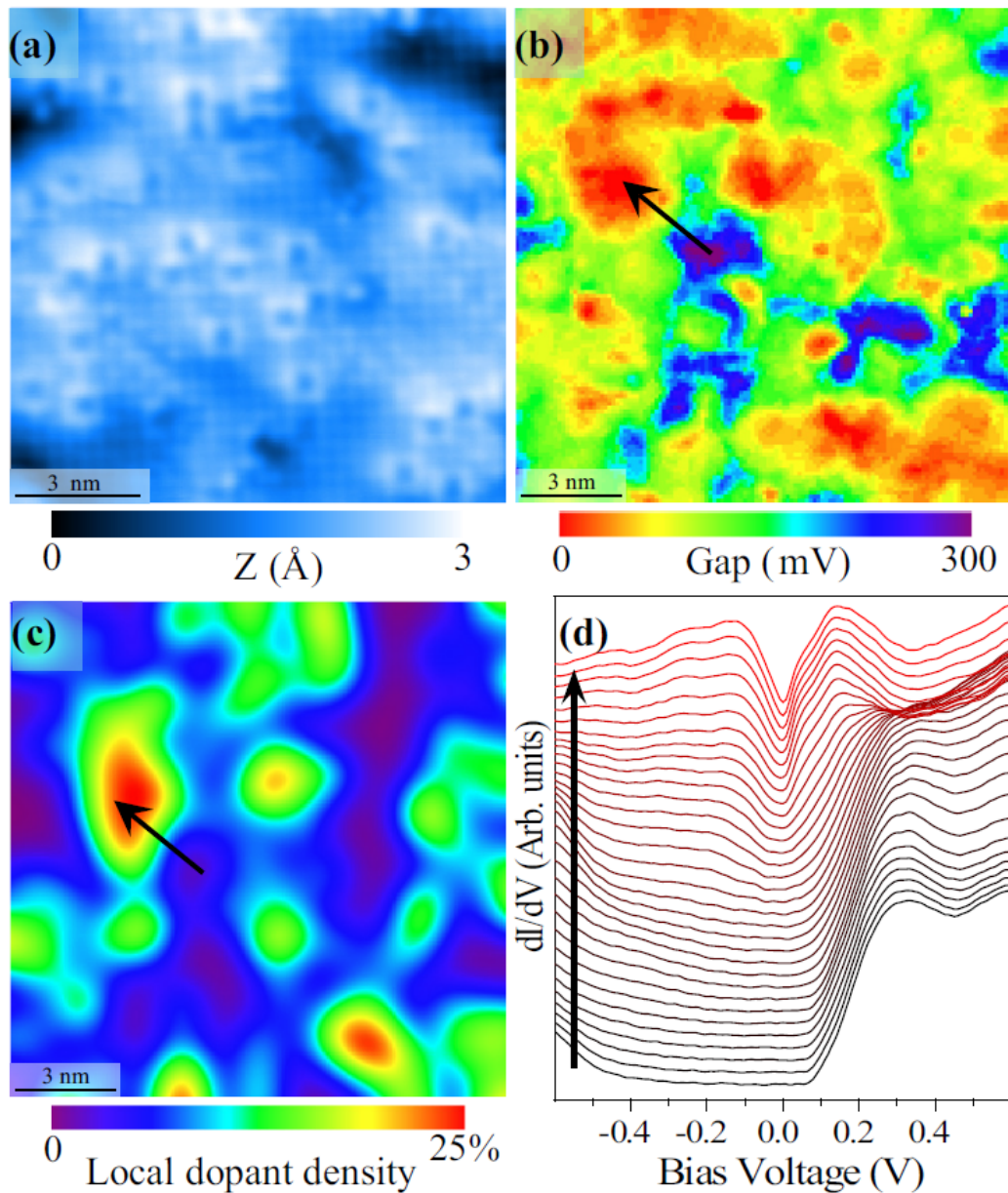


Figure 4.14: (a) A representative, $12 \times 12 \text{ nm}^2$ STM topography of a sample with $x \approx 0.05$ nominal La doping, taken at $V_b = +300 \text{ mV}$ at $I_{\text{set}} = 80 \text{ pA}$. (b) Gap map extracted from a $\frac{\delta I}{\delta I}$ map, $15 \times 15 \text{ nm}^2$, taken on the same sample as in (a) but over a different area. (c) Dopant density map taken in the same area as (b); dopants were counted visually. (d) Line cut showing the evolution of the $\frac{\delta I}{\delta I}$ spectra from fully gapped (purple) to no gap (red). The position and orientation of the line cut is indicated by the black arrows in (b) and (c).

in Fig. 4.14 (a). The crystal cleaves between adjacent SrO planes, and from previous experiments [126], we expect that the maxima in the STM topographies are associated with the Sr atoms. Correspondingly, in Fig. 4.14 (a), the La dopants

appear as dark-centered bright squares [118], whose number is consistent with the nominal $x = 0.05$ doping of the sample.

Insulating patches (*e.g.*, at the upper right corner of Fig. 4.14 (a)) are visible as dark regions in the topography, where the low local density of states forces the tip to push in so as to maintain a constant tunneling current. To examine the local density of states more closely, $\frac{\delta I}{\delta V}$ spectra were collected over on a dense grid ($0.9 \text{ spectra}/\text{\AA}^2$) in a $15 \times 15 \text{ nm}^2$ area with an energy range -0.6 to $+0.6 \text{ eV}$. The results are summarized in Figs. 4.14 (b) and 4.14 (d). Spectra far from La dopants show a large, $\approx 300 \text{ mV}$ insulating gap, but clusters of La dopants show metallic behavior, with finite density of states at E_F . The evolution of the $\frac{\delta I}{\delta V}$ spectra between these two extremes is shown in Fig. 4.14 (d).

To quantify the inhomogeneity in the density of states, a gap map is produced, shown in Fig. 4.14 (b), where the gap is defined as the energy range in each spectrum in which the measured $\frac{\delta I}{\delta V}$ was zero within a small noise threshold. In Fig. 4.14 (c), we show the local La doping in the same area as the $\frac{\delta I}{\delta V}$ map, obtained from counting the La dopants in the STM topography. Here, each dopant is represented as a normalized Gaussian with $\sigma = 1.5 \text{ nm}$. The metallic spectra are somewhat correlated with the La dopant density, with a correlation coefficient between Figs. 4.14 (b) and 4.14 (c) of $R \approx 0.4$. The observed electronic structure is potentially also influenced by La dopants in the second SrO plane from the surface, which are not seen with STM.

4.3.7 Discussion

The global picture provided by a combined analysis of the neutron scattering, transport, STM, and magnetization data demonstrates that electron doping into the spin-orbit coupled state of Sr214 renders an electronically phase separated ground state. This separation into nanoscale patches of doped charge and persistent insulating regions persists beyond the disappearance of long-range AF order and argues for a percolative origin to the sharply reduced resistivity of Sr214 upon alloying La into the lattice. For La-doped Sr214 with $x \geq 0.04$, this percolation mechanism leads to

a high-temperature metallic state whose conduction switches to weakly insulating at low temperatures.

The definitive origin of this persistent low-temperature upturn remains elusive. Traditional models of weak localization driven transport fail to fully capture the resistivity data in this regime [127, 128]. Additionally, the inflection in $\rho(T)$ marking the transition from weakly insulating to metallic behavior (*i.e.*, where $\frac{d\rho}{dT}$ changes sign) of the highest measured La concentration ($x = 0.06$) at $T \approx 100$ K does not directly coincide with the onset of irreversibility in the low-field susceptibility at $T_{\text{AF}} \approx 125$ K. We note here that this minimum in conductivity decoupled from the onset of AF order is similar to the tunneling transport behavior observed in other lightly doped Mott states such as the high- T_C cuprates [25, 129]. A recent angle-resolved photoemission study report of a pseudogap in La-doped Sr214 is also consistent with our observation of a gradual gapping out of the conductivity at low temperatures [130]. In analyzing the metallic behavior at high temperatures within the two-dimensional limit of planar transport, the high-temperature resistivity for the $x = 0.06$ sample appears to violate the Mott limit for metallic transport where $k_f l \approx 0.6 < 1$ [131]. This is likely reflective of the phase segregated nature of the electronic ground state where only a fraction of the sample volume contributes to conduction.

Interestingly, upon electron doping, low-temperature spin glass-like order appears in bulk magnetization measurements below an energy scale T_F . While this state is most evident under light electron substitution, signatures associated with this frozen state also appear to some degree in undoped parent Sr214 samples. This incipient spin glass behavior likely arises from defect states and impurity doping within the nominally undoped parent material. Crystals of parent Sr214 are prone to low levels of impurity doping via defects and slight off stoichiometry in oxygen content. These can be healed somewhat via post growth annealing, which are difficult to remove entirely. The broadened T_F transition in parent Sr214 as well as the apparent enhancement in the onset temperature (Figs. 4.7 and 4.8) are consistent with the modification of a spin glass state in the presence of disorder. This supports

an impurity driven origin of this freezing behavior in the parent material.

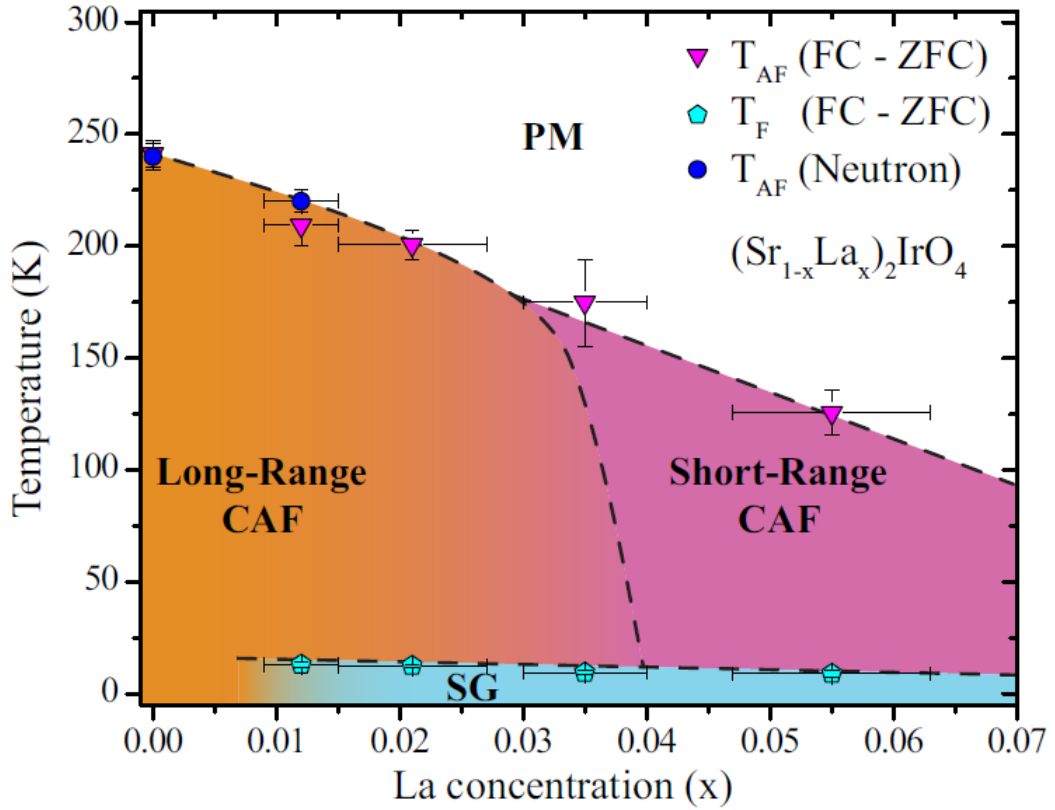


Figure 4.15: Evolution of magnetic order in La-doped Sr214. Blue circles denote the AF ordering transition measured directly with neutron scattering data, and pink triangles denote the onset of irreversibility in magnetization data. Dashed lines mark the suggested boundaries between short- and long-range AF order. The proposed low-temperature spin glass phase boundary is denoted by cyan pentagons.

A magnetic phase diagram summarizing our measurements is plotted in Fig. 4.15. Onset temperatures for AF magnetic order obtained via bulk magnetization and neutron scattering measurements are plotted with a dashed line denoting the crossover from long-range to short-range AF order. The spin glass phase onset temperatures T_F are also plotted as a low-temperature phase boundary. Given the recent parallels drawn between electron-doped Sr214 and hole-doped cuprates [91], it is worthwhile to consider parallels between the electronic phase diagrams of the two systems. In particular, the phase diagram of Sr214 iridate is somewhat reminiscent of the hole-doped phase diagram of its $3d$ -analog La_2CuO_4 [25]. In both systems, light carrier substitution leads to a phase separated state where AF is rapidly sup-

pressed. As the parent systems AF order is degraded, an intermediate spin glass state appears in both phase diagrams prior to the onset of a global metallic state. It is worth noting, however, that the suppression of T_F with continued doping is much more gradual in electron-doped Sr214 than in hole-doped La_2CuO_4 .

Unlike the hole-doped cuprates, short-range AF order persists over a wider doping range in La-doped Sr214. This also contrasts the electron-doped phase diagram of $(\text{Sr}_{1-x}\text{La}_x)_3\text{Ir}_2\text{O}_7$ where static AF order abruptly vanishes across the MIT phase boundary [118]. Within both La-substituted Sr214 and Sr327, light electron doping renders an electronically phase separated ground state with coexisting metallic and gapped regions; however, beyond a threshold value of 6% electrons per Ir in Sr327, AF order collapses into a globally gapless metal. In Sr214, continued electron doping beyond 6% electrons per Ir fails to fully destabilize the SOC Mott state, and a phase separated state persists until the limit of La substitution ($\approx 12\%$ electrons per Ir). This is likely due to either a nearby competing electronic instability in Sr327 [118] or simply due to the inherently stronger Mott state of Sr214.

4.3.8 Section summary

Combined neutron scattering, magnetization, and STM/STS data reveal a complex evolution of the electronic properties of the spin-orbit Mott ground state of $(\text{Sr}_{1-x}\text{La}_x)_2\text{IrO}_4$. Electron-doping results in electronic phase separation into coexisting metallic and insulating nanoscale regions and percolative transport. Long-range AF order collapses beyond $x \approx 0.03$. Short-range AF order, however, survives and persists up to the upper limit of La substitution in an electronically phase segregated ground state. Furthermore, electron doping stabilizes a new low-temperature phase transition consistent with the formation of a spin glass-like state likely comprised of frozen clusters of CAF nanoscale domains. This spin glass phase is necessarily intermediate to the formation of a globally gapless metallic ground state in electron-doped Sr214, reminiscent of the electronic phase diagram of monolayer hole-doped high- T_C cuprates.

4.4 Unidirectional spin density wave state in metallic

$(\text{Sr}_{1-x}\text{La}_x)_2\text{IrO}_4$

The work presented here has been published as "Unidirectional spin density wave state in metallic $(\text{Sr}_{1-x}\text{La}_x)_2\text{IrO}_4$ " by Xiang Chen, Julian L. Schmehr, Zahirul Islam, Zach Porter, Eli Zoghlin, Kenneth Finkelstein, Jacob P.C. Ruff, Stephen D. Wilson, Nature communications (2018) 9, 103 (Ref [132]).

4.4.1 Introduction

Short-range AF order has been proposed in the metallic $(\text{Sr}_{1-x}\text{La}_x)_2\text{IrO}_4$ in the last section, however broad diffuse scattering from such a state would be below the detection limit of neutron scattering, due to experimental obstacles such as the small sample sizes for neutron diffraction and strong absorption of neutrons resulting from the presence of Iridium element. These difficulties are overcome by the recent development of resonant elastic X-ray scattering (REXS) technique, which witnessed the great success in applications to iridates, with some examples include [31, 133, 134, 135, 117, 136, 137, 75, 138, 118, 139, 140]. Therefore, high-resolution REXS is applied to examine the diffuse short-range AF state in metallic $(\text{Sr}_{1-x}\text{La}_x)_2\text{IrO}_4$ single crystals. As the Mott state is suppressed and the material is driven into an electronically phase-separated regime, we observe the collapse of long-range antiferromagnetism and the appearance of an additional magnetic state that stabilizes coincident with the formation of a coherent Fermi surface in this system. Our data unveil a spin density wave phase with a character suggestive of the incommensurate spin density wave state known to stabilize in the metallic regions of far underdoped, electronically phase-separated $(\text{La}_{1-x}\text{Sr}_x)_2\text{CuO}_4$ [141, 142, 143]. This commonality demonstrates universality in the electronic responses of the partially quenched Mott states of the monolayer hole-doped cuprates and electron-doped iridates.

4.4.2 Synchrotron X-ray scattering experiments

Resonant elastic x-ray scattering (REXS) experiments were carried out at A2 (samples with $x = 0.02$ and $x = 0.041$) and C1 ($x = 0.028$) beamlines at CHESS at Cornell University, and the 6-ID-B,C beamline ($x = 0.04$) at the Advanced Photon Source at Argonne National Laboratory. Samples were mounted on the horizontal top of the Cu posts, secured with GE varnish. A vertical scattering plane is exploited at all time. Samples were aligned in the (HOL) or (OKL) scattering plane. The experimental setup is shown schematically in Fig 3.15. The data was collected at the incident energy tuned to the magnetic resonant peak corresponding to the Ir L_3 edge ($E \approx 11.215$ keV, Table 4.1). Si(111) single crystals and NaI detectors were employed at C1 and 6-ID-B,C beamlines for polarization analysis and collecting the diffracted signals respectively. At A2, scattered photon energy and polarization were analyzed using the symmetric (0,0,8) reflection from a flat HOPG analyzer crystal, and collected using a small photon counting area detector. The X-ray beam is vertically focused. For all experiments, the slits are wide open ($\sim mm$) to maximize the intensity.

Table 4.1: Summary of samples measured, their crystal mosaic, and corresponding beam lines. The relative shifts in energy calibration for each beam line are also tabulated by denoting the observed Ir L_3 absorption edge energies.

$(\text{Sr}_{1-x}\text{La}_x)_2\text{IrO}_4$	Instrument	L_3 (keV)	Mosaic ($^\circ$)
$x = 0.02$	CHESS,A2	11.217	0.09(1)
$x = 0.028$	CHESS,C1	11.215	0.05(1)
$x = 0.04$	APS,6-ID-B,C	11.214	0.008(1)
$x = 0.041$	CHESS,A2	11.217	0.024(1)

Various samples with different quality (mosaic) are performed at different instruments. Table 4.1 summarize the related key information, such as the energy chosen for REXS, the mosaic of samples and the instrumental resolutions.

4.4.3 Scattering geometry

Fig 3.15 a schematic depicting the scattering geometry employed in the experiment, using conventional notations for the photon polarization vectors [117]. A vertical

scattering plane of $(H, 0, L)$ or $(0, K, L)$ was employed, and the incoming beam was horizontally σ polarized. Magnetic scattering was isolated in the polarization rotated $\sigma - \pi$ channel, and unless otherwise specified, data were collected in $\sigma - \pi$ scattering channel at temperature 10 K.

Once the vertical scattering plane $(H, 0, L)$ was defined, only the $(0, 1, 4N + 2)$ or $(1, 0, 4N)$ ($N = \text{integer}$) type magnetic reflections are resolvable [31, 45, 46]. $(1, 0, 4N + 2)$ and $(0, 1, 4N)$ type magnetic reflections arising from the other magnetic domain (with rotated moments and modified interplane phasing) are hidden due to the azimuthal dependence of the scattering intensity. Correspondingly, when the sample is rotated by 90° with respect to the crystal's c -axis (Figs 4.19 and 4.20), then the $(0, K, L)$ scattering plane is accessed and only those previously silent $(1, 0, 4N + 2)$ or $(0, 1, 4N)$ type magnetic peaks from the other domain set will contribute. In short, only one domain of the crystal will contribute to scattering either in the $(H, 0, L)$ or $(0, K, L)$ vertical scattering planes as a result of the azimuthal dependence of the magnetic intensity. Finally, the incident X-ray beam has a large horizontal divergence perpendicular to the scattering plane. As a result, the instrumental resolution is broadened along this direction (e.g. broad along K for the $(H, 0, L)$ scattering plane), as shown in Fig. 4.17 and Figs 4.19(a-b).

4.4.4 Remnant long-range and short-range order ($x < 0.04$)

Previous reports have identified that, beyond a critical concentration of 2% electrons/Ir, long-range magnetic order collapses [12] and short-range, remnant order survives up to the solubility limit of La into the lattice [11, 12]. While previous resonant inelastic X-ray (RIXS) measurements have observed the rapid formation of diffuse short-range magnetic correlations at electron-doping levels of 2% electrons/Ir [12], our REXS data collected near the Ir L_3 edge shown in Fig. 4.16 demonstrate that some fraction of the sample retains long-range antiferromagnetic (AF) order up to 6% electrons/Ir. This is not unexpected given the first order nature of the insulator to metal transition out of the Mott state and the known electron phase separation in this doping regime.

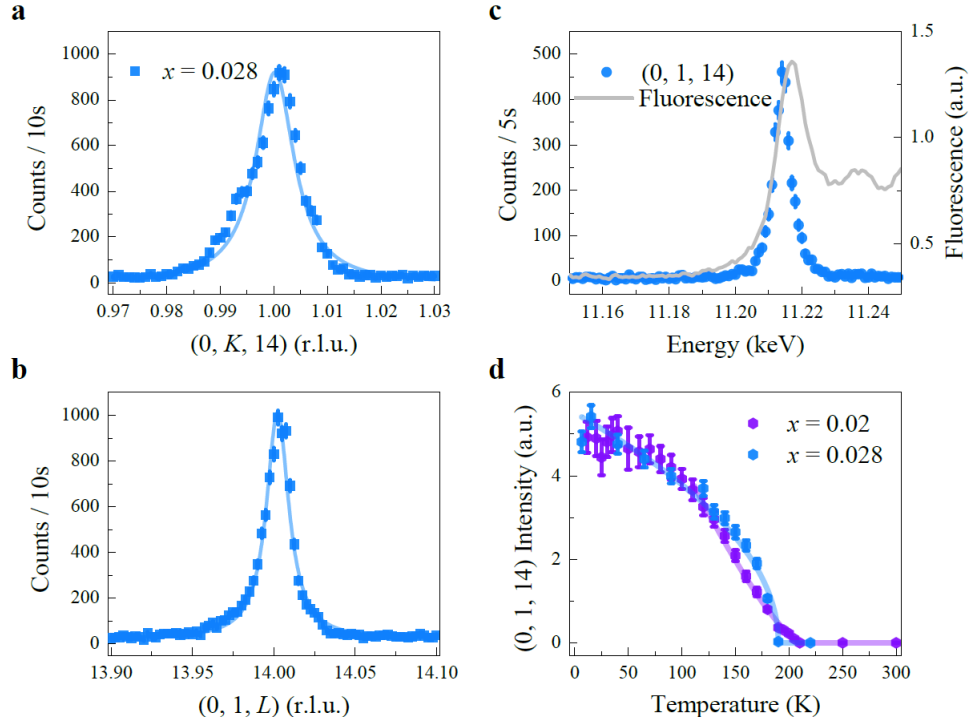


Figure 4.16: REXS data in the polarization flipped $\sigma - \pi$ channel of sample $x = 0.02$ (purple) and $x = 0.028$ (blue). **a** and **b** show K and L scans through the $(0, 1, 14)$ position at $T = 10$ K respectively. **c** Energy dependence of the $(0, 1, 14)$ peak at 10 K and its comparison to the Ir L_3 fluorescence line. **d** Temperature dependence of the $(0, 1, 14)$ peaks for both samples. Data have been normalized to appear on the same scale. The solid lines in **(a, b, d)** are the fits to the data. Data are collected at the energies of 11.217 and 11.215 keV for the $x = 0.02$ and $x = 0.028$ sample, respectively. All vertical error bars in the figure represent 1 standard deviation (s.d.) statistical errors.

To further demonstrate this remnant long-range order, Fig. 4.16 (a - d) show diffraction data collected on two samples with La concentrations $x = 0.02$ and $x = 0.028$ respectively at $T = 10$ K in the polarization flipped $\sigma - \pi$ scattering channel at the AF ordering wave vectors. For reference, the $\mathbf{Q} = (0, 1, 4N + 2)$ and $(1, 0, 4N)$ type magnetic peaks of the parent state access one magnetic domain [31, 45, 46, 117], while the $\mathbf{Q} = (0, 1, 4N)$ and $(1, 0, 4N + 2)$ positions access another. Consistent with earlier neutron diffraction studies [11], sharp, resolution limited peaks in the $x = 0.02$ sample indicate that a small fraction of long-range order survives in the sample and that the ordering temperature decreases slightly with increased doping. As the doping level is increased to $x = 0.028$, this remnant AF order broadens slightly along the L -axis with a finite out-of-plane correlation length

$\xi = 320 \text{ \AA}$ (Fig. 4.22) and presages the transition to short-range magnetic order. As the doping concentration increases beyond this value, the long-range component of the remnant AF state is fully quenched at the commensurate $\mathbf{Q} = (0, 1, 14)$ wave vector; however, as additional electrons suppress this commensurate signal, they also drive the formation of a second set of peaks split along the H -axis from the AF wave vectors.

4.4.5 Observation of spin density wave phase ($x = 0.04$)

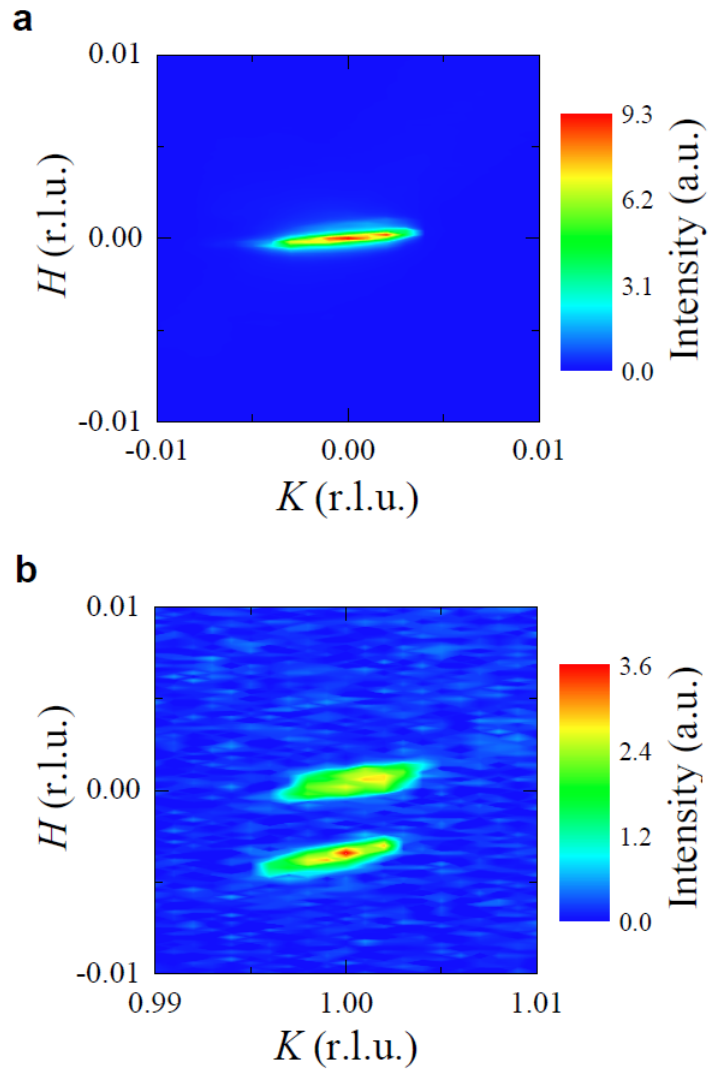


Figure 4.17: REXS data from sample $x = 0.04$ collected at 6-ID-B. **a, b** H, K maps at the $(0, 0, 16)$ and $(0, 1, 14)$ zones at $T = 10 \text{ K}$.

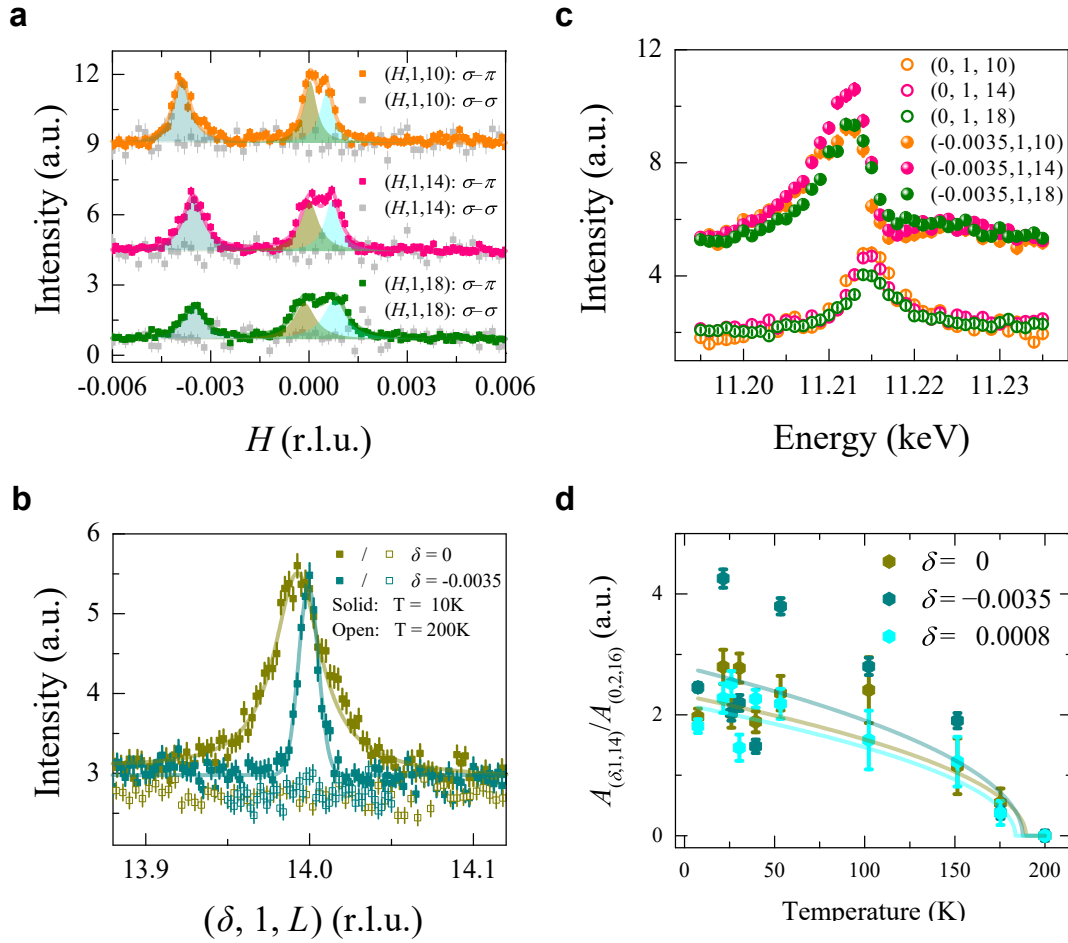


Figure 4.18: Additional REXS data from sample $x = 0.04$ collected at 6-ID-B. **a**, H scans at select $(0, 1, 4N + 2)$ ($N = 2, 3, 4$) magnetic zone centers at 10 K collected both in the $\sigma - \pi$ channel and the $\sigma - \sigma$ channel. Solid lines are fits to the data with three Lorentzian peaks, which are individually represented by blue tan and cyan shaded areas. Data collected at different zones and in different channels are offset for comparison. **b**, L scans at the commensurate $(0, 1, 14)$ and incommensurate $(-0.0035, 1, 14)$ positions at 10 K (solid symbols) and at 200 K (empty symbols). The solid lines are fits to the data with a single Lorentzian peak and the dashed line denotes the instrumental resolution. **c**, Energy scans at the commensurate and incommensurate peak positions. Data are offset for clarity. **d**, Temperature dependence of the three peaks resolved in the H scan of $(0, 1, 14)$ from **a**. Other than (c), all data are collected at the energy of 11.214 keV. All vertical error bars in the figure represent 1 *s.d.* statistical errors

Fig. 4.17 illustrates the appearance of this additional channel of incommensurate scattering in a crystal with La concentration $x = 0.04$. Data in Fig. 4.17a and b depict scattering meshes collected at $T = 10$ K about the charge position $\mathbf{Q} = (0, 0, 16)$ in the $\sigma - \pi$ scattering channel and about the magnetic position $\mathbf{Q} = (0, 1, 14)$

in the $\sigma - \pi$ scattering channel. While the mesh about the charge peak reveals only a single-crystal grain, the mesh about the magnetic position reveals two incommensurate peaks split transversely along the H -direction in addition to the short-range commensurate AF peak. This is illustrated via momentum scans cutting through $(0, 1, 4N + 2)$ magnetic zone centers (Fig. 4.18a). These additional peaks are absent in the $\sigma - \sigma$ scattering channel (Fig. 4.18a) and appear below a temperature $T = 188 \pm 10$ K (Fig. 4.18d) coincident with the onset of the remnant short-range AF order in this system [11]. Momentum scans performed along the L -axis at the commensurate and incommensurate in-plane positions in Fig. 4.18b reveal that both peaks are quasi two-dimensional with finite out-of-plane correlation lengths of $\xi_c = 59 \pm 3$ Å (approximately 2 unit cells) for the remnant AF order of the parent state and a longer $\xi_c \approx 200$ Å (8 unit cells) for the newly stabilized incommensurate scattering. The incommensurate scattering remains nearly resolution limited in the (H, K) -plane with a minimum correlation length of $\xi_{a,\text{min}} = 500 \pm 30$ Å.

Notably, the incommensurate peaks are asymmetrically split from the commensurate peak position along the H -axis at positions $(\delta, 1, 14)$ with $\delta_1 \approx 0.001$ *r.l.u.* and $\delta_2 = -0.0035$ *r.l.u.*. Mesh scans collected at charge peak positions such as that shown in Fig. 4.17a show that this anomalous splitting is not due to a trivially misoriented grain in the sample and suggest the appearance of magnetic scattering with a different periodicity than the underlying lattice structure, coincident with the appearance of a Fermi surface at $x = 0.04$ as reported in previous photoemission experiments [130].

Energy scans at both the commensurate and incommensurate positions are shown in Fig. 4.18c where both commensurate and incommensurate scattering components exhibit a well-defined resonance near the Ir L_3 edge. The resonance energy of the incommensurate signal is subtly shifted 1.5 eV lower than that of the short-range commensurate order and reflects resonant scattering from a different local electronic state within the sample. Such a negative shift in energy is consistent with the reported 1.3 eV shift downward in energy upon adding an electron into the Ir⁴⁺ state and is likely reflective of a local Ir³⁺ environment [133]. While this

absolute energy difference is within the energy resolution of the monochromator, the subtle, relative shift is suggestive of resonant scattering from metallic regions of the sample where the Mott gap has collapsed.

4.4.6 Unidirectionality of spin density wave phase ($x = 0.04$)

Figs 4.19 and 4.20 show data obtained after the sample was rotated counterclockwise by 90° with respect to the crystal c -axis. Following this rotation, the scattering plane becomes $(0,K,L)$, and Fig 4.19 (a-b) shows the H, K map of scattering intensities collected about the $(1, 0, 10)$ magnetic zone center at the temperature 10 K. It should be noted that for the parent magnetic structure, the $(1, 0, 10)$ peak

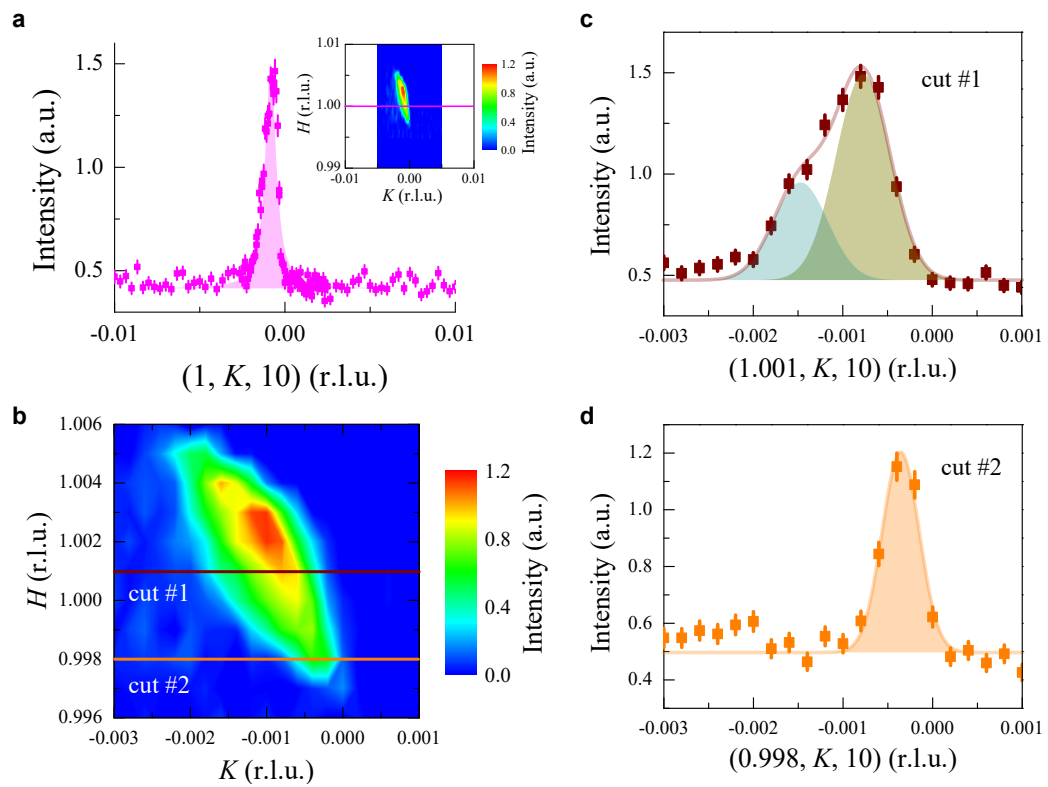


Figure 4.19: REXS data from sample $x = 0.04$ collected at 6-ID-B after the sample was rotated counterclockwise by 90° . (a), K scan at $(1, 0, 10)$ at $T = 10$ K. The inset shows the H, K map about the $(1, 0, 10)$ position and the magenta line denotes the scan direction in the main panel. (b), the detailed H, K map around the resulting $(1, 0, 10)$ reflection. Data from K scans through this map (cuts #1 and #2) are shown in panels (c) and (d). No splitting along K is observed, and additional analysis suggests a splitting still occurs along the H direction.

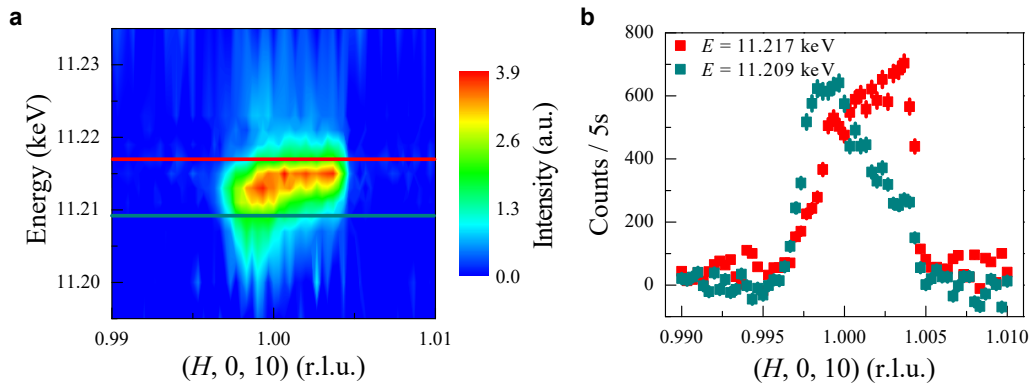


Figure 4.20: Additional REXS data from sample $x = 0.04$ collected at 6-ID-B after the sample was rotated counterclockwise by 90° . (a) Energy dependence of H scans about the $(1,0,14)$. Select H scans around $(1,0,14)$ at energies $E = 11.209$ keV (dark cyan) and $E = 11.217$ keV (red) are illustrated as lines with the corresponding data plotted in (b).

intensity is interpreted as arising from the second allowed magnetic domain in the crystal. After the sample rotation, the resolution along K (estimated to be 0.0005 r.l.u.) becomes much better than that along H (estimated to be 0.0023 r.l.u.) rendering any small incommensurate splitting along H difficult to resolve. The K scan in Fig. 4.19a shows only one peak, demonstrating no equivalent splitting along K .

A remaining question concerns the degree to which the unidirectional incommensurate splitting along H is resolvable in the rotated $(1,0,10)$ zone. Cuts taken through the resolution broadened peak (indicated by lines marked #1 and #2 in Fig 4.19b) are plotted in Fig 4.19 (c-d). These cuts suggest the presence of two weakly resolved components split along H . This implies that the incommensurate splitting is still present along H after the sample's rotation, yet it is largely blurred by the instrumental resolution.

The observation of weakly resolvable incommensurate splitting in the 90° rotated zone is further supported by H scans collected through the equivalent $(1,0,14)$ magnetic zone at a range of different energies plotted in Fig. 4.20. As shown in Fig. 4.18c, the resonance energies of the commensurate and incommensurate magnetic peaks of this sample are shifted from one another by approximately 1.5 eV. By tuning to each resonance energy individually and performing H scans (denoted by lines in Fig. 4.20a, subtle shifts between convolved components forming the single

peak can potentially be resolved. Fig. 4.20b shows the resulting scans at energy $E = 11.217$ keV, where the right shoulder of the broad peak is promoted, and at energy $E = 11.209$ keV where the left shoulder of the peak is enhanced. This subtle offset in the spectral weight of the peak with changing energy suggests the presence of the lower energy incommensurate peaks convolved within the resolution broadened peak.

A rough estimation of the splitting between the convolved peaks in this rotated zone shows the separation between two components along H to be about 0.005 *r.l.u.*, close to the measured splitting of 0.0045 *r.l.u.* in the $(0, K, L)$ zone. This combined analysis strongly suggests that the incommensurate peaks split along H are still present in the scattering data after the sample is rotated by 90° . This is consistent with the incommensurate state being unidirectional and occurring only along H direction, regardless of the magnetic zones chosen or the relative orientation of the sample.

4.4.7 Further evolution of spin density wave phase ($x = 0.041$)

To probe this new channel of order further, a separate sample with slightly higher La concentration $x = 0.041$ and better chemical homogeneity was also investigated with the results shown in Fig. 4.21. Scattering from this sample reveals only the presence of asymmetric incommensurate peaks split along H about the $(0, 1, 4N + 2)$ positions and reflects a suppressed contribution from the remnant, competing short-range commensurate AF order. Fig. 4.21(a-b) illustrate this via a mesh scan collected near the Ir L_3 edge in the $\sigma - \pi$ channel as well as via momentum scans illustrating the two peaks of magnetic scattering. With the removal of the remnant, competing shortrange AF phase, the asymmetric incommensurate splitting is enhanced to $\delta_1 = -0.003$ *r.l.u.* and $\delta_2 = 0.006$ *r.l.u.* (Fig. 4.21c), and momentum scans exploring the same magnetic domain at the $(-1, 0, 20)$ position again demonstrate the inherent splitting only along the H -direction (Fig. 4.21d). Scans along the L -axis of the incommensurate peaks of this sample revealed an out-of-plane correlation length comparable to that observed in the mixed-phase sample (Fig. 4.22)

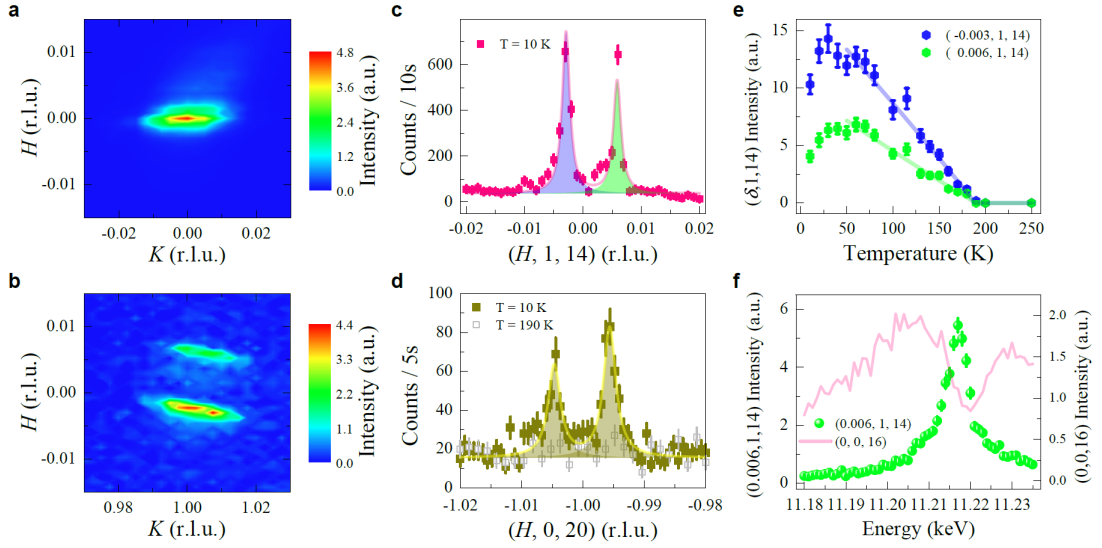


Figure 4.21: REXS data from sample $x = 0.041$ taken at CHESS, A2. **a** and **b** show H, K maps $T = 10$ K around the nuclear $(0, 0, 16)$ and magnetic $(0, 1, 14)$ zones respectively. **c**, H scan at $(0, 1, 14)$ at 10 K exhibiting two IC peaks at $(-0.003, 1, 14)$ and $(0.006, 1, 14)$. **d**, H scan at $(-1, 0, 20)$ showing the two IC peaks split along the H direction 10 K and their absence at 190 K. IC peaks in **c** and **d** are both separated by 0.009 *r.l.u.* **e**, The temperature dependence of the two IC peaks. Both IC peaks disappear at the same temperature $T_{\text{SDW}} = 182 \pm 8$ K. **f**, Energy dependence of the IC peak at $(0.006, 1, 14)$ and its comparison to the $(0, 0, 16)$ charge peak. The solid lines in **c**–**e** are the fits to the data. Other than **f**, all data are collected at the energy of 11.217 keV. All vertical error bars in the figure represent 1 *s.d.* statistical errors.

and the in-plane correlation lengths remain resolution limited.

4.4.8 Comparison of spin-spin correlation lengths

The out-of-plane correlation lengths along c -axis were determined at 10 K for all the samples studied and are plotted in Fig. 4.22. For La concentrations below $x \approx 0.02$, the magnetic peaks are resolution-limited in all directions, indicating true long-range order [11]. This agrees with the previously reported long-range order in neutron diffraction studies exploring concentrations up to $x = 0.02$ [11]. Upon increasing electron doping, the correlation length along c decreases drastically before the emergence of the incommensurate order beyond the critical doping $x = 0.04$. The decrease in correlation length along c with increasing doping suggests the transition from true three-dimensional long-range order toward a quasi two-dimensional

state.

Upon electron doping up to $x = 0.041$, the in-plane correlation lengths remain nearly long range, as suggested by the comparable magnetic (shaded peaks) and resolution peak (dashed lines) widths in Fig. 4.23. At this limit comparing the crystallinity and resolution-convolved widths of the charge peaks (at different \mathbf{Q} s) with the slightly broader magnetic peaks may give somewhat misleading correlation lengths, and instead the minimum spin-spin in-plane correlation length is quoted. Thus close to the doping threshold of $x = 0.04$, the antiferromagnetic correlations are reflective of quasi two-dimensional short-range order. The gradual transition

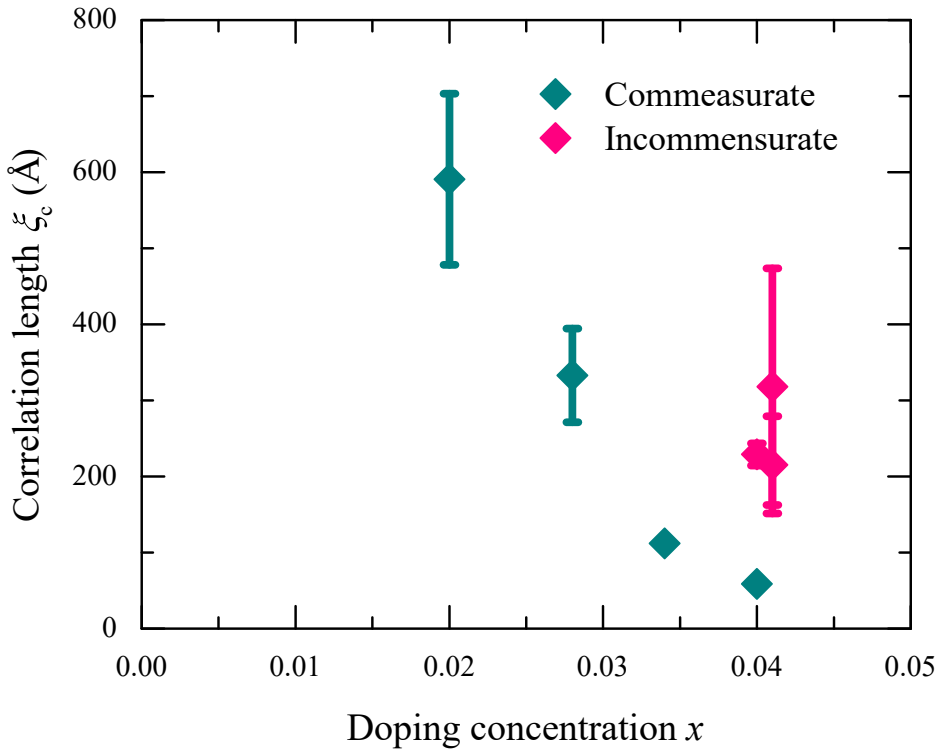


Figure 4.22: Resolution deconvolved c -axis correlation lengths for the saturated antiferromagnetic states ($T = 10$ K) are plotted as a function of doping x in $(\text{Sr}_{1-x}\text{La}_x)_2\text{IrO}_4$. Below $x \approx 0.02$, the magnetic peaks are resolution limited, indicating the true long range nature. With increasing doping, the correlation length decreases drastically before the emergence of the incommensurate order above the critical doping $x = 0.04$. Vertical error bars originate from the uncertainties in deconvolving the magnetic peak full width at half maximum (FWHM) Γ_{Mag} from the experimental resolution peak FWHM Γ_{Res} and are obtained through the error propagation from $\xi_c = \frac{0.44c}{2\pi(\Gamma_{\text{Mag}} - \Gamma_{\text{Res}})}$, where c is the lattice parameter along L .

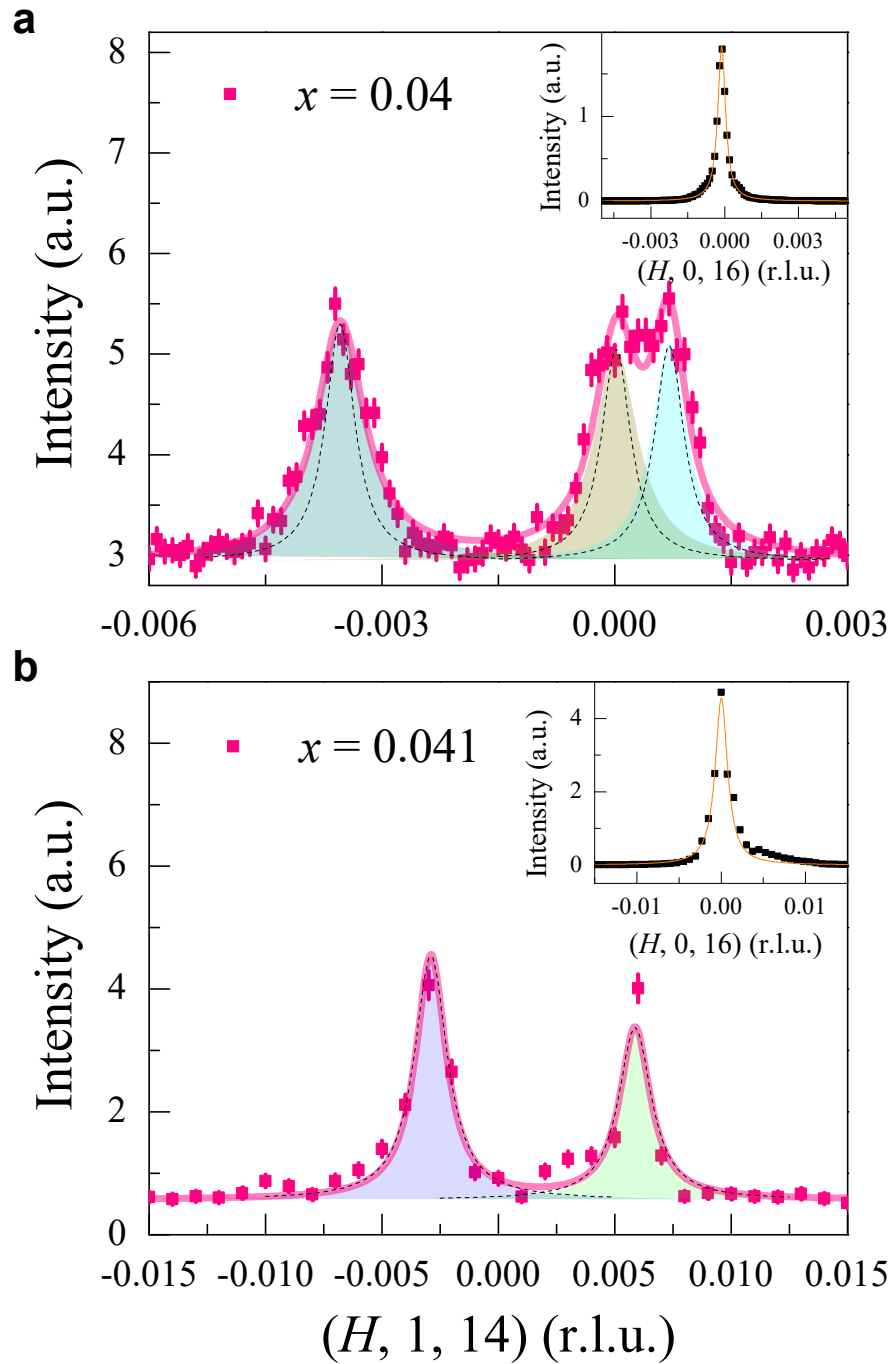


Figure 4.23: Comparison of magnetic and charge peak widths for the $x = 0.04$ (a) and $x = 0.041$ (b) samples. Upper right insets in (a-b) show the charge peak widths and these widths are over-plotted as dashed lines inside of the magnetic peaks for reference. The magnetic peaks around $(0, 1, 14)$ are reproduced from Fig. 4.18a and Fig. 4.21c. Vertical error bars represent 1 s.d. statistical errors.

between these extremes is summarized in the phase diagram (Fig. 4.24).

4.4.9 Phase diagram: Magnetic order in $(\text{Sr}_{1-x}\text{La}_x)_2\text{IrO}_4$

High-resolution REXS is applied to explore the diffuse short-range AF state in metallic $(\text{Sr}_{1-x}\text{La}_x)_2\text{IrO}_4$ single crystals. The evolution of magnetic order as electrons are introduced into $(\text{Sr}_{1-x}\text{La}_x)_2\text{IrO}_4$ is summarized in Fig. 4.24, with a combination of data from magnetization and neutron scattering [11], RIXS [12]. The long-range to short-range canted antiferromagnetic (CAF) transition occurs near x

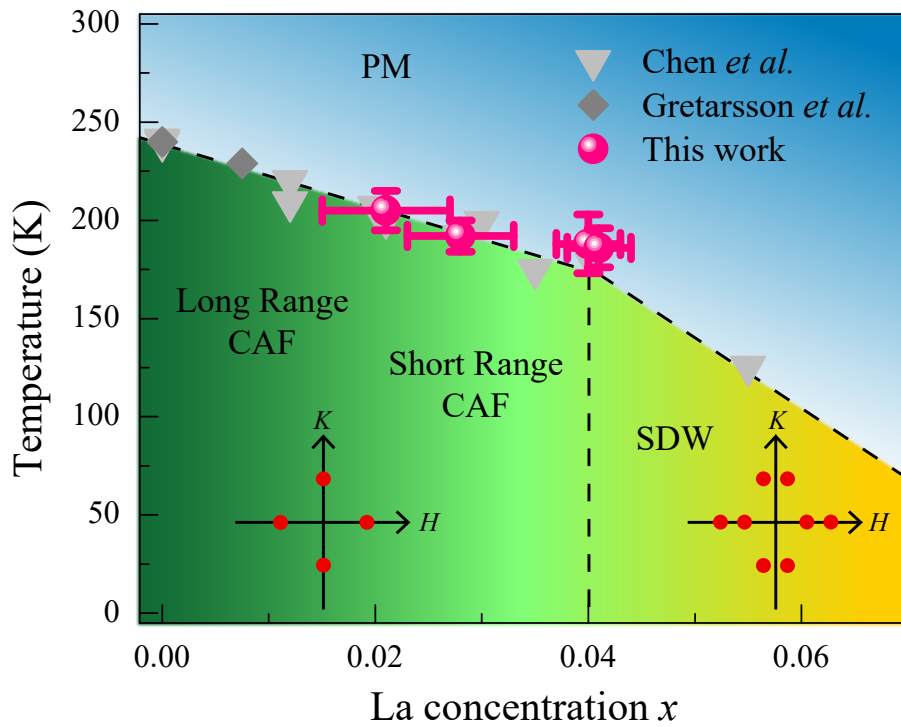


Figure 4.24: Phase diagram of $(\text{Sr}_{1-x}\text{La}_x)_2\text{IrO}_4$, as determined from a combination of magnetization and neutron scattering [11], RIXS [12], and REXS (this work) measurements. The long-range to short-range canted antiferromagnetic (CAF) transition occurs near $x = 0.02$. At the critical doping $x = 0.04$, part of the material transitions into an incommensurate spin density wave (SDW) state. Dash lines are guides to eyes. The insets with red dots schematically represent commensurate and incommensurate (IC) peak positions investigated in this experiment. Horizontal error bars originate from repeated energy dispersive spectroscopy (EDS) measurements. Vertical error bars are estimated from the disappearance of magnetic peak intensity in Fig. 4.16d and Fig. 4.18d and Fig. 4.21e.

= 0.02. At the critical doping $x = 0.04$, part of the material transitions into an incommensurate spin density wave (SDW) state. Our magnetic resonant X-ray scattering data reveal the presence of an incommensurate magnetic state reminiscent of the diagonal spin density wave state observed in the monolayer cuprate $(\text{La}_{1-x}\text{Sr}_x)_2\text{CuO}_4$. This link supports the conjecture that the quenched Mott phases in electron-doped Sr_2IrO_4 and hole-doped La_2CuO_4 support common competing electronic phases.

4.4.10 Discussion

The emergent incommensurate electronic order observed in our scattering measurements for $x \geq 0.04$ coincides with the heterogeneous collapse of the Mott gap at this same doping. Prior scanning tunneling spectroscopy measurements [11, 144] have shown that, while the local electronic structure is largely unperturbed for $x < 0.04$, at $x \approx 0.04$ dopants begin to locally stabilize a glassy pseudogap state and unidirectional electronic order within a nanoscale, phase-separated setting. The incommensurate state observed in our REXS measurements necessarily coexists with a background of diffuse magnetic scattering from the suppressed AF parent state previously reported in RIXS studies [12]. While previous RIXS measurements integrate larger swaths of momentum space and resolve this diffuse signal more readily, our complementary high-resolution REXS measurements are able to resolve the appearance of quasi two-dimensional order associated with the growing pseudogap phase fraction of the doped system. For higher La concentrations with $x \approx 0.05$, our measurements were unable to resolve any signatures of the spin density wave state. This is potentially due to a dramatic intensity reduction associated with the order becoming fully two-dimensional (diffuse along L) or due to a further suppression of the ordered magnetic moment as the metallic fraction of the sample grows.

At the limit of La-doping into Sr_2IrO_4 , metallic nanopuddles comprise the bulk of the sample volume and are known to exhibit a pseudogap along antinodal regions considered analogous to quasiparticle spectra observed in the high- T_c cuprates [130]. Similarly, hole doping into Sr_2IrO_4 also reveals parallel phenomenology such as the pseudogap and hidden order in cuprates [145, 146, 147, 148]. The

underlying nature of this pseudogap state is currently debated; however, the onset of short-range magnetic order is proposed as one possible origin. The quasi two-dimensional incommensurate order observed in our measurements is consistent with an electronic order parameter that may account for this pseudogap state; however, the detailed temperature dependence of the pseudogap phase remains unreported and currently limits further comparison.

Intriguingly, our measurements of $(\text{Sr}_{1-x}\text{La}_x)_2\text{IrO}_4$ at doping concentrations where a Fermi surface emerges seemingly parallel the appearance of a phase-separated spin density wave state in the analogous hole-doped cuprate $\text{La}_{2-x}\text{Sr}_x\text{CuO}_4$. Within the cuprate system, the parent Mott state along with long-range Néel order rapidly collapse with hole substitution, and a competing unidirectional diagonal spin density wave (DSDW) state emerges [141, 142, 143]. This DSDW order stabilizes at the phase-separated limit of small doping and coexists with short-range commensurate AF order. The incommensurability inherent to the DSDW scales with the effective doping of the system with the smallest observed $2\delta \sim 0.016$ *r.l.u.* [149], and the propagation vector is split transverse to the commensurate AF wave vector denoting a spin density wave modulation along the bond diagonal. Furthermore, at the low doping limit, coexistence of long-range DSDW correlations and AF order is observed in $\text{La}_{2-x}\text{Sr}_x\text{CuO}_4$ ($x = 0.0192$) [150] and ($x = 0.01$) [151]. These features parallel those observed for the competing incommensurate state in $(\text{Sr}_{1-x}\text{La}_x)_2\text{IrO}_4$ and are suggestive of a common instability in the phase diagrams of both systems. Given that the incommensurability in La-doped Sr_2IrO_4 is smaller than that observed in $\text{La}_{2-x}\text{Sr}_x\text{CuO}_4$ ($x = 0.01$), $(\text{Sr}_{1-x}\text{La}_x)_2\text{IrO}_4$ seemingly maps into the far under-doped regime of the same phase diagram where the in-plane correlation lengths remain long range.

Recent reports of the DSDW state at the low-doping limit of $\text{La}_{2-x}\text{Sr}_x\text{CuO}_4$ found a similar asymmetry in the incommensurate scattering [150]. The likely origin for the asymmetry in the incommensurability of doped $(\text{Sr}_{1-x}\text{La}_x)_2\text{IrO}_4$ is from a subtle orthorhombicity in the lattice below our current experimental resolution, as demonstrated in Fig 4.25. A subtle shift of 0.0015 *r.l.u.* would rectify the scattering

to be symmetric about the zone center, and this offset can readily be generated by an undetected orthorhombicity and twin domain structure within the lattice when aligned using a tetragonal cell. Since the spin modulation reflects a unidirectional density wave, the underlying lattice is necessarily orthorhombic or lower symmetry. A similar asymmetric incommensurate splitting was observed in hole-doped monolayer cuprates when the data is analyzed in a tetragonal cell [152], and for the small offset observed in our experiments, this would imply a rotation of twin domains by only 0.085° and an underlying orthorhombicity of $(a-b)/(a+b) = 0.001499$. Future high-resolution measurements of the domain structures in $(\text{Sr}_{1-x}\text{La}_x)_2\text{IrO}_4$ will be required to verify such a scenario in the monolayer iridates.

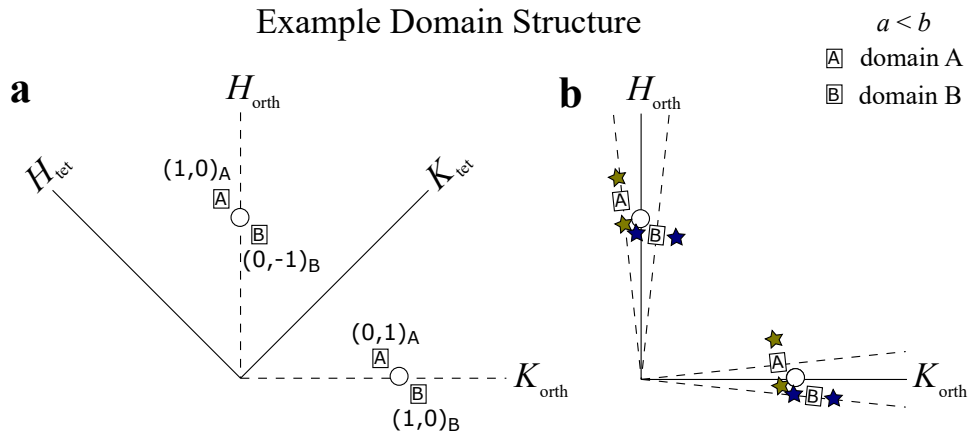


Figure 4.25: Illustration of how domain structure can alter apparent incommensurate positions. **(a)** Tetragonal and orthorhombic axes for the IrO_2 planes. Tetragonal here denotes the smaller unit cell where H and K point along the Ir-Ir bond direction while orthorhombic denotes the larger unit cell with H and K parallel to the bond diagonals. Two potential domains A and B are marked if the lattice were to be subtly orthorhombic. **(b)** H and K axes again in the larger cell are depicted with circles denoting the aligned $(1,0)$ and $(0,1)$ positions assuming $a_{\text{orth}} = b_{\text{orth}}$ and the relative orientations of the A and B domains are also illustrated under this assumption. Stars denote the unidirectional splitting from each domain with modulation along its local H_{orth} -axis.

The mechanism for generating the incommensurate magnetic state for $x \geq 0.04$ at the edge of the Mott states stability is likely to parallel previous proposals of a $t-t'-J$ model in the cuprates where, in the low doping limit, hopping of carriers can be maximized by a renormalized magnetic ground state [153, 154, 155]. Within this localized approach, Nel order in the Mott state becomes unstable above a critical

doping threshold and twists into a spiral or noncollinear spin texture whose pitch evolves with carrier density. Details regarding the critical doping threshold and propagation wave vector of this modulated spin state can be material dependent, and notably, the introduction of appreciable Dzyaloshinskii-Moriya (DM) interactions in the case of electron-doped Sr_2IrO_4 will further modify the effect. While itinerant effects such as Fermi surface nesting cannot be completely ruled out, the spin modulation observed shows an inherently small incommensurability and no well-defined nesting wave vectors have been reported that would support such a state [130]. Further theoretical study of the stability of AF order in a $J_{\text{eff}} = 1/2$ Mott state with large DM interactions under light carrier doping will be required to more fully explain the origin of the DSDW state in Sr_2IrO_4 .

4.4.11 Conclusions

While the microscopic origin of the DSDW state in Sr_2IrO_4 and the details of its domain structure remain open questions, our data directly reveal the presence of a competing magnetic order parameter which stabilizes in the metallic regime of $(\text{Sr}_{1-x}\text{La}_x)_2\text{IrO}_4$ and whose momentum space structure is reminiscent of the intermediate DSDW state of the high- T_c cuprates. DSDW order is the magnetic precursor to superconductivity in the monolayer cuprates and, given this analogy, our data suggest that electron-doped $(\text{Sr}_{1-x}\text{La}_x)_2\text{IrO}_4$ ($x \geq 0.04$) is on the verge of a bulk superconducting state. The emergence of a competing spin density wave upon electron-doping $(\text{Sr}_{1-x}\text{La}_x)_2\text{IrO}_4$ establishes a common feature in the collapse of the Mott states of the monolayer cuprates and iridates and motivates a push for higher electron concentrations as a route to realizing superconductivity in $(\text{Sr}_{1-x}\text{La}_x)_2\text{IrO}_4$.

Chapter 5

Isovalent destabilization of spin-orbit

Mott state in Ca doped Sr_2IrO_4

Isoelectronic substitution provides an alternative approach to perturb the spin orbit assisted Mott state in Sr_2IrO_4 . The effect of isoelectronic substitution within single crystals of $(\text{Sr}_{1-x}\text{Ca}_x)_{2-y}\text{IrO}_{4+z}$ is explored. Our data provide a detailed mapping of the electronic and structural properties accessible as the structural framework of the canonical spin orbit Mott insulator Sr_2IrO_4 is destabilized via isovalent chemical substitution.

The work presented here has been published as "*Structural evolution and electronic properties of $(\text{Sr}_{1-x}\text{Ca}_x)_{2-y}\text{IrO}_{4+z}$ spin-orbit assisted insulators*" by Xiang Chen, Stephen D. Wilson, Physical Review B 94 (19), 195115 (Ref [\[57\]](#)).

5.1 Introduction

Perturbing the bandwidth of spin-orbit Mott (SOM) compounds via isoelectronic substitution and steric effects presents an alternative approach to destabilizing the SOM state. As one example, in Sr214 either Ba or Ca substitution onto the Sr-site (A-site) should decrease or increase the in-plane IrO_6 octahedral rotation respectively and ultimately modify the system's bandwidth and noncollinear AF ground state. Currently however, there are relatively few studies harnessing chemical pressure as a means of modifying the SOM ground states of the RP iridates. While earlier exploration of polycrystalline samples achieved relatively low levels of A-site substitution [156], more recent single crystal studies have shown that larger substitution levels are still possible [118]. For the case of Ca-substitution into Sr214, the fully substituted end point $\text{Ca}_{2-y}\text{IrO}_4$ is known to form a quasi-one dimensional lattice structure at ambient pressure; however the broader evolution of the structural and electronic phase stability between these two endpoints is an open question.

Here we report a study of isovalent substitution within single crystals of the form $(\text{Sr}_{1-x}\text{Ca}_x)_{2-y}\text{IrO}_{4+z}$, where progressive substitution of Ca^{2+} onto Sr^{2+} sites drives the structure to evolve across a series of structure types, each with insulating ground states where spin-orbit coupling plays an important role. Three distinct structural phases form as a function of increasing Ca content in $(\text{Sr}_{1-x}\text{Ca}_x)_{2-y}\text{IrO}_{4+z}$: For low Ca substitution levels $0 \leq x \leq 0.11$, the $y = 0, z = 0$ single layer R.P. structure of Sr_2IrO_4 remains stable. Beyond $x \approx 0.11$ a miscibility gap opens and leads to the nucleation of the $x = 1/4, z = 1/2$ phase of $\text{Sr}_3\text{CaIr}_2\text{O}_9$ —a three-dimensional buckled honeycomb lattice of IrO_6 octahedra. For $x > 0.7$, the $y = 1/3, z = 0$ quasi one-dimensional chain structure of $\text{Ca}_5\text{Ir}_3\text{O}_{12}$ then stabilizes. Across this phase diagram, charge transport measurements reveal that these three structure types retain their insulating ground states, and resistivity data reflects variable range hopping mechanisms of differing effective dimensionality within each structure-type. The canted antiferromagnetic (AF) structure of Sr214 persists in lightly substituted $(\text{Sr}_{1-x}\text{Ca}_x)_2\text{IrO}_4$ phase ($0 \leq x \leq 0.11$) with an enhancement in the saturated ferromagnetic moment observed, attributable to the

increase in the *ab*-plane canting of IrO_6 octahedra. The $\text{Sr}_3\text{CaIr}_2\text{O}_9$ phase, on the other hand, remains non-magnetic due to its $J_{\text{eff}} = 0$ ground state, consistent with a recent powder study [21]. The heavily substituted single crystals in the $\text{Ca}_5\text{Ir}_3\text{O}_{12}$ phase show an AF phase transition at $T_N = 9\text{K}$; however at higher temperatures an anomalous anisotropy is observed in the local moment behavior. Our data provide a global view of the evolution of the ambient pressure electronic ground states and lattice stabilities of Sr214 as increasing chemical pressure is introduced via isovalent substitution of smaller Ca cations.

5.2 Experimental details

Single crystals were grown via a platinum (Pt) crucible-based flux growth method similar to procedures reported earlier [11]. Stoichiometric amounts of precursor materials of SrCO_3 (99.99%, Alfa Aesar), CaCO_3 (99.99%, Alfa Aesar), IrO_2 (99.99%, Alfa Aesar), and anhydrous SrCl_2 (99.5%, Alfa Aesar) were weighted in a $2(1-x) : 2x : 1 : 6$ molar ratio, where x is the nominal Ca concentration. The starting powders were fully ground, mixed and sealed inside a Pt crucible, covered by a Pt lid, and placed inside an outer alumina crucible. Mixtures were heated slowly to 1380°C , soaked for 5 hours, slowly cooled to 850°C over 120 hours and then furnace cooled to room temperature over ≈ 5 hours. Single crystals were then obtained after dissolving excess flux with deionized water.

As an initial check of the structural phases of crystals nucleated, single crystals within a single batch were randomly chosen, ground into powder, and measured in a PANalytical Empyrean x-ray diffractometer at room temperature. Both phase pure and mixed phase batches were found, depending the nominal doping concentration x . For mixed phase batches, the relative percentage of each constituent phase was obtained from the Rietveld refinement of powder X-ray data with the Fullprof Suite [157]. Elemental concentrations and atomic ratios were also determined via energy dispersive spectroscopy (EDS) measurements. Typical standard deviations of the relative Ca concentrations found within one growth batch were less than 1%.

Measured standard deviations of Ca content are shown as horizontal error bars in plots versus Ca-concentration and were obtained by repeated EDS measurements on random spots across a crystal.

Only single crystals grown from batches with starting Ca concentrations that yielded phase pure crystals were chosen for further detailed characterization and measurement. Select crystals were crushed into powders and measured on the 11-BM beam line at the Advanced Photon Source at Argonne National Laboratory for synchrotron powder X-ray diffraction (PXRD) measurements. Transport measurements were performed within a Quantum Design Physical Property Measurement System (PPMS), and magnetization measurements were performed using a Quantum Design MPMS 5XL SQUID magnetometer.

5.3 Experimental results

5.3.1 $0 \leq x \leq 0.11$, $y = 0$, $z = 0$, $(\text{Sr}_{1-x}\text{Ca}_x)_2\text{IrO}_4$ Ruddlesden-Popper phase

For starting compositions of $0 \leq x_{\text{nominal}} \leq 0.12$, the $n = 1$ R.P. structure remained stable, and batches yielded phase pure crystals of $(\text{Sr}_{1-x}\text{Ca}_x)_2\text{IrO}_4$. Select crystals in this doping regime were crushed and synchrotron powder XRD data collected at 300 K. As shown in Fig 5.1, the data can be indexed and fit within the space group $I4_1/acd$; however we note that the distinction between this and the lower symmetry space group $I4_1/a$ recently reported for parent Sr_2IrO_4 system [113, 114] is beyond the resolution of our measurements. No further symmetry lowering is observed upon Ca substitution for $x < 0.10$ and no additional structural phases were observed within the ground crystals. Crystals with Ca-concentrations from a nominal $x_{\text{nominal}} = 0.15$ batch began to show inclusions of intergrowths of the $\text{Sr}_3\text{CaIr}_2\text{O}_9$ structure (discussed further in section 5.3.3) at a level of $\approx 4\%$ as well as a small inclusion of the $n = 2$ R.P. phase at a level of $\approx 6\%$.

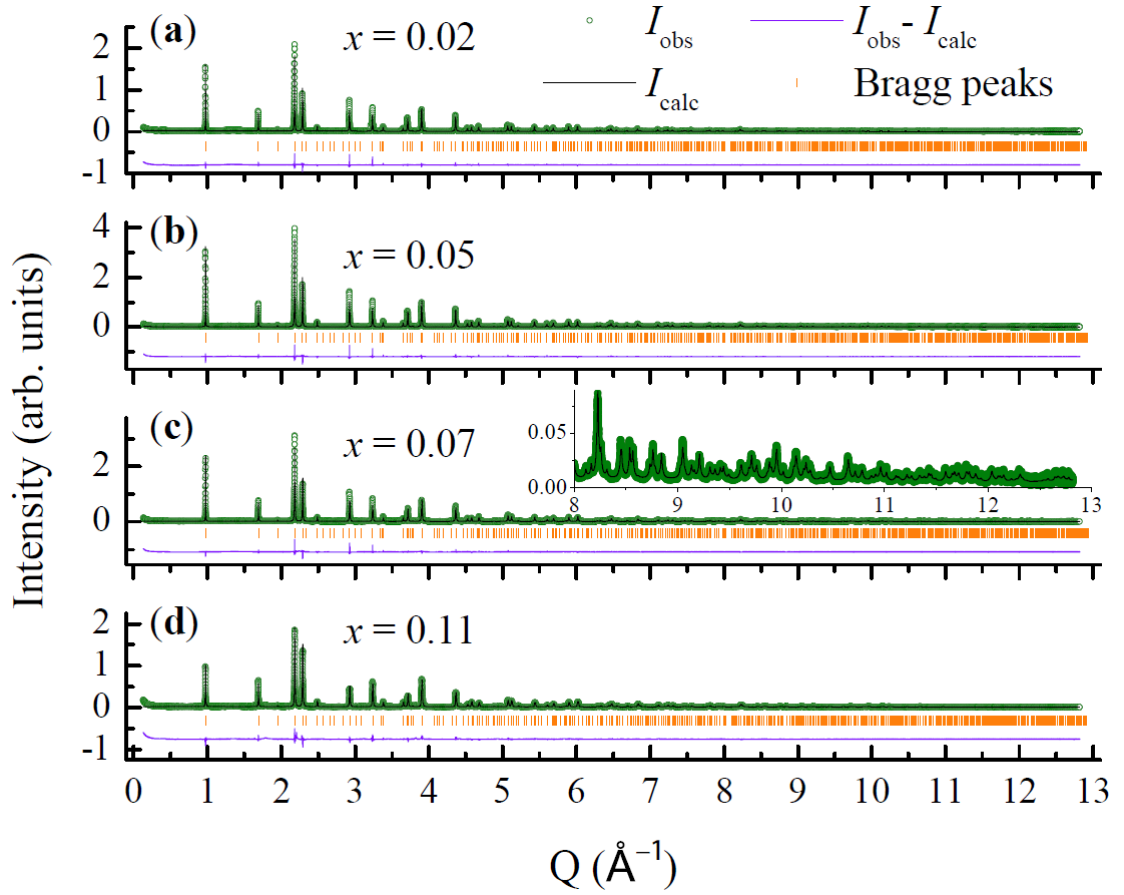


Figure 5.1: Synchrotron powder x-ray diffraction collected at 300 K on select Ca concentrations of $(\text{Sr}_{1-x}\text{Ca}_x)_2\text{IrO}_4$ with (a) $x = 0.02$, (b) $x = 0.05$, (c) $x = 0.07$ (d) $x = 0.11$. Inset shows expanded portion of the data and corresponding fit.

The structural parameters obtained from refinement of crushed single crystal powder XRD data are summarized in Table 5.1. From these data, the lattice parameters a , c and the in-plane octahedral canting angles θ were extracted and plotted in Fig. 5.2, where $\theta = (180^\circ - \alpha)/2$ and α is the Ir-O-Ir nearest neighbor bond angle. For comparison, corresponding data for La doping (blue symbols) are also included. As Sr^{2+} is replaced by the smaller Ca^{2+} ion [156] both the lattice a and c axes decrease as expected. This contrasts the case of when Sr^{2+} is replaced by the smaller electron donor La^{3+} and preferentially swells the a axis [11], likely by adding carriers into the antibonding e_g orbitals.

The low temperature insulating ground state persists through the limit of Ca solubility ($x \approx 0.11$) in the $n = 1$ R.P. Sr214 phase. Charge transport data for select

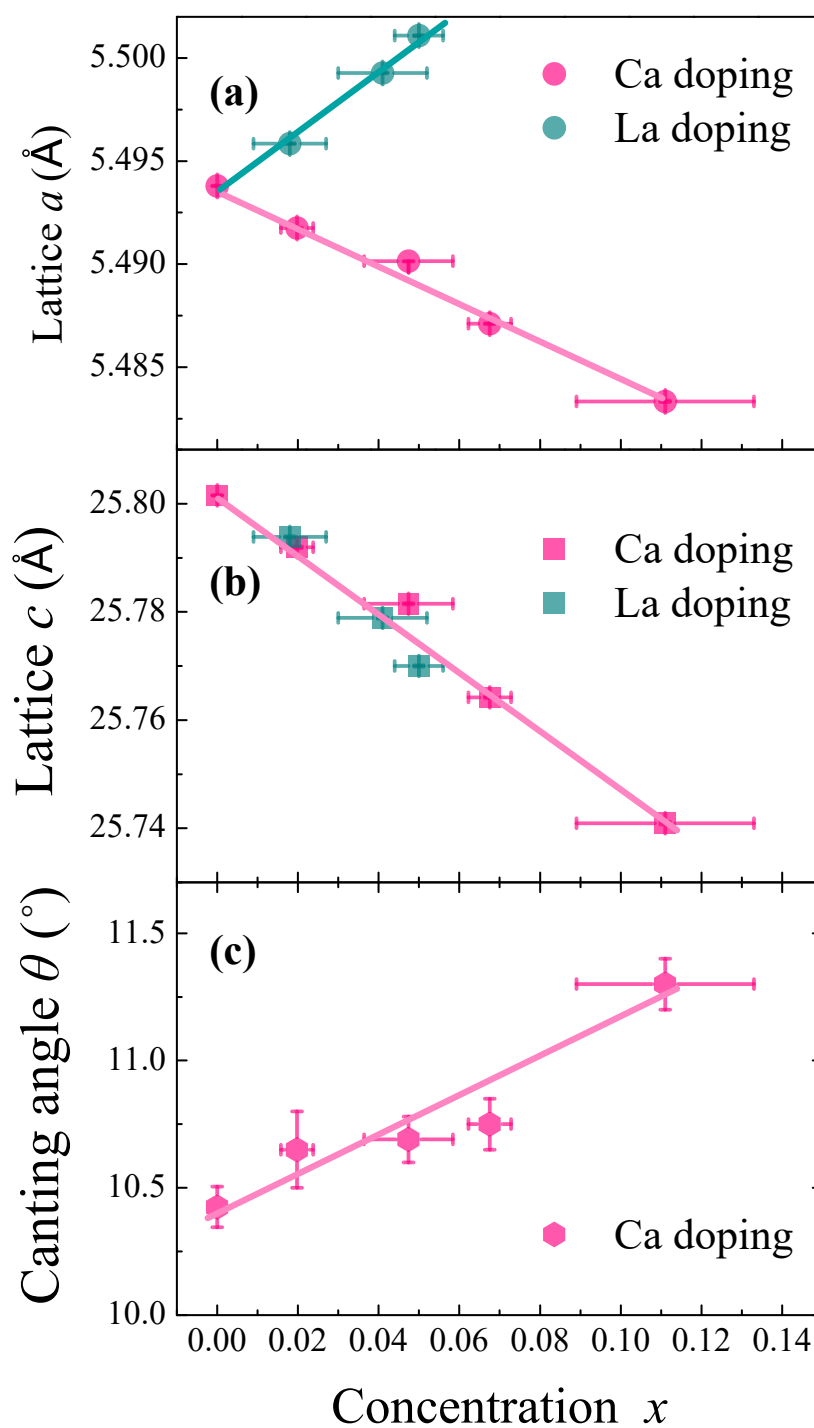


Figure 5.2: Lattice parameters and in-plane IrO_6 canting angles θ determined at 300 K from synchrotron PXRD refinement. (a) a -axis lattice parameters, (b) c -axis lattice parameters, and (c) in-plane IrO_6 octahedral canting angles θ are plotted as a function of Ca-substitution x . For comparison, data resulting from La^{3+} substitution reported previously [11] are overplotted with effect of Ca^{2+} substitution. Pink symbols represent Ca substitution, while dark cyan symbols represent La doping.

Table 5.1: Structural and refinement parameters for $(\text{Sr}_{1-x}\text{Ca}_x)_2\text{IrO}_4$ phase ($0 \leq x \leq 0.11$) at $T = 295\text{K}$ with space group $I4_1/acd$. The atomic positions of (Sr/Ca), Ir, O1 and O2 are $(0, 0.25, z)$, $(0, 0.25, 0.375)$, $(x, x+0.25, 0.125)$, $(0, 0.25, z)$ respectively. The isotropic thermal parameters U of O1 and O2 at $x = 0.11$ are constrained to be the same.

$(\text{Sr}_{1-x}\text{Ca}_x)_2\text{IrO}_4$	$x = 0$	$x = 0.02$	$x = 0.05$	$x = 0.07$	$x = 0.11$
$a(\text{\AA})$	5.49379(1)	5.49175(2)	5.49014(1)	5.48711(2)	5.48332(4)
$c(\text{\AA})$	25.80154(5)	25.79193(15)	25.78151(12)	25.76421(14)	25.74093(24)
$V(\text{\AA}^3)$	778.734(2)	777.866(6)	777.098(5)	775.720(5)	773.948(10)
Atomic z/x and U:					
Sr/Ca					
z	0.05051(1)	0.05033(2)	0.05030(1)	0.05018(1)	0.04996(2)
$U(\text{\AA}^2)$	0.350(7)	0.282(15)	0.233(11)	0.210(12)	0.285(14)
O1					
x	0.20401(37)	0.20298(68)	0.20282(50)	0.20255(55)	0.20142(69)
$U(\text{\AA}^2)$	0.402(61)	0.948(131)	0.873(95)	1.026(107)	2.172(92)
O2					
z	0.95535(10)	0.95631(21)	0.95624(16)	0.95688(18)	0.95664(25)
$U(\text{\AA}^2)$	0.493(45)	1.034(87)	1.023(66)	1.319(73)	2.172(92)
Bond length (\AA):					
Ir-O1	1.975(3)	1.976(4)	1.975(3)	1.975(4)	1.975(4)
Ir-O2	2.073(3)	2.097(6)	2.094(5)	2.110(5)	2.100(8)
Bond angles ($^\circ$):					
Ir-O1-Ir	159.15(16)	158.7(3)	158.62(18)	158.5(2)	158.0(3)
R-factors:					
χ^2	4.28	3.64	4.55	4.27	5.43
R_{wp}	11.9	13.6	11.8	12.1	12.9
R_p	8.87	11.3	9.47	9.74	9.81

Ca concentrations are shown in Fig. 5.3 where increased levels of Ca impurities reduce the low temperature resistivity as this limit is approached. Resistivity data did not fit to a thermally activated hard gap or variable range hopping (VRH) models over an appreciable temperature range. We note that the $x = 0$ parent material is known to display three-dimensional VRH at low temperatures[121]; however this is likely obscured by the added effect of Ca-impurities. The low temperature plateau in resistivity apparent in $x = 0.05$ and $x = 0.07$ samples seemingly suggests the approach of a percolative metal-insulator transition; however no insulator to metal transition was observed below 300 K in any of the measured crystals.

In order to further parameterize the evolution of the SOM state in Sr214 upon Ca-substitution, magnetization measurements were performed. Fig. 5.4 shows field

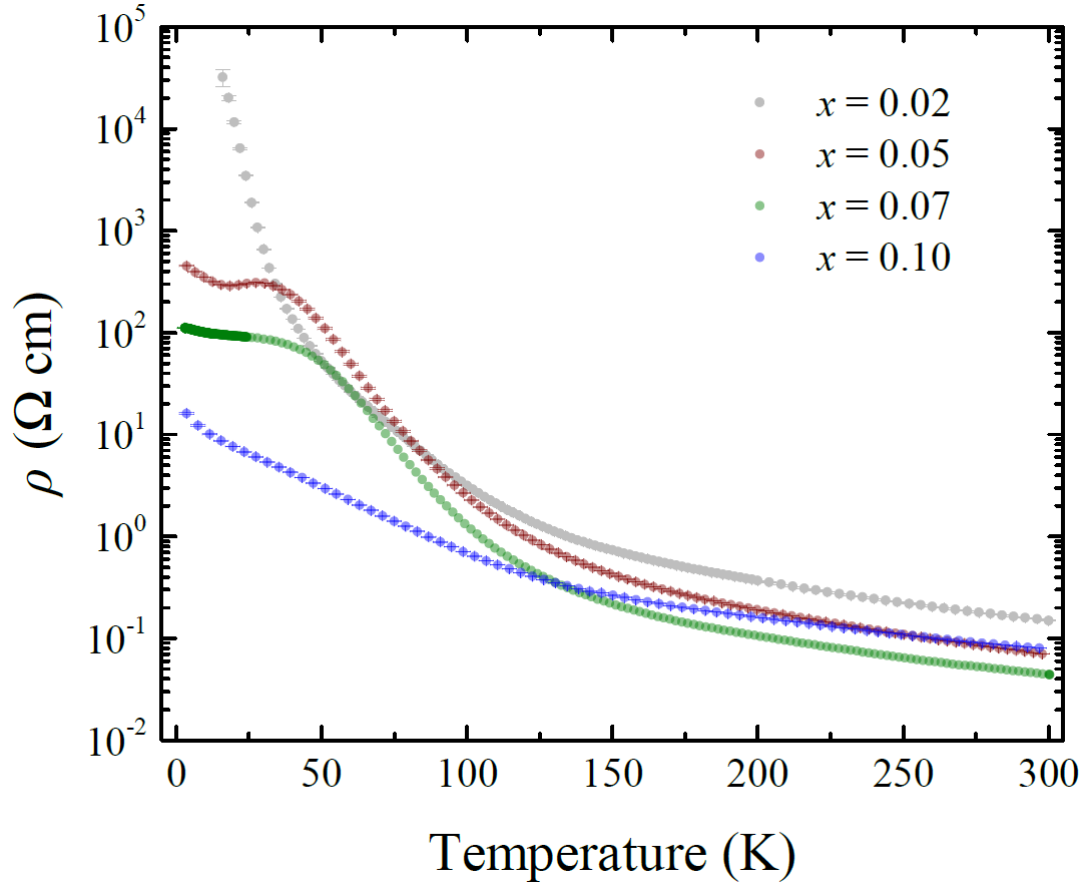


Figure 5.3: The temperature dependence of the ab -plane resistivity of $(\text{Sr}_{1-x}\text{Ca}_x)_2\text{IrO}_4$ plotted for Ca concentrations of $x = 0.02$ (grey symbols), $x = 0.05$ (dark red symbols), $x = 0.07$ (dark green symbols), and $x = 0.11$ (blue symbols).

cooled (FC) and zero-field cooled (ZFC) magnetization data collected under an $\mu_0 H = 300$ Oe applied within the ab -plane (Fig. 5.4(a)). Upon cooling under a fixed field, the maximum in susceptibility associated with the onset of AF order as well as the magnitude of irreversibility associated with the AF transition are enhanced with progressive Ca substitution. The enhancement in irreversibility is better illustrated in Fig. 5.4(b) where the introduction of Ca impurities is shown to reduce the onset of irreversibility and enhance the low field polarization of the canted spin structure. The latter point is further illustrated in Fig. 5.5(a) where $T = 5$ K isothermal magnetization curves are plotted. Namely, from the inset of Fig. 5.5(a), there is an enhanced remnance of the ab -plane magnetization of the canted AF spin structure. This likely reflects the role of disorder in Ca-substituted samples where Ca-substitution within the rock-salt layers disrupts the extended spin

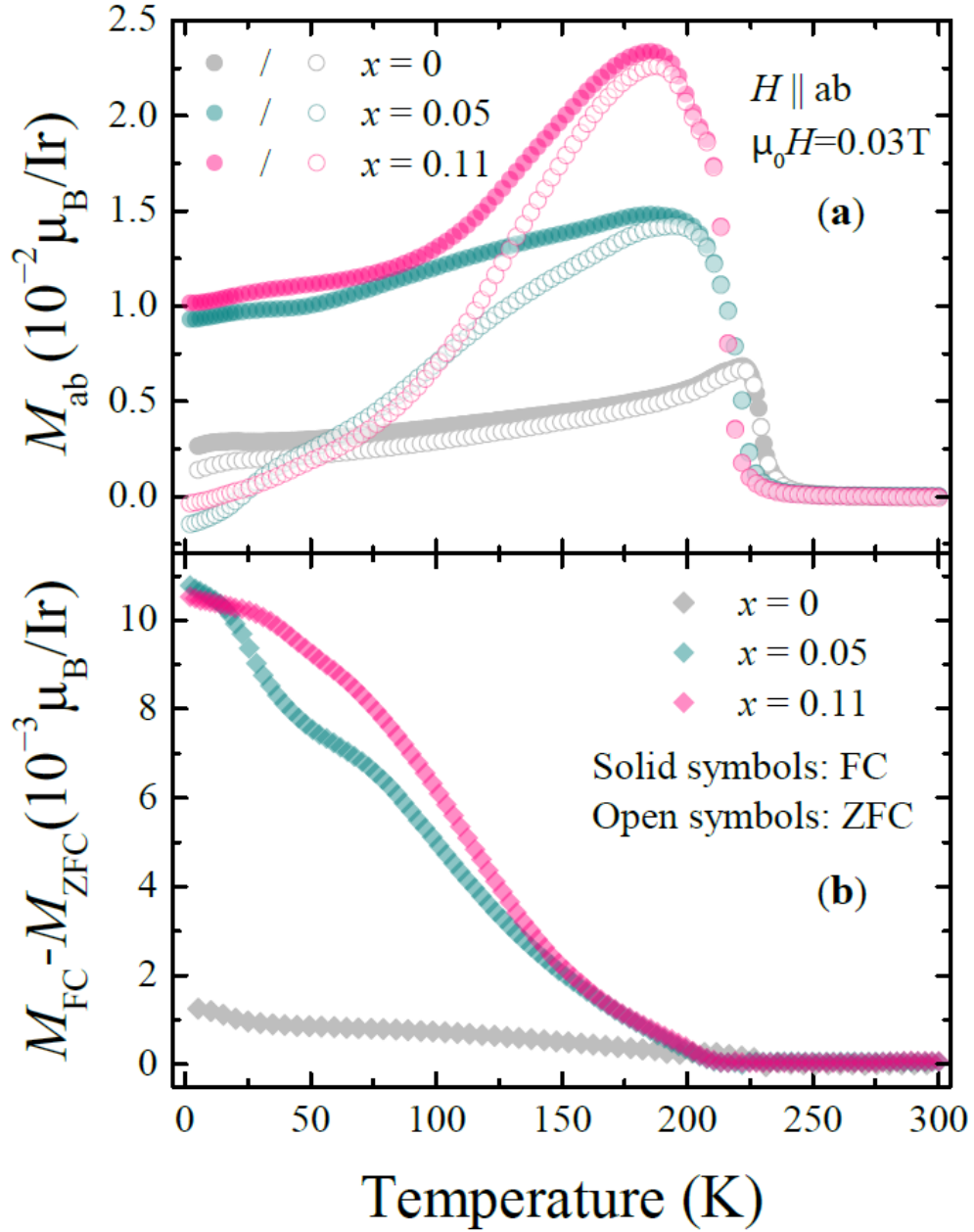


Figure 5.4: Magnetization data collected on $(Sr_{1-x}Ca_x)_2IrO_4$ samples. (a) Temperature dependent magnetization data collected under ZFC and FC with the magnetic field applied in the ab -plane and $\mu_0 H = 0.03$ T. (b) Irreversibility of the magnetization data plotted in panel (a) determined by subtracting FC and ZFC data.

canting sequence between layers and prevents the spin structure from relaxing when the field is removed. As a result, after cycling the field the sample retains a net ferromagnetic moment even under zero applied field.

The field-driven transition out of the zero net moment AF state and into the spin phase with aligned moment canting persists for all Ca concentrations at nearly the same critical field of $H_c \approx 0.2\text{T}$ [31]. The remnant spin reorientation implies that the magnetic structure remains qualitatively similar to the unalloyed Sr214 system [45, 46] despite the slight suppression of the onset of AF order in Ca-substituted samples from $T_{AF} = 240\text{K}$ for $x = 0$ to $T_{AF} \approx 210\text{K}$ for $x = 0.11$. An increase in the coercivity of the field-induced transition occurs with increasing Ca-content and is consistent with a disorder induced pinning of the domain structure. Additionally, the magnitude of the saturated magnetization in the aligned, canted state increases with increasing Ca-content.

Curiously, the increase in the saturated magnetization cannot be explained by a trivial geometric factor such as moments locked to an increase in the *ab*-plane IrO_6 octahedral rotation [117]. As a simple estimation, by assuming a fixed moment of $\approx 0.46\mu_B$ on the Ir-site (close to the zero field value of $0.36 \pm 0.06\mu_B$ [45]) and using the refined canting angle of 10.5° , the canted Ir moments within each layer should give rise to the net magnetization of $0.083 \mu_B/\text{Ir}$ observed under 5 T (assuming a single polarized magnetic domain). If the ordered moment remains fixed as Ca is substituted, the net moment should increase as $\sin(\theta)$, where θ can be obtained from the PXRD structural refinement. However, the refined in-plane Ir-O-Ir angles decrease only slightly ($< 1\%$) in the most heavily Ca-substituted samples relative to the $x = 0$ parent system, while the saturation magnetization increases more than than 23%. This discrepancy between the field polarized net ferromagnetic moments and the expectations of fixed Ir moments locked to the octahedral rotations is illustrated in Fig. 5.5(b). A further enhancement in the magnitude of the ordered moment suggests that a modified canting of the Ir-moments relative to the in-plane IrO_6 octahedral rotation should occur; however a future full neutron refinement of both the oxygen positions and ordered moment is necessary to fully explore this

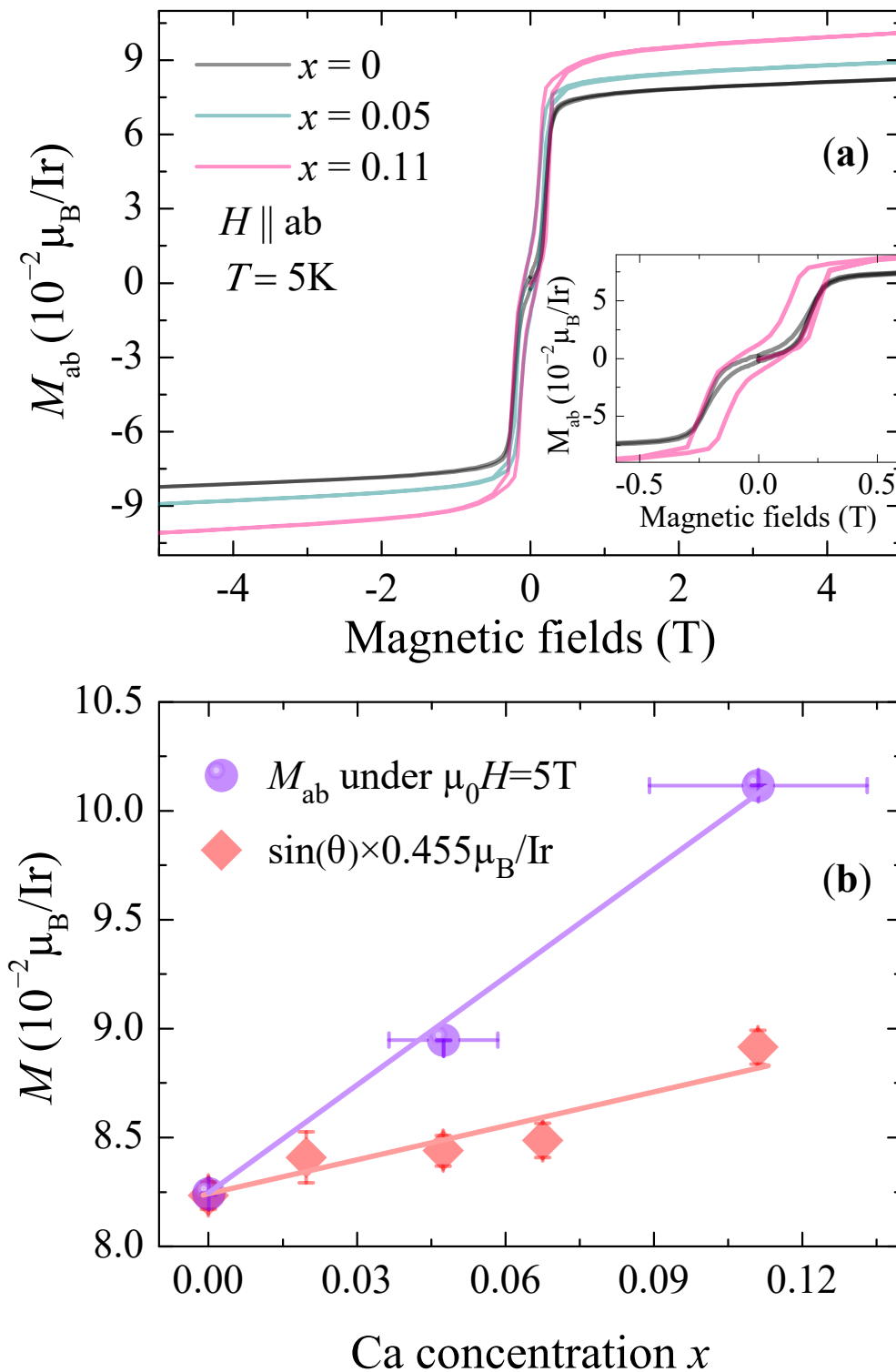


Figure 5.5: (a) ab -plane isothermal magnetization of $(\text{Sr}_{1-x}\text{Ca}_x)_2\text{IrO}_4$ collected at $T = 5\text{K}$. Inset shows an expanded subset of the data with the field swept between -0.6T to 0.6T . (b) Saturated magnetization plotted as a function of Ca concentration x and collected with $\mu_0 H = 5\text{T}$ applied parallel to the ab -plane. Overplotted are the canted projections of the net magnetization using an assumed ordered moment $m_{AF} = 0.455 \mu_B/\text{Ir}$ and the measured IrO_6 octahedral canting angles θ .

possibility.

5.3.2 $x = 1/4$, $y = 0$, $z = 1/2$, $\text{Sr}_3\text{CaIr}_2\text{O}_9$ honeycomb lattice phase

When the starting Ca-concentration was increased to $0.15 \leq x_{\text{nominal}} \leq 0.70$, cube-like single crystals with typical dimensions of $0.9 \times 0.9 \times 0.8 \text{ mm}^3$ were obtained. Synchrotron PXRD (Fig. 5.6) data were collected on crushed single crystals with this morphology, and the data agree well with the recently reported $\text{Sr}_3\text{CaIr}_2\text{O}_9$ structure type [21]. EDS measurements on this phase indicated atomic ratios of (Sr+Ca):Ir as 2:1 and Ca:(Ca+Sr) as 1:3.7. The crystal structure is shown in Fig 5.7 where all of the octahedra (Ir and Ca octahedra) are corner sharing and form a three-dimensional network. The Ir cations sit on two chemically distinct sites and

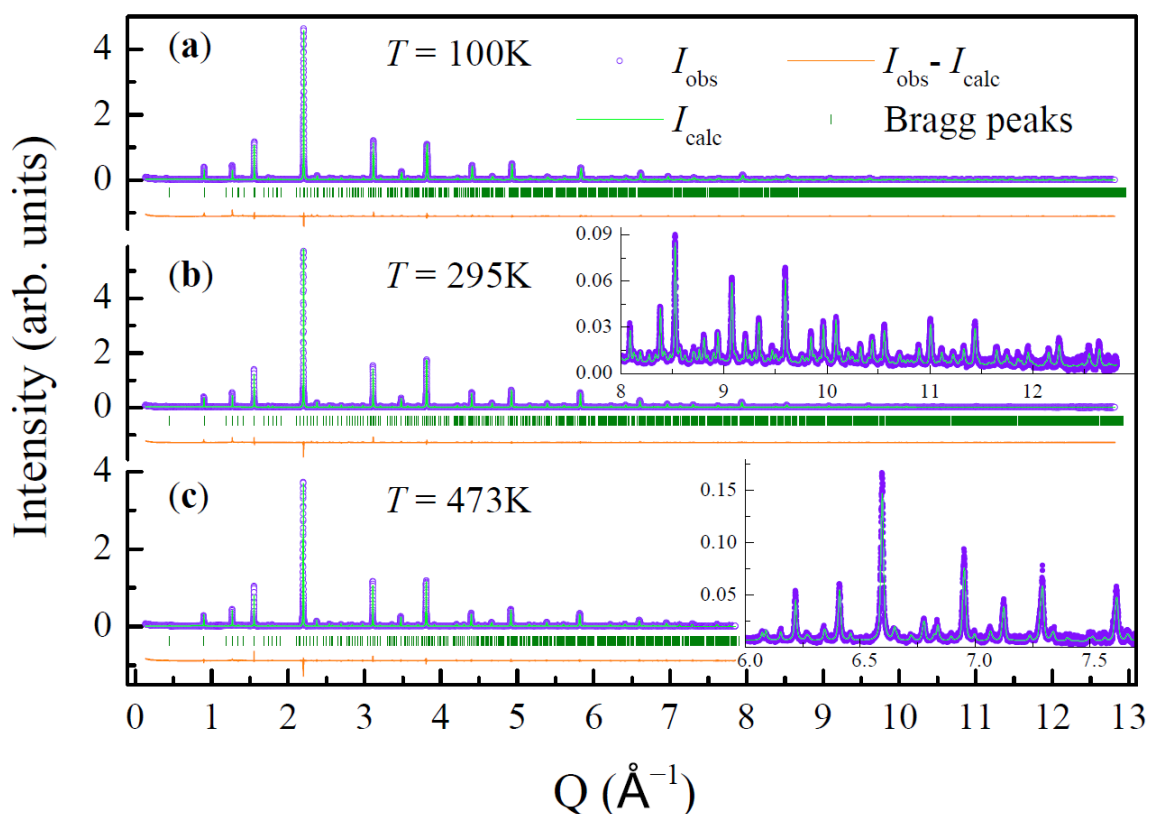


Figure 5.6: Synchrotron PXRD of crushed $\text{Sr}_3\text{CaIr}_2\text{O}_9$ single crystals collected at (a) 100 K, (b) 295 K, and (c) 473 K. The data are indexed fit within space group $P2_1/c$. Inset in panel (c) shows the magnified view of the data and fit.

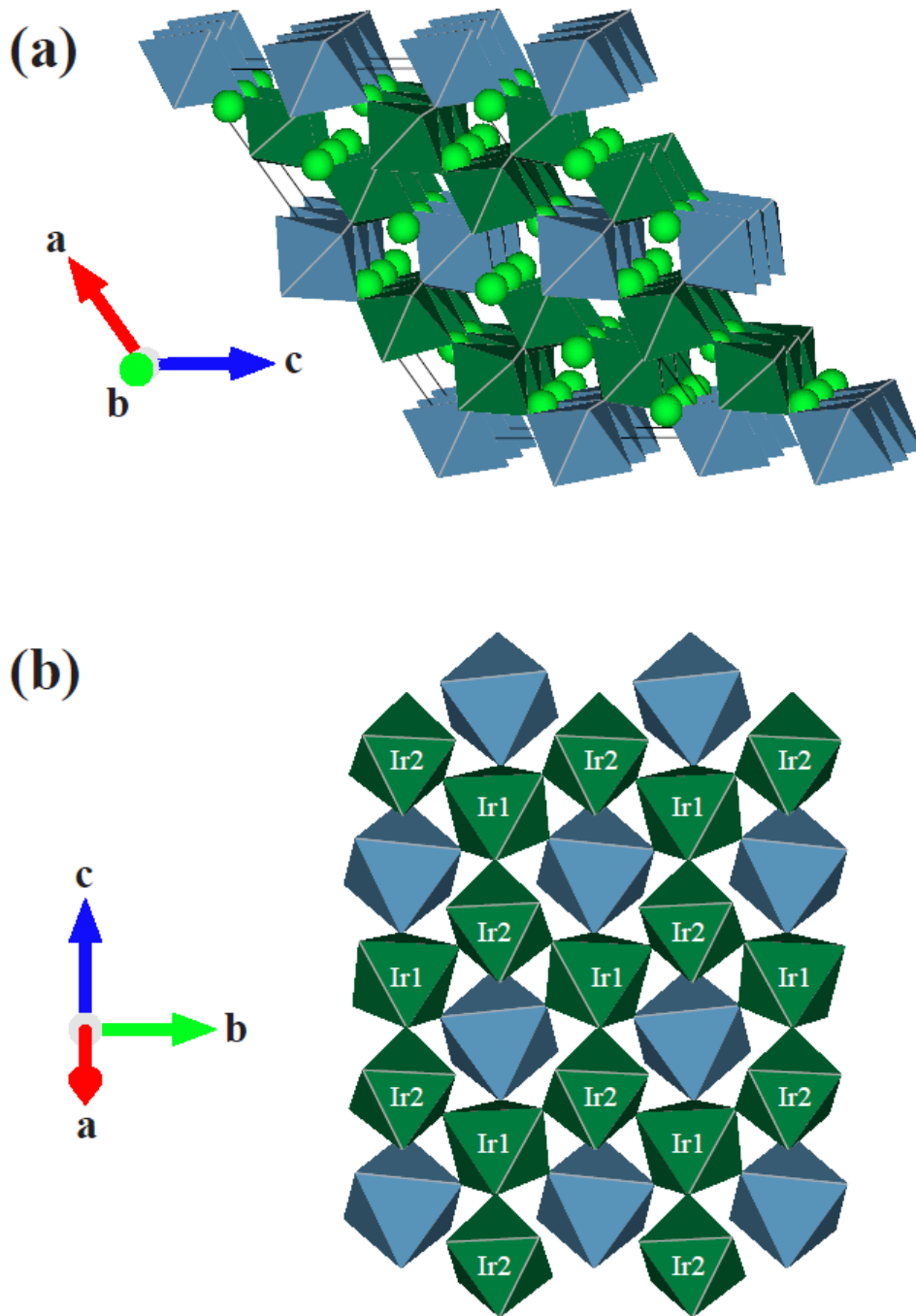


Figure 5.7: (a) Crystal structure of $\text{Sr}_3\text{CaIr}_2\text{O}_9$. For oxygen at the vertices of Ca and Ir centered octahedra are omitted. Sr atoms are represented by green balls. Ca-centered octahedra are plotted in blue and Ir-centered octahedra are plotted in green. (b) Projected bc -plane view of the lowest three layers of $\text{Sr}_3\text{CaIr}_2\text{O}_9$ from panel (a) showing the formation of buckled honeycomb lattice of Ir-octahedra. Distinct Ir-octahedra positions are labeled as Ir1 and Ir2. VESTA software was used for crystal structure visualization [13].

are labelled as Ir1 and Ir2 respectively. Looking down the b axis, the Ir octahedra are connected through a corner sharing network and form buckled planes, separated by layers of Ca octahedra. Looking down the a^* direction (perpendicular to the bc plane) the Ir octahedra form a buckled honeycomb lattice as shown from the projected view in Fig 5.7(b). We note here that Ir cations in this system are nominally in the d^4 nonmagnetic $J = 0$ state [21]. PXRD data were collected at three temperatures ($T = 100, 295,$ and 473 K) and fit within the space group $P2_1/c$. No signature of a structural phase transition was observed, and structural parameters are summarized in Table 5.2. Due to the nine unique oxygen sites and their small contribution to the PXRD profiles, refinement of the oxygen positions and atomic displacement parameters were constrained.

To explore the electronic properties of the $\text{Sr}_3\text{CaIr}_2\text{O}_9$ phase, charge transport measurements were also performed. Fig. 5.8 shows the resistivity data of a single crystal of $\text{Sr}_3\text{CaIr}_2\text{O}_9$ along the (1,1,1) axis [158] where the expected spin-orbit stabilized insulating state comprised of a filled $J_{\text{eff}} = 3/2$ band is observed. A variable range hopping (VRH) model was applied to model the low temperature resistivity: $\rho = \rho_0 \cdot \exp((T_0/T)^{1/(1+D)})$, where D is the dimensionality of charge transport and T_0 is assumed to be a temperature independent constant. The best fit was achieved using a dimensionality of $D = 2$, consistent with an earlier study of powder samples [21]. Illustrating this, Fig. 5.8 inset shows $\ln \rho$ versus $(\frac{1}{T})^{\frac{1}{3}}$, where data fit

Table 5.2: Structural and refinement parameters for $\text{Sr}_3\text{CaIr}_2\text{O}_9$ phase at select temperatures. The space group $P2_1/c$, initial atom positions and fixed thermal parameters are adopted from D.C. Wallace *et al.* [21].

$\text{Sr}_3\text{CaIr}_2\text{O}_9$	$T = 100\text{K}$	$T = 295\text{K}$	$T = 473\text{K}$
$a(\text{\AA})$	17.09503(9)	17.12849(20)	17.16315(17)
$b(\text{\AA})$	5.71275(3)	5.71084(5)	5.71382(7)
$c(\text{\AA})$	9.86065(7)	9.88008(9)	9.89488(11)
$\beta(^{\circ})$	125.28085(45)	125.25529(110)	125.24737(72)
$V(\text{\AA}^3)$	786.117(8)	789.192(13)	792.465(15)
R-factors:			
χ^2	3.59	3.76	4.25
R_{wp}	11.6	12.3	12.8
R_p	9.18	9.99	9.91

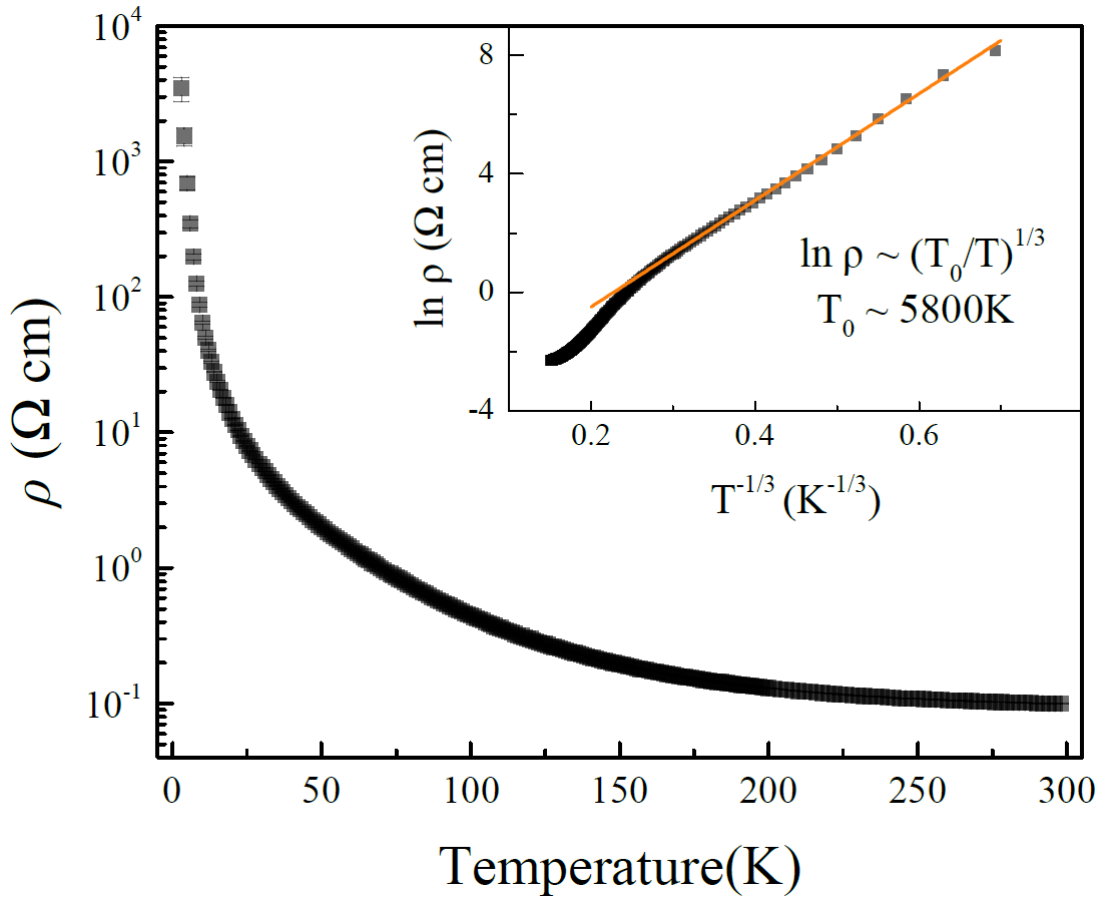


Figure 5.8: Resistivity plotted as a function of temperature measured on a $\text{Sr}_3\text{CaIr}_2\text{O}_9$ single crystal. Inset shows the same data plotted as $\ln \rho$ versus $T^{-1/3}$ where the orange line shows a fit to VRH behavior with $D = 2$ and $T_0 = 5800\text{K}$.

between $2 \geq T \geq 125 \text{ K}$ render an effective $T_0 \approx 5800\text{K}$. Naively, this suggests an underlying conduction mechanism facilitated via tunneling of carriers constrained to planes within the lattice; for instance via an effective layered crystal structure of buckled IrO_6 planes located between Ca spacer layers. Transport measurements along orthogonal crystal axes however failed to resolve any appreciable anisotropy. Absent a detailed understanding of potential twinning in the crystal, more detailed analysis is presently precluded.

The magnetic properties of $\text{Sr}_3\text{CaIr}_2\text{O}_9$ were also explored and temperature dependent magnetization data collected under an applied field of $\mu_0 H = 0.03 \text{ T}$ along the (1,1,1)-axis are plotted in Fig. 5.9. Negligible anisotropy was observed upon orienting the H -field along orthogonal axes. Rather, the observed magnetization is weak and the measured susceptibility can be captured via a Curie-Weiss (CW)

fit of the form $\chi = \chi_0 + \frac{C}{T - \Theta_{\text{CW}}}$ where χ_0 is the temperature independent constant, $C = \frac{\mu_{\text{eff}}^2}{3k_B}$, μ_{eff} is the effective local magnetic moment, and Θ_{CW} is the Curie-Weiss temperature. No irreversibility was resolved between the FC and ZFC magnetization data, the CW temperature $\Theta_{\text{CW}} = -1.7(1)\text{K}$ is near zero, and $\mu_{\text{eff}} = 0.18(1) \mu_B$. Taken together this suggests that this weak paramagnetic response has an extrinsic, impurity driven origin.

To further explore this, isothermal magnetization measurements were performed at $T = 5\text{K}$ with the results shown in Fig. 5.9(b). No field sweep hysteresis was observed, and for clarity, Fig. 5.9(b) shows only the data with the magnetic field sweeping from 0 to 5 T. The data can be modeled with a simple Brillouin function: $M = \eta g \mu_B J \left(\frac{2J+1}{2J} \coth\left(\frac{2J+1}{2J}x\right) - \frac{1}{2J} \coth\left(\frac{1}{2J}x\right) \right)$ where M is the magnetization per Ir, g is the g -factor, and $x = \frac{g \mu_B J B}{k_B T}$. Assuming an isotropic $g = 2$ and $J = \frac{1}{2}$, the data was fit with the impurity fraction scaling factor $\eta = 0.015(3)$. Using this impurity fraction scaling factor, the corrected effective moment μ_{eff} obtained from the CW fit to data in Fig. 5.9(a) becomes $1.53(9)\mu_B$ per impurity site. This suggests that the observed susceptibility arises from a 2% molar fraction of Ir^{4+} moments in the sample; likely driven via a small number ($\approx 1\%$) of oxygen vacancies.

5.3.3 $x \geq 0.75$, $y = 1/3$, $z = 0$, $(\text{Sr}_{1-x}\text{Ca}_x)_5\text{Ir}_3\text{O}_{12}$ edge-sharing IrO_6 chain phase

When the starting Ca concentration reached $x = 0.75$, crystals possessing the quasi one-dimensional $\text{Ca}_{2-y}\text{IrO}_4$ structure began to nucleate [159]. It is known that Ca_2IrO_4 is prone to hosting a substantial amount of Ca vacancies, which results in the formation of the more stable $\text{Ca}_5\text{Ir}_3\text{O}_{12}$ phase [160]. Single crystals were removed, crushed, and PXRD data collected. PXRD data were best fit within the space group $P\bar{6}2m$ using the previously reported structure of $\text{Ca}_5\text{Ir}_3\text{O}_{12}$ [161, 162]. EDS measurements revealed the atomic ratio of Ca:(Ca+Sr) to be 0.89(2); however, due to strong preferred orientation, reliable (Ca/Sr)-site occupancy information was not obtained within our PXRD analysis. A small inclusion of the $\text{Sr}_3\text{CaIr}_2\text{O}_9$ phase

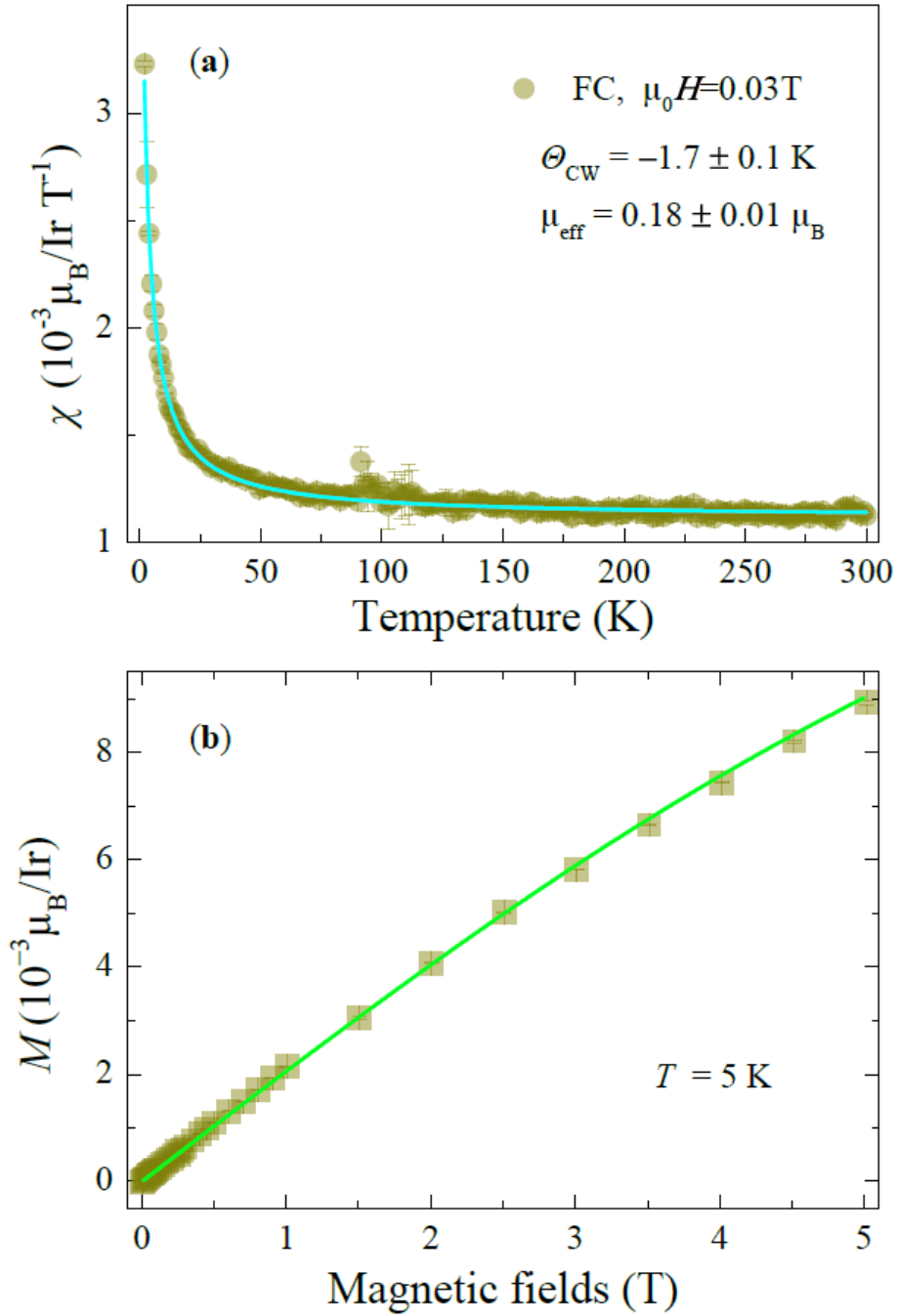


Figure 5.9: (a) Temperature dependent susceptibility of $\text{Sr}_3\text{CaIr}_2\text{O}_9$ under an applied magnetic field of 0.03T. Cyan line is the Curie-Weiss fit across the whole temperature range, which lead to a small Curie temperature $\Theta_{\text{CW}} = -1.7 \pm 0.1 \text{ K}$ and a small effective moment $\mu_{\text{eff}} = 0.18 \pm 0.01 \mu_B$. (b) Isothermal magnetization measured at $T = 5 \text{ K}$. Green line is the Brillouin function fit multiplied by an additional scaling constant 0.015, assuming $g = 2$ and $J = 1/2$. The necessity of applying the scaling constant is because not all Ir contribute to the magnetism, whereas the magnetization is normalized to the total number of Ir sites.

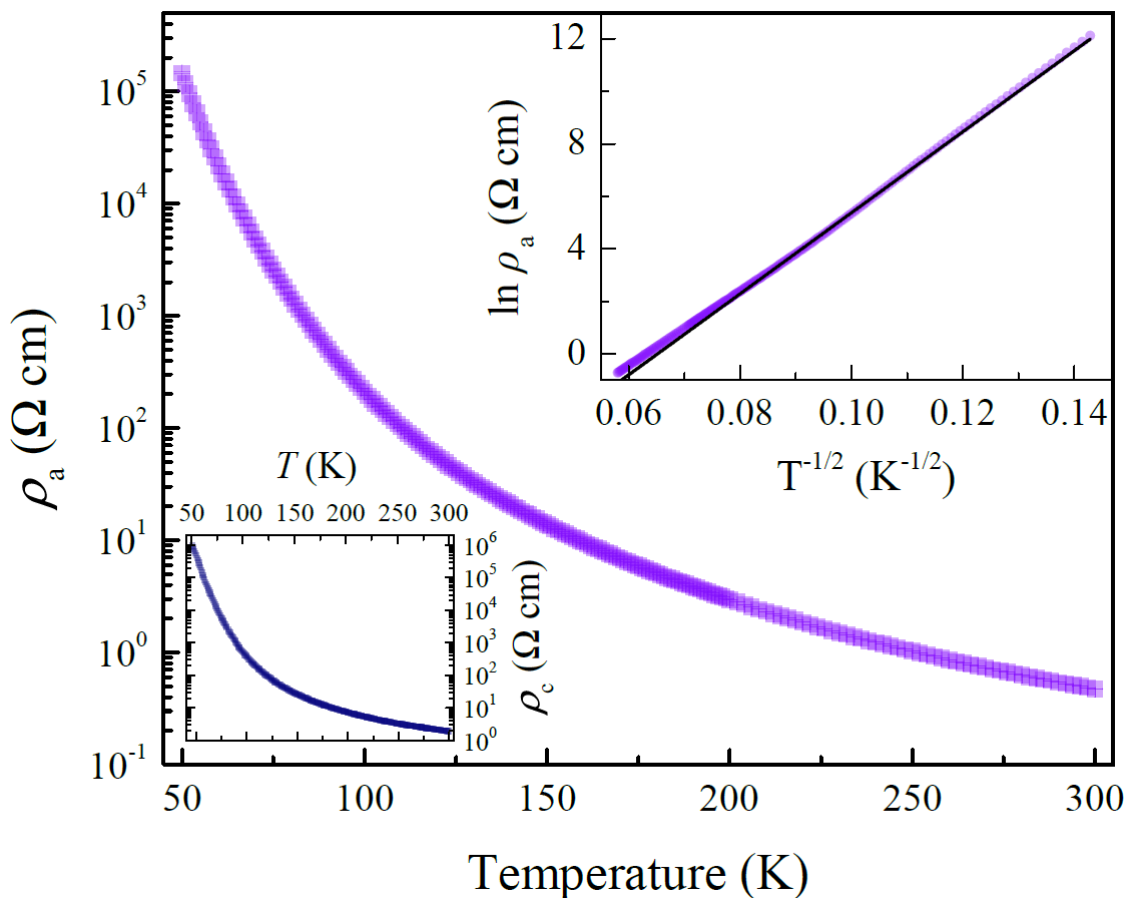


Figure 5.10: Temperature dependence of resistivity measured along the a and c -axes of $(\text{Ca}_{0.89}\text{Sr}_{0.11})_5\text{Ir}_3\text{O}_{12}$. The main panel shows ρ_a along the a -axis and the lower left inset plots ρ_c along the c -axis. Upper inset shows plot of $\ln \rho_a$ versus $T^{-1/2}$ and the corresponding VRH fit of resistivity with $D = 1$ and $T_0 = 23800\text{K}$.

also appeared in the PXRD data with a relative molar fraction refined to be less than 0.5%. Lattice parameters were determined to be $a = b = 9.45626(14)\text{\AA}$, $c = 3.20520(6)\text{\AA}$, slightly larger than those reported for $\text{Ca}_5\text{Ir}_3\text{O}_{12}$ ($a = b = 9.4208\text{\AA}$, $c = 3.1941\text{\AA}$) [163, 162] and consistent with the partial substitution of larger Sr^{2+} cations onto Ca^{2+} -sites. Given the dearth of evidence supporting the stability of bulk stoichiometric Ca_2IrO_4 , we assign the $\text{Ca}_5\text{Ir}_3\text{O}_{12}$ phase to the new crystals found nucleating in this $x \geq 0.75$ regime.

Fig. 5.10 shows charge transport measurements along the a and c directions of a $(\text{Ca}_{0.89}\text{Sr}_{0.11})_5\text{Ir}_3\text{O}_{12}$ crystal. Insulating behavior was observed along both the a and c axes across all temperature ranges probed. Transport along the a -axis is shown in Fig. 5.10's main panel while c -axis transport data are plotted in the lower

left inset. We note here that due to the constraints of the samples' dimensions, c -axis transport data could only be acquired via a two-probe measurement whereas a -axis measurements used a conventional four probe measurement. Contact resistance in the former case should be a small percentage of the resistance values at low temperature, and comparison of the a and c axis low temperature transport data in this regime reveals minimal anisotropy.

a -axis charge transport data were best fit with a VRH model with $D = 1$ as shown in Fig. 5.10's upper right inset. This naively agrees well with the quasi 1-D nature of this compound; however the absence of appreciable anisotropy in charge transport instead suggests that the Efros-Shklovskii (E.S.) form of VRH [120] is the more likely transport mechanism. A similar analysis of the c -axis transport data also best fits to the ES form of tunneling transport, $\rho(T) \propto e^{(\frac{T_0}{T})^{1/2}}$. Magnetization data are plotted in Fig. 5.11 where an antiferromagnetic transition at $T_{AF} = 9(1)$ K appears via the onset of irreversibility between FC and ZFC data (Fig. 5.11) with the field applied either within the ab -plane or along the c -axis. CW fits were performed to the data above this transition using the form $\chi = \frac{C}{T-\Theta} + \chi_0$ where χ_0 encodes the weak core level diamagnetism, any temperature independent Van Vleck contribution, and the background contribution from the sample mount.

The upper inset in Fig. 5.11 shows the results of CW fits along both directions which yielded $\Theta_{CW} = -7.7(1)$ and $-5.8(2)$ K for the magnetic field oriented within the ab -plane and along the c -axis respectively. The temperature independent χ_0 terms were identical within error for both field orientations and was comprised of intrinsic and extrinsic background contributions where $\chi_0 = \chi_{intr} + \chi_{bckg}$. The χ_{bckg} was measured independently and the χ_{intr} contributions were $\chi_{intr} = 0.00234(1)\mu_B/\text{Ir}$ and $\chi_{intr} = 0.00224(1)\mu_B/\text{Ir}$ for the c -axis and ab -plane field orientations respectively. Curiously, the local moments extracted from the Curie constant C values were substantially different for the two field orientations. In accounting for the mixed valence of Ir-cations inherent to the $\text{Ca}_5\text{Ir}_3\text{O}_{12}$ structure (*i.e.* 1/3 of the Ir cations are Ir^{4+} and 2/3 are Ir^{5+}), the local moments from CW fits should arise from the Ir^{4+} sites alone. Correcting for this gives $\mu_{\text{eff}} = 1.76 \pm 0.02 \mu_B$ for Ir^{4+} moments

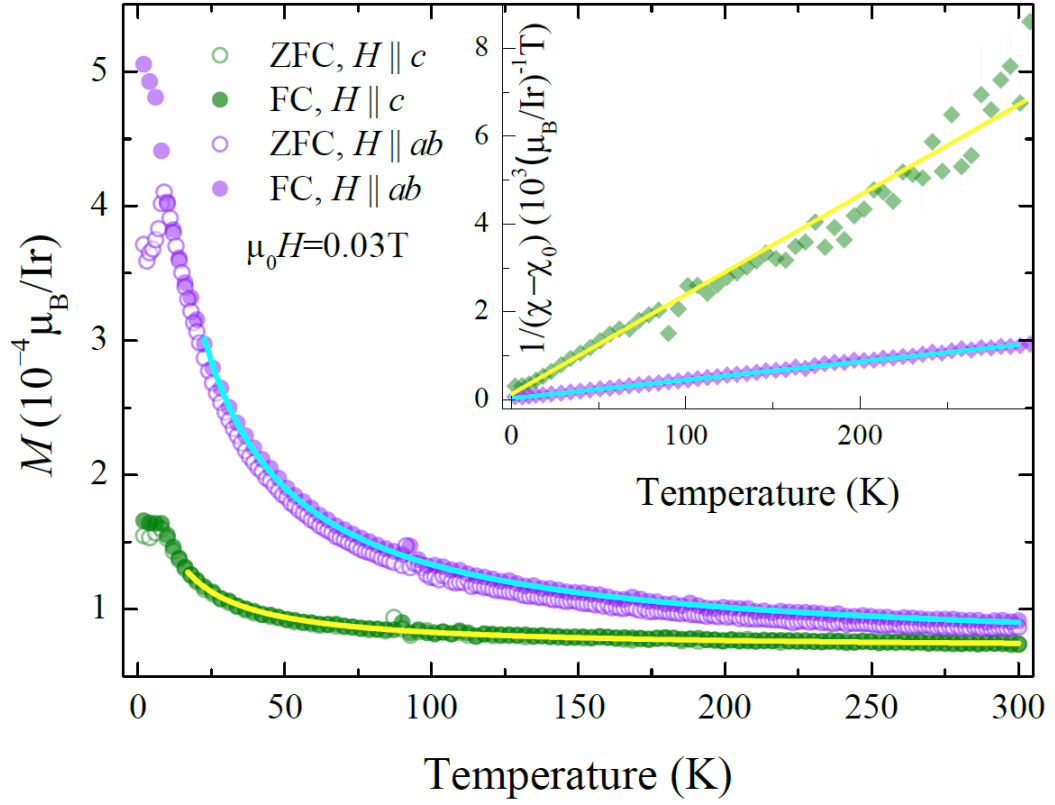


Figure 5.11: Temperature dependence of the magnetization of $(\text{Ca}_{0.89}\text{Sr}_{0.11})_5\text{Ir}_3\text{O}_{12}$ collected under FC (closed symbols) and ZFC (open symbols) with $\mu_0 H = 0.03$ T applied within the ab -plane and along the c -axis. Inset shows the corresponding inverse susceptibilities with temperature independent background and Van Vleck terms removed, $1/(\chi - \chi_0)$. CW fits to the data are plotted as solid lines.

in measurements with the field applied within the ab -plane and $\mu_{\text{eff}} = 0.76 \pm 0.02 \mu_B$ for measurements with the field applied along the c -axis. This implies a substantial orbital component to the moments where an anisotropic g -factor suppresses the apparent local moment along the chain direction.

5.4 Discussion

Fig. 5.12 summarizes the structural phase evolution of crystals yielded as the nominal starting ratio of $2(\text{Sr}(1-x):\text{Ca}(x))\text{CO}_3:\text{IrO}_2:6\text{SrCl}_2$ was varied. Symbols denote the typical phase content of individual crystals harvested within a batch, and overlaps between structure types denote regions where individual crystals contained of

mixture of two phases. The relative molar fractions of crystals in this mixed phase region are indicated by the phase percentage axis. The $n = 1$ R.P. phase remains stable until $x_{\text{nominal}} \approx 11\%$, where increased Ca-substitution into $(\text{Sr}_{1-x}\text{Ca}_x)_2\text{IrO}_4$ enhances the weak ferromagnetism of the $x_{\text{nominal}} = 0$ parent system. Beyond this starting Ca-composition, a miscibility gap opens and the dominant phase yielded in crystal growth was the $\text{Sr}_3\text{CaIr}_2\text{O}_9$ state, yet crystals still included intergrowths of $n = 1$ R.P. phase for concentrations $x_{\text{nominal}} \leq 0.5$. Phase pure $\text{Sr}_3\text{CaIr}_2\text{O}_9$ crystals nucleated in the composition range $0.5 \leq x_{\text{nominal}} \leq 0.7$ before switching to the quasi one-dimensional $\text{Ca}_5\text{Ir}_3\text{O}_{12}$ structure beyond $x_{\text{nominal}} = 0.9$.

Within the $n = 1$ R.P. phase, Ca-substitution into Sr_2IrO_4 serves as only a small perturbation to the lattice where the unit cell volume contracts by only 0.6% under approximately 10% Ca-substitution. When compared to previous hydrostatic pressure studies that affect a much larger volume reduction [105], the relative reduction in the low temperature resistivity of Ca-substituted samples is substantially greater than externally applied pressure. This verifies that the enhanced conductivity is defect-driven, where the added A-site disorder generates states within the gap. The low temperature flattening in the resistivity further suggest a percolative network formed by defect states; however a crossover to metallic transport was not observed up to the solubility limit of Ca within the Sr_2IrO_4 lattice. The persistence of magnetic order up to this limit further supports this picture of a small volume of defects dominating transport data, where previous hydrostatic pressure studies resolved the collapse of AF order at pressures far below the collapse of the charge gap in this compound [105].

The enhancement of the weak ferromagnetic moment observed in Ca-substituted Sr_2IrO_4 cannot be trivially accounted for by assuming a fixed ordered moment size locked to the in-plane octahedral rotation. Rather, a change in the relative coupling between degree of spin canting and octahedral rotation likely occurs. This enhancement in the canting of moments relative to the IrO_6 octahedral rotations can potentially be driven via an enhanced tetragonal distortion of the ligand field at the Ir^{4+} sites [68]. As expected with the substitution of the small Ca-cation

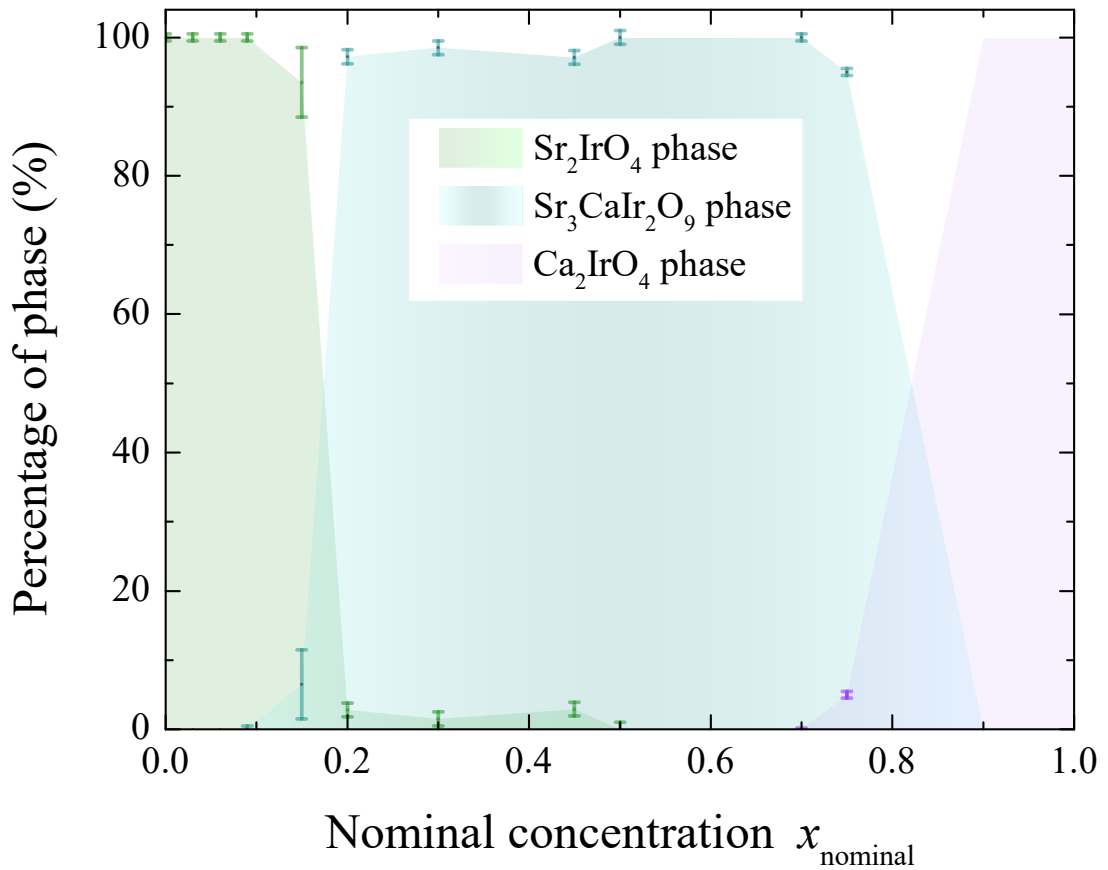


Figure 5.12: Phase diagram generated based on the growth sequence and procedures detailed in Section 5.2. Predominant structure types of $(\text{Sr}_{1-x}\text{Ca}_x)_{2-y}\text{IrO}_{4+z}$ that crystallize in each region of the phase diagram are shaded as light green (Sr_2IrO_4), light cyan ($\text{Sr}_3\text{CaIr}_2\text{O}_9$), and light purple (Ca_2IrO_4). Regions of overlap denote concentrations where mixed phase crystals were obtained with the relative phase fractions denoted on the phase percentage axis. We note here that the bottom axis denotes the nominal, starting concentration (x_{nominal}) of Ca in the synthesis run.

within the rock-salt layers of the $n = 1$ R.P. structure, our PXRD refinements reveal that a slight elongation ($\approx 2\%$) of the octahedra results near the $x = 0.11$ limit of Ca-substitution. However, this enhanced elongation should naively reduce the canting angle of the moments relative to the octahedral rotation, highlighting the need for detailed neutron diffraction data sensitive to the ordered moment size and oxygen positions to fully resolve the mechanism of the apparent moment enhancement.

Data collected on crystals grown within the $\text{Sr}_3\text{CaIr}_2\text{O}_9$ structure agree with an earlier powder study of this material [21]. No relaxation of the structure into a higher symmetry space group was observed as the system was heated to 473 K;

however our PXRD measurements have poor sensitivity to the oxygen site positions and occupancies. Minimal anisotropy was observed in both transport and magnetization measurements, and our magnetization data are consistent with the picture of $\text{Sr}_3\text{CaIr}_2\text{O}_9$ possessing a non-magnetic $J = 0$ ground state. The weak moments observed in magnetization measurements are consistent with a trace amount of oxygen vacancies generating small fractions of Ir^{4+} sites and $J = 1/2$ moments. This was indicated by the small and variable scaling factors $\eta \approx 0.02$ needed to account for Brillouin function fits of the isothermal magnetization data at $T = 5\text{K}$ in different crystals.

For crystals that nucleated in the one-dimensional $\text{Ca}_5\text{Ir}_3\text{O}_{12}$ structure at the Ca-rich end of the phase diagram, the substitution of Sr into the lattice seems to have a substantial influence on the physical properties of the material. Specifically, for 11% Sr-substitution onto the Ca-sites, a number of electronic properties observed differ from an earlier report studying the unalloyed $x = 1$ system [163]. No thermally-driven metal to insulator was observed in ab -plane transport data in our Sr-substituted crystals, where instead the entirety of resistivity data was modeled via E.S. VRH. Susceptibility data do not reveal any broad maxima consistent with a one-dimensional quantum antiferromagnet [164]. Rather CW fits of Sr-alloyed crystals reveal Θ_{CW} values in accordance with the onset temperature of AF order at $T_{\text{AF}} = 9(1)\text{K}$, in contrast to the large $\Theta_{\text{CW}} \approx 280\text{K}$ and high frustration parameter reported for the $x = 1$ system. While the anisotropy in the low field magnetization data of the $x = 0.89$, 11% Sr-substituted, system matches that of the $x = 1$ parent compound, the anisotropy observed in the apparent μ_{eff} values of the $x = 0.89$ system under different field orientations suggests a highly anisotropic g -factor for this system. Future work exploring this via paramagnetic spin resonance techniques directly sensitive to the g -tensor are required to fully explore the origin of this effect.

5.5 Conclusions

In summary, the structural and electronic phase evolution of $(\text{Sr}_{1-x}\text{Ca}_x)_{2-y}\text{IrO}_{4+z}$ crystals was explored. Ca substitution into the spin-orbit Mott insulator $(\text{Sr}_{1-x}\text{Ca}_x)_2\text{IrO}_4$ was possible for $x_{\text{nominal}} \leq 0.11$ before a miscibility gap opens and the $\text{Sr}_3\text{CaIr}_2\text{O}_9$ phase intermixes. Prior to this, the spin-orbit Mott insulating state survives the relatively weak perturbation to the structure driven via Ca impurities within the lattice. An anomalous enhancement of the net ferromagnetic moment results with Ca substitution, suggestive of a decoupling between the in-plane canted antiferromagnetism and the in-plane IrO_6 octahedral rotation. As the nominal Ca substitution level is increased to $x_{\text{nominal}} = 0.5$, phase pure $\text{Sr}_3\text{CaIr}_2\text{O}_9$ nucleates and manifests a nonmagnetic $J = 0$ insulating ground state consistent with recent powder studies. At higher nominal Ca concentrations $x_{\text{nominal}} > 0.7$, the one dimensional chain structure $(\text{Sr}_{1-x}\text{Ca}_x)_5\text{Ir}_3\text{O}_{12}$ stabilizes. For partially alloyed crystals in this system ($x = 0.89$), the low temperature insulating ground state reveals an antiferromagnetic phase transition below $T = 9$ K with an anomalous high temperature anisotropy in the CW susceptibility not present in the $x = 1$ system. Future studies exploring the electronic phase evolution close to the $x = 1$ end point of this system are a promising future direction in understanding the origin of this response.

Chapter 6

Itinerant excitations in prototypical helimagnet MnSi

In this chapter, the prototypical weak itinerant metal MnSi, an old *3d* material yet possessing fertile and intriguing physical phenomena, will be examined by inelastic neutron scattering up to the small wave length limit, focusing on the magnetic excitations. The itinerant excitations will be explored in details, to the high energy limit, with the discussion of the possible role of Higgs mechanism involved. A new phase diagram will be proposed for weak itinerant metals.

6.1 Introduction

The chiral helimagnet metal MnSi has been in the center of stage for decades [165, 166, 167, 168, 169, 15, 170, 47, 48, 171, 172, 173, 54, 174, 175, 176, 177, 178, 179, 180, 181, 182, 14, 183, 184, 185, 186, 187, 188, 189, 190, 191, 192], resulting from the abundant existence of crystalline orders composing distinct phase diagrams woven by a set of parameters including pressure (P), field (B) and temperature (T). One prominent example is the establishment of a lattice of topological magnetic vortex, *i.e.* Skyrmions, stabilized near the border between paramagnetic state and long-range helimagnetic order under a small external magnetic field [182, 14, 193, 194, 195, 196, 189]. Another tunable physical parameter, P , is known for being able to drive a breakdown of Fermi liquid regime in metallic MnSi [174, 178, 180, 181]. Leaving the influence of external field or pressure, the spontaneous breaking of rotational symmetry in the low temperature ordered helical phase warrant the helical Goldstone mode, *i.e.* helimagnon, which shows anisotropic dispersion relation as in chiral liquid crystals and is verified by later inelastic neutron scattering experiments [197, 186, 191]. This short list of examples highlight the intrinsic Fermi liquid instability that is prone to be influenced by other degrees of freedom, which are responsible for the stabilizations of various intriguing phases.

Another important characteristic that renders the metallic MnSi subjecting to extensive studies in the 1980s is its prototypical itinerant nature [165, 166, 167, 168, 169, 15, 170, 171, 172, 54], which demonstrates distinct features compared to strongly localized Heisenberg magnets. Some of the noticeable dissimilarities include metallic conductivity [166], non-integer number of magnetic moment value or reduced carrier numbers below the ordering temperature T_c (introduced in section 2.5.3) [165, 166], contrasting magnetic response respect to fields [168] and vanishingly small entropy change at the critical temperature [167], compared to the characteristics expected for localized spin systems. The most solid evidence perhaps comes from inelastic neutron scattering experiments [15, 170, 171, 54], which establishes the peculiar attributes from magnetic excitations in stark contrast to well-understood linear spin wave patterns in localized Heisenberg models, such

as the presence of strong spin wave damping once entering a particular energy scale that signals the existence of single particle Stoner continuum [15, 170].

Recently, a gapped Higgs boson mode is predicted in addition to the massless Goldstone mode in ferromagnetic metals, which can be directly applied to the nearly ferromagnetic metal MnSi [198, 199]. The essential deviation from Stoner's model is that higher order Fermi liquid parameter stabilizes the Higgs amplitude mode, which pulls out spectral weight from incoherent particle-hole continuum. The predicted dispersion is well detectable within inelastic neutron experiment. In addition, the spin wave dispersion is not fully characterized inside the Stoner continuum because of the weak intensity and strong Landau damping [15, 170]. Therefore, inelastic neutron scattering is performed to potentially access the newly proposed amplitude mode. Most importantly, the characteristics of spin wave dispersion inside the Stoner continuum will be explored up to high energy limit.

6.2 Bulk properties of MnSi

6.2.1 Basic properties

Chiral MnSi crystallizes in the cubic B20 structure with space group $P2_13$ (lattice constant $a = 4.558 \text{ \AA}$) and each unit cell contains four manganese and silicon atoms in the positions (u, u, u) ; $(u+0.5, -u+0.5, -u)$; $(-u+0.5, -u, u+0.5)$; $(-u, u+0.5, -u+0.5)$ with $u_{\text{Mn}} = 0.138$ and $u_{\text{Si}} = 0.845$ [165, 15]. The crystal structure is shown in Fig. 6.1.

Fig 6.2 shows the detailed magnetic phase diagram of MnSi under fields [15, 173, 175, 14]. At ambient pressure and zero applied magnetic field, MnSi develops the helical order below $T_c = 29.5 \text{ K}$ with a long period of 180 \AA propagating along the $\langle 1, 1, 1 \rangle$ direction [15]. Since the helical modulation spans almost 23 unit cells along $\langle 1, 1, 1 \rangle$ direction, the spins only rotate about 8° between unit cells along the diagonal direction. Therefore, the low temperature helical phase can be

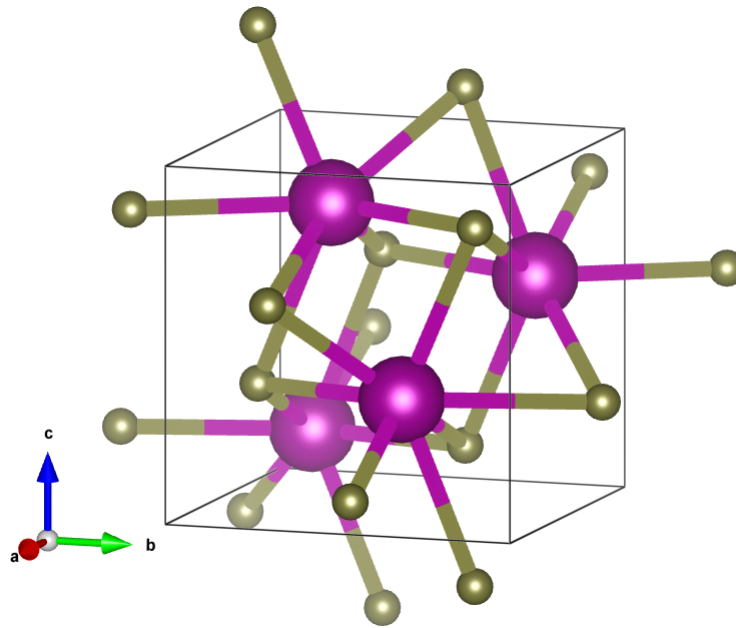


Figure 6.1: Crystal structure of MnSi. Mn (cyan spheres) and Si (dark yellow spheres)

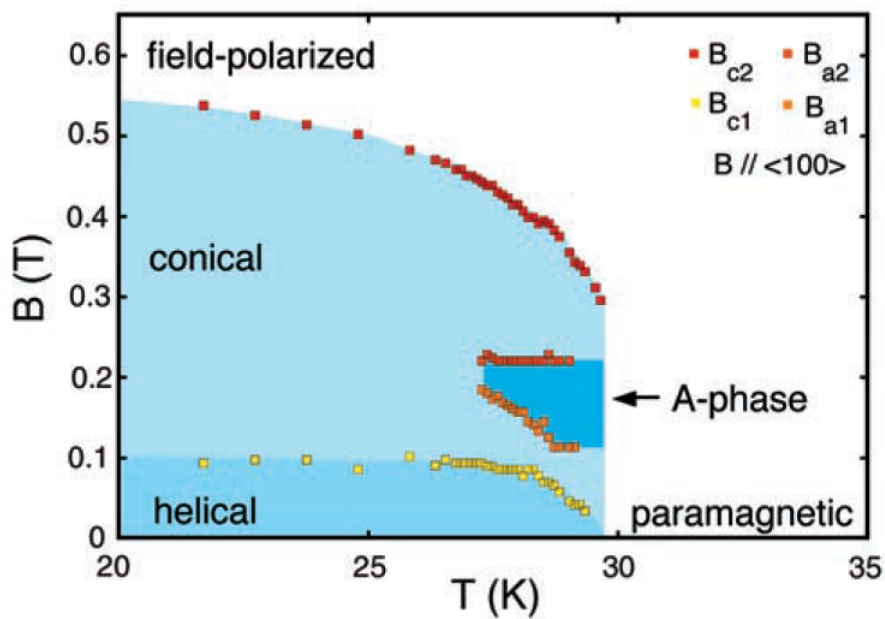


Figure 6.2: Magnetic phase diagram of MnSi at ambient pressure. At $B = 0$, MnSi develops the helical order below $T_c = 29.5$ K. The helical order can be polarized by external field with the transition from helical to conical to field-polarized state with increasing fields. Near the board between paramagnetic state and ordered state, an anomalous phase can be stabilized by a small external field. This phase is later identified as the topological skyrmions. Adopted from [14].

approximated as a ferromagnetic phase. Near the board between the ordered phase and paramagnetic state, there exists an anomalous phase under a small external field, which is later identified as topological skyrmions [15, 173, 175, 182, 14, 183, 184]. At low enough temperatures (*e.g.* 10 K), the helical order can be polarized by external fields, with the magnetic order transiting from helical, through conical, and eventually fully field polarized with increasing field [15].

In a magnetic field greater than 0.6 T, the spin structure is saturated with a magnetic moment $\mu_S \approx 0.4\mu_B$ per Mn atom, which is substantially smaller than the spontaneous magnetic moment $\mu_{\text{eff}} = 2.2\mu_B$ [166, 192]. This anomaly together with other characteristics, such as metallic ground state [166], strong magnetic response respecting to external field perturbations [168] and vanishingly small entropy change at critical temperature T_c [167], suggest MnSi is a weak itinerant metal.

6.2.2 Energy scales and Hamiltonian

The complex magnetic phase diagram of MnSi in Fig. 6.2 is the result of a hierarchical of energy scales [47, 48]. The strongest one is the ferromagnetic exchange interaction, which aligns the spins. The less dominant scale is the rotationally invariant Dzyaloshinsky Moriya (DM) interaction, which results from weak spin orbit coupling in non-centrosymmetric B20 crystal structure in MnSi [43, 44]. This DM interaction term is responsible for the magnetic helix structure. The weakest energy scales are higher order correction terms, which include the SOC induced weak anisotropic exchange (Ani) interaction and also the magnetic dipolar terms. Although being the smallest interaction terms, the anisotropic interaction and dipolar terms break the rotational symmetry and ultimately fix the spiral prorogating direction along the diagonal direction.

Now the Hamiltonian for MnSi can be rearranged in a way similarly to Eq. 2.15, but with a descending order of influence:

$$\mathcal{H} = \mathcal{H}_{\text{EX}} + \mathcal{H}_{\text{DM}} + \mathcal{H}_{\text{Ani}} + \mathcal{H}_{\text{Dipolar}} + \mathcal{H}_{\text{B}} \quad (6.1)$$

6.2.3 Early neutron scattering experiments

As being the prototypical weak itinerant magnet, plenty of neutron scattering experiments have been done in MnSi in the past [169, 15, 170, 171, 172, 173, 54, 200, 179, 14, 185, 186, 16, 201, 191]. Here only the relevant work will be introduced in the following.

The most relevant work to the current study is from Ishikawa *et al.* [15], who performed the inelastic neutron scattering up to maximum energy of ≈ 20 meV. The essential result is that at 5 K temperature the spin wave is well-defined (resolution limited) and follows $E = 0.13 + 52q^2(\text{\AA})^2$ meV along $[1, 0, 0]$ direction in the $q \rightarrow 0$ limit, but becomes increasingly heavily-damped with larger reduced momentum q , as shown in the line scans and also the contour map from Fig. 6.3 (Note: results along other directions are similar). Specifically, Fig. 6.3(c) shows the evolution of linewidths with respect to q , which clearly indicates the abrupt increase of linewidth

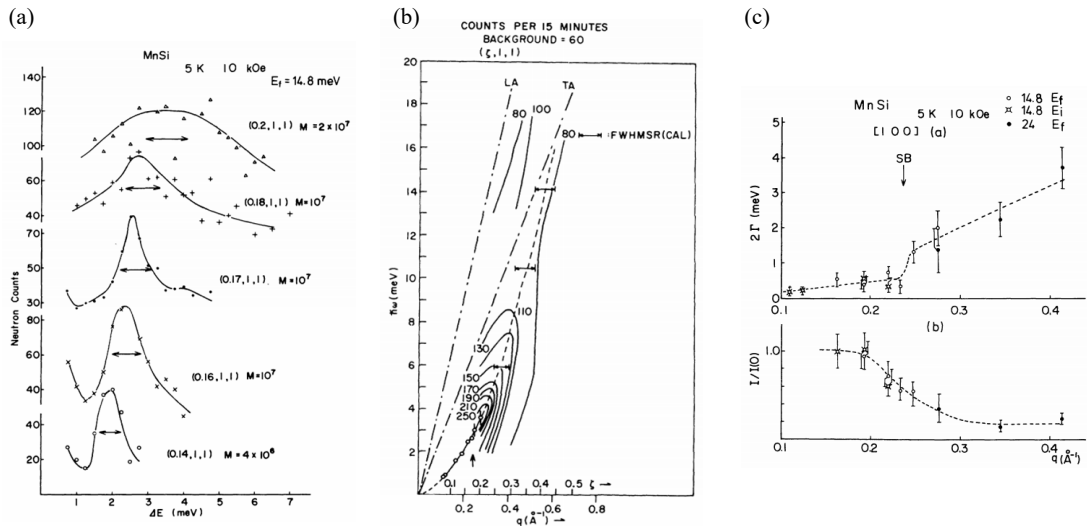


Figure 6.3: Inelastic neutron scattering data on MnSi observed at 5 K in a field of 10 kOe along $[100]$ direction around (011) zone with different energies. (a) Spin wave excitations with constant Q scans using $E_f = 14.8$ meV. M is monitor counts. Arrows indicate the FWHM. (b) Contour maps of magnetic scattering with $E_f = 24$ meV. Spin wave dispersion determined from (a) is also included as circles. Phonon contribution was subtracted. Quadratic dispersion is shown by broken lines. (c) Intrinsic linewidth (upper panel) as well as integrated intensity (lower panel) of spin waves with three different conditions $14.8 E_i$, $14.8 E_f$ and $24 E_f$ plotted against q . Adopted from [15].

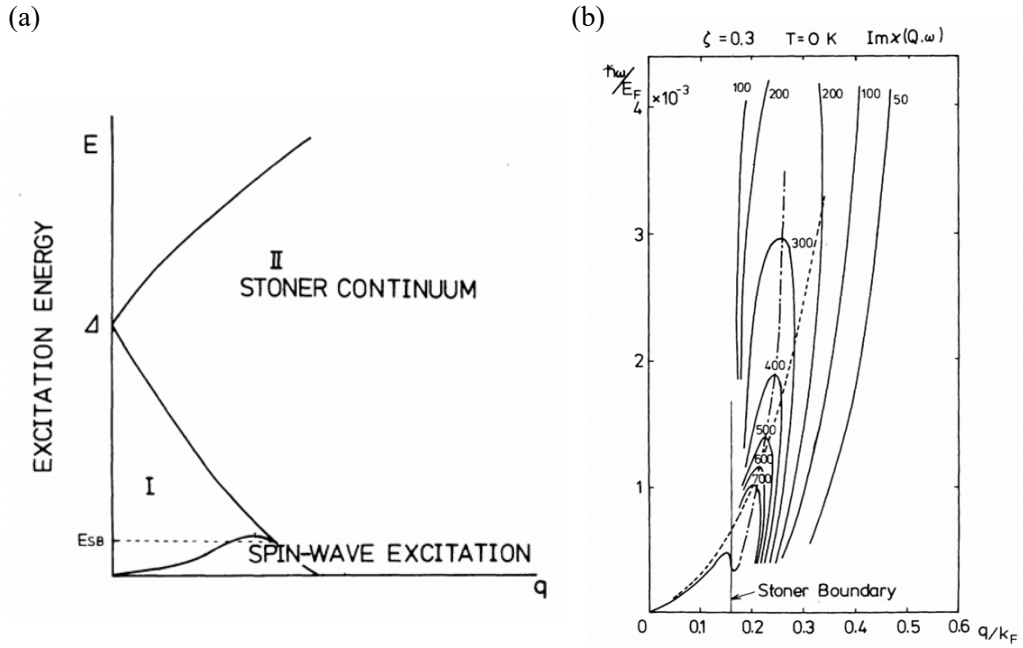


Figure 6.4: Magnetic excitation in a ferromagnetic electron gas calculated from RPA theory. (a) Schematic plot. (b) Magnetic excitation at 0 K. Excitation in the Stoner continuum is displayed as contour lines. Adopted from [15].

at $q_{SB} \approx 0.24\text{\AA}^{-1}$ along the $[1,0,0]$ direction. Correspondingly, it implies that spin wave mode enters the incoherent single particle Stoner continuum beyond energy $E_{SB} \approx 3\text{ meV}$, which accounts for the significantly reduced lifetimes of magnons at $q > q_{SB}$ (or $E > E_{SB}$).

The experimental observations are further corroborated by performing the RPA simulations of the dynamical magnetic response in itinerant electron ferromagnetic systems [15]. This simple RPA picture of magnetic excitations in the electron gas capture the essential features of the magnetic excitations in MnSi, as shown in Fig. 6.4. For instance, the low lying spin wave excitations propagate with infinite lifetime in the small q region; reduced intensity and pronounced broadening when the spin wave mode enters the Stoner continuum. Therefore, from these similarities between the experimental results and the electron-gas model, MnSi is an itinerant electron system with a Stoner boundary of $\sim 3\text{ meV}$ [15].

Despite these encouraging observations, the experimental data have some limitations. First, the phonon contributions are not well accounted for which could

potentially affect the experimental characterizations such as the distribution of intensity in the large q limit. Second, the intrinsic difficulties such as the weak intensity and exceptionally broadened spin wave modes prevent the detailed explorations to the higher energy limit (above 20 meV). In the following sections, the experimental work by inelastic neutron scattering focusing the high energy excitations will be explored and characterized in details. The above mentioned difficulties are less severe mainly because of the instrumental advancement, especially the time of flight inelastic neutron scattering techniques. Before presenting the details, it is worth introducing the recent work which demonstrates detailed characterizations of phonons in MnSi, as in Ref. [16]. Fig. 6.5 summarizes the observed phonon dispersion along high symmetry directions, which display good agreements between experimental results and theoretical calculations. There are some key features of phonons that can be utilized later.

- **Acoustic phonons below $E = 20$ meV**

Well-behaved acoustic phonons (two transverse and one longitudinal) exist below $E = \sim 20$ meV. The dispersion relations are well characterized and thus can be utilized to separate the phonon and spin wave contributions. Notice that phonons retain higher velocity along the [1,1,1] direction compared to other directions.

- **Optical phonons exist in energy between [20 43] and [48 56] meV**

Optical phonons dispersing like flat bands exist in the energy range of [20 43] and [48 56] meV. These phonon components are hard to characterize and therefore could severely affect the experimental interpretations in these energy ranges. However, there is a small window between [44 48] meV, free of optical phonons. This tiny window could potentially be quite useful.

- **Phonon cut-off above $E \approx 60$ meV**

Although no experimental supports in this work, the calculations indicates that the phonon cut-off energy is about 60 meV. If there is any magnetic excitations survive above this energy, it could be easily disentangled from phonon

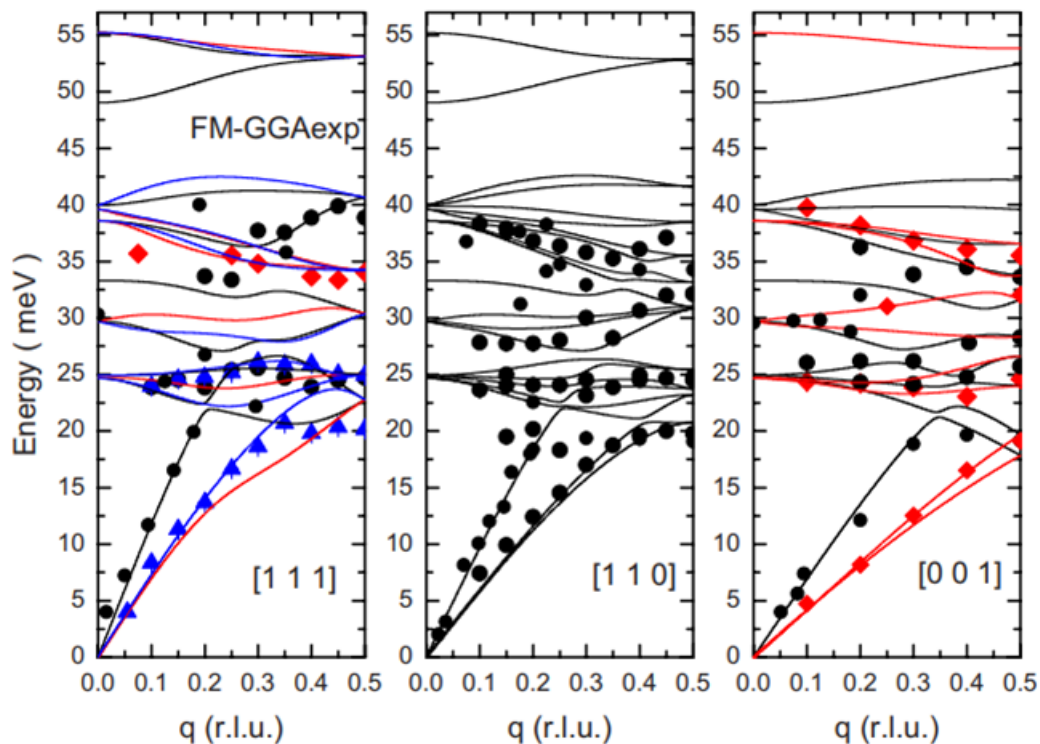


Figure 6.5: Measured (symbols with colors correspond to different symmetries of the phonon modes) and calculated (solid lines) phonon frequencies in MnSi at $T = 15$ K. Curves obtained from spin polarized GGA calculations using the experimental value of the lattice constant while optimizing the positions of the Mn and Si atoms in the unit cell. Adopted from [16].

contributions since there is zero contribution.

6.3 Experimental details

Unpolarized inelastic neutron scattering experiments were performed on a gigantic MnSi single crystal with a total mass of ~ 52 grams at SEQUOIA at SNS, adopting a direct geometry time of flight chopper spectrometer. Data was collected by rotating the sample by more than 180° with a typical step size of 0.5° with different incident energies $E_i = 18, 30, 70, 150, 300$ and 700 meV, respectively. The typical energy resolution is about $3 \sim 5\%$ of the incident energy. At each incident energy, the total count time is more than 15 hours. Data was collected at different temperatures, with 5 K for all of incident energies.

6.4 Experimental results

Note: since this work is still not published by the time of writing, some of the details are not presented. The work is focusing on the high energy excitation, the details of the low energy excitations are relevant, for instance the helimagnons.

6.4.1 Separation of phonon contributions

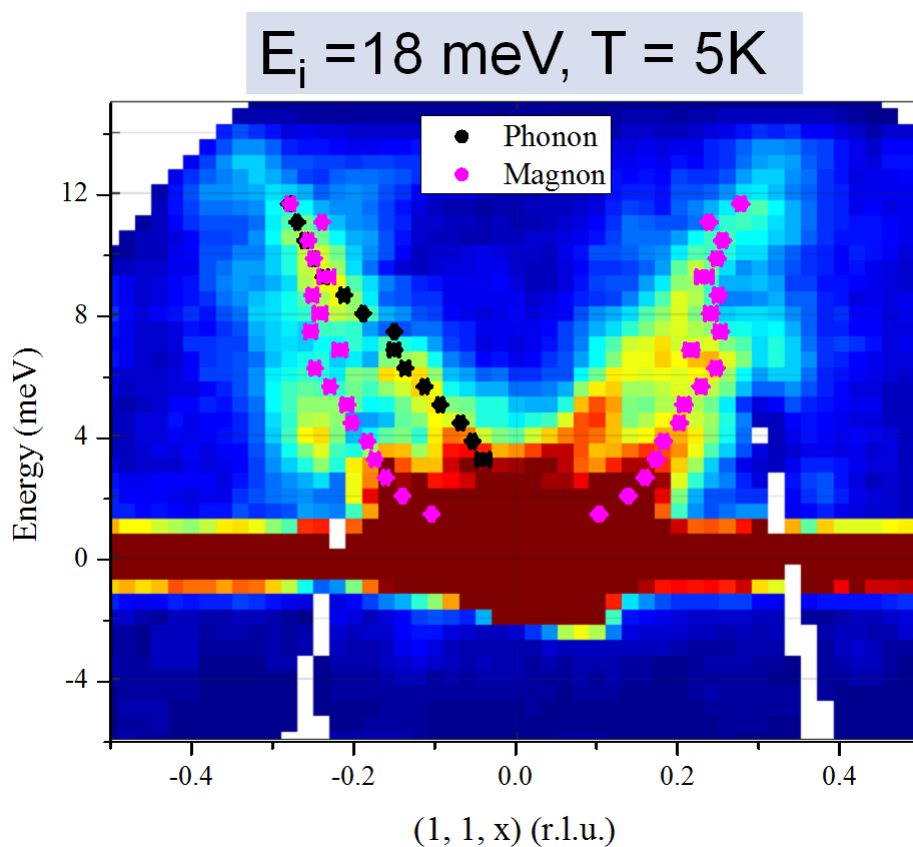


Figure 6.6: Raw inelastic neutron scattering (INS) data of MnSi, scanned along $[0,0,1]$ direction around the $(1,1,0)$ zone with the incident energy $E_i = 18$ meV. Data was collected at 5 K without external field. Phonon dispersions are marked by black symbols, obtained by performing the detailed constant E scans. The magenta symbols represent the spin wave dispersions obtained by constant E scans of the map.

Below $E = 20$ meV, the phonon and magnon contributions can be well separated. Fig. 6.6 shows the INS data of MnSi, scanned along $[0,0,1]$ direction around the $(1,1,0)$ zone with the incident energy $E_i = 18$ meV, collected at 5 K without

any external field. It is apparent there are two branches of dispersions, with one corresponds to spin wave dispersion and the other phonon contribution. The two components are generally well separated. By doing the constant E or Q scans, the detailed dispersing relations can be obtained. The colored symbols show the dispersions obtained by constant E scans, where black symbols represent the phonon contribution and magenta symbols represent the spin wave dispersions.

Above $E = 20$ meV, the phonon contributions are hard to subtract. But the experimental data show some clean windows free of phonons, exactly as mentioned in section 6.2.3, which can be utilized to characterize the high energy magnetic excitations.

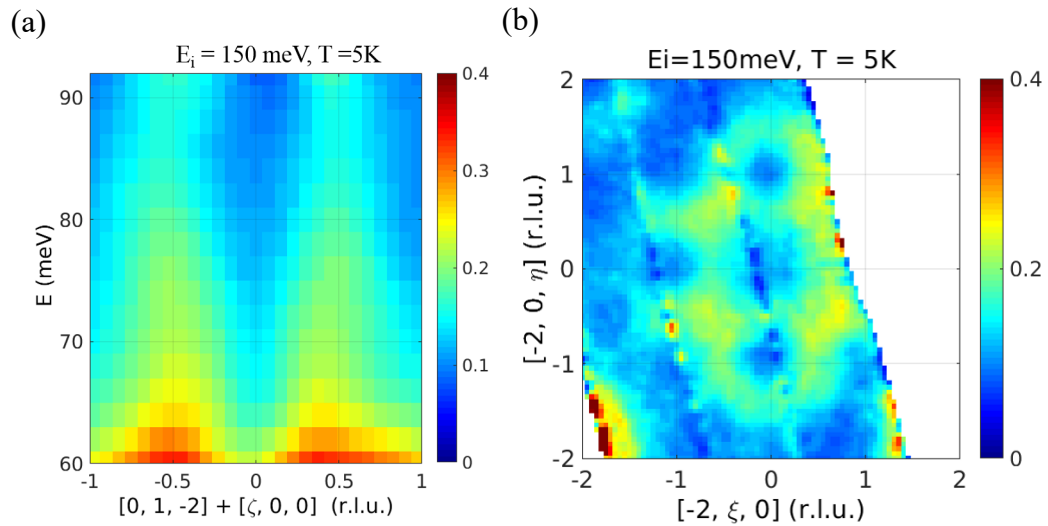


Figure 6.7: INS data of MnSi, collected with the incident energy $E_i = 150$ meV at 5 K. (a) Momentum-energy map along the $[1,0,0]$ direction around the $(0, 1 -2)$ zone, highlighting the "pillar" like magnetic signals. (b) Constant E slices with H fixed to -2. Since there is little dispersion along momentum direction, the energy is integrated from 66 to 116 meV, highlighting the broad ring like features in the KL plane.

Fig. 6.7 shows the INS data of MnSi, collected with the incident energy of 150 meV. To better highlight the features, only the data with energy above the phonon cut-off energy are shown, which clearly indicates the existence of extremely damped and broad magnetic scattering signals. Fig. 6.7(a) shows the "pillar" like magnetic signals from the momentum-energy map along the $[1,0,0]$ direction around the $(0, 1 -2)$ zone, with the dispersion velocity approaching infinity, *i.e.* dispersion continues

along E direction only. Fig. 6.7(b) shows the constant E slices with H fixed to -2. Since there is little dispersion along momentum direction, the energy is integrated from 66 to 116 meV, highlighting the broad ring like features in the KL plane.

6.4.2 High energy magnetic excitations in MnSi

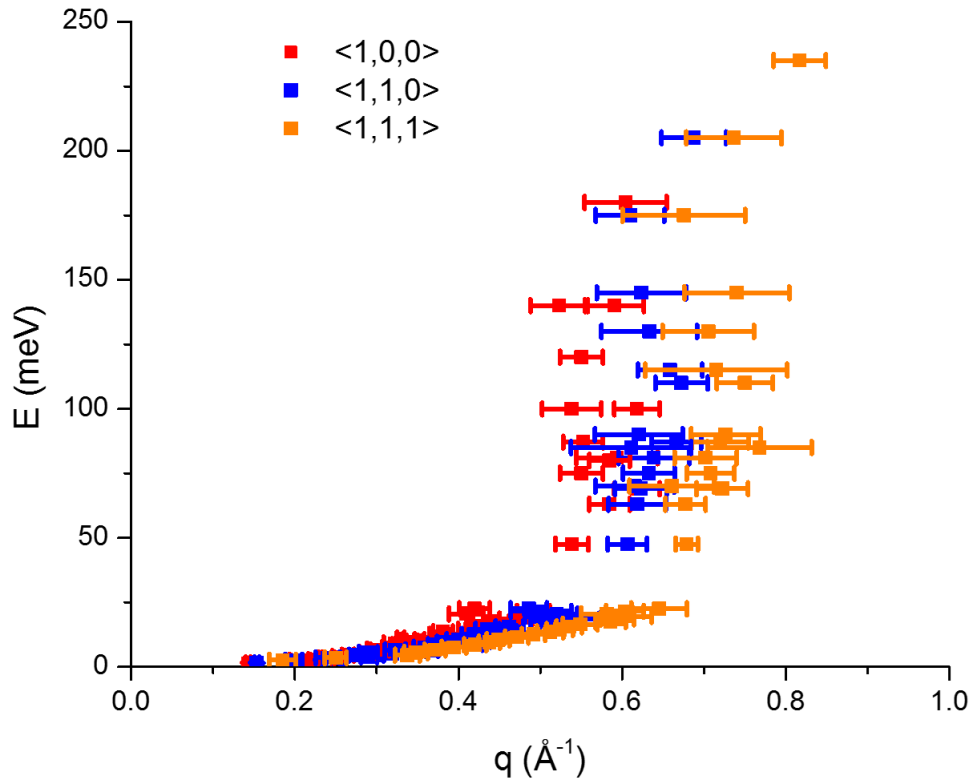


Figure 6.8: Anisotropic spin wave dispersions in MnSi at 5 K, with a combination of data from various incident energies. The "chimney" or "pillar" effect is apparent.

Anisotropic spin wave dispersions in MnSi at 5 K are shown in Fig. 6.8, resulting from a combination of INS data collected with different incident energies. This figure illustrates some important features that are distinct from linear spin wave modes encountered in localized moment systems, although some similarities exist as well.

- **Low q low E dispersions:** $E = \Delta + Dq^2$

The low q dispersions follow q^2 dependence, which are already shown in Ref.

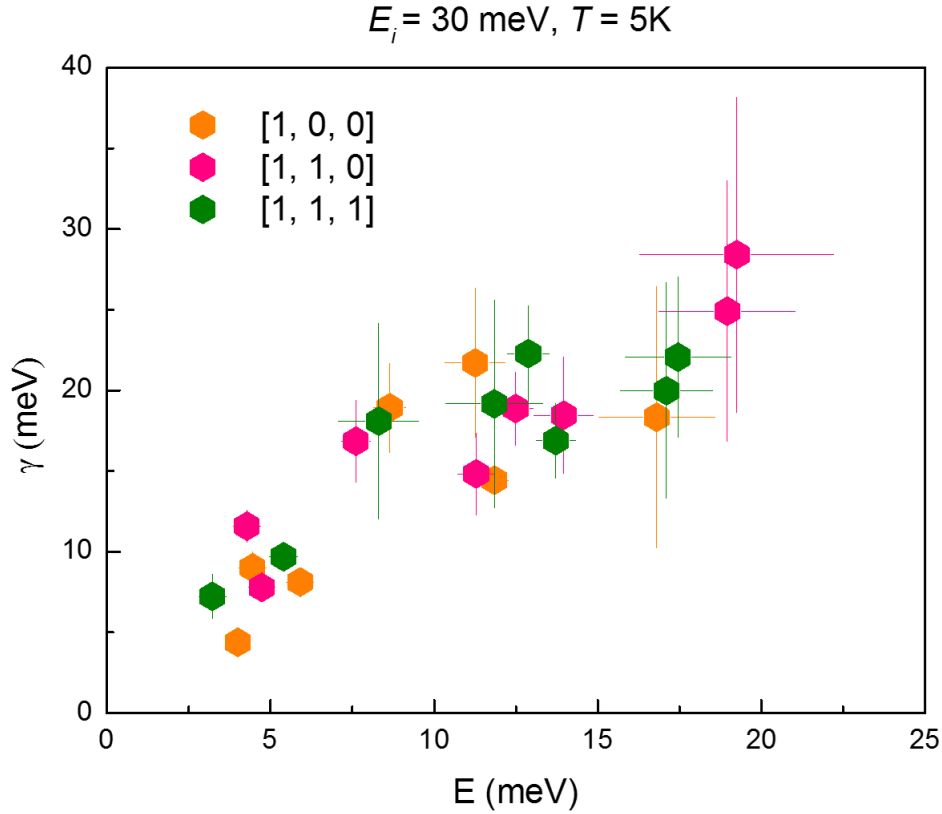


Figure 6.9: Energy dependent damping coefficients at 5 K. Damped simple harmonic oscillators are adopted to fit the constant Q scans.

[15]. For instance, along $\langle 1,0,0 \rangle$ direction, the fit to our data indicates $D = 63 \pm 4 \text{ meV } \text{\AA}^2$, which is close to reported spin stiffness constant $D = 50 \pm 2 \text{ meV } \text{\AA}^2$ in Ref. [15], given that our resolution is not as high since the larger q regime is our focus.

- **Strong damping**

Above the Stoner boundary, the spin wave excitations are becoming increasingly damped. As shown in Fig. 6.9, the damping constants are shown below energy $E = 20 \text{ meV}$. Even at this small energy scale, the maximum damping constant is about 30 meV , which is 1.5 times the corresponding scale of spin wave energy. This number is much larger than other localized or quasi-localized systems, such as CaFe_2As_2 [202], demonstrating the itinerant nature of excitations.

- **Intensity survives at large E , which is at least 240 meV**

The experimental data indicates the magnetic excitations survive at least up to 240 meV in energy, which is more than one order of magnitude higher than what was established in Ref. [15].

- **Critical regime beyond q_c or E_c**

It is apparent from the dispersion relations there are critical limits, beyond which the dispersions are in a distinctly different regime. For instance, along the $\langle 1,1,1 \rangle$ direction (yellow symbols), $q_c \approx 0.65 \text{ \AA}$. Beyond this point, the dispersion resembles "chimney" or "pillar", where it only move forward along the energy direction. This clearly indicates a transition, which renders the dispersion "truly" itinerant. This behavior is similarly observed along other high symmetry directions as well, with different critical values in reduced momentum.

6.4.3 Local dynamic susceptibility

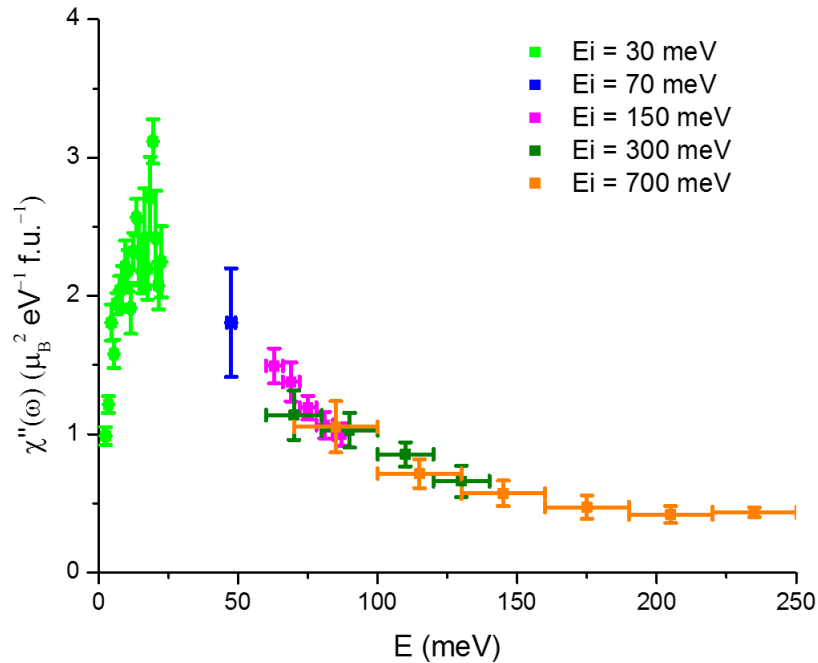


Figure 6.10: Local dynamic susceptibility of MnSi at 5K.

The existence of a transition to another regime is also indicated from the local dynamic susceptibility, which is defined as:

$$\chi''(\omega) = \frac{\int \chi''(\mathbf{Q}, \omega) d\mathbf{Q}}{\int d\mathbf{Q}} \quad (6.2)$$

The peak energy scale in Fig. 6.10 is about 20~40 meV, which is exact the critical energy scale shown in Fig. 6.8. Therefore, our data establishes another potential energy scale, that lies in energy between 20 to 40 meV and strongly renormalize the spin wave excitations.

6.5 Discussion

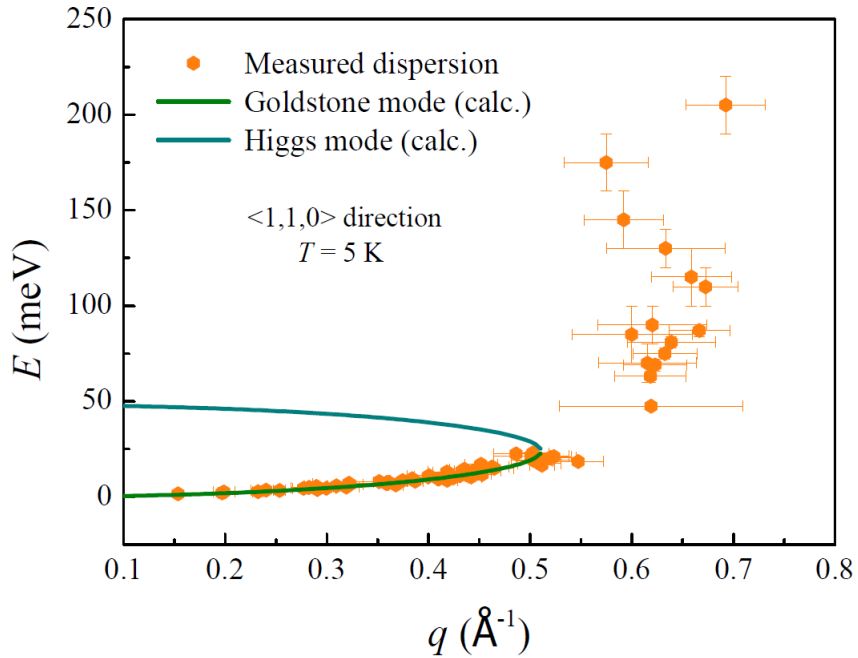


Figure 6.11: Magnetic dispersion relation along $\langle 1, 1, 0 \rangle$ direction in MnSi, collected at 5 K (orange symbols). The generalized ferromagnetic Fermi liquid theory (FFLT) for itinerant ferromagnets are applied to fit the data with two branches of collective modes, *i.e.* gapless Goldstone mode (dark green line) and gapped Higgs amplitude mode (dark cyan line). Spin wave stiffness constant D is obtained from fit to the low-lying Goldstone mode in the small q limit. The fit parameters $\Delta_{\text{Higgs}} = 48$ meV, and $D = 46$ meV \AA^2 .

The generalized ferromagnetic Fermi liquid theory (FFLT) for itinerant ferromagnets, from which Higgs amplitude mode is predicted in MnSi [198, 199], is applied to account for the experimental observations. The generalized theory pro-

pose that both the Goldstone mode and Higgs mode can be described by the same equation

$$E^2 - \Delta_{\text{Higgs}}E + (D \cdot \Delta_{\text{Higgs}})q^2 = 0 \quad (6.3)$$

where both Δ_{Higgs} and $D \cdot \Delta_{\text{Higgs}}$ can be expressed by Fermi liquid parameters. D is the spin wave stiffness constant and can be adjusted to match the experimental value. Δ_{Higgs} is the Higgs gap. Notice that this quadratic equation has two branches of coherent solutions, which are given by:

$$E_{\text{Goldstone}} = \frac{\Delta_{\text{Higgs}} - \sqrt{\Delta_{\text{Higgs}}^2 - 4(D \cdot \Delta_{\text{Higgs}})q^2}}{2} \quad (6.4)$$

$$E_{\text{Higgs}} = \frac{\Delta_{\text{Higgs}} + \sqrt{\Delta_{\text{Higgs}}^2 - 4(D \cdot \Delta_{\text{Higgs}})q^2}}{2}$$

These two branches of solutions correspond to collective Goldstone and Higgs modes only when

$$\Delta_{\text{Higgs}} - 4Dq^2 \geq 0 \quad (6.5)$$

Therefore, there is a critical value for reduced momentum, which satisfies

$$\Delta_{\text{Higgs}} - 4Dq_c^2 = 0 \quad (6.6)$$

or

$$q_c = \frac{1}{2} \sqrt{\frac{\Delta_{\text{Higgs}}}{D}} \quad (6.7)$$

Since the Higgs gap can not be determined experimentally for the time being, this parameter can be adjusted to match the observed dispersing relation of the Goldstone mode in experiments. Also, since this model does not contain any detailed microscopic information, it can not explain the anisotropic magnetic dispersion relations established before. Therefore, the theory is applied to the dispersion along the $\langle 1, 1, 0 \rangle$ direction, as shown in Fig. 6.11. The overall fit is very satis-

fying, with the fit parameters $\Delta_{\text{Higgs}} = 48 \text{ meV}$, and $D = 46 \text{ meV \AA}^2$. The calculated $q_c = 0.505 \text{ \AA}^{-1}$.

When q cross the boundary q_c , *i.e.* $q > q_c$, from Eq. 6.3 two incoherent solutions can be realized instead, which follow

$$E = \frac{\Delta_{\text{Higgs}}}{2} \pm i \sqrt{(D \cdot \Delta_{\text{Higgs}})q^2 - \frac{\Delta_{\text{Higgs}}^2}{4}} \quad (6.8)$$

Therefore, the two modes in the $q > q_c$ regime are not prorogating, since the real part is independent of q . The solutions in this scenario also agree with the experimental observed "chimney" effect.

6.6 Conclusions

The inelastic neutron scattering experiment on MnSi demonstrates anisotropic dispersion relations with strong damping effects. Our data establishes that the intensity survives at least up to 240 meV in energy, which is more than one order of magnitude higher than expected [15]. Our data also indicates the existence of critical regimes, beyond which the excitation spectrum are "chimney" like, with no prorogation along momentum direction. The simple generalized FFLT can account for the essential features observed in experiments.

Chapter 7

Conclusions and perspective

The magnetic properties of two prototypical magnetic compounds where spin-orbit coupling plays a prominent role, each falling into the opposite extremes, *i.e.*, the spin-orbit coupled Mott insulator Sr214 described by the localized Heisenberg model and the itinerant helical (nearly-ferromagnetic) metal MnSi pictured with band or Stoner magnetism.

In Sr214, the spin orbit coupled Mott state is perturbed through electron doping and isovalent doping. In the former case, the spin-orbit assisted $J_{\text{eff}} = \frac{1}{2}$ collapses with electron doping. From the detailed study through a combination of techniques such as transport, magnetization, X-ray and neutron scattering, the magnetic phase diagram is proposed. Basically, the data indicates that the long range canted AF order evolves with increasing doping, to short range order, and then to a unidirectional spin density wave state above the critical doping level. The phase diagram based on the experimental observations is reminiscent of the phase diagram in the monolayer cuprate $(\text{La}_{1-x}\text{Sr}_x)_2\text{CuO}_4$. Therefore, our data establishes the link and supports the conjecture that the quenched Mott phases in electron-doped Sr_2IrO_4 and hole-doped La_2CuO_4 support common competing electronic phases.

The spin-orbit Mott insulating state survives the relatively weak perturbation to the structure driven via isovalent Ca impurities within the lattice. However, an anomalous enhancement of the net ferromagnetic moment results with Ca substitution, suggestive of a decoupling between the in-plane canted antiferromagnetism and the in-plane IrO_6 octahedral rotation. Furthermore, the Ca substitution in the

full range demonstrates diversified ground states inhabiting numerous lattice geometries, which can be utilized for realizing desired ground states.

Although the Mott state in Sr214 collapses with electron doping, the chemical solubility severely limits the future realization of proposed superconducting states, therefore it is necessary to seek another route of introducing more carriers into the systems, such as ionic gating. Alternatively, other external parameters can be applied to the same system simultaneously which could potentially bring the system closer to the expected superconducting regime.

In the second part, high energy inelastic neutron scattering experiments are performed to explore the prototypical itinerant helimagnet MnSi. The Stoner continuum in its magnetic excitation spectrum is observed up to at least ~ 240 meV, which is surprisingly one order of magnitude larger than the previous installment [15]. More importantly, our data indicates the existence of threshold values of q_c (or E_c), beyond which the excitation spectrum resembles "chimney" or "pillar" with no prorogation along the energy direction only. The simple generalized FFLT, which contains no much microscopic details, can account for the essential features observed in experiments.

Although with no sold evidence proving the existence of Higgs mode as proposed, the good agreement between the experiment and theory suggests the valuable role of Higgs amplitude excitation, which is crucial for the emergence of "chimney"-like spectrum, crossing the threshold q_c (or E_c). Our experimental work complete the picture of magnetic excitation in the prototypical itinerant helimagnet and anticipate the observed phenomena can be generalized to other itinerant systems. A few itinerant candidates that worth the attentions are ZrZn₂, Sc₃In and TiAu [3]. This will be the future direction for explorations.

Bibliography

- [1] William Witczak-Krempa, Gang Chen, Yong Baek Kim, and Leon Balents. Correlated Quantum Phenomena in the Strong Spin-Orbit Regime. *Annual Review of Condensed Matter Physics*, 5(1):57–82, mar 2014.
- [2] T Moriya. *Spin Fluctuations in Itinerant Electron Magnetism*. Springer, Berlin, 1985.
- [3] J M Santiago, C-L Huang, and E Morosan. Itinerant magnetic metals. *Journal of Physics: Condensed Matter*, 29(37):373002, 2017.
- [4] Yoshinori Takahashi. *Spin Fluctuation Theory of Itinerant Electron Magnetism*. Springer, Berlin, 2013.
- [5] <https://www.qdusa.com/products/index.html>.
- [6] JM Tranquada G Shirane, SM Shapiro. *Neutron Scattering with a Triple-Axis Spectrometer*. Cambridge University Press, 2002.
- [7] <https://neutrons.ornl.gov/fietax>.
- [8] G E Granroth, A I Kolesnikov, T E Sherline, J P Clancy, K A Ross, J P C Ruff, B D Gaulin, and S E Nagler. SEQUOIA: A Newly Operating Chopper Spectrometer at the SNS. *Journal of Physics: Conference Series*, 251(1):012058, 2010.
- [9] D McMorrow J Als-Nielsen. *Elements of modern X-ray physics*. Clarendon Press; Oxford (UK), 1984.

- [10] Lecture note from National School on Neutron and X-Ray Scattering: <https://neutrons.ornl.gov/nxs>.
- [11] Xiang Chen, Tom Hogan, D. Walkup, Wenwen Zhou, M. Pokharel, Mengliang Yao, Wei Tian, Thomas Z. Ward, Y. Zhao, D. Parshall, C. Opeil, J. W. Lynn, Vidya Madhavan, and Stephen D. Wilson. Influence of electron doping on the ground state of $(\text{Sr}_{1-x}\text{La}_x)_2\text{IrO}_4$. *Phys. Rev. B*, 92:075125, Aug 2015.
- [12] H. Gretarsson, N. H. Sung, J. Porras, J. Bertinshaw, C. Dietl, Jan A. N. Bruin, A. F. Bangura, Y. K. Kim, R. Dinnebier, Jungho Kim, A. Al-Zein, M. Moretti Sala, M. Krisch, M. Le Tacon, B. Keimer, and B. J. Kim. Persistent Paramagnons Deep in the Metallic Phase of $\text{Sr}_{2-x}\text{La}_x\text{IrO}_4$. *Phys. Rev. Lett.*, 117:107001, Sep 2016.
- [13] Koichi Momma and Fujio Izumi. VESTA3 for three-dimensional visualization of crystal, volumetric and morphology data. *Journal of Applied Crystallography*, 44(6):1272–1276, Dec 2011.
- [14] S. Mühlbauer, B. Binz, F. Jonietz, C. Pfleiderer, A. Rosch, A. Neubauer, R. Georgii, and P. Böni. Skyrmion Lattice in a Chiral Magnet. *Science*, 323(5916):915–919, 2009.
- [15] Y. Ishikawa, G. Shirane, J. A. Tarvin, and M. Kohgi. Magnetic excitations in the weak itinerant ferromagnet MnSi. *Phys. Rev. B*, 16:4956–4970, Dec 1977.
- [16] D. Lamago, E. S. Clementyev, A. S. Ivanov, R. Heid, J.-M. Mignot, A. E. Petrova, and P. A. Alekseev. Lattice dynamics in the itinerant helical magnet MnSi. *Phys. Rev. B*, 82:144307, Oct 2010.
- [17] Jeffrey G. Rau, Eric Kin-Ho Lee, and Hae-Young Kee. Spin-Orbit Physics Giving Rise to Novel Phases in Correlated Systems: Iridates and Related Materials. *Annual Review of Condensed Matter Physics*, 7(1):195–221, 2016.

- [18] Antoine Georges, Luca de' Medici, and Jernej Mravlje. Strong Correlations from Hunds Coupling. *Annual Review of Condensed Matter Physics*, 4(1):137–178, 2013.
- [19] Vladimir I. Anisimov, Jan Zaanen, and Ole K. Andersen. Band theory and Mott insulators: Hubbard U instead of Stoner I. *Phys. Rev. B*, 44:943–954, Jul 1991.
- [20] Han-Jin Noh, B J Kim, S-J Oh, J-H Park, H-J Lin, C T Chen, Y S Lee, K Yamaura, and E Takayama-Muromachi. Comparative study of the electronic structures of SrMO₃ (M = Ti, V, Mn, Fe, and Co; M = Zr, Mo, Ru, and Rh) by O 1s X-ray absorption spectroscopy. *Journal of Physics: Condensed Matter*, 20(48):485208, 2008.
- [21] David C. Wallace and Tyrel M. McQueen. New honeycomb iridium(v) oxides: NaIrO₃ and Sr₃CaIr₂O₉. *Dalton Trans.*, 44:20344–20351, 2015.
- [22] Patrick A. Lee, Naoto Nagaosa, and Xiao-Gang Wen. Doping a Mott insulator: Physics of high-temperature superconductivity. *Rev. Mod. Phys.*, 78:17–85, Jan 2006.
- [23] J. G. Bednorz and K. A. Müller. Possible high T_c superconductivity in the Ba-La-Cu-O system. *Zeitschrift für Physik B Condensed Matter*, 64(2):189–193, Jun 1986.
- [24] Warren E. Pickett. Electronic structure of the high-temperature oxide superconductors. *Rev. Mod. Phys.*, 61:433–512, Apr 1989.
- [25] M. A. Kastner, R. J. Birgeneau, G. Shirane, and Y. Endoh. Magnetic, transport, and optical properties of monolayer copper oxides. *Rev. Mod. Phys.*, 70:897–928, Jul 1998.
- [26] B Keimer, S A Kivelson, M R Norman, S Uchida, and J Zaanen. From quantum matter to high-temperature superconductivity in copper oxides. *Nature*, 518(7538):179–186, 2014.

- [27] G.H. Jonker and J.H. Van Santen. Ferromagnetic compounds of manganese with perovskite structure. *Physica*, 16(3):337 – 349, 1950.
- [28] Leon Balents. Spin liquids in frustrated magnets. *Nature*, 464(7286):199–208, mar 2010.
- [29] Yi Zhou, Kazushi Kanoda, and Tai-Kai Ng. Quantum spin liquid states. *Rev. Mod. Phys.*, 89:025003, Apr 2017.
- [30] B. J. Kim, Hosub Jin, S. J. Moon, J.-Y. Kim, B.-G. Park, C. S. Leem, Jaejun Yu, T. W. Noh, C. Kim, S.-J. Oh, J.-H. Park, V. Durairaj, G. Cao, and E. Rotenberg. Novel $J_{\text{eff}} = 1/2$ Mott State Induced by Relativistic Spin-Orbit Coupling in Sr_2IrO_4 . *Phys. Rev. Lett.*, 101:076402, Aug 2008.
- [31] B. J. Kim, H. Ohsumi, T. Komesu, S. Sakai, T. Morita, H. Takagi, and T. Arima. Phase-Sensitive Observation of a Spin-Orbital Mott State in Sr_2IrO_4 . *Science*, 323(5919):1329–1332, 2009.
- [32] Electron correlations in narrow energy bands. *Proceedings of the Royal Society of London A: Mathematical, Physical and Engineering Sciences*, 276(1365):238–257, 1963.
- [33] R. Coldea, S. M. Hayden, G. Aeppli, T. G. Perring, C. D. Frost, T. E. Mason, S.-W. Cheong, and Z. Fisk. Spin Waves and Electronic Interactions in La_2CuO_4 . *Phys. Rev. Lett.*, 86:5377–5380, Jun 2001.
- [34] N. S. Headings, S. M. Hayden, R. Coldea, and T. G. Perring. Anomalous High-Energy Spin Excitations in the High- T_c Superconductor-Parent Antiferromagnet La_2CuO_4 . *Phys. Rev. Lett.*, 105:247001, Dec 2010.
- [35] Efstratios Manousakis. The spin- $1/2$ Heisenberg antiferromagnet on a square lattice and its application to the cuprous oxides. *Rev. Mod. Phys.*, 63:1–62, Jan 1991.
- [36] Pengcheng Dai. Antiferromagnetic order and spin dynamics in iron-based superconductors. *Rev. Mod. Phys.*, 87:855–896, Aug 2015.

- [37] F. Ye, Pengcheng Dai, J. A. Fernandez-Baca, D. T. Adroja, T. G. Perring, Y. Tomioka, and Y. Tokura. Spin waves throughout the Brillouin zone and magnetic exchange coupling in the ferromagnetic metallic manganites $\text{La}_{1-x}\text{Ca}_x\text{MnO}_3$ ($x = 0.25, 0.30$). *Phys. Rev. B*, 75:144408, Apr 2007.
- [38] Jungho Kim, D. Casa, M. H. Upton, T. Gog, Young-June Kim, J. F. Mitchell, M. van Veenendaal, M. Daghofer, J. van den Brink, G. Khaliullin, and B. J. Kim. Magnetic Excitation Spectra of Sr_2IrO_4 Probed by Resonant Inelastic X-Ray Scattering: Establishing Links to Cuprate Superconductors. *Phys. Rev. Lett.*, 108:177003, Apr 2012.
- [39] Jungho Kim, A. H. Said, D. Casa, M. H. Upton, T. Gog, M. Daghofer, G. Jackeli, J. van den Brink, G. Khaliullin, and B. J. Kim. Large Spin-Wave Energy Gap in the Bilayer Iridate $\text{Sr}_3\text{Ir}_2\text{O}_7$: Evidence for Enhanced Dipolar Interactions Near the Mott Metal-Insulator Transition. *Phys. Rev. Lett.*, 109:157402, Oct 2012.
- [40] RM White. *Quantum theory of magnetism*. Springer, Berlin, 1983.
- [41] Stephen Blundell. *Magnetism in condensed matter*. Oxford University Press, 2001.
- [42] Peter Mohn. *Magnetism in the solid state: an introduction*. Springer, Berlin, 2006.
- [43] I. Dzyaloshinsky. A thermodynamic theory of weak ferromagnetism of anti-ferromagnetics. *Journal of Physics and Chemistry of Solids*, 4(4):241 – 255, 1958.
- [44] Tôru Moriya. Anisotropic Superexchange Interaction and Weak Ferromagnetism. *Phys. Rev.*, 120:91–98, Oct 1960.
- [45] Chetan Dhital, Tom Hogan, Z. Yamani, Clarina de la Cruz, Xiang Chen, Sovit Khadka, Zhensong Ren, and Stephen D. Wilson. Neutron scattering

- study of correlated phase behavior in Sr_2IrO_4 . *Phys. Rev. B*, 87:144405, Apr 2013.
- [46] Feng Ye, Songxue Chi, Bryan C. Chakoumakos, Jaime A. Fernandez-Baca, Tongfei Qi, and G. Cao. Magnetic and crystal structures of Sr_2IrO_4 : A neutron diffraction study. *Phys. Rev. B*, 87:140406, Apr 2013.
- [47] P Bak and M H Jensen. Theory of helical magnetic structures and phase transitions in MnSi and FeGe. *Journal of Physics C: Solid State Physics*, 13(31):L881, 1980.
- [48] O. Nakanishi, A. Yanase, A. Hasegawa, and M. Kataoka. The origin of the helical spin density wave in MnSi. *Solid State Communications*, 35(12):995–998, 1980.
- [49] Steven T. Bramwell and Michel J. P. Gingras. Spin Ice State in Frustrated Magnetic Pyrochlore Materials. *Science*, 294(5546):1495–1501, 2001.
- [50] Sae Hwan Chun, Jong-Woo Kim, Jungho Kim, H Zheng, Constantinos C. Stoumpos, C. D. Malliakas, J. F. Mitchell, Kavita Mehlawat, Yogesh Singh, Y Choi, T Gog, A. Al-Zein, M. Moretti Sala, M Krisch, J Chaloupka, G Jackeli, G Khaliullin, and B J Kim. Direct evidence for dominant bond-directional interactions in a honeycomb lattice iridate Na_2IrO_3 . *Nature Physics*, 11(6):462–466, may 2015.
- [51] A. Banerjee, C. A. Bridges, J. Q. Yan, A. A. Aczel, L. Li, M. B. Stone, G. E. Granroth, M. D. Lumsden, Y. Yiu, J. Knolle, S. Bhattacharjee, D. L. Kovrizhin, R. Moessner, D. A. Tennant, D. G. Mandrus, and S. E. Nagler. Proximate Kitaev quantum spin liquid behaviour in a honeycomb magnet. *Nature Materials*, 15:733, 2016.
- [52] D. J. Scalapino. A common thread: The pairing interaction for unconventional superconductors. *Rev. Mod. Phys.*, 84:1383–1417, Oct 2012.

- [53] Dmytro Pesin and Leon Balents. Mott physics and band topology in materials with strong spin-orbit interaction. *Nature Physics*, 6(5):376–381, 2010.
- [54] Y. Ishikawa, Y. Noda, Y. J. Uemura, C. F. Majkrzak, and G. Shirane. Paramagnetic spin fluctuations in the weak itinerant-electron ferromagnet MnSi. *Phys. Rev. B*, 31:5884–5893, May 1985.
- [55] Antoine Georges, Gabriel Kotliar, Werner Krauth, and Marcelo J. Rozenberg. Dynamical mean-field theory of strongly correlated fermion systems and the limit of infinite dimensions. *Rev. Mod. Phys.*, 68:13–125, Jan 1996.
- [56] Julian L. Schmehrer and Stephen D. Wilson. Active Crystal Growth Techniques for Quantum Materials. *Annual Review of Materials Research*, 47(1):153–174, 2017.
- [57] Xiang Chen and Stephen D. Wilson. Structural evolution and electronic properties of $(\text{Sr}_{1-x}\text{Ca}_x)_{2-y}\text{IrO}_{4+z}$ spin-orbit-assisted insulators. *Phys. Rev. B*, 94:195115, Nov 2016.
- [58] GL Squires. *Introduction to the theory of thermal neutron scattering*. Cambridge University Press, 2012.
- [59] SW Lovesey. *Theory of neutron scattering from condensed matter*. Clarendon Press; Oxford (UK), 1984.
- [60] J. P. Hannon, G. T. Trammell, M. Blume, and Doon Gibbs. X-Ray Resonance Exchange Scattering. *Phys. Rev. Lett.*, 61:1245–1248, Sep 1988.
- [61] J. P. Hill and D. F. McMorrow. Resonant Exchange Scattering: Polarization Dependence and Correlation Function. *Acta Crystallographica Section A*, 52(2):236–244, Mar 1996.
- [62] J Fink, E Schierle, E Weschke, and J Geck. Resonant elastic soft X-ray scattering. *Reports on Progress in Physics*, 76(5):056502, 2013.

- [63] Luigi Paolasini. Resonant and magnetic X-ray diffraction by polarized synchrotron radiation. *Collection SFN*, 13:03002, 2014.
- [64] F. de Bergevin and M. Brunel. Diffraction of X-rays by magnetic materials. I. General formulae and measurements on ferro- and ferrimagnetic compounds. *Acta Crystallographica Section A*, 37(3):314–324, May 1981.
- [65] M. Blume. Magnetic scattering of X rays (invited). *Journal of Applied Physics*, 57(8):3615–3618, 1985.
- [66] L. Paolasini, C. Detlefs, C. Mazzoli, S. Wilkins, P. P. Deen, A. Bombardi, N. Kernavanois, F. de Bergevin, F. Yakhou, J. P. Valade, I. Breslavetz, A. Fondacaro, G. Pepellin, and P. Bernard. ID20: a beamline for magnetic and resonant X-ray scattering investigations under extreme conditions. *Journal of Synchrotron Radiation*, 14(4):301–312, Jul 2007.
- [67] Xiangang Wan, Ari M. Turner, Ashvin Vishwanath, and Sergey Y. Savrasov. Topological semimetal and Fermi-arc surface states in the electronic structure of pyrochlore iridates. *Phys. Rev. B*, 83:205101, May 2011.
- [68] G. Jackeli and G. Khaliullin. Mott Insulators in the Strong Spin-Orbit Coupling Limit: From Heisenberg to a Quantum Compass and Kitaev Models. *Phys. Rev. Lett.*, 102:017205, Jan 2009.
- [69] S. J. Moon, H. Jin, K. W. Kim, W. S. Choi, Y. S. Lee, J. Yu, G. Cao, A. Sumi, H. Funakubo, C. Bernhard, and T. W. Noh. Dimensionality-Controlled Insulator-Metal Transition and Correlated Metallic State in $5d$ Transition Metal Oxides $\text{Sr}_{n+1}\text{Ir}_n\text{O}_{3n+1}$ ($n = 1, 2, \text{ and } \infty$). *Phys. Rev. Lett.*, 101:226402, Nov 2008.
- [70] Itamar Kimchi and Ashvin Vishwanath. Kitaev-Heisenberg models for iridates on the triangular, hyperkagome, kagome, fcc, and pyrochlore lattices. *Phys. Rev. B*, 89:014414, Jan 2014.

- [71] Yogesh Singh and P. Gegenwart. Antiferromagnetic Mott insulating state in single crystals of the honeycomb lattice material Na_2IrO_3 . *Phys. Rev. B*, 82:064412, Aug 2010.
- [72] Atsuo Shitade, Hosho Katsura, Jan Kuneš, Xiao-Liang Qi, Shou-Cheng Zhang, and Naoto Nagaosa. Quantum Spin Hall Effect in a Transition Metal Oxide Na_2IrO_3 . *Phys. Rev. Lett.*, 102:256403, Jun 2009.
- [73] T. Takayama, A. Kato, R. Dinnebier, J. Nuss, H. Kono, L. S. I. Veiga, G. Fabbris, D. Haskel, and H. Takagi. Hyperhoneycomb Iridate $\beta\text{-Li}_2\text{IrO}_3$ as a Platform for Kitaev Magnetism. *Phys. Rev. Lett.*, 114:077202, Feb 2015.
- [74] K a Modic, Tess E Smidt, Itamar Kimchi, Nicholas P Breznay, Alun Biffin, Sungkyun Choi, Roger D Johnson, Radu Coldea, Pilanda Watkins-Curry, Gregory T McCandless, Julia Y Chan, Felipe Gandara, Z Islam, Ashvin Vishwanath, Arkady Shekhter, Ross D McDonald, and James G Analytis. Realization of a three-dimensional spin-anisotropic harmonic honeycomb iridate. *Nature communications*, 5(May):4203, 2014.
- [75] A. Biffin, R. D. Johnson, I. Kimchi, R. Morris, A. Bombardi, J. G. Analytis, A. Vishwanath, and R. Coldea. Noncoplanar and Counterrotating Incommensurate Magnetic Order Stabilized by Kitaev Interactions in $\gamma\text{-Li}_2\text{IrO}_3$. *Phys. Rev. Lett.*, 113:197201, Nov 2014.
- [76] Yoshihiko Okamoto, Minoru Nohara, Hiroko Aruga-Katori, and Hidenori Takagi. Spin-Liquid State in the $S = 1/2$ Hyperkagome Antiferromagnet $\text{Na}_4\text{Ir}_3\text{O}_8$. *Phys. Rev. Lett.*, 99:137207, Sep 2007.
- [77] Michael J. Lawler, Arun Paramakanti, Yong Baek Kim, and Leon Balents. Gapless Spin Liquids on the Three-Dimensional Hyperkagome Lattice of $\text{Na}_4\text{Ir}_3\text{O}_8$. *Phys. Rev. Lett.*, 101:197202, Nov 2008.
- [78] Rebecca Dally, Tom Hogan, Alex Amato, Hubertus Luetkens, Chris Baines, Jose Rodriguez-Rivera, Michael J. Graf, and Stephen D. Wilson. Short-

- Range Correlations in the Magnetic Ground State of $\text{Na}_4\text{Ir}_3\text{O}_8$. *Phys. Rev. Lett.*, 113:247601, Dec 2014.
- [79] Kazuyuki Matsuhira, Makoto Wakeshima, Yukio Hinatsu, and Seishi Takagi. Metal-Insulator Transitions in Pyrochlore Oxides $\text{Ln}_2\text{Ir}_2\text{O}_7$. *Journal of the Physical Society of Japan*, 80(9):094701, 2011.
- [80] S. Nakatsuji, Y. Machida, Y. Maeno, T. Tayama, T. Sakakibara, J. van Duijn, L. Balicas, J. N. Millican, R. T. Macaluso, and Julia Y. Chan. Metallic Spin-Liquid Behavior of the Geometrically Frustrated Kondo Lattice $\text{Pr}_2\text{Ir}_2\text{O}_7$. *Phys. Rev. Lett.*, 96:087204, Mar 2006.
- [81] Yo Machida, Satoru Nakatsuji, Shigeki Onoda, Takashi Tayama, and Toshiro Sakakibara. Time-reversal symmetry breaking and spontaneous Hall effect without magnetic dipole order. *Nature*, 463(7278):210–213, 2010.
- [82] Eric Yue Ma, Yong-Tao Cui, Kentaro Ueda, Shujie Tang, Kai Chen, Nobumichi Tamura, Phillip M. Wu, Jun Fujioka, Yoshinori Tokura, and Zhi-Xun Shen. Mobile metallic domain walls in an all-in-all-out magnetic insulator. *Science*, 350(6260):538–541, 2015.
- [83] M. K. Crawford, M. A. Subramanian, R. L. Harlow, J. A. Fernandez-Baca, Z. R. Wang, and D. C. Johnston. Structural and magnetic studies of Sr_2IrO_4 . *Phys. Rev. B*, 49:9198–9201, Apr 1994.
- [84] Q. Huang, J.L. Soubeyroux, O. Chmaissem, I. Natali Sora, A. Santoro, R.J. Cava, J.J. Krajewski, and W.F. Peck. Neutron Powder Diffraction Study of the Crystal Structures of Sr_2RuO_4 and Sr_2IrO_4 at Room Temperature and at 10 K. *Journal of Solid State Chemistry*, 112(2):355 – 361, 1994.
- [85] M.A. Subramanian, M.K. Crawford, and R.L. Harlow. Single crystal structure determination of double layered strontium iridium oxide $\text{Sr}_3\text{Ir}_2\text{O}_7$. *Materials Research Bulletin*, 29(6):645 – 650, 1994.

- [86] H. Okabe, M. Isobe, E. Takayama-Muromachi, A. Koda, S. Takeshita, M. Hiraiishi, M. Miyazaki, R. Kadono, Y. Miyake, and J. Akimitsu. Ba_2IrO_4 : A spin-orbit Mott insulating quasi-two-dimensional antiferromagnet. *Phys. Rev. B*, 83:155118, Apr 2011.
- [87] R. Arita, J. Kuneš, A. V. Kozhevnikov, A. G. Eguiluz, and M. Imada. *Ab initio* Studies on the Interplay between Spin-Orbit Interaction and Coulomb Correlation in Sr_2IrO_4 and Ba_2IrO_4 . *Phys. Rev. Lett.*, 108:086403, Feb 2012.
- [88] G. Cao, J.E. Crow, R.P. Guertin, P.F. Henning, C.C. Homes, M. Strongin, D.N. Basov, and E. Lochner. Charge density wave formation accompanying ferromagnetic ordering in quasi-one-dimensional BaIrO_3 . *Solid State Communications*, 113(11):657 – 662, 2000.
- [89] G. Cao, Y. Xin, C. S. Alexander, J. E. Crow, P. Schlottmann, M. K. Crawford, R. L. Harlow, and W. Marshall. Anomalous magnetic and transport behavior in the magnetic insulator $\text{Sr}_3\text{Ir}_2\text{O}_7$. *Phys. Rev. B*, 66:214412, Dec 2002.
- [90] G. Cao, J. Bolivar, S. McCall, J. E. Crow, and R. P. Guertin. Weak ferromagnetism, metal-to-nonmetal transition, and negative differential resistivity in single-crystal Sr_2IrO_4 . *Phys. Rev. B*, 57:R11039–R11042, May 1998.
- [91] Fa Wang and T. Senthil. Twisted Hubbard Model for Sr_2IrO_4 : Magnetism and Possible High Temperature Superconductivity. *Phys. Rev. Lett.*, 106:136402, Mar 2011.
- [92] Hiroshi Watanabe, Tomonori Shirakawa, and Seiji Yunoki. Monte Carlo study of an unconventional superconducting phase in Ir-oxide $J_{\text{eff}} = 1/2$ Mott insulators induced by carrier doping. *Physical Review Letters*, 110(2):027002, dec 2012.
- [93] Zi Yang Meng, Yong Baek Kim, and Hae-Young Kee. Odd-Parity Triplet Superconducting Phase in Multiorbital Materials with a Strong Spin-Orbit Coupling: Application to Doped Sr_2IrO_4 . *Phys. Rev. Lett.*, 113:177003, Oct 2014.

- [94] Yang Yang, Wan-Sheng Wang, Jin-Guo Liu, Hua Chen, Jian-Hui Dai, and Qiang-Hua Wang. Superconductivity in doped Sr_2IrO_4 : A functional renormalization group study. *Phys. Rev. B*, 89:094518, Mar 2014.
- [95] Y. K. Kim, N. H. Sung, J. D. Denlinger, and B. J. Kim. Observation of a d-wave gap in electron-doped Sr_2IrO_4 . *Nature Physics*, 12(1):37–41, oct 2015.
- [96] Y. J. Yan, M. Q. Ren, H. C. Xu, B. P. Xie, R. Tao, H. Y. Choi, N. Lee, Y. J. Choi, T. Zhang, and D. L. Feng. Electron-Doped Sr_2IrO_4 : An Analogue of Hole-Doped Cuprate Superconductors Demonstrated by Scanning Tunneling Microscopy. *Phys. Rev. X*, 5:041018, Nov 2015.
- [97] O. B. Korneta, Tongfei Qi, S. Chikara, S. Parkin, L. E. De Long, P. Schlottmann, and G. Cao. Electron-doped $\text{Sr}_2\text{IrO}_{4-\delta}$ ($0 \leq \delta \leq 0.04$): Evolution of a disordered $J_{\text{eff}} = \frac{1}{2}$ Mott insulator into an exotic metallic state. *Phys. Rev. B*, 82:115117, Sep 2010.
- [98] M. Ge, T. F. Qi, O. B. Korneta, D. E. De Long, P. Schlottmann, W. P. Crummett, and G. Cao. Lattice-driven magnetoresistivity and metal-insulator transition in single-layered iridates. *Phys. Rev. B*, 84:100402, Sep 2011.
- [99] T. F. Qi, O. B. Korneta, L. Li, K. Butrouna, V. S. Cao, Xiangang Wan, P. Schlottmann, R. K. Kaul, and G. Cao. Spin-orbit tuned metal-insulator transitions in single-crystal $\text{Sr}_2\text{Ir}_{1-x}\text{Rh}_x\text{O}_4$ ($0 \leq x \leq 1$). *Phys. Rev. B*, 86:125105, Sep 2012.
- [100] Y Klein and I Terasaki. Insight on the electronic state of Sr_2IrO_4 revealed by cationic substitutions. *Journal of Physics: Condensed Matter*, 20(29):295201, 2008.
- [101] J. S. Lee, Y. Krockenberger, K. S. Takahashi, M. Kawasaki, and Y. Tokura. Insulator-metal transition driven by change of doping and spin-orbit interaction in Sr_2IrO_4 . *Phys. Rev. B*, 85:035101, Jan 2012.

- [102] R. J. Cava, B. Batlogg, K. Kiyono, H. Takagi, J. J. Krajewski, W. F. Peck, L. W. Rupp, and C. H. Chen. Localized-to-itinerant electron transition in $\text{Sr}_2\text{Ir}_{1-x}\text{Ru}_x\text{O}_4$. *Phys. Rev. B*, 49:11890–11894, May 1994.
- [103] S. J. Yuan, S. Aswartham, J. Terzic, H. Zheng, H. D. Zhao, P. Schlottmann, and G. Cao. From $J_{\text{eff}} = 1/2$ insulator to p -wave superconductor in single-crystal $\text{Sr}_2\text{Ir}_{1-x}\text{Ru}_x\text{O}_4$ ($0 \leq x \leq 1$). *Phys. Rev. B*, 92:245103, Dec 2015.
- [104] J. C. Wang, S. Aswartham, Feng Ye, J. Terzic, H. Zheng, Daniel Haskel, Shalinee Chikara, Yong Choi, P. Schlottmann, Radu Custelcean, S. J. Yuan, and G. Cao. Decoupling of the antiferromagnetic and insulating states in Tb-doped Sr_2IrO_4 . *Phys. Rev. B*, 92:214411, Dec 2015.
- [105] D. Haskel, G. Fabbris, Mikhail Zhernenkov, P. P. Kong, C. Q. Jin, G. Cao, and M. van Veenendaal. Pressure Tuning of the Spin-Orbit Coupled Ground State in Sr_2IrO_4 . *Phys. Rev. Lett.*, 109:027204, Jul 2012.
- [106] D A Zocco, J J Hamlin, B D White, B J Kim, J R Jeffries, S T Weir, Y K Vohra, J W Allen, and M B Maple. Persistent non-metallic behavior in Sr_2IrO_4 and $\text{Sr}_3\text{Ir}_2\text{O}_7$ at high pressures. *Journal of Physics: Condensed Matter*, 26(25):255603, 2014.
- [107] N. H. Sung, H. Gretarsson, D. Proepper, J. Porras, M. Le Tacon, A. V. Boris, B. Keimer, and B. J. Kim. Crystal growth and intrinsic magnetic behaviour of Sr_2IrO_4 . *Philosophical Magazine*, 96(4):413–426, 2016.
- [108] S. Calder, G.-X. Cao, M. D. Lumsden, J. W. Kim, Z. Gai, B. C. Sales, D. Mandrus, and A. D. Christianson. Magnetic structural change of Sr_2IrO_4 upon Mn doping. *Phys. Rev. B*, 86:220403, Dec 2012.
- [109] S. Calder, J. W. Kim, G.-X. Cao, C. Cantoni, A. F. May, H. B. Cao, A. A. Aczel, M. Matsuda, Y. Choi, D. Haskel, B. C. Sales, D. Mandrus, M. D. Lumsden, and A. D. Christianson. Evolution of competing magnetic order in the $J_{\text{eff}} = 1/2$ insulating state of $\text{Sr}_2\text{Ir}_{1-x}\text{Ru}_x\text{O}_4$. *Phys. Rev. B*, 92:165128, Oct 2015.

- [110] Chetan Dhital, Tom Hogan, Wenwen Zhou, Xiang Chen, Zhensong Ren, Mani Pokharel, Yoshinori Okada, M. Heine, Wei Tian, Z. Yamani, C. Opeil, J. S. Helton, J. W. Lynn, Ziqiang Wang, Vidya Madhavan, and Stephen D. Wilson. Carrier localization and electronic phase separation in a doped spin-orbit-driven Mott phase in $\text{Sr}_3(\text{Ir}_{1-x}\text{Ru}_x)_2\text{O}_7$. *Nature Communications*, 5:1–7, 2014.
- [111] Junfeng He, T. Hogan, Thomas R. Mion, H. Hafiz, Y. He, J. D. Denlinger, S-K. Mo, C. Dhital, X. Chen, Qisen Lin, Y. Zhang, M. Hashimoto, H. Pan, D. H. Lu, M. Arita, K. Shimada, R. S. Markiewicz, Z. Wang, K. Kempa, M. J. Naughton, A. Bansil, S. D. Wilson, and Rui-Hua He. Spectroscopic evidence for negative electronic compressibility in a quasi-three-dimensional spin-orbit correlated metal. *Nature Materials*, 14(6):577–582, 2015.
- [112] John J. Randall, Lewis Katz, and Roland Ward. The Preparation of a Strontium-Iridium Oxide Sr_2IrO_4 . *Journal of the American Chemical Society*, 79(2):266–267, 1957.
- [113] D. H. Torchinsky, H. Chu, L. Zhao, N. B. Perkins, Y. Sizyuk, T. Qi, G. Cao, and D. Hsieh. Structural Distortion-Induced Magnetoelastic Locking in Sr_2IrO_4 Revealed through Nonlinear Optical Harmonic Generation. *Phys. Rev. Lett.*, 114:096404, Mar 2015.
- [114] Feng Ye, Xiaoping Wang, Christina Hoffmann, Jinchen Wang, Songxue Chi, Masaaki Matsuda, Bryan C. Chakoumakos, Jaime A. Fernandez-Baca, and G. Cao. Structure symmetry determination and magnetic evolution in $\text{Sr}_2\text{Ir}_{1-x}\text{Rh}_x\text{O}_4$. *Phys. Rev. B*, 92:201112, Nov 2015.
- [115] Jixia Dai, Eduardo Calleja, Gang Cao, and Kyle McElroy. Local density of states study of a spin-orbit-coupling induced Mott insulator Sr_2IrO_4 . *Phys. Rev. B*, 90:041102, Jul 2014.

- [116] John Nichols, Noah Bray-Ali, Armin Ansary, Gang Cao, and Kwok-Wai Ng. Tunneling into the Mott insulator Sr_2IrO_4 . *Phys. Rev. B*, 89:085125, Feb 2014.
- [117] S Boseggia, H C Walker, J Vale, R Springell, Z Feng, R S Perry, M Moretti Sala, H M Rønnow, S P Collins, and D F McMorrow. Locking of Iridium magnetic moments to the correlated rotation of Oxygen octahedra in Sr_2IrO_4 revealed by X-ray resonant scattering. *Journal of Physics: Condensed Matter*, 25(42):422202, 2013.
- [118] Tom Hogan, Z. Yamani, D. Walkup, Xiang Chen, Rebecca Dally, Thomas Z. Ward, M. P. M. Dean, John Hill, Z. Islam, Vidya Madhavan, and Stephen D. Wilson. First-Order Melting of a Weak Spin-Orbit Mott Insulator into a Correlated Metal. *Phys. Rev. Lett.*, 114:257203, Jun 2015.
- [119] Anderson Janotti, Bharat Jalan, Susanne Stemmer, and Chris G. Van de Walle. Effects of doping on the lattice parameter of SrTiO_3 . *Applied Physics Letters*, 100(26):262104, 2012.
- [120] A L Efros and B I Shklovskii. Coulomb gap and low temperature conductivity of disordered systems. *Journal of Physics C: Solid State Physics*, 8(4):L49, 1975.
- [121] N S Kini, A M Strydom, H S Jeevan, C Geibel, and S Ramakrishnan. Transport and thermal properties of weakly ferromagnetic Sr_2IrO_4 . *Journal of Physics: Condensed Matter*, 18(35):8205, 2006.
- [122] Ping Sheng, B. Abeles, and Y. Arie. Hopping Conductivity in Granular Metals. *Phys. Rev. Lett.*, 31:44–47, Jul 1973.
- [123] J. Wu, J. W. Lynn, C. J. Glinka, J. Burley, H. Zheng, J. F. Mitchell, and C. Leighton. Intergranular Giant Magnetoresistance in a Spontaneously Phase Separated Perovskite Oxide. *Phys. Rev. Lett.*, 94:037201, Jan 2005.

- [124] J. A. Mydosh. Spin glasses: Some recent experiments. *Hyperfine Interactions*, 31(1):347–362, Dec 1986.
- [125] K. Binder and A. P. Young. Spin glasses: Experimental facts, theoretical concepts, and open questions. *Rev. Mod. Phys.*, 58:801–976, Oct 1986.
- [126] Yoshinori Okada, Daniel Walkup, Hsin Lin, Chetan Dhital, Tay-Rong Chang, Sovit Khadka, Wenwen Zhou, Horng-Tay Jeng, Mandar Paranjape, Arun Bansil, Ziqiang Wang, Stephen D. Wilson, and Vidya Madhavan. Imaging the evolution of metallic states in a correlated iridate. *Nature Materials*, 12(8):707–713, 2013.
- [127] E. Abrahams, P. W. Anderson, D. C. Licciardello, and T. V. Ramakrishnan. Scaling Theory of Localization: Absence of Quantum Diffusion in Two Dimensions. *Phys. Rev. Lett.*, 42:673–676, Mar 1979.
- [128] Tsuneya Ando, Alan B. Fowler, and Frank Stern. Electronic properties of two-dimensional systems. *Rev. Mod. Phys.*, 54:437–672, Apr 1982.
- [129] Yoichi Ando, A. N. Lavrov, Seiki Komiya, Kouji Segawa, and X. F. Sun. Mobility of the Doped Holes and the Antiferromagnetic Correlations in Underdoped High- T_c Cuprates. *Phys. Rev. Lett.*, 87:017001, Jun 2001.
- [130] A. de la Torre, S. McKeown Walker, F. Y. Bruno, S. Ricco, Z. Wang, I. Gutierrez Lezama, G. Scheerer, G. Girit, D. Jaccard, C. Berthod, T. K. Kim, M. Hoesch, E. C. Hunter, R. S. Perry, A. Tamai, and F. Baumberger. Collapse of the Mott Gap and Emergence of a Nodal Liquid in Lightly Doped Sr_2IrO_4 . *Phys. Rev. Lett.*, 115:176402, Oct 2015.
- [131] N. F. Mott. Conduction in non-crystalline systems IX. the minimum metallic conductivity. *The Philosophical Magazine: A Journal of Theoretical Experimental and Applied Physics*, 26(4):1015–1026, 1972.
- [132] Xiang Chen, Julian L. Schmehr, Zahirul Islam, Zach Porter, Eli Zoghlin, Kenneth Finkelstein, Jacob P. C. Ruff, and Stephen D. Wilson. Unidirec-

- tional spin density wave state in metallic $(\text{Sr}_{1-x}\text{La}_x)_2\text{IrO}_4$. *Nature Communications*, 9(1):103, 2018.
- [133] J. P. Clancy, N. Chen, C. Y. Kim, W. F. Chen, K. W. Plumb, B. C. Jeon, T. W. Noh, and Young-June Kim. Spin-orbit coupling in iridium-based $5d$ compounds probed by X-ray absorption spectroscopy. *Phys. Rev. B*, 86:195131, Nov 2012.
- [134] S. Boseggia, R. Springell, H. C. Walker, A. T. Boothroyd, D. Prabhakaran, D. Wermeille, L. Bouchenoire, S. P. Collins, and D. F. McMorrow. Antiferromagnetic order and domains in $\text{Sr}_3\text{Ir}_2\text{O}_7$ probed by X-ray resonant scattering. *Phys. Rev. B*, 85:184432, May 2012.
- [135] S. Fujiyama, H. Ohsumi, T. Komesu, J. Matsuno, B. J. Kim, M. Takata, T. Arima, and H. Takagi. Two-Dimensional Heisenberg Behavior of $J_{\text{eff}}=1/2$ Isospins in the Paramagnetic State of the Spin-Orbital Mott Insulator Sr_2IrO_4 . *Phys. Rev. Lett.*, 108:247212, Jun 2012.
- [136] S. Boseggia, R. Springell, H. C. Walker, H. M. Rønnow, Ch. Rüegg, H. Okabe, M. Isobe, R. S. Perry, S. P. Collins, and D. F. McMorrow. Robustness of basal-plane antiferromagnetic order and the $J_{\text{eff}}=1/2$ state in Single-Layer Iridate Spin-Orbit Mott Insulators. *Phys. Rev. Lett.*, 110:117207, Mar 2013.
- [137] Kenya Ohgushi, Jun-ichi Yamaura, Hiroyuki Ohsumi, Kuniyoshi Sugimoto, Soshi Takeshita, Akihisa Tokuda, Hidenori Takagi, Masaki Takata, and Takahisa Arima. Resonant X-ray Diffraction Study of the Strongly Spin-Orbit-Coupled Mott Insulator CaIrO_3 . *Phys. Rev. Lett.*, 110:217212, May 2013.
- [138] J. P. Clancy, A. Lupascu, H. Gretarsson, Z. Islam, Y. F. Hu, D. Casa, C. S. Nelson, S. C. LaMarra, G. Cao, and Young-June Kim. Dilute magnetism and spin-orbital percolation effects in $\text{Sr}_2\text{Ir}_{1-x}\text{Rh}_x\text{O}_4$. *Phys. Rev. B*, 89:054409, Feb 2014.
- [139] C. Donnerer, M. C. Rahn, M. Moretti Sala, J. G. Vale, D. Pincini, J. Stremper, M. Krisch, D. Prabhakaran, A. T. Boothroyd, and D. F. Mc-

- Morrow. All-in-all-Out Magnetic Order and Propagating Spin Waves in $\text{Sm}_2\text{Ir}_2\text{O}_7$. *Phys. Rev. Lett.*, 117:037201, Jul 2016.
- [140] Nicholas P. Breznay, Alejandro Ruiz, Alex Frano, Wenli Bi, Robert J. Birgeneau, Daniel Haskel, and James G. Analytis. Resonant X-ray scattering reveals possible disappearance of magnetic order under hydrostatic pressure in the Kitaev candidate $\gamma\text{-Li}_2\text{IrO}_3$. *Phys. Rev. B*, 96:020402, Jul 2017.
- [141] Robert J. Birgeneau, Chris Stock, John M. Tranquada, and Kazuyoshi Yamada. Magnetic Neutron Scattering in Hole-Doped Cuprate Superconductors. *Journal of the Physical Society of Japan*, 75(11):111003, 2006.
- [142] S. Wakimoto, G. Shirane, Y. Endoh, K. Hirota, S. Ueki, K. Yamada, R. J. Birgeneau, M. A. Kastner, Y. S. Lee, P. M. Gehring, and S. H. Lee. Observation of incommensurate magnetic correlations at the lower critical concentration for superconductivity in $\text{La}_{2-x}\text{Sr}_x\text{CuO}_4$ ($x = 0.05$). *Phys. Rev. B*, 60:R769–R772, Jul 1999.
- [143] S. Wakimoto, R. J. Birgeneau, M. A. Kastner, Y. S. Lee, R. Erwin, P. M. Gehring, S. H. Lee, M. Fujita, K. Yamada, Y. Endoh, K. Hirota, and G. Shirane. Direct observation of a one-dimensional static spin modulation in insulating $\text{La}_{1.95}\text{Sr}_{0.05}\text{CuO}_4$. *Phys. Rev. B*, 61:3699–3706, Feb 2000.
- [144] I Battisti, K M Bastiaans, V Fedoseev, A De Torre, N Iliopoulos, A Tamai, E C Hunter, R S Perry, J Zaanen, F Baumberger, and M P Allan. Universality of pseudogap and emergent order in lightly doped Mott insulators. *Nature Physics*, 13(January):21–26, 2017.
- [145] Yue Cao, Qiang Wang, Justin A. Waugh, Theodore J. Reber, Haoxiang Li, Xiaoqing Zhou, Stephen Parham, S. R. Park, Nicholas C. Plumb, Eli Rotenberg, Aaron Bostwick, Jonathan D. Denlinger, Tongfei Qi, Michael A. Hermele, Gang Cao, and Daniel S. Dessau. Hallmarks of the Mott-metal crossover in the hole-doped pseudospin-1/2 Mott insulator Sr_2IrO_4 . *Nature Communications*, 7:1–7, 2016.

- [146] L. Zhao, D. H. Torchinsky, H. Chu, V. Ivanov, R. Lifshitz, R. Flint, T. Qi, G. Cao, and D. Hsieh. Evidence of an odd-parity hidden order in a spin-orbit coupled correlated iridate. *Nature Physics*, 12(1):32–36, 2016.
- [147] Jaehong Jeong, Yvan Sidis, Alex Louat, Véronique Brouet, and Philippe Bourges. Time-reversal symmetry breaking hidden order in $\text{Sr}_2(\text{Ir,Rh})\text{O}_4$. *Nature Communications*, 8:8–13, 2017.
- [148] Sen Zhou, Kun Jiang, Hua Chen, and Ziqiang Wang. Correlation Effects and Hidden Spin-Orbit Entangled Electronic Order in Parent and Electron-Doped Iridates Sr_2IrO_4 . *Phys. Rev. X*, 7:041018, Oct 2017.
- [149] M. Fujita, K. Yamada, H. Hiraka, P. M. Gehring, S. H. Lee, S. Wakimoto, and G. Shirane. Static magnetic correlations near the insulating-superconducting phase boundary in $\text{La}_{2-x}\text{Sr}_x\text{CuO}_4$. *Phys. Rev. B*, 65:064505, Jan 2002.
- [150] Gil Drachuck, Elia Razzoli, Galina Bazalitski, Amit Kanigel, Christof Niedermayer, Ming Shi, and Amit Keren. Comprehensive study of the spin-charge interplay in antiferromagnetic $\text{La}_{2-x}\text{Sr}_x\text{CuO}_4$. *Nature communications*, 5:3390, 2014.
- [151] M. Matsuda, M. Fujita, K. Yamada, R. J. Birgeneau, Y. Endoh, and G. Shirane. Electronic phase separation in lightly doped $\text{La}_{2-x}\text{Sr}_x\text{CuO}_4$. *Phys. Rev. B*, 65:134515, Mar 2002.
- [152] H. Kimura, H. Matsushita, K. Hirota, Y. Endoh, K. Yamada, G. Shirane, Y. S. Lee, M. A. Kastner, and R. J. Birgeneau. Incommensurate geometry of the elastic magnetic peaks in superconducting $\text{La}_{1.88}\text{Sr}_{0.12}\text{CuO}_4$. *Phys. Rev. B*, 61:14366–14369, Jun 2000.
- [153] Boris I. Shraiman and Eric D. Siggia. Spiral phase of a doped quantum antiferromagnet. *Phys. Rev. Lett.*, 62:1564–1567, Mar 1989.

- [154] C. L. Kane, P. A. Lee, T. K. Ng, B. Chakraborty, and N. Read. Mean-field theory of the spiral phases of a doped antiferromagnet. *Phys. Rev. B*, 41:2653–2656, Feb 1990.
- [155] Andreas Lüscher, Alexander I. Milstein, and Oleg P. Sushkov. Structure of the Spin-Glass State of $\text{La}_{2-x}\text{Sr}_x\text{CuO}_4$: The Spiral Theory. *Phys. Rev. Lett.*, 98:037001, Jan 2007.
- [156] Tetsuo Shimura, Yoshiyuki Inaguma, Tetsuro Nakamura, Mitsuru Itoh, and Yukio Morii. Structure and magnetic properties of $\text{Sr}_{2-x}\text{A}_x\text{IrO}_4$ ($A = \text{Ca}$ and Ba). *Phys. Rev. B*, 52:9143–9146, Oct 1995.
- [157] Juan Rodríguez-Carvajal. Recent advances in magnetic structure determination by neutron powder diffraction. *Physica B: Condensed Matter*, 192(1):55 – 69, 1993.
- [158] We define the measured direction as (1, 1, 1), however due to the low symmetry, there are other possible orientations: (-3, 1, 1); (3, 1, -1); (0, 0, 2); (4, 0, -2); (-1, 1, -1). Nevertheless no appreciable difference is observed when measurements along orthogonal directions of the crystal were performed.
- [159] Hk Mller-Buschbaum. The crystal chemistry of AM_2O_4 Oxometallates. *Journal of Alloys and Compounds*, 349(1C2):49 – 104, 2003.
- [160] Y.G. Shi, Y.F. Guo, S. Yu, M. Arai, A.A. Belik, A. Sato, K. Yamaura, E. Takayama-Muromachi, T. Varga, and J.F. Mitchell. High-pressure crystal growth and magnetic and electrical properties of the quasi-one dimensional osmium oxide Na_2OsO_4 . *Journal of Solid State Chemistry*, 183(2):402 – 407, 2010.
- [161] Dietrich Babel, Walter Rüdorff, and Renate Tschöpp. Ternäre Oxide der Übergangsmetalle. VI. Erdalkaliiridium(IV)-oxide: Struktur von Dicalciumiridium(IV)-oxid, Ca_2IrO_4 . *Zeitschrift für anorganische und allgemeine Chemie*, 347(5-6):282–288.

- [162] Makoto Wakeshima, Nobuyuki Taira, Yukio Hinatsu, and Yoshinobu Ishii. Electrical and magnetic properties of pseudo-one-dimensional calcium iridium oxide $\text{Ca}_5\text{Ir}_3\text{O}_{12}$. *Solid State Communications*, 125(6):311 – 315, 2003.
- [163] G. Cao, V. Durairaj, S. Chikara, S. Parkin, and P. Schlottmann. Partial antiferromagnetism in spin-chain $\text{Sr}_5\text{Rh}_4\text{O}_{12}$, $\text{Ca}_5\text{Ir}_3\text{O}_{12}$, and Ca_4IrO_6 single crystals. *Phys. Rev. B*, 75:134402, Apr 2007.
- [164] Jill C. Bonner and Michael E. Fisher. Linear Magnetic Chains with Anisotropic Coupling. *Phys. Rev.*, 135:A640–A658, Aug 1964.
- [165] H. J. Williams, J. H. Wernick, R. C. Sherwood, and G. K. Wertheim. Magnetic Properties of the Monosilicides of Some 3d Transition Elements. *Journal of Applied Physics*, 37(3):1256–1256, 1966.
- [166] J.H. Wernick, G.K. Wertheim, and R.C. Sherwood. Magnetic behavior of the monosilicides of the 3d-transition elements. *Materials Research Bulletin*, 7(12):1431 – 1441, 1972.
- [167] E. Fawcett, J. P. Maita, and J. H. Wernick. Magnetoelastic and thermal properties of mnsi. *Int. J. Magn.*, 1:29, 1970.
- [168] D. Bloch, J. Voiron, V. Jaccarino, and J.H. Wernick. The high field-high pressure magnetic properties of MnSi. *Physics Letters A*, 51(5):259 – 261, 1975.
- [169] Y. Ishikawa, K. Tajima, D. Bloch, and M. Roth. Helical spin structure in manganese silicide MnSi. *Solid State Communications*, 19(6):525 – 528, 1976.
- [170] Y. Ishikawa. Neutron scattering studies of itinerant electron magnetism. *Journal of Applied Physics*, 49(3):2125–2130, 1978.
- [171] Y. Ishikawa, Y. Noda, C. Fincher, and G. Shirane. Low-energy paramagnetic spin fluctuations in the weak itinerant ferromagnet MnSi. *Phys. Rev. B*, 25:254–263, Jan 1982.

- [172] G. Shirane, R. Cowley, C. Majkrzak, J. B. Sokoloff, B. Pagonis, C. H. Perry, and Y. Ishikawa. Spiral magnetic correlation in cubic MnSi. *Phys. Rev. B*, 28:6251–6255, Dec 1983.
- [173] Yoshikazu Ishikawa and Masatoshi Arai. Magnetic Phase Diagram of MnSi near Critical Temperature Studied by Neutron Small Angle Scattering. *Journal of the Physical Society of Japan*, 53(8):2726–2733, 1984.
- [174] C. Pfleiderer, G. J. McMullan, S. R. Julian, and G. G. Lonzarich. Magnetic quantum phase transition in MnSi under hydrostatic pressure. *Phys. Rev. B*, 55:8330–8338, Apr 1997.
- [175] C Thessieu, C Pfleiderer, A N Stepanov, and J Flouquet. Field dependence of the magnetic quantum phase transition in MnSi. *Journal of Physics: Condensed Matter*, 9(31):6677, 1997.
- [176] D. Belitz, T. R. Kirkpatrick, and Thomas Vojta. First Order Transitions and Multicritical Points in Weak Itinerant Ferromagnets. *Phys. Rev. Lett.*, 82:4707–4710, Jun 1999.
- [177] N Manyala, Y Sidis, J. F. DiTusa, G Aeppli, DP Young, and Z Fisk. Magneto resistance from quantum interference effects in ferromagnets. *Nature*, 404(6778):581–584, 2000.
- [178] C. Pfleiderer, S. R. Julian, and G. G. Lonzarich. Non-Fermi-liquid nature of the normal state of itinerant-electron ferromagnets. *Nature*, 414(6862):427–430, 2001.
- [179] B. Roessli, P. Böni, W. E. Fischer, and Y. Endoh. Chiral Fluctuations in MnSi above the Curie Temperature. *Phys. Rev. Lett.*, 88:237204, May 2002.
- [180] N. Doiron-Leyraud, I. R. Walker, L. Taillefer, M. J. Steiner, S. R. Julian, and G. G. Lonzarich. Fermi-liquid breakdown in the paramagnetic phase of a pure metal. *Nature*, 425(6958):595–599, 2003.

- [181] C. Pfleiderer, D. Reznik, L. Pintschovius, H. v Löhneysen, M. Garst, and A. Rosch. Partial order in the non-Fermi-liquid phase of MnSi. *Nature*, 427:227–231, 2004.
- [182] U. K. Rößler, A. N. Bogdanov, and C. Pfleiderer. Spontaneous skyrmion ground states in magnetic metals. *Nature*, 442(7104):797–801, 2006.
- [183] Minhyea Lee, W. Kang, Y. Onose, Y. Tokura, and N. P. Ong. Unusual Hall Effect Anomaly in MnSi under Pressure. *Phys. Rev. Lett.*, 102:186601, May 2009.
- [184] A. Neubauer, C. Pfleiderer, B. Binz, A. Rosch, R. Ritz, P. G. Niklowitz, and P. Böni. Topological Hall Effect in the A Phase of MnSi. *Phys. Rev. Lett.*, 102:186602, May 2009.
- [185] C. Pappas, E. Lelièvre-Berna, P. Falus, P. M. Bentley, E. Moskvin, S. Grigoriev, P. Fouquet, and B. Farago. Chiral Paramagnetic Skyrmion-like Phase in MnSi. *Phys. Rev. Lett.*, 102:197202, May 2009.
- [186] M. Janoschek, F. Bernlochner, S. Dunsiger, C. Pfleiderer, P. Böni, B. Roessli, P. Link, and A. Rosch. Helimagnon bands as universal excitations of chiral magnets. *Phys. Rev. B*, 81:214436, Jun 2010.
- [187] F. Jonietz, S. Mulbauer, C. Pfleiderer, A. Neubauer, W. Munzer, A. Bauer, T. Adams, R. Georgii, P. Boni, R. A. Duine, K. Everschor, M. Garst, and A. Rosch. Spin Transfer Torques in MnSi. *Science*, 330(September):1648–1652, 2011.
- [188] T. Schulz, R. Ritz, A. Bauer, M. Halder, M. Wagner, C. Franz, C. Pfleiderer, K. Everschor, M. Garst, and A. Rosch. Emergent electrodynamics of skyrmions in a chiral magnet. *Nature Physics*, 8(4):301–304, 2012.
- [189] Naoto Nagaosa and Yoshinori Tokura. Topological properties and dynamics of magnetic skyrmions. *Nature Nanotechnology*, 8(12):899–911, 2013.

- [190] R. Ritz, M. Halder, M. Wagner, C. Franz, A. Bauer, and C. Pfleiderer. Formation of a topological non-Fermi liquid in MnSi. *Nature*, 497(7448):231–234, 2013.
- [191] M. Kugler, G. Brandl, J. Waizner, M. Janoschek, R. Georgii, A. Bauer, K. Seemann, A. Rosch, C. Pfleiderer, P. Böni, and M. Garst. Band Structure of Helimagnons in MnSi Resolved by Inelastic Neutron Scattering. *Phys. Rev. Lett.*, 115:097203, Aug 2015.
- [192] Hiroshi Yasuoka, Kiyochiro Motoya, Mayukh Majumder, Sebastian Witt, Cornelius Krellner, and Michael Baenitz. Chiral Magnetism in an Itinerant Helical Magnet, MnSi – An Extended ^{29}Si NMR Study. *Journal of the Physical Society of Japan*, 85(7):073701, 2016.
- [193] X. Z. Yu, Y. Onose, N. Kanazawa, J. H. Park, J. H. Han, Y. Matsui, N. Nagaosa, and Y. Tokura. Real-space observation of a two-dimensional skyrmion crystal. *Nature*, 465(7300):901–904, 2010.
- [194] X. Z. Yu, N. Kanazawa, Y. Onose, K. Kimoto, W. Z. Zhang, S. Ishiwata, Y. Matsui, and Y. Tokura. Near room-temperature formation of a skyrmion crystal in thin-films of the helimagnet FeGe. *Nature Materials*, 10(2):106–109, 2011.
- [195] Stefan Heinze, Kirsten Von Bergmann, Matthias Menzel, Jens Brede, André Kubetzka, Roland Wiesendanger, Gustav Bihlmayer, and Stefan Blügel. Spontaneous atomic-scale magnetic skyrmion lattice in two dimensions. *Nature Physics*, 7(9):713–718, 2011.
- [196] S. Seki, X. Z. Yu, S. Ishiwata, and Y. Tokura. Observation of skyrmions in a multiferroic material. *Science*, 336(6078):198–201, 2012.
- [197] D. Belitz, T. R. Kirkpatrick, and A. Rosch. Theory of helimagnons in itinerant quantum systems. *Phys. Rev. B*, 73:054431, Feb 2006.

- [198] Yi Zhang, P. Farinas, and K. Bedell. The "Higgs" Amplitude Mode in Weak Ferromagnetic Metals. *Acta Physica Polonica A*, 127:153–156, 02 2015.
- [199] Kevin S. Bedell and Krastan B. Blagoev. Quantum spin hydrodynamics and a new spin-current mode in ferromagnetic metals. *Philosophical Magazine Letters*, 81(7):511–517, 2001.
- [200] S Tixier, P Böni, Y Endoh, B Roessli, and G Shirane. Polarisation dependence of the magnetic fluctuations in the weak itinerant ferromagnet MnSi below T_c . *Physica B: Condensed Matter*, 241-243:613 – 615, 1997. Proceedings of the International Conference on Neutron Scattering.
- [201] Peter Böni, Bertrand Roessli, and Klaudia Hradil. Inelastic neutron and X-ray scattering from incommensurate magnetic systems. *Journal of Physics: Condensed Matter*, 23(25):254209, 2011.
- [202] Jun Zhao, D. T. Adroja, Dao-Xin Yao, R. Bewley, Shiliang Li, X. F. Wang, G. Wu, X. H. Chen, Jiangping Hu, and Pengcheng Dai. Spin waves and magnetic exchange interactions in CaFe_2As_2 . *Nature Physics*, 5(8):555–560, 2009.